CHAPTER-I

Introduction

This chapter highlights about the exciting and emerging field of conducting polymers with an emphasis on different nanostructures of conducting polymers. The chapter deals with the historical background and potential applications of conducting polymers. The mechanism of electrical transport in conducting polymers and various synthesis methods for preparation of conducting polymer nanostructures as intelligent material systems along with the potential importance of swift heavy ion irradiation for modification of physico-chemical properties of conducting polymers are also discussed. In the end, the chapter outlines the scope of the thesis and statement of the thesis problem.

1.1. Conducting polymers: Historical background

Discovery of polymers has given a new dimension in the present era. In general, polymers are known as a class of heat sensitive, flexible, electrically insulating amorphous materials. The polymers either natural or synthetic are large macromolecules comprising of small building blocks or repeating units connected by each other by covalent bonds. The polymers are generally known for their insulating properties because of the covalent bond present in the saturated carbon compounds [1]. After the discovery of polyacetylene as a highly conductive organic material in 1977 [2], a class of materials called the conjugated polymers or intrinsically conducting polymers (ICPs) could be differentiate from the rest of the polymers. The path breaking discovery of conducting polymers was celebrated in the form of Nobel Prize in chemistry to A. G. MacDiarmid, A. J. Heeger and H. Shirakawa in the year of 2000. Conducting polymers are also known as "conjugated polymers" because of their ability to conduct electricity due to the presence of alternate single and double bonds along the backbone structures [3]. The special conjugation in the chain of conducting polymers enables to some of the π-electrons to be delocalized. The delocalized π-electrons can move throughout the whole system and become the charge carriers to make the polymer conductive. Thus this type of polymers can be transformed into a conductive state when electrons are removed from the backbone resulting in cations or added to the backbone resulting as

anions. The anions and cations behave as charge carriers which jump from one site to the other site under the influence of electric field resulting increasing in electrical conductivity [4]. During the last few decades the conducting polymers have attracted an overwhelming interest around the world due to their considerable potential applications in scientific and industrial areas. Because of the broad range of electrical conductivities and vast uses in number of electronics and optoelectronics applications, conducting polymers can replace the conventionally used metallic conductors. Different types of conductive polymers such as polypyrrole (PPy), polyaniline (PAni), Polythiophene (PTh) and poly(3, 4-ethylenedioxythiophene) (PEDOT) have been studied extensively with a broad range of electrical conductivities i.e. from 10^{-10} to 10^{5} S/cm [5]. Fig. 1.1 depicts the chemical structures of some of the mostly studied conducting polymers. The comparison of conductivity values of conducting polymers with some common metallic and semiconducting materials are shown in Fig. 1.2.

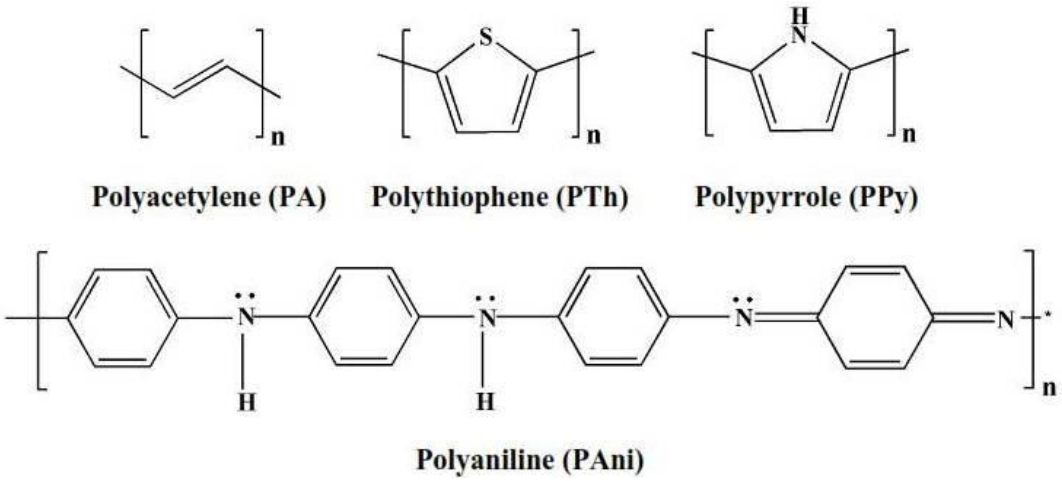

Figure 1.1: *Chemical structure of some mostly studied conducting polymers.*

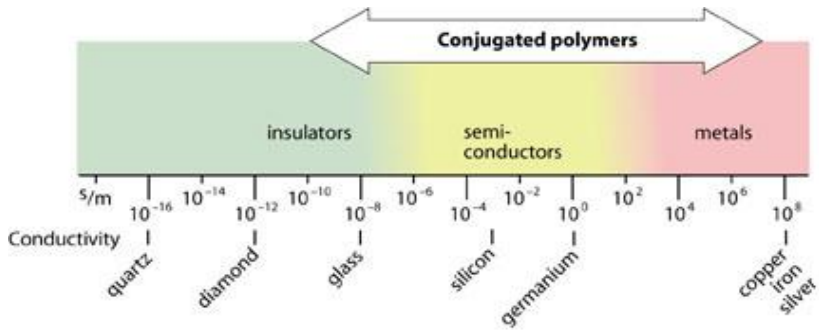

Figure 1.2: *Diagram showing range of conductivity for various materials including conducting polymers [6].*

1.2. Applications of conducting polymers

Conducting polymers are functional materials which can be used as organic conductors taking the advantages of excellent mechanical strength and light weight. The potential applications of various conducting polymers include in sensors (including gas and bio sensors) [7, 8], actuators [9], super capacitors [10], polymeric rechargeable batteries [11], electro-chromic windows and displays [12], functional membrane [13], drug and bio molecule release [14], corrosion protection, light emitting devices [15, 16], photovoltaic applications [17, 18] etc. Fig. 1.3 shows pictorial diagrams of different applications of conducting polymers.

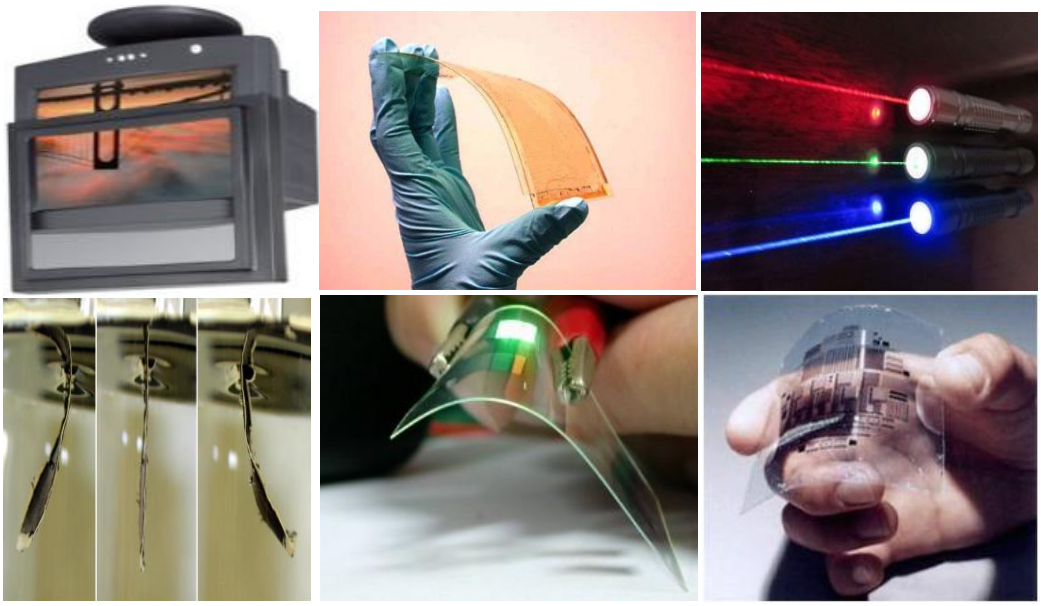

Figure 1.3: *Different applications of conducting polymers as smart window, solar cell, actuator, organic light emitting diodes and organic thin film transistor.*

1.2.1. Field effect transistor

The field effect transistor (FET) is a type of transistor that relies on an electric field to control the shape and hence the conductivity of a channel one type of charge carriers in semiconducting materials. FETs are also called the unipolar transistor to contrast their single carrier type operation with the dual-carrier-type operation of bipolar junction transistors (BJT). An organic field-effect transistor (OFET) is a field effect transistor that uses an organic semiconductor such as conducting polymers in its channel. These

devices have been fabricated to realize low-cost, large area electronic products. Xue et al. [19] developed two field effect transistors by both spin-coating and ink-jet-printing methods using conducting polypyrrole (PPy) as semiconducting materials. The spin-coated transistor showed better device performance than that of the ink-jet-printed transistor. Covington et al. [20] fabricated polymer FET for gas sensor applications. Ashizawa et al. [21] developed the fabrication of a metal-insulator-semiconductor field effect transistor (MISFET) using poly(3,4-ethylenedioxythiophene) doped with poly(4-styrenesulfonate) as an active channel by the multiple line patterning which is one of the most simple, rapid and inexpensive method capable of making patterns of conducting polymers, insulators and metals using a standard laser printer. The MISFET operated both in the depletion and enhancement modes in response to positive and negative gate voltages, respectively, where the gate current was crucial to the performance of the device. Liu et al. [22] fabricated an all-polymer field-effect transistor (FET) using an ink-jet printing technique. Poly(3, 4-ethylenedioxythiophene) works as the source/drain/gate electrode material because of its good conductivity. Polypyrrole acts as the semiconducting layer and Poly(vinyl pyrrolidone); an insulating polymer with a dielectric constant of 60 operates as the dielectric layer.

1.2.2. Sensors

Conducting polymers have wide range of applications as sensors. There are different types of sensors that use conducting polymers such as polyaniline, polypyrrole, polythiophine etc. as the active layers. Bai et al. [8] reviewed fabrication of the gas sensors using different conducting polymers such as polyaniline (PAni), polypyrrole (PPy) and poly(3, 4-ethylenedioxythiophene) (PEDOT) as the active layers. The conducting polymer films were prepared using different fabrication methods such as the electrochemical deposition, dip coating, spin coating etc. Shrivas et al. [23] studied the toxic gas sensing property by PAni thin film for ammonia gas. One dimensional conducting polymer nanofibers are promising materials due to their chemical doping specificities, large surface areas, high electrical conductivity, light weights, low cost, easy processing and scalable productions. The nanofibrillar morphology significantly improves the performance of conducting polymer in applications such as biosensors [24] and chemical sensors [25, 26]. S. Virji et al. [27] developed Polyaniline (PAni) nanofibers gas sensor and compared them to the conventional PAni sensors. The higher

surface area, porosity and small diameters enhanced the diffusion of molecules and dopants into the PAni nanofibers and hence the PAni nanofibers showed enhanced sensing compared to the conventional thin films. The basic requirement for a chemical or biological sensor is to convert a molecular binding event into a measurable signal. Conducting polymers are attractive for sensor applications because of their ability to directly convert the binding event into an electrical signal. Additionally conducting polymers can be modified chemically with functional groups for specific recognition and detection of different analytes. Because of these unique properties, many groups have applied conducting polymers into the chemical and biosensors applications [28-30]. Forzani et al. [31] presented different chemical sensor applications based on nanoscale functionalized conducting polymer junction arrays.

1.2.3. Shielding of electromagnetic interference

In recent years, electromagnetic interference (EMI) problem or electromagnetic pollution has received wide attention because of the malfunctioning of the electronic equipments from the radiations generated from the source or emanating from other electronic equipments. The research on the last past decades has established the ability of polymer composites made with electrically conducting polymers to be suitable as a shield against the electromagnetic interference [32-36]. Koul et al. [37] studied the electromagnetic interference shielding effectiveness of conducting PAni-ABS composites at 101 GHz. The shielding effectiveness of the composites increases with the increase in the loading levels of the conducting polymer doped with hybrid dopants. Kim et al. [38] fabricated intrinsically conducting polymer (ICP)/PET textile composites by chemical and electrochemical polymerization approach and investigated the effects of the chemical or electrochemical polymerization conditions on the properties of resulting composites, such as electrical conductivity and electromagnetic interference shielding effectiveness (EMI SE). ICPs are new alternative candidates for EMI shielding applications because of their corrosion resistance, lightweight, ease of processing and tunable electrical conductivities.

1.2.4. Polymer light-emitting diodes

Conjugated polymers show the semiconducting behavior due to the presence of delocalized π-electron along the polymer chain. The π-bonding and π^*-antibonding form the delocalized valence and conduction wave functions, which support the mobile charge carriers. The electroluminescence from conducting polymers was first reported using poly(phenylene vinylene) (PPV) as the single semiconductor layer between aluminium electrodes [39]. In this structure, the indium-tin oxide (ITO) layer behaves as a transparent electrode and allows the light generated within the diode to leave the device. The LED operation can be obtained with sufficient biased to achieve injection of positive and negative charge carriers from opposite electrodes. The capture of oppositely charged carriers within the region of the polymer layer can then result in photon emission. Such type of LED can be fabricated by solution processing of the semiconducting polymer onto the ITO-coated glass such that the film thickness is no more than typically of 100 nm.

1.2.5. Solar cells

Polymer solar cells are a type of organic solar cell which produces electricity from sunlight using polymers. In general, solar cells are made from the refined, highly purified silicon crystal. However, the high cost and complex production process of silicon solar cell has increased interest in alternative photovoltaic technologies. As compared to silicon-based solar cells, the conducting polymer solar cells have the advantages of their lightweight, disposable, inexpensive to fabricate, flexible, customizable on the molecular level and have lower potential for negative environmental impact.

1.2.6. Artificial muscles

The use of conducting polymers as artificial muscles was first demonstrated by Baughman and co-workers in 1990 [40]. The conducting polymer artificial muscles use the dimensional changes resulting from electrochemical ion insertion, possibly along with associated solvating species. Since both the electrodes can comprise conducting polymers, they can be used as artificial muscles. Depending upon the conducting polymer/electrolyte system used, the initial state and the rate of potential change used

for actuation, electron insertion into one electrode can be accompanied by a volume increase as cations are inserted or a volume decrease as anions are removed. Similar processes can occur at the counter-electrode. Hara et al. [41] reported on the artificial muscles based on polypyrrole actuators with large strain and stress. In another previous study, Otero et al. [42] reported on the construction and electrochemomechanical characterization of the polypyrrole artificial muscles.

1.3. Doping in conducting polymers

The concept of doping is the unique, central, underlying and unifying theme which distinguishes conducting polymers from all other types of polymers [43, 44]. In general the intrinsic conducting polymers exhibit poor electrical conductivity (~ 10^{-12} S/cm) in their intrinsic states and behave as insulator. The intrinsic conducting polymers need to be treated with a suitable oxidizing or reducing agent to increase their electrical conductivity to the metallic or semiconducting regime. This phenomenon is termed as "doping". In general, doping can be regarded as the insertion or injection of electrons and doping in conducting polymers results in dramatic changes in electrical, optical, magnetic and structural properties of the polymer. Upon doping the electrical conductivity of iodine doped polyacetylene (PA) can be increased by 9-13 orders of magnitude [43]. Doping is accomplished by the chemical methods of direct exposure of the intrinsic conducting polymer to a charge transfer agent, called the dopant in the gas or solution phase, or the electrochemical oxidation or reduction. Doping of conducting polymers is usually quantitative and the carrier concentration is directly proportional to the dopant concentration and doping in conducting polymers involves the random dispersion or aggregation of dopants in molar concentration in the disordered structure [45]. Doping of conducting polymers leads to the formation of conjugation defects viz. solitons, polarons or bipolarons in the polymer chains. X-ray diffraction study on iodine doped polyacetylene showed that the C-C bond length in polyacetylene chain increased with donor doping while the C-C length decreased with the acceptor doping. The presence of localized electronic states of energies less than the band gap arising from changes in the local bond order, including the formation of soliton, polaron or bipolarons have led to the possibility of new types of charge conduction present in these polymer systems. Table 1.1 shows the charge and spin characteristics of these defects.

Table 1.1: Typical properties of solitons, polarons and bipolarons.

Defect	Spin	Charge	
Soliton	1/2	neutral	0
Soliton	0	charged	+ e or - e
Polaron	1/2	charged	+ e or - e
Bipolaron	0	charged	+ 2e or - 2e

The resultant conductivity in conducting polymers depend on many factors, viz. nature and concentration of dopant, homogeneity of doping, carrier mobility, crystallinity and morphology of the polymer. In general, n-type doping is achieved with an electron acceptor and p-type doping is conducted with an electron donor. The dopants are either strong oxidizing or reducing agents and on doping, either positive or negative charges are created in conducting polymers.

$$Polymer + Dopant \rightarrow [Polymer^{+} - Dopant^{-}]$$

(Acceptor) **Charge transfer complex**

$$Polymer + Dopant \rightarrow [Polymer^{+} - Dopant^{-}]$$

(Donor) **Charge transfer complex**

Figure 1.4: *Action of a dopant on polymer.*

1.3.1. Different types of doping

The doping of conducting polymers can be done by the following methods [6]:

- ✓ **Redox doping**

Redox doping is the most common method of doping and is also known as oxidative doping which is accomplished by removing π-electrons from the conjugated polymers. The conducting polymers such as PAni, PPy, PTh etc. undergo p- and/or n- redox doping by chemical and /or electrochemical processes during which the number of electrons associated with the conducting polymer backbone changes.

✓ ***Photo doping***

When the polymers are exposed to radiation of energy greater than the band gap energy, the electrons are promoted across the band gap and polymer undergoes "photo-doping".

✓ ***Charge injection doping***

The charge injection doping is most conveniently carried out using a metal/insulator/semiconductor (MIS) configuration involving a metal and a conducting polymer separated by a thin layer of a high dielectric strength insulator. Application of an appropriate potential across the structure can give rise, for example, to a surface charge layer, the "accumulation" layer which has been extensively investigated for conducting polymers [46, 47]. The resulting charges in the polymer, for example $(CH)_X$ or poly(3-hexylthiophene) is present without any associated dopant ion. The spectroscopic properties of the charged species so formed can therefore be examined in the absence of dopant ion. Using this approach, the spectroscopic studies of $(CH)_x$ show the signature characteristic of solitons and the mid-gap absorption band observed in the chemically and electronically doped conducting polymers.

✓ ***Non redox doping***

This type of doping differs from the redox doping is that the number of electrons associated with the polymer backbone does not change during the doping process. The energy levels are rearranged during doping process. The emeraldine base form of polyaniline (PAni) was the first example of doping of a conjugated polymer to a highly conducting regime by this process to produce an environmentally stable polysemiquinone radical cation. This was accomplished by the treating emeraldine base with aqueous protonic acids and conductivity increased by nine to ten orders of magnitude [48, 49]. Protonic acid doping has subsequently been extended to systems such as poly(heteroaromatic vinylenes) [50].

1.3.2. Doping techniques

Doping in polymers can be done by following ways,

- Gaseous doping
- Solution doping
- Electrochemical doping
- Self doping
- Radiation induced doping
- Ion exchange doping

In gaseous doping process, the conducting polymers are exposed to the vapour of the dopant under vacuum. The level of doping can easily be controlled by controlling the temperature, vacuum and the time of exposure. Solution doping involves the use of a solvent in which all the products of doping are soluble and the polymer is treated with the dopant solution. In the electrochemical doping process, the simultaneous polymerization and doping occurs. In this method only ionic type dopants are used as the electrolyte in polar solvents.

1.4. Conduction mechanism in conducting polymers

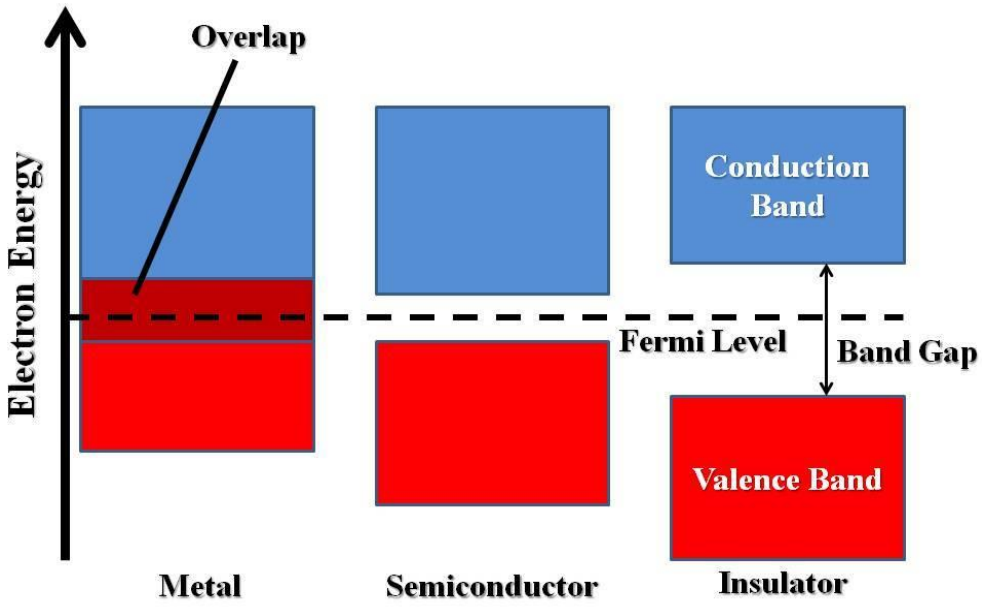

Figure 1.5: *Energy level diagrams for metal, semiconductor and insulator.*

The conducting polymers are a special class of organic semiconductors and hence the electrical properties of conducting polymers can be explained in a simple and straightforward way called the HOMO (Highest occupied molecular orbital)-LUMO (Lowest unoccupied molecular orbital) theory [51]. Although the conducting polymers possess a relatively large number of delocalized π-electrons, a fairly large energy gap exists between the valence band and conduction band (greater than 1 eV). Thus the conducting polymers are considered as semiconductors and hence must be doped (i.e. altering the number of π-electrons) in order to render electrical conductivity. The basic requirement for a polymer to become conductive is that there should be overlapping of molecular orbitals to allow the formation of delocalized molecular wave functions. This electronic delocalization provides the highway for charge carriers and the overall conducting properties depend on two components, namely (i) intrachain mobility which corresponds to the charge transfer along the polymer backbone chain and (ii) interchain mobility which involves the hopping and tunnelling of the charge carriers from a bond to neighboring bonds [52].

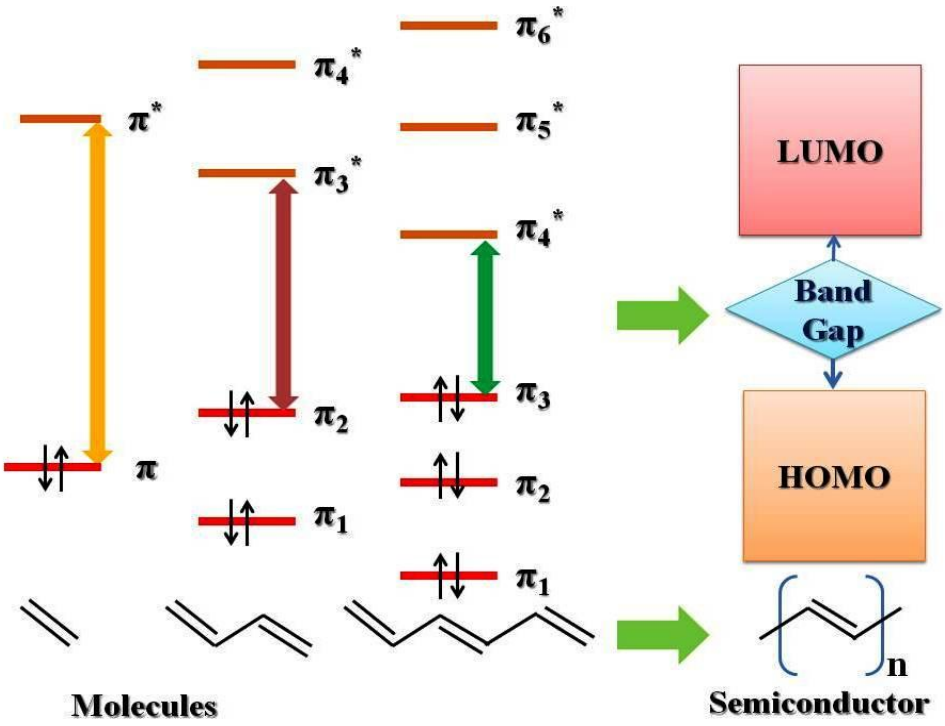

Figure 1.6: *HOMO-LUMO theory in organic semiconductor polymers.*

The transport behavior in conducting polymers depends on the type of charge carriers and band structure. The conduction mechanism and charge carriers' behavior

can be explained using the concept of polarons and bipolarons. A radical cation that is partially delocalized over some polymer segment is called a polaron (spin ½) that stabilizes itself by polarizing the medium around it. When the electron is removed from the top of the valence band, a hole (or radical cation) is generated that does not delocalize completely. Due to partial delocalization over several monomeric units, they form deformed structure. The energy level associated with this radical cation represents a destabilized bonding orbital having higher energy as compared to the valence band energy. If now another electron is removed from the already oxidized polymer containing polaron, two phenomena can happen: this removing electron can come from either a different segment of polymer chain generating another independent polaron, or from the first polaron level (removal of unpaired electron) to create a dication called the bipolaron. In particular, low doping level results polarons wherein the higher doping level produces bipolarons. As compared to the polaron, bipolaron is doubly charged but spin less. Both the polarons and bipolarons are mobile and can move along the polymer chain by rearrangement of double and single bonds in the conjugated system. If the polymer is highly doped, many bipolarons are formed as a result of which their energies can start overlapping at the edges, which creates narrow bipolaron bands in the band gap. The energy difference between the top of the valence band and bottom of the conduction band is called the band gap energy of the material. The conducting polymers either have a zero band gap or a very low band gap. The band gap controls the electronic and optical properties of conducting polymers. A reduction in optical band gap energy leads to a higher conductivity in conducting polymers and hence attempts have been made to reduce the band gap energy in such polymers by using the various methods.

1.5. Polypyrrole as a promising conducting polymer

Polypyrrole (PPy) is one of the most widely studied intrinsic conducting polymers among the family of conducting polymers in different areas of science and technology. PPy can be obtained from the polymerization of pyrrole (Py) monomer. The most common methods applied to synthesis PPy are chemical oxidative polymerization with doping, electrochemical polymerization, plasma polymerization and the organic synthesis. The general mechanism of oxidative polymerization of pyrrole (Py) monomer can be explained in the following way as shown in Fig. 1.7.

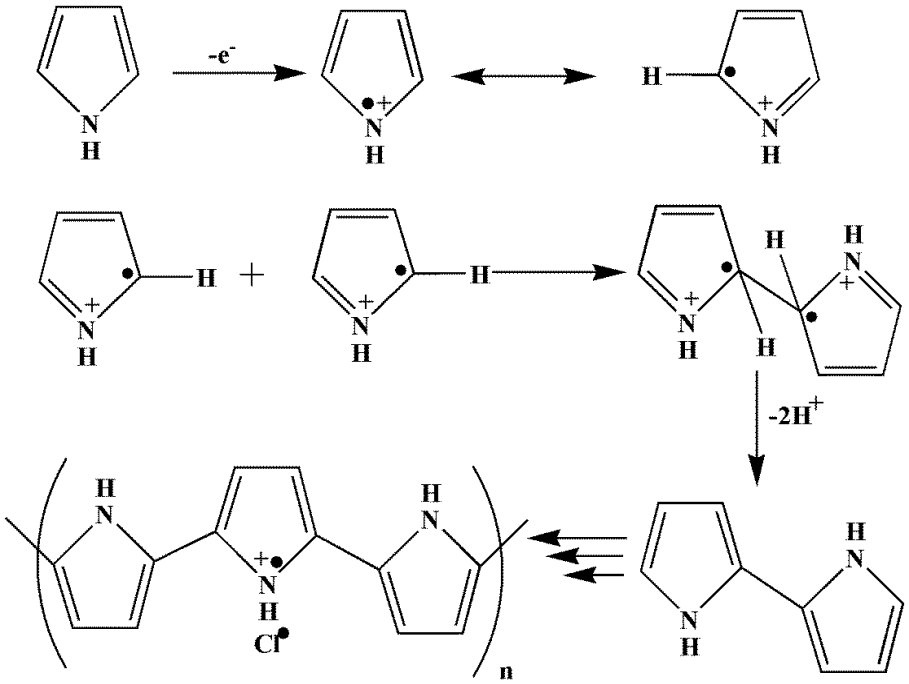

Figure 1.7: *Chemical oxidative polymerization and doping process in pyrrole.*

Cationic free radical forms after the loss of an electron from the monomer structure which is followed by the coupling of active resonance structures in different positions during the reaction (oxidation of monomer, radical-radical coupling). These coupled structures finally form polypyrrole chain at the end of the polymerization reaction (deprotonation, re-aromatization and chain propagation). The traditional π-conjugated structure of polypyrrole usually is not enough to possess significant conductivity on its own [53]. The electrical conductivity of this polymer can remarkably be change from insulating to metallic level through the process of doping [53].

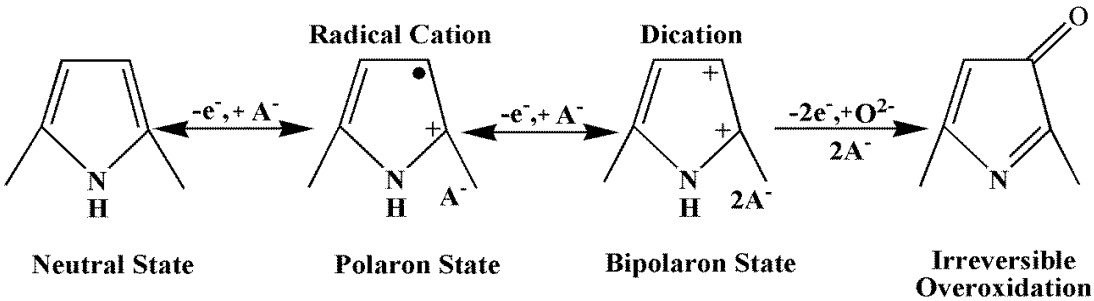

Figure 1.8: *Oxidation states of pyrrole.*

That is why the partial charge extraction (doping) process is needed and can be explained for this polymer in the following way as depicts in Fig. 1.8. Initially an electron is removed from the polymer backbone by yielding a radical and a spin less positive charge [54]. The newly formed cation and the radical are coupled to each other by local resonance. During coupling the quinoid-like sequential rings are also formed and utilized to provide higher energy of distortion than the remaining part of the chain. In general, the lattice distortion extends to four pyrrole rings (charged sites) and when they coupled with a radical, this structure is called polaron. Further oxidation of this polaron yields a new spineless defect called the bipolaron having lower energy than that of the two distinct polarons. At higher doping level, polarons are eventually replaced by bipolarons. For the higher doping level in PPy, it is suggested that the upper and lower bipolaron merge to the valence and conduction bands respectively to produce partially filled bands and provide metal like conductivity for the final polymer [53].

Having the conductivity values between 10-50 S/cm, PPy has been used extensively in different types of applications such as electrodes for rechargeable batteries and supercapacitor, electromagnetic shielding materials, electro-chromic devices and membranes, actuators, corrosion protecting materials and fuel-cell membranes [55]. Because of the unique and tunable physico-chemical and conductivity properties along with the better environmental stability, biocompatibility and higher surface area for various applications, the PPy nanostructures have become a great prominence throughout the different studies [56-59].

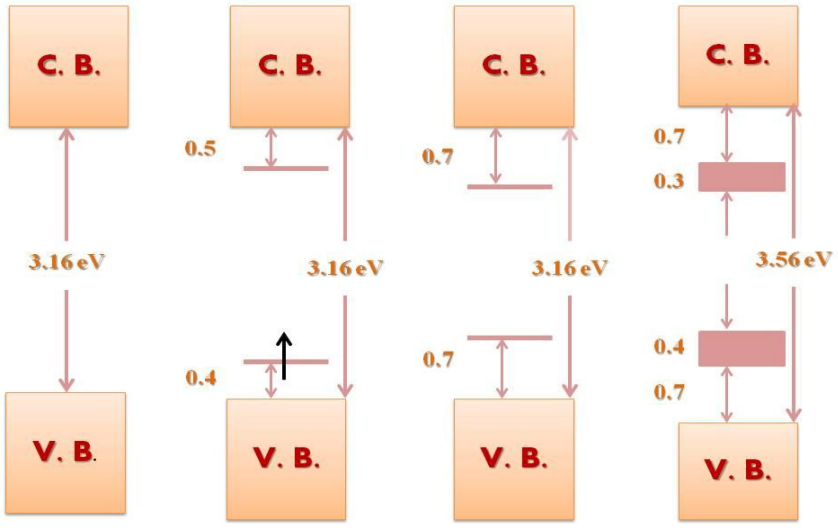

Figure 1.9: *Electronic energy diagrams for (a) neutral, (b) polaron (c) bipolaron and (d) fully doped polypyrrole [53].*

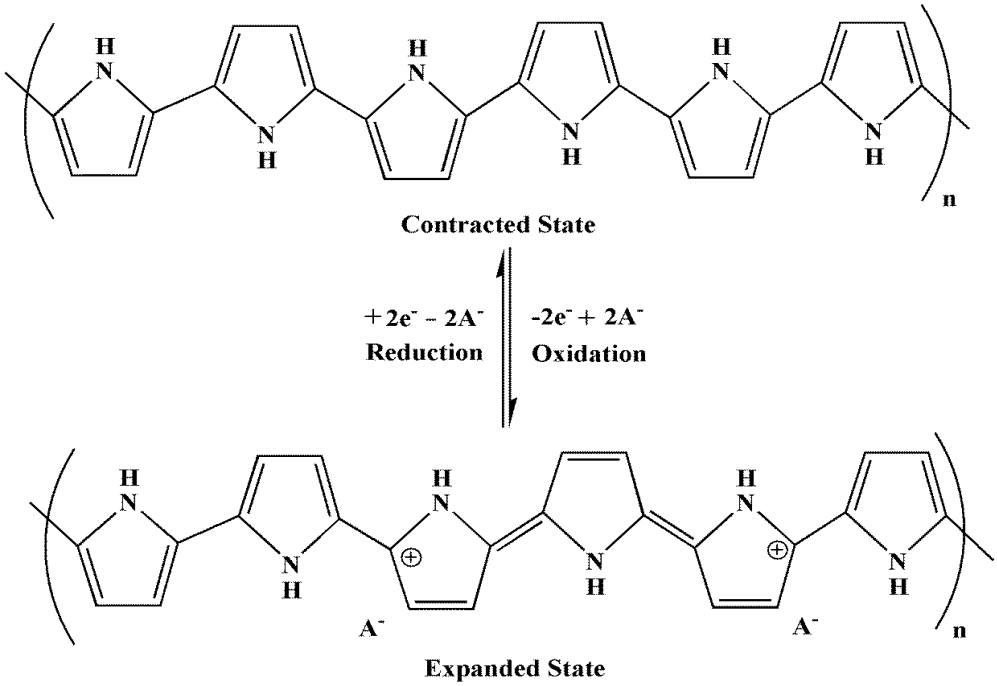

Figure 1.10: *Reduced (top) and oxidized (bottom) states of polypyrrole.*

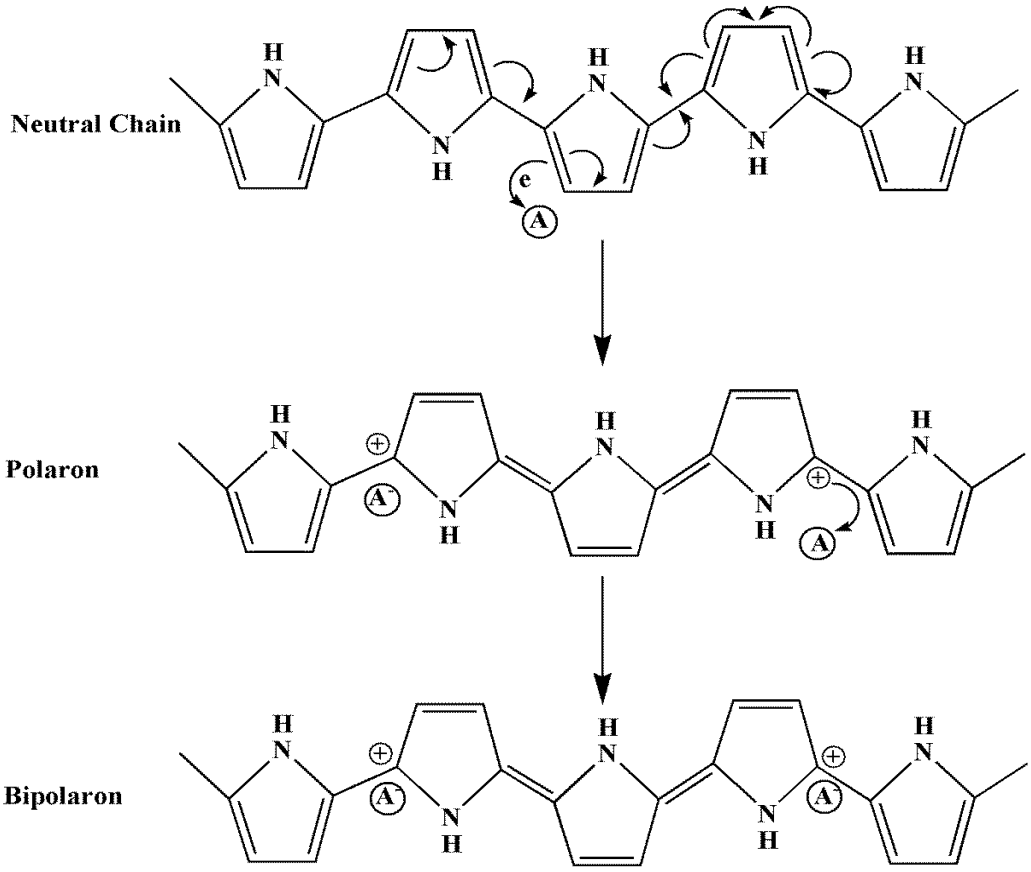

Figure 1.11: *Conduction mechanism for the oxidative polymerization of polypyrrole.*

1.6. Conducting polymer nanostructures

In the last few decades, nanostructured materials have attracted tremendous interest amongst the scientific community because of their peculiar and fascinating properties, as well as their unique applications as compared to their bulk counterparts. The nanostructured materials can lead to superior physical and chemical properties with molecular and supramolecular structures. The widespread interest in nanostructured materials mainly originates from their different properties such as the optical, electrical, mechanical and chemical performance that are usually different from those of the bulk materials. The improvement in the physico-chemical properties of nanostructured materials originated from the quantum chemical effects including quantum confinement and finite size effect as well as their nano-sized effect. Recently, nanostructured conducting polymers have received special attention in the area of nanoscience and nanotechnology because of their highly π-conjugated polymeric chains and metal like conductivity meaning that they can be regarded not only as molecular wires but also for the basic unit for the formation of nanodevices [60]. In addition, special characteristics of conducting polymer nanostructures are result from their size (1-100 nm) and large surface area; hence the electrical properties of conducting polymers are expected to be different from that of their bulk counterparts. The high performance of conducting polymer nanostructures is expected because of their nano-dimension: high conductivity, large surface area and light weight. Different conducting polymer nanostructures such as nanoparticles, nanotubes, nanofibers, nanorods, nanoneedles, nanocapsules etc. show improved physico-chemical properties as compared to their bulk polymers.

1.7. Synthesis methods for conducting polymer nanostructures

The synthesis method is one of the most fundamental and important object for developing conducting polymer nanostructures. A variety of synthesis methods have been developed for the fabrication of conducting polymer nanomaterials. Among the various synthesis strategies, the template approach (including hard and soft template), interfacial polymerization, self-assembly, micro-emulsion polymerization, rapid mixing polymerization, seeding polymerization, etc. have been widely employed to synthesize conducting polymer nanostructures and their composite nanostructures. The most

widely used synthesis methods have been discussed in the following subsections in details.

1.7.1. Template guided method

Template method is a powerful and promising method for the synthesis of conducting polymer nanostructures. In general, the template method is classified by soft and hard templates. Soft template method relies on the molecular self-assembly to form nanostructures, while the hard template method needs existing nanostructure as template by physical or chemical interactions.

1.7.1.1. Soft-template method

Soft template also called the template free or self-assembly method is a relatively simple, cheap and powerful approach for synthesizing conducting polymer nanostructures. By now, the surfactant, colloidal particles, structure directing molecules have served as "soft templates" and various soft template methods have been developed that includes template-free method [61-63], rapid mixing method [64], dilute polymerization [65], reverse emulsion polymerization [66], ultrasonic irradiation [67], and radiolytic synthesis [68]. The soft-template methods are based on the self-assembly mechanisms due to hydrogen bonding, π-π stacking, Van-der Waals forces and electrostatic interactions as driving forces. The disadvantage of the soft-template method is poor control of the morphology, orientation and diameter of the conducting polymer nanostructures.

Surfactant is a class of molecules that form thermodynamically stable aggregates of inherently nanoscale dimensions both in solutions and at interfaces. In equilibrium, the allowed packing of surfactant molecules into the aggregates can be described by a dimensionless parameter, referred to as the critical packing parameter (P). This critical parameter of the aggregates is controlled by the volume (V) and length (l) of the surfactant tail within the hydrophobic core of the surfactant aggregates and the effective area (a) occupied by each surfactant head group of the aggregate, which can be expressed as [69],

$$P = V/al \tag{1.1}$$

In general, the aggregate morphology of a surfactant in a solution is spherical, cylindrical or a flat bi-layer, depending on these parameters [69]. For a spherical micelle of radius *R* and aggregation number *N*, the total volume of the micelle can be written as

$$\frac{4}{3}\pi R^3 = NV \tag{1.2}$$

and the total surface area of the micelle can be written as

$$4\pi R^2 = Na \tag{1.3}$$

The packing criteria impose the restriction that the radius of the micelle cannot be greater than the length *l* of the hydrocarbon tail of the surfactant molecule.

i.e., $$R = (3V/a) \leq l \tag{1.4}$$

In terms of packing parameter $P\,(P = V/al) \leq 1/3$, which means that when the packing parameter *P* is less than 1/3, spherical micelles are the preferred form of aggregate structure. By a similar argument, it can be easily shown that the cylindrical micelles form when the packing parameter is between 1/3 and 1/2 (i.e. 1/3 ≤ P ≤ 1/2). The self-assembled surfactants form the micelles which act as soft templates to form conducting polymer nanostructures as shown in Fig. 1.12.

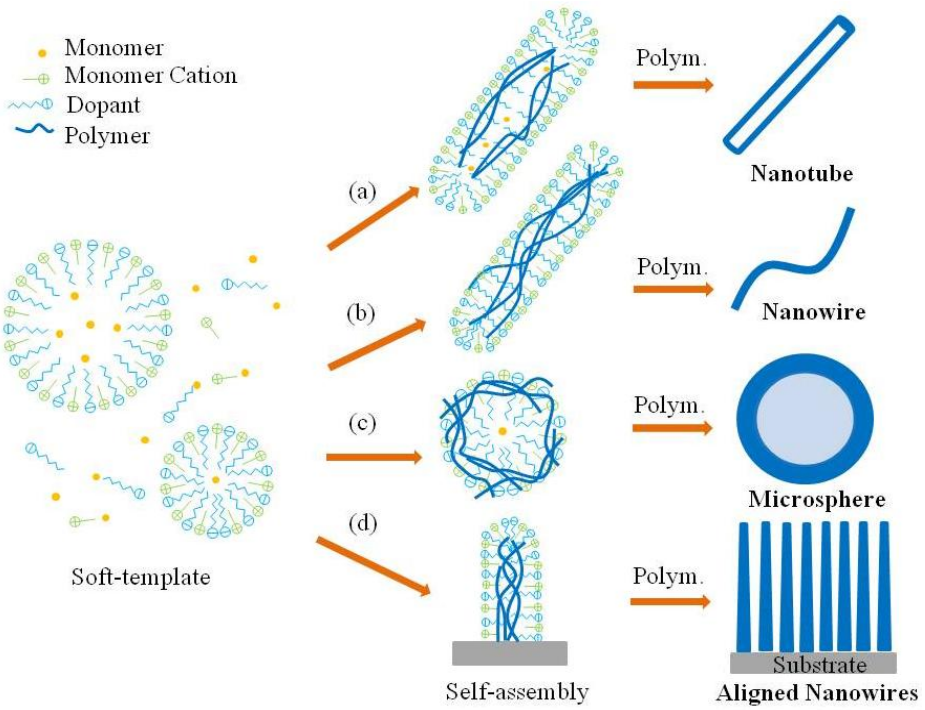

Figure 1.12: *Pictorial representation of soft-template synthesis of different nanostructures of conducting polymers.*

For a template-free method, the formation, size and morphology of the micelles as the soft-templates are greatly affected by the nature of the dopant, polymeric chain and the oxidant as well as the polymerization conditions. Different nanostructures of PPy such as wires, ribbons, sphere etc. have been synthesized by surfactants as soft templates [70]. Typical synthesis of this sort includes micro-emulsion polymerization and reversed micro-emulsion polymerization [71]. In general the micro-emulsion (oil-in-water) polymerization method is used to produce conducting polymer nanoparticles with control size. The concentration and structure of the surfactant plays the critical role for the formation of conducting polymer nanoparticles and to controll their morphology [72]. The surfactants that suitable for the micro-emulsion polymerization should have alkyl chain lengths between C-6 to C-16, since the alkyl chains shorter than C-6 processes weak hydrophobic interactions, however alkyl chains longer than C-16 process a very high viscosity to form the self-assembled conducting polymer nanostructures. Moreover, the critical micelle concentration (CMC) of the surfactant plays a critical role for the formation of nanostructures.

The reversed micro-emulsion which is defined as an aggregate of surfactant molecules containing a nanometer sized aqueous pool in the oil phase is another common method for the synthesis of conducting polymer nanostructures with controlled morphology. The most commonly used surfactant to form reverse micelles is sodium bis(2-ethylhexyl) sulfosuccinate (AOT), which is an anionic surfactant with two hydrophobic tail-groups. The AOT molecules form the reverse micelles in the oil phase because of their bulky hydrophobic tail-groups compared with the hydrophilic head-groups [73]. Jang et al. [73] synthesized polypyrrole nanotubes via oxidation polymerization in sodium bis(2-ethylhexyl) sulfosuccinate (AOT) reverse emulsions. PPy nanotubes with diameter 94 nm and length 2 mm were synthesized by using AOT reverse cylindrical micelles as the soft-templates. Zhang et al. [74] reported the soft template reverse emulsion polymerization of conducting poly(3,4-ethylenedioxythiophene) (PEDOT) nanotubes having diameters in the range of 50-100 nm. The soft template method owns low cost and produce large scale yields of conducting polymer nanostructures. The shortage of soft template method in energy storage devices rises from the discontinuous morphology of particles in electrode, which increases the electronic impedance in a certain extent.

1.7.1.2. Hard template method

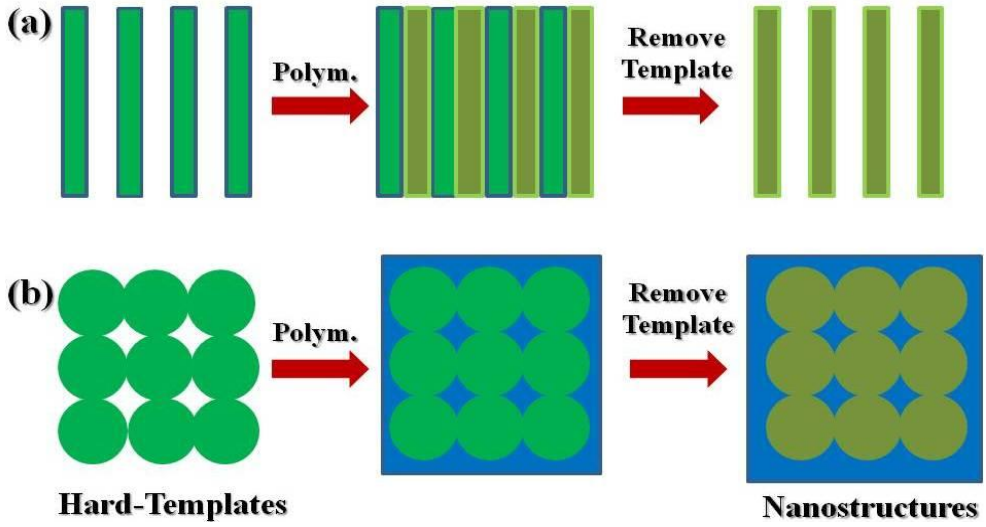

Figure 1.13: *Schematic of hard template synthesis of different conducting polymer nanostructures: (a) porous membrane as the hard template to produce conducting polymer nanotubes and nanowires. At first the growth of the conducting polymer is guided within the pores or channels of the membrane and then the template is removed after the polymerization; (b) Colloidal particles as the hard template to produce nanoporous membranes. The monomer is polymerized in the voids between the colloidal particles. When the colloidal particles are removed, a 3-D particle structure results.*

Hard template method is an effective technique to synthesize aligned nanotubes and nanowires of conducting polymers with controllable diameter and length. This method is simple to handle and following steps are followed for synthesis of nanostructures: (i) fill the nanoscale pores of a membrane with a monomer, (ii) polymerize the monomer inside the pores and (iii) remove the template in order to obtain the pure polymer. The porous membrane is the basic and most important part of the hard template method. The porous aluminium membranes (Al_2O_3) prepared by electrochemical method [75] and polycarbonate (PC) membranes prepared by a ‘‘track-etch” method [76], are widely used as commercial membranes. These membranes contain a wide range of a pore diameters (down to 10 nm) and with pore densities approaching 10^9 pores/cm^2 across the membrane surface [77].

Till date, nanotubes and nanowires of different conducting polymers such as polyaniline (PAni) [78], polypyrrole (PPy) [79] and PEDOT [80] have been chemically

or electro-chemically synthesized by this hard template approach. A range of pore sizes have been synthesized and some as small as 5 nm have been reported [81, 82]. The polymerization takes place on the surface of the template resulting core-shell structure [83-85]. After removal of the template, hollow nanocapsules or nanotubes can be obtained [86, 87]. The advantages of the hard template method are as follows: (i) Materials nanostructures including metal, semiconductor and conducting polymers can be synthesized either chemically or electrochemically and (ii) The diameter of the nanostructures is controlled by the size of the pores or channels in the membrane, whereas the length and thickness of the nanostructures can be adjusted changing the polymerization time. That is why the hard-template method is most commonly used synthesis approach for preparation of the well controlled and highly oriented nanostructures and the diameter of the conducting polymer nanowires can be obtained as small as 3 nm [88]. On the other hand, the disadvantages of this synthesis method are summarized as follows: (i) Using a membrane as a template requires post processing to remove the template which complicates the preparation process and the post process can destroy or disorder the resulting nanostructures and (ii) The quantity of the nanostructures produced by this method is limited by size of the template membrane, which limits its applications in large-scale production.

In the hard-template method, the synthesis of conducting polymer nanostructures is carried out by either chemical or electrochemical polymerization. Chemical hard-template synthesis approach is accomplished by simply immersing a membrane in a solution of the desired monomer, dopant and oxidant, and then allowing the polymerization of monomer within the pores of the templates which served as the ‘‘nano-reactor” [89, 90]. However, different types of nanostructures can be produced by controlling the polymerization time [91]. In general, the short polymerization results the tubular nanostructures with thin walls, while long polymerization leads to thick wall tubular or even fibrillar nanostructures.

In the electrochemical synthesis method, a metal film coated on one surface of the membrane is required to carry out the polymerization of the desired polymer within the pores of the membrane [92]. Compared to the chemical hard-template method, the electrochemical hard-template approach is more complex and expensive, but this method is more controllable through changing current density, applied potential and polymerization time. On the other hand, the large mass production by the

electrochemical hard-template method is impossible due to the limiting size of the membrane that used as the template.

1.7.2. Interfacial polymerization

Based on the traditional synthesis method, Kraner et al. [93, 94] have developed a simple chemical route to synthesize conducting polymer nanostructures under ambient condition using the aqueous/organic interfacial polymerization. This method allows the oxidative polymerization of monomer only at the interface of the aqueous/organic phase. The organic phase consists of monomer droplet whereas the oxidant is in aqueous phase and the resulting product enters into the aqueous phase. Interfacial polymerization does not depend on any specific template or dopant. An important aspect of interfacial polymerization method is that it enables the addition of various surfactant molecules, either negatively or positively charged, to the organic phase or even hydrophilic surfactants to the aqueous phase. As a result, the morphological and structural characteristics of the resulting polymer can be easily controlled according to the reaction conditions. Moreover, the high formation yields make the method easily scalable and reproducible. Haung et al. [94] successfully synthesized polyaniline nanofibers with diameter of 50 nm using the interfacial polymerization method. The interfacial polymerization method has also been applied to synthesis the nanorods of PAni, PPy and PEDOT with an average diameter of 30 nm [95, 96].

1.7.3. Electrospinning method

The electrospinning is an effective technique to fabricate conducting polymer nanofibers with diameter ranging from micrometers to 100 nm by using strong electrostatic forces [97, 98]. In this method, the polymer solution is extruded from an orifice to form a small droplet in presence of an electric field and the charged solution jets are extruded from the cone. The fluid extension occur first in uniform, and then the straight flow lines undergo vigorous whipping and/or splitting motion due to fluid instability and electrically driven bending instability. Finally, the spun fibers are deposited as a nonwoven web on a collector. In previous studies, micro and nanoscale fibers of polyaniline/polyethylene oxide [99, 100], pure polyaniline [101] and polypyrrole [102, 103] nanotubes have been prepared by this technique. Compared with

other methods, electrospinning method seems to be the only method that can produce continuous long nanofibers.

1.8. Different nanostructures of polypyrrole

Polypyrrole is one of the most promising conducting polymers because of its ease of synthesis, high electrical conductivity, reversible redox property and environmental stability. PPy can be prepared by the chemical or electrochemical polymerization via the oxidation of pyrrole monomer [104]. In general, the chemical polymerization leads to intractable powder, whereas the electrochemical polymerization results in film deposited on the electrode. The different nanostructures of PPy have been discussed in the following subsections.

1.8.1. Nanoparticles

Spherical PPy nanoparticles have been fabricated by the chemical oxidation polymerization with the aid of surfactant or stabilizer in an aqueous solution. Among all, the micro-emulsion polymerization has been extensively used to synthesize conducting polymer nanoparticles. Micro-emulsion synthesis of PPy nanoparticles with diameter of several nanometers could be obtained at low temperature [105]. At low temperature, the inner space of the micelles reduces by virtue of deactivating the chain mobility of the surfactant. As the polymerization temperature increased, the size of the PPy nanoparticles grew as a result of the enhanced chain mobility of the surfactant molecules. However, the size of the PPy nanoparticles decreased with shortening the chain length of the surfactant. The micelle aggregation number, defined as the number of surfactant molecules needed to form a micelle for polymerization, becomes smaller as the chain length of surfactant molecules decreases. The reduced micelle results the formation of smaller size nanoparticle. In an another micro-emulsion polymerization approach, PPy nanoparticles were synthesized using ferric chloride ($FeCl_3$) as oxidizing agent, and dodecylbenzenesulfonic acid (DBSA) and butanol were used as a surfactant and a co-surfactant, respectively [106]. It was observed that the micro-emulsion polymerization not only increased the yield of resulting PPy nanoparticles but also the extent of the conjugation length in the polymer as compared with solution and conventional emulsion polymerization.

Dispersion polymerization has also been widely used to synthesis PPy nanoparticles by several research groups. Zelenev et al. [107] synthesized the PPy nanoparticles with diameter of 20-60 nm by the oxidation of pyrrole monomer with sodium persulfate (oxidizing agent) and 4-ethylbenzenesulfonic acid (doping agent) in the presence of Rhodasurf TB970 (polymeric stabilizer). Recently, PPy nanoparticles with uniform diameter of 46 nm were prepared via a facile one step aqueous dispersion polymerization using poly-vinyl alcohol (PVA) as stabilizer [108]. It was observed that with increasing pyrrole concentration, the resultant PPy nanoparticles became coarser with broadening the particle size distribution. Furthermore, increase in the PVA concentration resulted in faster polymerization and smaller size PPy nanoparticles.

1.8.2. Hollow nanospheres

Hollow nanospheres of PPy have been obtained using various template approaches [109-113]. PPy-chitosan hollow nanosphere of core diameter of 20±3 nm and shell thickness of 15±4 nm have been successfully fabricated using AgCl nanoparticles as sacrificial core at 2 °C [111, 112]. The chitosan stabilized the AgCl nanoparticle and prevented the aggregation of PPy nanospheres during the synthetic process. Additionally, PPy hollow nanospheres were stable in acidic aqueous media and insoluble in basic media due to the presence of chitosan in the shell part. In recent studies, PPy hollow nanospheres have been fabricated using core-shell nanomaterials composed of an identical polymer [112].

1.8.3. Nanofibers

A bulk synthesis of PPy nanofibers with diameter ranging from 60 nm to 90 nm was carried out using the nanofiber seeds as a template [58]. V_2O_5 nanofibers with diameter of 15 nm treated by chemical method with pyrrole monomer were used as reactive seed templates. Yang et al. [114] synthesized the high yield PPy nanofibers using the reactive template approach. The reactive template of $FeCl_3$ and methyl orange (MO) guided the formation of uniform PPy nanofibers. Chronakis et al. [115] reported the synthesis of PPy nanofibers with average diameter in the range about 70-300 nm by the electrospinning method. The resulting PPy nanofibers exhibited well defined

morphology and physical stability. Moreover, Feng et al. [116] reported the synthesis of PPy micro/nanofibers via the self-assembly method in presence of $FeCl_3$ as oxidant.

1.8.4. Nanotubes

In general, PPy nanotubes have been mainly synthesized by the hard template method [117-122]. PPy nanotubes with highly uniform surface and controlled morphology were fabricated by one-step VDP using AAO membrane [118]. Recently, a reliable synthesis method called the soft template was developed for synthesizing PPy nanotubes against the hard template synthesis [66, 123]. Jang et al. [66] reported the synthesis of PPy nanotubes with average diameter of 95 nm and length more than 5 μm using the reverse micro-emulsion polymerization method. The PPy nanotubes have exhibited higher electrical conductivity of 30.4 Scm^{-1}. Yang et al. [124] reported the facial fabrication of functional PPy nanotubes via the reactive self degrade template method with outer and inner diameters of 70 and 50 nm, respectively.

1.9. Swift heavy ion irradiation in conducting polymers

Swift heavy ion (SHI) irradiation in conducting polymers has proven to be a unique technique for altering their different physico-chemical properties due to tremendous electronic energy deposition in the target polymer which till date is not possible by any other methods [125, 126]. SHI irradiation in polymers can induce irreversible changes in their macroscopic properties such as structural, electrical, optical and thermal properties which can be ascribed to the transformations at microscopic level through the processes of electronic excitation, ionization, cross-linking, chain scissioning, bond breaking and cluster formation as well as mass losses in the polymer material due to large deposition of electronic energy [127, 128]. The SHI irradiation induced physico-chemical modifications in polymeric materials depend on the different parameters such as the ion species, fluence, ion energy and nature of the target materials. In general for polymer irradiation, the ion fluence used is in the range of 10^9-10^{12} ions/cm^2. Higher ion fluence may lead to the destruction of polymer chains and also result in more amorphization of the target polymer [129]. Different studies on SHI irradiation induced effects on conducting polymers reveal modifications in their structural, electrical, optical and thermal properties change including their processes such as polymer main

chain scission, intermolecular cross-linking, creation of unsaturated bonds, formation of volatile fragments and creation of carbon clusters [130]. The phenomena such as chain-scissoning and cross-linking of the polymer chains depend on the energy loss mechanism during irradiation. An important parameter, which characterizes ion-to-target energy transfer is the energy loss *dE/dx* (eV/Å) which is defined as the energy deposition per unit length along ion track. When an energetic ion passes through a material, it loses its energy mainly by two independent processes: (a) elastic collisions with the nuclei of target material known as nuclear energy loss $(dE/dx)_n$, which dominates at an energy of about 1 keV/amu and (b) inelastic collisions with the atomic electrons of the material known as electronic energy loss $(dE/dx)_e$ which dominates at an energy of about 1 MeV/amu or more. In the electronic energy loss, the energy is transferred from the projectile to the atoms through excitation and ionization of the surrounding electrons. The amount of electronic loss in each inelastic collision varies from tens of eV to a few keV per Angstrom (Å). For a swift heavy ion (SHI) moving at a velocity comparable to the Bohr velocity of the electron the inelastic collision is the dominant mechanism for transfer of energy to the material for producing track when its value crosses a threshold value for track formation. However, the diameter and length of the cylindrical ion track depend on the type and energy of the beam and the electrical and thermal conductivity of the material [131]. There are two fundamental models that govern the ion-solid interaction mechanisms viz. the Coulomb explosion model [132] and thermal spike model [133]. According to the Coulomb explosion model, during the passage of SHI through the target material, positive ions are produced by the electronic excitation which is mutually repulsive in nature. The time to cover atomic sites is short in comparison to the response time of the conduction electrons. Therefore during the passage of the SHI, a long cylinder containing charge ions are produced. This cylinder containing the charged ions explodes radially due to conversion of electrostatic energy to coherent radial atomic movements under the Coulomb forces until ions are screened by the conduction electrons. Due to the cylindrical shock wave, ion tracks result along the trajectory of the ion due to radial Coulomb explosion. On the other hand, according to the thermal spike model, during the passage of SHI the kinetic energy of the electrons ejected due to inelastic collision induced electronic excitation which is transmitted to the lattice by electron phonon interaction that increases the local lattice temperature above the melting point of the material. The temperature increase is then

followed by a rapid quenching (10^{13}-10^{14} K/s) that results in an amorphous linear structure when the melt solidifies.

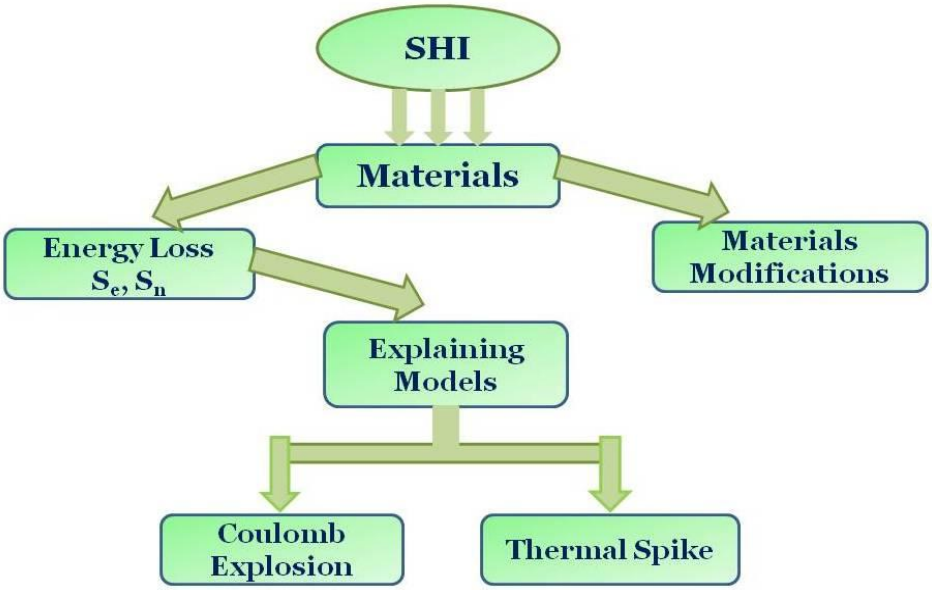

Figure 1.14: *Block diagram for SHI irradiation in materials.*

1.10. Scope of the thesis and statement of thesis problem

Conducting polymers such as polypyrrole (PPy), polyaniline (PAni), polythiophene (PTh), poly(3,4-ethylene dioxythiophene) (PEDOT) etc. have been the subject of considerable interest because of their unique properties such as high electrical conductivity, good environmental stability and optical properties in doped and neutral state [134, 135], ease of synthesis [136], thermal stability [137], biocompatibility [138] and numerous applications including sensors [139], actuators [140], rechargeable batteries [141], energy storage devices [142], drugs delivery devices [143], electro-chromatic window and display [144], organic light emitting diodes [145], field effect transistor [146], electrodes for redox supercapacitor [147], solar cells [148] and molecular electronic [149]. The characteristic properties which make the conducting polymers potentially attractive for such wide range of potential application are strongly dependent on the synthesis procedure, type and concentration of dopant, dopant to monomer molar ratio and other variables [150, 151]. Because of the difficulty in controlling the parameters all together, the relationship between properties and structure is not yet fully understood. However, being a complex disordered system and due to various potential applications in electronic devices, the understanding of nature of

charge carriers and charge transport mechanism in conducting polymers is a widely open problem both from the fundamental and application viewpoint. Dielectric relaxation spectroscopy and ac conductivity provide information regarding the relaxation dynamics and charge transport mechanism in disordered conducting polymers [152].

Recently, conducting polymer nanostructures have become a rapidly growing field of research, because they display new properties related to their nanoscale size and have greatly improved the performance of devices [153, 154]. Although, in the last two decades, there has been intense interest in the conducting polymer nanostructures, the relaxation dynamics and charge transport mechanism in these nanostructures still remain poorly understood. A detailed understanding of the morphology, structural, optical and thermal properties, and charge transport mechanism of conducting polymer nanostructures is very crucial for successful fabrication of sophisticated nanodevices and application of conducting polymers in nanoelectronics. It is well established that the nanostructures of conducting polymers display improved physico-chemical properties over their bulk polymers. However, conducting polymers are irradiation sensitive and swift heavy ion (SHI) irradiation in conducting polymers can be used to modify or engineer their different physico-chemical properties irreversibly which cannot be achieved by any other methods till date. SHI irradiated conducting polymer nanostructures are expected to display several interesting physico-chemical modifications leading to the enhancement in their performance.

In view of the foregoing, the present work aspires to investigate the various physico-chemical properties of conducting polymer nanostructures. Although swift heavy ion irradiation can be used as a specific tool to modify various properties of conducting polymers, the irradiation induced modification on conducting polymer nanostructures have not been properly elucidated. Aim of the present work is a detailed study of SHI irradiated induced modifications on the morphology, structural, optical and thermal properties, and dielectric relaxation and charge transport mechanism of the conducting polymer nanostructures. To fulfil the above mentioned objectives, we consider polypyrrole (PPy) among the family of conducting polymers as the material of interest in the present work as it has many versatile properties, which makes it one of the most promising candidates of the family of conducting polymers for different application purposes. The prime objectives of the thesis are to investigate the

morphological, structural, optical and thermal properties, and dielectric relaxation and electrical transport in different nanostructures of PPy by varying the dopant concentration, dopant/monomer molar ratio and dopant type with a view to study their different properties and to gain a deeper understanding of the type of charge carriers in different nanostructures. The following PPy nanostructures have been investigated in the present thesis.

1. Polypyrrole nanoparticles synthesized by the micro-emulsion polymerization method with varying the sodium dodecylsulfate (SDS) concentration as dopant cum surfactant.
2. Polypyrrole nanotubes synthesized by the self-assembly polymerization method with varying the dopant/monomer molar ratio.
3. Polypyrrole nanofibers synthesized by the interfacial polymerization method doped with different alkylbenzenesulfonic acids (ABSA).

The following characterizations and measurements have been carried out for the three different nanostructures of PPy.

1. High resolution transmission electron microscopy (HRTEM) has been carried out to study the morphology, shape and size of the PPy nanostructures.
2. X-ray diffraction (XRD) studies have been carried out to investigate the degree of crystallinity or ordering of polymer chain, domain length, interplanar spacing and hopping distance or inter chain separation of the different PPy nanostructures.
3. Fourier transform infrared spectroscopy (FTIR) has been conducted to investigate the conformational variations, chemical interaction and vibration assignments.
4. UV-visible spectroscopy (UV-vis) has been performed to study the optical properties of the PPy nanostructures.
5. Thermo-gravimetric (TGA) measurements have been carried out to study the thermal stability of PPy nanostructures.
6. Dielectric relaxation spectroscopy and ac conductivity studies have been carried out to study the relaxation dynamics and charge transport mechanisms in different nanostructures of PPy.

The samples that show the best properties of each PPy nanostructures have been irradiated with 160 MeV Ni^{12+} swift heavy ions using the 15 UD Pelletron Accelerator

at the Inter University Accelerator Centre (IUAC), New Delhi. The systems have been irradiated at the normal beam incidence with ion fluences ranging from 10^{10}-10^{12} ions/cm^2 with a view to investigate the fluence dependent variation in various physico-chemical properties of PPy nanostructures. The above mentioned methodology has been repeated to characterize and study the charge transport in the irradiated systems of different PPy nanostructures.

CHAPTER-II

Theoretical Aspects

This chapter presents an overview of charge transport mechanism in disordered materials. Formulation of dielectric permittivity and electric modulus has been discussed to elucidate the permittivity mechanism and relaxation dynamics of charge carriers in disordered conducting polymers. Also, the theoretical models governing the ion-solid interactions have been discussed briefly in this chapter.

2.1. Models for frequency dependent ac conduction in disordered materials

Several theoretical models have been proposed to account for the frequency dependence of ac conductivity in disordered materials. The ac charge transport in amorphous semiconductors can be related to two macroscopic relaxation mechanisms: (a) classical hopping of charge carriers over the potential barrier separating two energetically favourable sites and (b) phonon-assisted quantum-mechanical tunnelling through the barrier separating two equilibrium positions. In this section, a brief discussion on the salient features of these models with a special emphasis on the correlated barrier hopping model has been made to account for the ac conduction in conducting polymers [155].

The frequency dependence of total conductivity $\sigma'(\omega)$ for disordered materials can be expressed as [156, 157]:

$$\sigma'(\omega) = \sigma_{dc} + \sigma_{ac}(\omega) \tag{2.1a}$$

$$\sigma_{ac}(\omega) = \sigma'(\omega) - \sigma_{dc} = A\omega^{s} \tag{2.1b}$$

where σ_{dc} is the dc or low frequency conductivity, s is the frequency dependent universal exponent ($0 < s < 1$) and A is the pre-exponential factor that depends only on temperature, not on the frequency. Both dc and ac conductivities when originated from the same kind of mechanism, σ_{dc} can be treated as $\sigma'(\omega)$ in the limit of $\omega \to 0$ giving rise to a plateau in the $\sigma'(\omega)$ vs. ω plot and separation of dc and ac contribution is no longer meaningful.

The study of the temperature dependence of frequency exponent s is helpful in elucidating the microscopic charge transport mechanism in disordered materials. The

microscopic charge transport mechanism in disordered materials are governed by the two models namely the quantum mechanical tunnelling (QMT) model and the correlated barrier hopping (CBH) model. According to the QMT model, the charge transfer takes place through a barrier in which the spatial extent of the localized wave functions is assumed to be constant over all sites. Within the pair approximation, the ac conductivity for single electron motion undergoing QMT is given by the following expression

$$\sigma'(\omega) = Ce^2 k_B T \alpha^{-1} \left[N(E_F)\right]^2 \omega R_\omega^4 \tag{2.2}$$

where C is a numerical constant with its value equal to $\pi^4/24$, $N(E_F)$ is the density of states at Fermi level which is assumed to be constant and R_ω is the hopping distance at a particular frequency ω which can be expressed by the following equation (2.3),

$$R_\omega = \frac{1}{2\alpha} \ln\left(1/\omega\tau_0\right) \tag{2.3}$$

In the QMT model, the expression for the frequency exponent *s* is given by [158],

$$s = 1 - \frac{4}{\ln\left(1/\omega\tau_0\right)} \tag{2.4}$$

where τ_0 is the characteristic relaxation time of the order of the inverse of Debye frequency (~10^{-12}-10^{-13} s). It is observed that the frequency exponent *s* is temperature independent, but it depends on the frequency. The above results are obtained in a wide band limit, i.e. for $(\Delta_0 >> k_B T)$, where Δ_0 is the bandwidth.

A temperature dependent frequency exponent can be obtained within the framework of the QMT model in the pair approximation by assuming that the carriers form non-overlapping small polarons (NSPT) [159], i.e. the total energy of a charge carrier is lowered by the polaron energy W_p resulting from the lattice distortion accompanying the occupation of a site by a carrier. The transport of an electron between the degenerate sites with a random distribution of separation generally involves activation energy, the polaron hopping energy $W_H \approx W_p/2$. In this case, the frequency exponent *s* becomes

$$s = 1 - \frac{4}{\ln\left(1/\omega\tau_0\right) - W_H/k_B T} \tag{2.5}$$

This expression reveals that the frequency exponent *s* in the NSPT model is temperature dependent and it increases with increasing the temperature. Also, the temperature dependent of frequency exponent *s* can arise from the simple QMT model if pair approximation breaks down i.e. when the carrier motion occurs within the clusters [160]. The tunnelling distance at a frequency ω in the non-overlapping small polaron model becomes

$$R_\omega = \frac{1}{2\alpha}\left[\ln\left(1/\omega\tau_0\right) - W_H/k_BT\right] \tag{2.6}$$

A mechanism for the polaron tunnelling, called the overlapping large polaron tunnelling (OLPT) model is proposed by Long [161], according to which the expression for the frequency exponent *s* is given by the following equation (2.7),

$$s = 1 - \frac{8\alpha R_\omega + 6\beta W_{H0} r_p / R_\omega}{\left(2\alpha R_\omega + \beta W_{H0} r_p / R_\omega\right)^2} \tag{2.7}$$

where $\beta = 1/k_BT$ and the parameters W_{H0} and R_ω can be calculated using the following relations [155, 159]:

$$W_{H0} = \frac{e^2}{4\varepsilon_p r_p} \tag{2.8}$$

$$R_\omega = \frac{1}{4\alpha}\left[\ln\left(\frac{1}{\omega\tau_0}\right) - \frac{W_{H0}}{k_BT}\right] + \left\{\left[\ln\left(\frac{1}{\omega\tau_0}\right) - \frac{W_{H0}}{k_BT}\right]^2 + \frac{8\alpha r_p W_{H0}}{k_BT}\right\}^{1/2} \tag{2.9}$$

where ε_p is the effective dielectric constant, α is the exponential decay parameter of the localized states wave function, R_ω is the hopping distance at frequency ω, and r_p is the polaron radius. The ac conductivity for the overlapping large polaron tunnelling (OLPT) model [161] is given by

$$\sigma'(\omega) = \frac{\pi^4}{12} e^2 (k_BT)^2 \left[N(E_F)\right]^2 \frac{\omega R_\omega^4}{2\alpha k_BT + W_{H0} r_p / R_\omega^2} \tag{2.10}$$

The OLPT model predicts that the frequency exponent *s* both frequency and temperature dependent beside its decrease from unity with increasing the temperature. For large polarons, *s* continues to decrease with increasing temperature tending to its value predicted by the QMT model for non-overlapping carriers. For small polaron, *s* exhibits a minimum at a certain temperature and subsequently increases with increasing the temperature.

Also, the model for ac conduction which correlates the relaxation variable W with the intersite separation R has been developed initially by Pike [162] for single-electron hopping and later extended by Elliott [155, 163] for pair-electron (bipolaron) hopping between the localized states over the potential barrier separating them. For neighbouring sites at separation R, the Coulomb well overlap resulting in a lowering of the effective barrier from W_H to a value W, which for the case of two electron transition is given by [155],

$$W = W_H - \frac{2e^2}{\pi\varepsilon\varepsilon_0 R} \tag{2.11}$$

where ε is the dielectric constant of the material and ε_0 is the value of the dielectric permittivity at free space. The ac conductivity in the CBH model [164] in the narrow-band limit $(\Delta_0 << k_B T)$ is expressed by

$$\sigma'(\omega) = \frac{\pi^3}{12} N^2 \varepsilon\varepsilon_0 \omega R_\omega^6 \tag{2.12}$$

where N is the concentration of the pair of sites and R_ω is the hopping distance which is given by the following expression at a particular frequency and temperature as,

$$R_\omega = \frac{2e^2}{\pi\varepsilon\varepsilon_0 [W_H + k_B T \ln(\omega\tau_0)]} \tag{2.13}$$

where e is the electronic charge, k_B is the Boltzman constant and T is the temperature and τ_0 is the characteristic relaxation time.

The temperature dependent frequency exponent s in this model is evaluated as [155]

$$s = 1 - \frac{6k_B T}{W_H + k_B T \ln(\omega\tau_0)} \tag{2.14}$$

which to a first approximation reduces to the simplest expression

$$s = 1 - \frac{6k_B T}{W_H} \tag{2.15}$$

Thus, in the CBH model a temperature dependent frequency exponent s is observed, with s increasing towards unity as $T \to 0$ K, in marked contrast to the QMT mechanism.

2.2. Scaling and universality of ac conductivity

The scaling and universality of ac conductivity of disordered solids are substantial concepts which indicate a common underlying physical characteristic of electric charge flow in disordered materials. One of the most important properties of ac conductivity is that frequency dependent conductivity $\sigma'(\omega)$ at different temperatures *T* can be scaled into one master curve and the shape of such master curve is almost the same for all disordered solids. This master curve can be represented by

$$\frac{\sigma'(\omega)}{\sigma(0)} = F\left[C\frac{\omega}{\sigma(0)}\right] \tag{2.16}$$

where $\sigma(0)$ is the dc conductivity and *C* is the scaling constant that depends on the temperature and the charge carrier concentration. From this, the Barton-Nakajima-Namikawa (BNN) can be derived [165-167].

$$\sigma(0) = p\Delta\varepsilon\varepsilon_0\omega_{\max} \tag{2.17}$$

which associates the dc conductivity with dielectric loss peak frequency $\omega_{\max}$, $\Delta\varepsilon = \varepsilon(0) - \varepsilon_\infty$ is the strength of the relaxation, ε_0 is the permittivity in free space and ε_∞ is the high frequency permittivity and *p* is a numerical constant of order of unity.

Later on Summerfield [168] assumes substantially that $\Delta\varepsilon$ follows a Curie law proposed

$$\frac{\sigma'(\omega)}{\sigma(0)} = F\left[\frac{A\omega}{T\sigma(0)}\right] \tag{2.18}$$

as the scaling law with *A* as a parameter that depends on the concentration of charge carriers.

A more general formula for scaling of ac conductivity was proposed by Sidebottom [169]

$$\frac{\sigma'(\omega)}{\sigma(0)} = F\left[\frac{\omega\varepsilon_0\nabla\varepsilon}{\sigma(0)}\right] \tag{2.19}$$

A widely applied empirical function [170-172] which approximates the scaling behavior of ac conductivity is [173, 174]

$$\sigma'(\omega) = \sigma(0)\left[1 + \left(\frac{f}{f_0}\right)^s\right] \tag{2.20}$$

where f_0 is a characteristic frequency.

2.3. Dielectric relaxation

Dielectric relaxation in solids is one of the most extensively studied research topic in physics and materials science, yet there is no satisfactory theoretical understanding of the relaxation phenomena. Relaxation in materials consists of the recovery of strain on removal of the stress and therefore it implies the time dependence, typically under sudden removal or sudden application of a steady stress. This is the basis of the time-domain (TD) measurements [175]. An equivalent and often preferable method is to subject the material to an oscillating electric filed with an angular frequency ω and this forms the basis of frequency-domain (FD) measurements [171, 176]. Materials are polarized under the application of ac electric field by various polarization mechanisms and their dielectric permittivity which is a measure of the polarization, shows frequency dependence, namely dielectric relaxation or dielectric dispersion. Dielectric relaxation spectroscopy is a powerful technique that measures the permittivity and conductivity as a function of frequency in a non-invasive way and can provide insights into the structures and electrical properties of materials at molecular and macroscopic levels. In general, in the frequency range of 10-10^7 Hz, the usual method of studying the dielectric relaxation in such materials is to prepare a disk-shaped sample with metal electrodes deposited on its two parallel faces. An ac bridge is used to measure the conductance G and capacitance C of the sample as a function of frequency ω. The material can be regarded as an equivalent circuit of impedance $Z = (G + iC\omega)^{-1}$.

According to Maxwell's equations, ε^* is time (or frequency) dependent if a time dependent process takes place within the sample. Resonance phenomena are due to atomic or molecular vibrations and can be analyzed by optical spectroscopy. Relaxation phenomena, on the other hand, are related to molecular fluctuations of dipoles due to molecules or part of them in a potential landscape. Moreover, drift motion of mobile charge carriers viz., electrons, ions or charged defects also contribute to the dielectric response.

In polymeric materials, there are two major polarization mechanisms that are studied by dielectric spectroscopy: (i) polarization due to charge migration resulting in conductivity and (ii) polarization due to orientation of permanent dipoles. The orientation or polarization of permanent dipoles involves cooperative motion of molecules with time scales measurable by dielectric spectroscopy. The time dependent

loss of orientation of dipoles upon removal of the applied electric field is called dipole relaxation. There are two additional aspects of induced polarization. The first is electrode polarization that results from the accumulation of charges at the electrode/polymer interface. The second aspect is the polarization due to the build up of charges at the interface which is known as interfacial polarization. These polarization effects can be studied by dielectric spectroscopy by using different formalisms. Detailed information about the dielectric properties of materials can be obtained in a number of equivalent ways; however it is important to use the most appropriate form to match the particular requirement. The four basic complex dielectric formalisms that are frequently used are permittivity (ε^*), modulus (M^*), impedance (Z^*) and admittance (Y^*). These formalisms are described in the following subsections.

2.3.1. Permittivity formalism

The frequency dependence of complex permittivity ε^* can be expressed as:

$$\varepsilon^*(\omega) = \varepsilon'(\omega) - j\varepsilon''(\omega) \tag{2.21}$$

where $\varepsilon'(\omega)$ and $\varepsilon''(\omega)$ are the real and imaginary parts of the complex permittivity ε^*, respectively. $\varepsilon'(\omega)$ is the measure of the amount of energy stored and $\varepsilon''(\omega)$ represents the measure of the amount of energy dissipated in the dielectric material under applied ac electric field. At higher frequency, the real part of permittivity is independent of frequency which is denoted by ε_∞ and is attributed to the contribution from rapid polarization of atoms and electrons present in the samples under applied field. In the intermediate frequency range, $\varepsilon'(\omega)$ increases with the decrease in frequency up to a certain value, at which a plateau like feature is observed and the value at this level is denoted as ε_s, the low frequency static value.

2.3.1.1. Analysis of permittivity spectra: model functions

Dielectric relaxation mechanism in disordered materials can be well understood using different theoretical models. Several theoretical models have been proposed to explain the experimentally measured permittivity data in both the time and frequency domain. The most important of these approaches are discussed below:

In the dielectric permittivity formulation, the Debye function for the frequency dependence of complex permittivity $\varepsilon^*(\omega)$ related to the free dipoles which are oscillating in an applied electric filed is given by [177],

$$\varepsilon^*(\omega) = \varepsilon_\infty + \frac{\varepsilon_s - \varepsilon_\infty}{1 + j\omega\tau_D} \tag{2.22}$$

The real part $\varepsilon'(\omega)$ of ε^* can be expressed by

$$\varepsilon' = \varepsilon_\infty + \frac{\varepsilon_s - \varepsilon_\infty}{1 + \omega^2\tau_0^2} \tag{2.23}$$

and the imaginary part $\varepsilon''(\omega)$ of ε^* can be expressed by

$$\varepsilon'' = \frac{(\varepsilon_s - \varepsilon_\infty)\omega\tau_0}{1 + \omega^2\tau_0^2} \tag{2.24}$$

where $\Delta\varepsilon = \varepsilon_s - \varepsilon_\infty$ is the dielectric relaxation strength, with $\varepsilon_s = \lim_{\omega\tau<<1} \varepsilon'(\omega)$ is the static dielectric permittivity in the limit of zero frequencies and $\varepsilon_\infty = \lim_{\omega\tau>>1} \varepsilon'(\omega)$ is the permittivity in the limit of infinite frequencies, $\omega = 2\pi f$, f is the measured frequency and τ_0 is the relaxation time.

In the complex plane plot, a perfect Debye relaxation with a single relaxation time is represented by a semicircle. The complex plane plot however deviates from a semicircle indicating a distribution of relaxation times. The deviation from the ideal Debye behaviour has been encountered in several experimental results and as such different models have been developed by various empirical equations proposed by Cole and Cole [178], Davidson and Cole [179] and Havriliak and Negami [180]. In the permittivity formalism, the influence of the distribution of relaxation times has been introduced by Cole-Cole [178] to account for the symmetrical distribution of relaxation times. According to the Cole-Cole, the frequency dependence of the complex permittivity ε^* is given by:

$$\varepsilon^* = \varepsilon_h + \frac{\Delta\varepsilon}{1 + (j\omega\tau)^{1-\alpha}} \tag{2.25}$$

where the parameter α describes the symmetrical distribution of relaxation times and its value lies between 0 and 1. The real and imaginary parts of the complex permittivity for the Cole-Cole formulation can be written as follows:

$$\varepsilon' = \varepsilon_h + \frac{\Delta\varepsilon[1+(\omega\tau)^{(1-\alpha)}\cos\{\pi(1-\alpha)/2\}]}{1+2(\omega\tau)^{(1-\alpha)}\cos\{\pi(1-\alpha)/2\}+(\omega\tau)^{(1-\alpha)}} \tag{2.26}$$

$$\varepsilon'' = \frac{\Delta\varepsilon(\omega\tau)^{(1-\alpha)}\sin\{\pi(1-\alpha)/2\}]}{1+2(\omega\tau)^{(1-\alpha)}\cos\{\pi(1-\alpha)/2\}+(\omega\tau)^{(1-\alpha)}} \tag{2.27}$$

Davidson and Cole [179] introduced the parameter β in the Debye's function to account for an asymmetric distribution of relaxation times resulting from a dielectric dispersion. According to this model, the complex permittivity can be expressed as follows:

$$\varepsilon^* = \varepsilon_h + \frac{\Delta\varepsilon}{(1+j\omega\tau)^{\beta}} \tag{2.28}$$

where the value of β lies between 0 and 1 and it describes the asymmetrical distribution of relaxation times. The real ε' and imaginary ε'' parts of complex permittivity according to this model are given by:

$$\varepsilon' = \varepsilon_h + \Delta\varepsilon\cos(\beta\theta)\cos^{\beta}\theta \tag{2.29a}$$

$$\varepsilon'' = \Delta\varepsilon\sin(\beta\theta)\cos^{\beta}\theta \tag{2.29b}$$

where $\theta = \tan^{-1}(\omega\tau)$.

A more general equation for complex permittivity was developed by Havriliak and Negami [180]. According to this model, the complex permittivity ε^* is given by

$$\varepsilon^* = \varepsilon_h + \frac{\Delta\varepsilon}{[1+(j\omega\tau)^{1-\alpha}]^{\beta}} \tag{2.30}$$

where the parameters α and β describe the symmetrical and asymmetrical distribution of relaxation times, respectively and values of both parameters lie between 0 and 1. The real and imaginary parts of the complex permittivity within this model can be expressed by the following equations (2.31a&b):

$$\varepsilon' = \varepsilon_h + r^{-\beta/2}\Delta\varepsilon\cos(\beta\theta) \tag{2.31a}$$

$$\varepsilon'' = r^{-\beta/2}\Delta\varepsilon\sin(\beta\theta) \tag{2.31b}$$

where the terms *r* and θ can be written as:

$$r = [1+(\omega\tau)^{(1-\alpha)}\sin(\alpha\pi/2)]^2 + [(\omega\tau)^{(1-\alpha)}\cos(\alpha\pi/2)]^2 \tag{2.32}$$

$$\theta = \tan^{-1}\frac{(\omega\tau)^{(1-\alpha)}\cos(\alpha\pi/2)}{1+(\omega\tau)^{(1-\alpha)}\sin(\alpha\pi/2)} \tag{2.33}$$

The general nature of the Havriliak-Negami model can be established from the fact that for $\beta = 1$ and $\alpha = 0$, the Debye equation can be obtained. The Cole-Cole equations can be obtained for $\beta = 1$ and $\alpha \neq 0$. Finally by considering, $\beta \neq 1$ and $\alpha = 0$, we get the Davidson-Cole equation.

2.3.2. Modulus formalism

Another alternative way to analyze the raw experimental data is in terms of the electric modulus which is the inverse of the permittivity formalism. The main advantage of the modulus formalism is that the electrode polarization can be suppressed [181]. The complex electric modulus $M^*(\omega)$ is defined as the inverse of the complex permittivity $\varepsilon^*(\omega)$ i.e.

$$M^*(\omega) = \frac{1}{\varepsilon^*(\omega)} = \frac{\varepsilon'(\omega)}{\varepsilon'^2(\omega) + \varepsilon''^2(\omega)} + j\frac{\varepsilon''(\omega)}{\varepsilon'^2(\omega) + \varepsilon''^2(\omega)} = M'(\omega) + jM''(\omega), \qquad (2.34)$$

which was developed by Macedo et al. [182]. This formalism is also useful in determining charge carrier parameters such as the conductivity relaxation time. The imaginary part of modulus shows a peak at a particular frequency known as the relaxation frequency. The low frequency side of the peak represents the range of frequencies in which charge carriers can move over long distances. The high frequency side of the *M*'' peak represents the range of frequencies in which charge carriers are spatially confined to their potential walls and can only make localized motion within the walls.

In the modulus formalism, the Havriliak-Negami (HN) equations have the following form [183],

$$M' = M_\infty M_s \times \frac{[M_s A^B + (M_\infty - M_s)\cos\beta\varphi]A^\beta}{M_s^2 A^{2\beta} + 2A(M_\infty - M_s)M_s\cos\beta\varphi + (M_\infty - M_s)^2}, \qquad (2.35)$$

$$M'' = M_\infty M_s \times \frac{[(M_\infty - M_s)\sin\beta\varphi]A^\beta}{M_s^2 A^{2\beta} + 2A(M_\infty - M_s)M_s\cos\beta\varphi + (M_\infty - M_s)^2}, \qquad (2.36)$$

where

$$A = [1 + 2(\omega\tau)^{1-\alpha}\sin\frac{\alpha\pi}{2} + (\omega\tau)^{2(1-\alpha)}]^{1/2}, \qquad (2.37)$$

$$\varphi = arctg\left[\frac{(\omega\tau)^{1-\alpha}\cos\frac{\alpha\pi}{2}}{1+(\omega\tau)^{1-\alpha}\sin\frac{\alpha\pi}{2}}\right], \tag{2.38}$$

$$M_s = \frac{1}{\varepsilon_s},\ M_\infty = \frac{1}{\varepsilon_\infty} \tag{2.39}$$

For the values of $\alpha = 0$ and $\beta = 1$, the relaxation represents the Debye relaxation and for non-Debye relaxation, $\alpha \neq 0$ and $\beta \neq 1$ that are characterized by a distribution of relaxation times and such distribution may originates from the non-homogeneity of the doping process [184] implying different environments for the charge carriers.

The symmetrical single relaxation peak in M'' spectra indicates the Debye type relaxation of charge carriers. However, the unsymmetrical profile of M'' indicates that the simple exponential (Debye) is inappropriate to describe the relaxation and should be replaced by a frequency dependent electric modulus

$$M^*(\omega) = M_\infty\left[1 - \int_0^\infty -\frac{d\phi(t)}{dt}\exp(-i\omega t)dt\right] \tag{2.40}$$

where $\phi(t)$ is the Kohlrausch-Williams-Watts (KWW) decay function and this function accounts for an asymmetrical distribution of relaxation times and can be expressed as follows [185],

$$\phi(t) = \exp\left(\frac{-t}{\tau_0}\right)^\beta \tag{2.41}$$

where the stretching parameter $\beta = 1.14/w$ and w is the full-width at half-maximum (FWHM) and it is 1.14 for Debye relaxation. With an approximate frequency representation of KWW function, proposed recently by Bergman [186] that allows a more direct and easy analysis in the frequency domain for the fitting of imaginary part of modulus $M''(\omega)$ as follows:

$$M'' = \frac{M''_{\max}}{1-\beta+[(\beta/(1+\beta))(\beta(\omega_{\max}/\omega)+(\omega/\omega_{\max})^\beta)]} \tag{2.42}$$

where $M_{\max}$ and $\omega_{\max}$ are the peak maximum and peak frequency of imaginary part of modulus, respectively and the parameters such as $M_{\max}$, $\omega_{\max}$ and β can be extracted from the best fitted curve.

2.3.3. Admittance formalism

Admittance (*Y*) is an expression of the ease with which alternating current flows through a complex circuit or system. Admittance is a vector quantity comprised of two independent scalar phenomena: conductance and susceptance. Conductance (*G*) is a measure of the ease with which charge carriers can pass through a component or substance. The more easily the charge carriers move in response to a given applied electric potential, the higher the conductance. Susceptance (*B*) is an expression of the readiness with which an electronic component, circuit, or system releases stored energy as the current and voltage fluctuate. It is observed for ac but not for dc. When ac passes through a component that contains susceptance, energy might be stored and released in the form of a magnetic field, in which case the susceptance is inductive or energy might be stored and released in the form of an electric field, in which case the susceptance is capacitive. Admittance is the vector sum of conductance and susceptance. The admittance of the sample representing the equivalent parallel conductance $G(\omega)$ and susceptance $B(\omega)$

$$Y^*(\omega) = (Z^*)^{-1} = G(\omega) + i\omega B(\omega) \tag{2.43}$$

The frequency dependence of these elements arises from the fact that they represent an equivalent circuit of a system that is not necessarily a parallel combination of frequency-independent elements.

2.3.4. Impedance formalism

Complex impedance (Z^*) is defined as the reciprocal of admittance as follows

$$Z^*(\omega) = V/I = 1/Y^*(\omega) \tag{2.44}$$

This formalism provides information about the electrical conductivity and nature of charge carrier relaxation processes present in a material. The complex impedance described according to Cole-Cole formalism can be expressed as:

$$Z^*(\omega) = Z'(\omega) + jZ''(\omega) = R_\infty + \frac{R_0 - R_\infty}{[1 + (i\omega\tau)^{1-\alpha}]} \tag{2.45}$$

where $Z'(\omega)$ and $Z''(\omega)$ are the real and imaginary parts of complex impedance Z^*, R_∞ and R_0 are the resistance when ($\omega\rightarrow\infty$) and ($\omega\rightarrow 0$), respectively. The parameter

$\tau=RC$ is the relaxation time and $0 \leq \alpha < 1$ characterizes the distribution of the relaxation times and for an ideal Debye relaxation $\alpha=0$.

These different formalisms are often used to study different relaxation processes occurring in solids. Electrical relaxation phenomena are usually analysed in terms of the dielectric permittivity by the relaxation of the electric displacement vector (*D)* under the constraint of constant electric field (*E)*. However, in dielectrics containing mobile charges, it seems convenient to concentrate on the relaxation of the electric field (*E)* under the constraint of a constant displacement vector (*D)* which leads to the inverse dielectric permittivity and the definition of electric modulus. An advantage of using the electric modulus to interpret bulk relaxation properties is that variations in the large values of permittivity and conductivity at low frequencies are minimized. In this way the familiar difficulties of electrode nature and contact, space charge injection phenomena and absorbed impurity conduction effects, which appear to obscure relaxation in the permittivity formulation can be resolved or even ignored.

2.4. Stopping power in materials and swift heavy ion irradiation

The stopping power of materials is not only of interest in the radiation physics but also of importance for several fields that deals with the charged particles and ions, such as radiation dosimetry, radiation therapy, ion implantation etc. and therefore the study of the slowing down of energetic ions in matter has been a great attraction for both experimental and theoretical fields. During the passage of the ion through material, electronic excitation in target materials is the dominant mechanism of ion energy loss over a wide ion-energy range. For high energy region, the stopping power is mainly described by the Bethe-Bloch (BB) formula [187, 188]. For the intermediate energy regions, the BB formula can also be extended by considering the inner shell corrections [189-191] and effective energies of projectiles [192-194]. Although, the consideration of these corrections the BB theory is not sufficiently accurate below 0.2 MeV/amu, and in general agreements with the experimental data are unsatisfactory. In 1953, Lindhard and Scharff [195] have proposed a useful statistical formula for mean excitation energy *I* of the target materials. Sugiyama have adopted this formula for the mean excitation energy I^* and obtained an electronic stopping formula for the intermediate energies [194]. Lindhard-Scharff-Schiøtt (LSS) [196] formula has predicted the average values at low energies. Sugiyama expressed the electronic stopping power as the sum of the

modified Bethe-Bloch and modified Lindhard-Scharff-Schiøtt formulas [194]. Applying the Bohr stripping criterion both to the projectile and to the target atoms in the modified BB formula and similarly in the modified LSS formula, Sugiyama used the quasi-molecule criterion. However in applying these criteria he used the Thomas-Fermi function and calculated the results numerically. Therefore, uncertainties resulted both due the nature of Thomas-Fermi function and numerical calculations. H. Gumus and F. Koksal [197] derived a valid expression for the stopping power for the whole energy region by obtaining the analytical formulas for the effective charge, effective mean excitation energy and the effective atomic number of the projectile and the target atoms.

2.4.1. Statistical theory and computational method of stopping power

The electronic stopping power of a heavy ion of effective charge Z_{1e}^{*} and velocity v_1, passing through a stopping medium is given by the modified Bethe formula within the first-order Born approximation,

$$S_{e0} = \frac{4\pi e^4 Z_1^{*2} N_0}{m v_1^2} \frac{N_0}{A} Z_2^{*} \left\{ \ln \frac{2mc^2\beta^2}{I^{*}} - \ln(1-\beta^2) - \beta^2 \right\} \qquad (2.46)$$

where m is the mass of the electron, $N = N_0 / A$ is the density of target atoms, Z_1^{*} and Z_2^{*} are the effective charges of projectile and target respectively, A is the atomic weight of target element, N_0 is the Avogadro's number and $\beta = v_1 / c$, where c is the velocity of light I^{*} is the effective mean excitation energy of the target. Bohr stripping criterion [197] is described that all outer shell electrons bound to moving ion in orbits with velocities less than v_1 are stripped off by the target

$$Z_1^{*} = \int_{r_b}^{\infty} 4\pi r^2 n(r) dr \qquad (2.47)$$

where r is the distance from the nucleus, r_b is determined by Bohr stripping criterion, $v_F(r_b) = (b\hbar / m)[3\pi^2 n(r_b)]^{1/3}$, $v_F(r)$ is the orbital electron velocity between r and $r + dr$, b is the proportional constant of order 1.26 and $n(r)$ is the electron charge density of Thomas-Fermi atom. Instead of inner shell corrections, it is better to consider

the effective charge of targets Z_2^* and the effective mean excitation energies I^* considering symmetry between the projectile and target atom:

$$Z_2^* = \int_{r_b}^{\infty} 4\pi r^2 n(r) dr \tag{2.48}$$

and from the Lindhard-Scharff theory [195]

$$\ln I^* = \frac{1}{Z_2^*} \int_{r_b}^{\infty} \ln\{\gamma\hbar\omega_p(r)\} 4\pi r^2 n(r) dr \tag{2.49}$$

where $\hbar\omega_p(r) = [4\pi e^2 \hbar^2 n(r)/m]^{1/2}$ is Plasmon energy and $\gamma = \sqrt{2}$ [198].

At low energies, Firsov [199] derived an energy loss formula due to the quasi-molecules in ion-atom collisions. The basic mechanism for the inelastic energy loss during the collision of the ion with the target atom is through the transfer of momentum of the electrons of one atom in the collision to the other atoms. A modification of the Firsov theory is a generalization of LSS formula [199] for arbitrary ion-target collision. The modified LSS formula can be written as,

$$S_{ei} = \xi_e 8\pi e^2 a_o N \left(\frac{Z_1' Z_2'}{Z_s^*} \right) \left(\frac{v_1}{v_o} \right) \tag{2.50}$$

where Z_1' and Z_2' are the effective atomic number of the projectile and target atom, respectively. Z' (Z' stands for Z_1' or Z_2') can be calculated from,

$$Z' = \int_0^{r_f} 4\pi r^2 n(r) dr \tag{2.51}$$

where r_f is determined from the criterion $v_1 \le f v_F(r_f)$.

The modified LSS formula given by equation (2.50) provides low velocity contribution to the stopping power of the target atom. a_o is the Bohr radius, v_o is the Bohr velocity and N is the density of target atoms with atomic number Z_2. ξ_e is the numerical correction factor in the order of $Z_1^{1/6}$ [196].

The universal nuclear stopping given by Ziegler and Biersack [200] is

$$S_n(E) = \frac{8.462 \times 10^{-15} Z_1 Z_2 M_1}{(M_1 + M_2)(Z_1^{0.23} + Z_2^{0.23})} S_n(\varepsilon) \text{ eV/ (atoms/cm}^2) \tag{2.52}$$

with the reduced energy ε being calculated as

$$\varepsilon = \frac{32.53 M_2 E}{Z_1 Z_2 (M_1 + M_2)(Z_1^{0.23} + Z_2^{0.23})} \tag{2.53}$$

and the reduced nuclear stopping power being calculated as

$$S_n(\varepsilon) = \frac{\ln(1 + 1.1383\varepsilon)}{2(\varepsilon + 0.1321\varepsilon^{0.21226} + 0.19593\varepsilon^{0.5})} \quad \text{for } \varepsilon \leq 30 \tag{2.54}$$

$$S_n(\varepsilon) = \frac{\ln(\varepsilon)}{2\varepsilon} \quad \text{for } \varepsilon > 30 \tag{2.55}$$

2.4.2. Theory of ion-solid interaction

The interaction of an energetic heavy ion with solid can produce irreversible dramatic changes of the properties in the target material. The energetic heavy ion-solid interaction involves many differences with respect to the other ionizing radiation (such as γ, *X*-ray and electrons, etc.) due to the deposition of localized high energy density within a confined volume and that the process is far from thermal equilibrium [201, 202]. The extreme energy density required for irreversible nanoscale modifications into solids can be achieved by the two principal categories of heavy ions: swift heavy ions (SHI) [203, 204] and highly charged ions [204, 205].

Any ion consisting of more than 20 nucleons and with kinetic energy greater than 1 MeV/nucleon is classified as a SHI. A SHI in solid loses its kinetic energy by interaction with target nuclei (nuclear energy loss S_n) and target electrons (electronic energy loss S_e). The interaction with the target nuclei dominates at ion energies below 0.1 MeV/u and leads to large angular scattering of the projectiles. The interaction with the target electrons leads to the excitation or ionization of the target atoms and the incident beam direction is retained. The type of interaction is dominated at ion energies ≥ 1 MeV/u and primarily generates hot electron gas around the trajectory. The energy deposited by the SHI irradiation in the material within a very small cylindrical volume along the ion trajectory (typically ~10 nm in diameter and ~10 μm in length depending on the kinetic energy of the SHI), resulting in the deposition of an extremely high energy density. The irradiated material can attain very high temperature during the passage of the heavy ion so that the target melts within a few picoseconds. The rapid solidification (~10-100 ps) can lead to a trail of defective or even amorphous material along the ion beam direction. The cylindrical ion tracks are well oriented along the beam trajectory and are themselves nanostructured that can be exploited for

nanotechnology [206-208]. The ion-polymer interaction is a complex process which involves lot of primary and secondary phenomena. Two phenomenological models have been proposed to describe the conversation mechanism of the energy of the excited electrons into the kinetic energy of the target atoms into materials: (a) Thermal Spike model and (b) Coulomb Explosion model. The two models associated with the ion-polymer interactions have been discussed briefly in the following subsections.

(a) Thermal spike model

The Thermal Spike model of the ion-solid interaction was first proposed by Szenes [132]. According to the Thermal Spike model, a large part of the intense excitation of the electron subsystem is transferred to the lattice system via electron-phonon coupling, and this can result in the melting of the material if the excitation is sufficiently intense [209]. The energy deposited by the ion leads to a transient temperature increase. The cylindrical volume around the ion path finally reaches the melting phase, which is subsequently quenched by the thermal conduction [210]. The analytic thermal spike model (ATSM) considers the atomic lattice subsystem where the SHI irradiation induced temperature distribution follows a Gaussian distribution [133, 211-213],

$$\nabla T(r,t) = \frac{Q}{\pi a^2(t)} e^{\frac{-r^2}{a^2(t)}} \tag{2.56}$$

where ∇T is the increase in target temperature at a distance r from the projectile trajectory, and time is zero when the spike temperature reaches its maximum. The time t is typically less than picoseconds after the passage of the ion [214]. The temporal coherence is contained in $a(t)$ which is closely related to the FWHM of the thermal spike. The heat conduction broadens the thermal spike and reduces the temperature in the centre of the track. Q describes the amplitude of the thermal spike and can be determined from the conservation of energy:

$$gS_e = \rho cQ + \rho\pi R^2 L \cong \rho cQ \tag{2.57}$$

where c is the specific heat capacity of the material calculated using the Dulong-Petit formula and ρ is the density. Only a fraction of deposited energy that equals to the kinetic energy of the projectile is used to heat the lattice subsystem and is expressed by the parameter g in equation (2.57). Also the velocity effect of the projectile ion is included in ATSM as a variation of the g factor having the value of $g = 0.4$ in the low

velocity regime ($E \leq 2.2$ MeV/Å) and $g = 0.17$ in the high velocity regime ($E \geq 8$ MeV/Å). Values of g between 0.17 and 0.4 can be found for intermediate velocities. The radius of the ion track is determined from the largest radius of the melt. The two solutions can be obtained as follows:

$$R^2 = a^2(0) \ln \frac{S_e}{S_{et}}, \; 1 \leq \frac{S_e}{S_{et}} \leq e \tag{2.58a}$$

$$R^2 = \frac{a^2(0)}{e} \frac{S_e}{S_{et}}, \; \frac{S_e}{S_{et}} \geq e \tag{2.58b}$$

$$S_{et} = \frac{\rho c \pi a^2(0) \nabla T_m}{g} \tag{2.58c}$$

where e is Euler's number and S_{et} is the energy loss threshold for the formation of the ion track. The melt extends during cooling at high S_e values, while the initial radius is the largest radius of the melt at lower S_e values. The expression for the threshold energy loss can be obtained from equations (2.56) and (2.57) by setting $r = 0$ and $t = 0$ by designating ∇T_m as the minimal temperature increase required for melting. Knowing the basic parameters of the material such as density, specific heat capacity and melting temperature, the ion track radius can be calculated if we assume the constant parameters $a(0)$ and g for a specific material and a given SHI energy range. In an alternative approach, by plotting the square of the ion track radius vs. energy loss on a semi-logarithmic graph, the values of $a(0)$ and S_{et} can be obtained from the linear fit of the experimental data. The fraction g can be determined via the data analysis in the linear regime by combining equations (2.58b) and (2.58c).

(b) Coulomb explosion model

The Coulomb Explosion model is based on the assumption that the intense excitation and ionization along the ion trajectory leads to an unstable zone in which atoms are ejected into the non excited part of the solid by Coulomb repulsion [215, 216]. The Coulomb explosion model was first proposed by Fleischer *et al.* [216], which suggested that the resulting repulsion between the transiently ionized atoms in the solid, called a "Coulomb explosion," can be the reason for the production of a latent track in an insulator which may be seen by chemical etching. The released electrons have a broad

spectrum of kinetic energies and causes considerable ionization on their own. This electronic collision cascade spreads out very rapidly and carries away energy and charge from the ion trajectories. A core of positive target ions remains and due to the electrostatic repulsion, these ions repel each other, thereby creating vacancies and interstitials (Coulomb explosion [216, 217]), provided that the time for electron-ion recombination is longer compared to the Coulomb explosion time. The range of the atomic collision defines the core of the latent track with diameter less than 10 nm. For a valid Coulomb explosion model, the following criteria were laid down by Fleischer *et al.* [216].

(i) Formation of tracks by the Coulomb explosion model is possible in materials with low mechanical strength, low dielectric constant and small inter-atomic spacing. Since the electrostatic stress has to be larger than the mechanical strength, which is possible only when

$$n^2 > R \equiv E\varepsilon a_0^4 / 10e^2 \tag{2.59}$$

(ii) Tracks must be continuous that require at least one ionization per atom and hence $n > 1$ is the second criterion for track formation by Coulomb explosion model.

(iii) For the track formation, the availability of electrons for replacing the ejected ones in the material must be low and must not be able to replace the ejected electrons within a time frame of less than ~ 10^{-13} sec. Thus for a track to be formed by the Coulomb explosion model one must have:

$$n_n < en_a / a_0 \mu_n \pi k_B T t \tag{2.60}$$

where n_n is the number of free electrons in the system, n_a is the number of ionizations per atomic plane, k_B is the Boltzmann constant and μ_n is the electron mobility.

(iv) The final criterion for the Coulomb explosion model for explaining track formation in solids is low mobility of the holes created by the ejection of electrons along the ionized track. In general, the mobility of holes μ_p must be less than $a_0^2 e / t k_B T$ for the material in order to sustain the latent tracks.

However, Bringa *et al.* [218] have elucidated that the Coulomb explosion and thermal spike are two basic events that define the early and late aspects of the ionized tracks produced in solid targets during the passage of a highly energetic ion. No matter

whether a Coulomb explosion has really taken place in the solid, a thermal spike will eventually occur since at higher excitation densities the repulsive energy in the track produces a spike [218]. Although these two models have been used extensively to explain ion track formation, there is still a lot of debate regarding the applicability of these models.

CHAPTER-III

Experimental Techniques

This chapter deals with the different chemical oxidative polymerization techniques for synthesizing different nanostructures viz. nanoparticles, nanofibers and nanotubes of polypyrrole. This chapter also presents the different characterization techniques with their working principles such as the Transmission electron microscopy, Powder X-ray diffraction, Fourier transform infrared spectroscopy, Ultraviolet-visible spectroscopy, Thermogravimetric analysis, Dielectric spectroscopy and AC conductivity measurements employed in the present work.

3.1. Parent materials

Monomer pyrrole (Aldrich) was used for the synthesis of polypyrrole (PPy) nanostructures. Pyrrole (Py) was distilled under reduced pressure and stored in dark before use. Sodium dodecylsulfate (SDS), camphorsulfonic acid (CSA), dodecylbenzenesulfonic acid (DBSA), octylbenzenesulfonic acid (OBSA), para-tolunesulfonic acid (*p*-TSA) purchased from E-Merck (Germany) were used as dopants cum surfactants. Oxidant ammonium peroxydisulfate (APS) was procured from Aldrich Chemical Inc. (USA). To study swift heavy ion (SHI) irradiation effects on PPy nanostructures, polyvinyl alcohol (PVA) (M_w = 145000) were used as plasticizer for preparation of thin films of PPy nanostructures. All other chemicals, solvents and reagents used in the synthesis and purification process were of analytical grade and used as received without further purification.

The physical properties of the materials used for synthesis of different nanostructures of PPy in the present work are tabulated in the following tables.

Table 3.1: Physical properties of the pyrrole monomer.

Monomer	**Molar mass (g/mol)**	**Melting point (^{0}C)**	**Boiling point (^{0}C)**	**Density at 25 ^{0}C (g/ml)**	**Oxidation potential (Volt)**
Pyrrole (C_4H_5N)	67.09	-23	129-131	0.967	0.8

Table 3.2: Physical properties of dopants, oxidant and plasticizer used in synthesis.

Dopants/Surfactants	**Molar Mass (g/mol)**	**Melting point (^{0}C)**	**Boiling point (^{0}C)**	**Density at 25 ^{0}C (g/cm^3)**
Sodium dodecylsulfate (SDS) ($NaC_{12}H_{25}SO_4$)	288.372	206	N/A	1.01
Camphorsulfonic acid (CSA) ($C_{10}H_{16}O_4S$)	232.30	195	N/A	N/A
Para-tolunesulfonic acid (*p*-TSA) ($CH_3C_6H_4SO_3H$)	172.20	38	140	1.24
Dodecylbenzenesulfonic acid (DBSA) ($C_{18}H_{30}O_3S$)	326.49	10	82	0.992
Octylbenzenesulfonic acid (OBSA) ($C_{14}H_{22}O_3S$)	270.39	N/A	N/A	N/A

Table 3.3: Physical properties of oxidant.

Oxidant	**Molar Mass (g/mol)**	**Melting point (^{0}C)**	**Boiling point (^{0}C)**	**Density at 25 ^{0}C (g/cm^3)**
Ammonium persulfate (APS) $(NH_4)_2S_2O_8$	228.18	120	N/A	1.98

Table 3.4: Physical properties of plasticizer.

Plasticizer	Molar Mass (repeat unit) (g/mol)	Melting point (^{0}C)	Boiling point (^{0}C)	Density at 25 ^{0}C (g/cm^3)
Polyvinyl alcohol (PVA) $[CH_2CH(OH)]_n$	44	230	228	1.19

Table 3.5: Physical properties of solvents.

Solvents	Molar mass (g/mol)	Melting point (^{0}C)	Boiling point (^{0}C)	Density at 25 ^{0}C (g/cm^3)
Methanol (CH_3OH)	32.04	-97	64.7	0.792
Ethanol (C_2H_5OH)	46.07	-114	78	0.789
Acetone $(CH_3)_2CO$	58.08	-94.9	56.53	0.7925

3.2. Synthesis of polypyrrole nanostructures

3.2.1. Synthesis of polypyrrole nanoparticles

PPy nanoparticles were synthesized using the micro-emulsion polymerization method in which resulting nanoparticle size is controlled by the micelle reactor size [219]. A micro-emulsion is a thermodynamically stable and isotropic transparent solution of two immiscible liquids primarily consisting of oil, water and surfactant molecules. In micro-emulsion, spontaneous aggregation of surfactant molecules form stable spherical, cylindrical and hexagonal micelles depending upon the amount of surfactants in aqueous solution and their size and shape affect on the formation of nanoparticles as the polymerization takes place inside the core of micelles. It has been reported that

surfactants with longer carbon chains produce bigger nanoparticles as compared to shorter carbon chains of surfactant molecules as they provide more inner space to grow necessary polymerization [220]. In previous studies, PPy nanoparticles were successfully synthesized using different surfactants or soft templates and surfactant-free methods. Kim *et al.* [221] reported the size controlled synthesis of unagglomerated PPy nanospheres through a surfactant-free emulsion method. Jang *et al.* [222] synthesized crystalline supramolecular assemblies of amorphous PPy nanoparticles using octyltrimethylammonium bromide (OTAB) surfactant. Wang *et al.* [223] prepared PPy nanoparticles by micro-emulsion method using ferric chloride ($FeCl_3$) as oxidant and dodecyltrimethyl ammonium bromide (DTAB) as surfactant and resulting nanoparticles size varied from 50 nm to 100 nm, 100 nm to 200 nm with changing the surfactant concentration. Ovando-Medina *et al.* [224] prepared spherical PPy nanoparticles of sizes lower than 50 nm by micro-emulsion polymerization using sodium dodecylsulfate (SDS) as anionic surfactant, ethanol as co-surfactant and potassium persulfate (KPS) as oxidizing agent. With these achievements the micro-emulsion polymerization has proved as a powerful method for synthesizing nanoparticles of conducting polymers.

In this study, polypyrrole (PPy) nanoparticles were synthesized by chemical oxidative micro-emulsion polymerization method [219] using sodium dodecylsulfate (SDS) as anionic surfactant which also acts as dopant and ammonium persulfate (APS) as oxidant. A variable amount of anionic surfactant SDS, concentration above its critical micelle concentration CMC-I (8×10^{-3} M) was magnetically stirred for 1 h in 100 ml of double distilled water at room temperature to make a uniform micellar solution. 0.2 M pyrrole was added drop wise into the above micelle solution and stirred for about 2 h such that surfactant molecules encapsulated the monomers into the micelles formed by spontaneous aggregation of surfactant molecules. 0.2 M ammonium persulfate (APS) was added into the surfactant-monomer mixed solution to occur oxidative polymerization under a constant magnetic stirring for another 24 h. The molar ratio of monomer to oxidant was kept at 1:1 throughout the whole synthesis process to avoid over oxidation. After complete polymerization, excess amount of methanol was added into the solution to stop the reaction and complete precipitation by breaking hydrophilic-lyphophilic balance of the system. The black precipitate was filtered out and centrifuge with methanol several times followed by double distilled water unless the solution became colourless indicating complete removal of surfactant molecules,

residual monomers, unreacted oxidant and other impurities presented. The black precipitate thus obtained was collected and dried under vacuum for 72 h at room temperature. Following this procedure, four samples of PPy nanoparticles were synthesized at SDS concentration of 0.01 M, 0.05 M, 0.1 M and 0.2 M such that the selected SDS concentration were between its two critical micelle concentrations CMC-I (0.8 mM) and CMC-II (0.2 M) at room temperature. The block diagram for synthesis of PPy nanoparticles by micro-emulsion polymerization method is shown in Fig. 3.1.

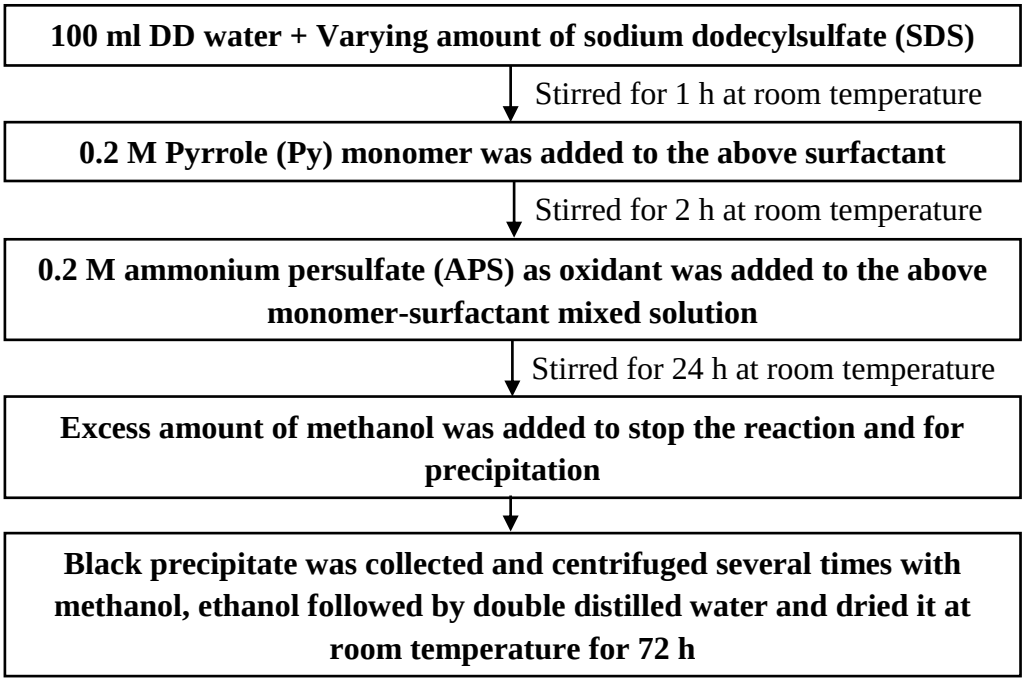

Figure 3.1: *Block diagram for synthesis of polypyrrole nanoparticles using micro-emulsion polymerization method.*

3.2.2. Synthesis of polypyrrole nanofibers

PPy nanofibers have been synthesized using various synthesis methods such as the template method [225], interfacial polymerization [93], seeding polymerization [58] etc. However, each currently used method has its own advantages as well as disadvantages. The template guided synthesis method uses structural directing agents such as zeolite, alumina, polycarbonate, porous membranes and surfactants as the templates [226, 227] and needs post polymerization step to remove externally applied templates, therefore produces lower yields with less reproducibility. The electrospinning method can produce nanofibers without using external template, but production scale are very limited [100]. Typically, a relatively new approach called interfacial polymerization

[228] has been developed to synthesize conducting polymer nanofibers as one of the most effective alternative chemical route. In this approach the polymerization occurs at the interface of two immiscible aqueous-organic biphasic medium and resulting products diffuse away from the interface to the aqueous solution because of their hydrophilic nature. In particular, interfacial method requires equal volume of organic solvent to the aqueous water and the major drawback of this method is that the organic solvents immiscible to water are typically very toxic to the environment and also makes the synthesis procedure costly. Therefore to design and synthesis of multifunctional PPy nanofibers it is crucial to find out a novel, reliable, cost effective, less toxic synthesis approach to realize their practical applications in nanodevices. To meet this objective, PPy nanofibers were synthesized by a novel interfacial polymerization method doped with a series of alkylbenzenesulfonic acids (ABSA) such as para-tolunesulfonic acid (*p*-TSA), camphorsulfonic acid (CSA), dodecylbenzenesulfonic acid (DBSA) and octylbenzenesulfonic acid (OBSA). The typical synthesis procedure using novel interfacial approach was as follows: 0.5 M pyrrole (Py) was dissolved in 1 ml xylene and the solution was added drop wise into the aqueous solution of 1 M of each of dopant (*p*-TSA, CSA, DBSA and OBSA) containing 0.5 M of APS oxidant. The mixture was allowed to react under constant stirring for 12 h at room temperature. The molar ratio of Py (monomer) to APS (oxidant) was kept as 1:1 and total volume of the mixture was kept at 100 ml. After complete polymerization, the precipitate was collected and washed off several times with ethanol, acetone and double distilled water and dried under vacuum at room temperature for 72 h. The block diagram for synthesis of PPy nanofibers using interfacial polymerization method is shown in Fig. 3.2.

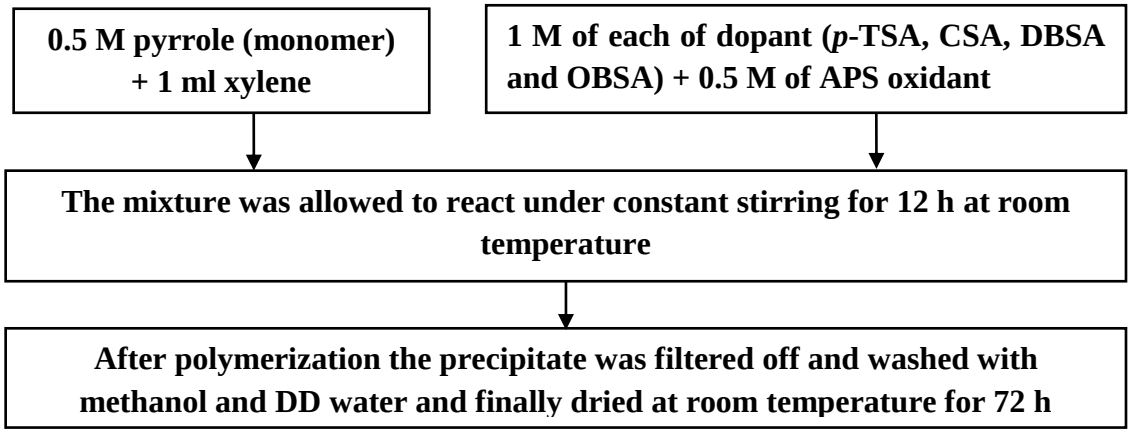

Fig. 3.2: *Block diagram for synthesis of PPy nanofibers using novel interfacial polymerization method.*

3.2.3. Synthesis of polypyrrole nanotubes

PPy nanotubes have been successfully synthesized using different synthesis methods such as the template synthesis [78], reactive self-degradation [124], electrochemical [229] and self-assembly polymerization [230]. Nanotubes with controlled morphology can be synthesized using hard template synthesis, but this method suffers a serious disadvantage of dissolution of the external template after polymerization. This can damage the resulting nanotubes of conducting polymers which limits their applicability in various applications. The reactive self-degrade approach needs a reactive template for polymerization making the synthesis costlier. Therefore, the template free self-assembly method has received more attention due to its simplicity, cost effectiveness and large-scale production. Another aspect of self-assembly method is that the dopant used during polymerization also acts as soft template in the process of formation of nanotubes [231, 232]. The morphology, diameter and length of the nanotubes can be determined by controlling the synthesis conditions such as dopant to monomer ratio, type and concentration of dopant and also on the reaction temperature [232, 233].

PPy nanotubes were synthesized using the chemical oxidative self-assembly polymerization method at different molar ratios of CSA/Py (dopant/monomer) keeping molar concentration of APS oxidant fixed. In a typical synthesis procedure, 0.15 M pyrrole (Py) and 0.075 M CSA was mixed in 40 ml double distilled water and stirred for 30 min. The reacted mixture formed a transparent solution of CSA-Py salt and the mixed solution was kept in an ice bath up to 0-5 ºC. A pre-cooled aqueous solution of 0.15 M APS in 20 ml double distilled water was added drop wise to the cooled mixed solution. Subsequently the mixture was allowed to react for 15 h at room temperature and after complete polymerization the precipitate was collected, filtered off and washed several times with methanol, acetone and double distilled water to remove the impurities, unreacted monomer and oxidant present in the resulting products. The filtered precipitate was dried at room temperature for 72 h. Following this procedure, four samples of PPy nanotubes were synthesized at CSA/Py molar ratios of 0.1:1, 0.5:1, 1:1 and 2:1 keeping the molar concentration of Py and APS fixed at 0.15 M. The block diagram for synthesis of PPy nanotubes by self-assembly polymerization method is shown in Fig. 3.3.

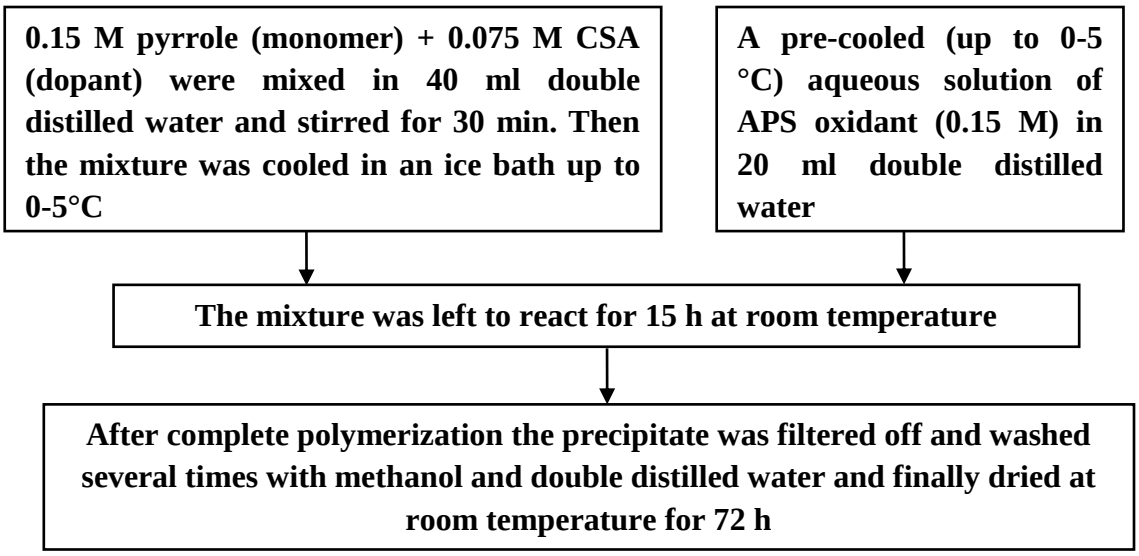

Figure 3.3: *Block diagram for synthesis of polypyrrole nanotubes by self-assembly polymerization method.*

3.3. Swift heavy ion irradiation

Swift heavy ion (SHI) irradiation on PPy nanostructures was carried out at the Inter University Accelerator Centre (IUAC), New Delhi, India. SHI irradiation experiments were performed in Materials Science (MS) beam line under high vacuum of 10^{-6} Torr. The high energy (> 1 MeV/u) of the projectile swift heavy ions was provided by the 15 UD Pelletron Accelerator at IUAC, New Delhi.

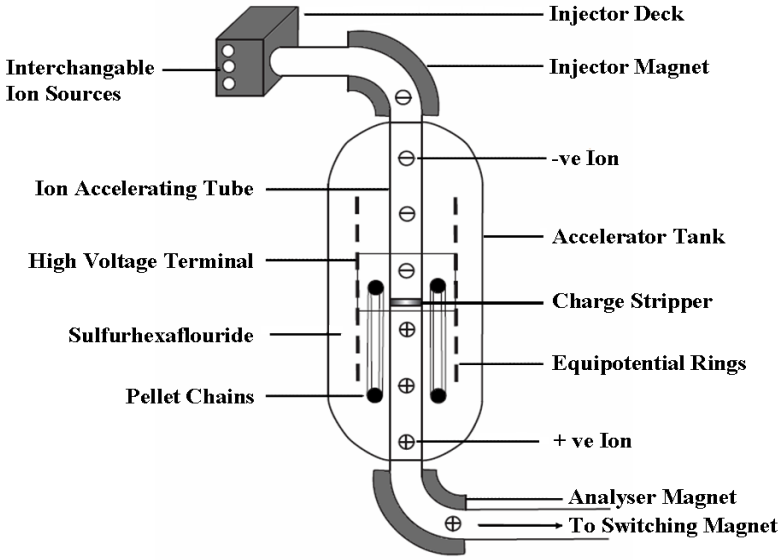

Figure 3.4: *Schematic block diagram showing the principle of acceleration of ions in a Pelletron.*

The schematic view of 15 UD Pelletron accelerator at IUAC and its different parts are shown in Fig. 3.4. The 15 UD Pelletron accelerators is a tandem electrostatic Van de Graff type accelerator capable of accelerating an ion up to energy of 200 MeV depending upon the ion source and the charge state. It consists mainly of two parts: (a) ion source and (b) accelerating column with many auxiliary parts in between. In the top portion of the tank there are three different ion sources such as R.F. source (ALPHATROSS), Source of Negative Ions by Cesium Sputtering (SNICS) and direct extraction negative ion source (Duoplasmatron), which can generate different negative ions to be injected in the pelletron tank. These three ion sources working on three different principles can produce almost every type of negative ions. Duoplasmatron works on the principle of gas discharge, SNICS works on the principle of surface ionization and R.F. source utilizes high frequency gas discharge.

The negative ions emerging from the ion source are at first accelerated to 250 keV by the high voltage deck potential and different optical elements focus and inject the same into the vertical accelerating tube. The injector magnet does mass selection by bending the ions by 90^{o} and then injects them into the accelerating tube. The ionized negative ions then follow a vertical downward path and get accelerated through the accelerating tube. It consists of a vertical insulating cylindrical tank of height 26.5 m and diameter 5.5 m, filled with SF_6 (Sulphur hexafluoride) at high pressure (> 200 psi) as an insulating gas. In the top portion of the tank, there is an ion source system consisting of a high negative potential deck, SNICS, vacuum system, power supplies and controls of the ion source required to produce and inject the negative ions into accelerating tank. The ion source system is followed by the high voltage accelerating terminal of height 3.18 m and diameter 1.52 m inside the tank. The terminal is connected to the tank vertically through ceramic titanium tubes called accelerating tubes. A potential gradient is maintained through the tubes from high voltage to ground, from top of the tank to the terminal as well as from the terminal to the bottom of the tank. The insulating column that supports the high potential terminal consists of thirty 1 MV modules, 15 on either side of the terminal. The upper portion of the column is referred to as low energy section and portion below the terminal is referred to as the high energy section. The shorted section with no potential gradient, commonly known as the Dead Section, is provided each in the low a high energy sections for equipment housing. The low energy dead section (LEDS) is also provided with an electrostatic

quadruple lens while the high energy dead section (HEDS) is equipped with a second foil striper assembly. A shorting rod system is also provided for temporarily shorting selected column modules without entering the pressure vessel. Two insulating shafts run one from each ground end to the terminal and are used to drive four 400 cycles per second (cps) generators, which provide power for the equipments like heater lenses, pumps, foil changer etc., housed in the column, dead sections and terminal. The charging process of high voltage terminal to 15 MeV is done by using the pelletron charging chains. There are two independent sub systems with one charging chain in each, so that each chain is required to supply 100 μA current. The negative ions from the ion source are focussed by different optical instruments and injected by the injector magnet into the accelerator with lower energy (>>300 KeV) provided by the negative potential deck at the ion source. In the terminal, the negative ions are stripped off few electrons by the positive ions which are again accelerated towards the bottom of the tank at the ground potential.

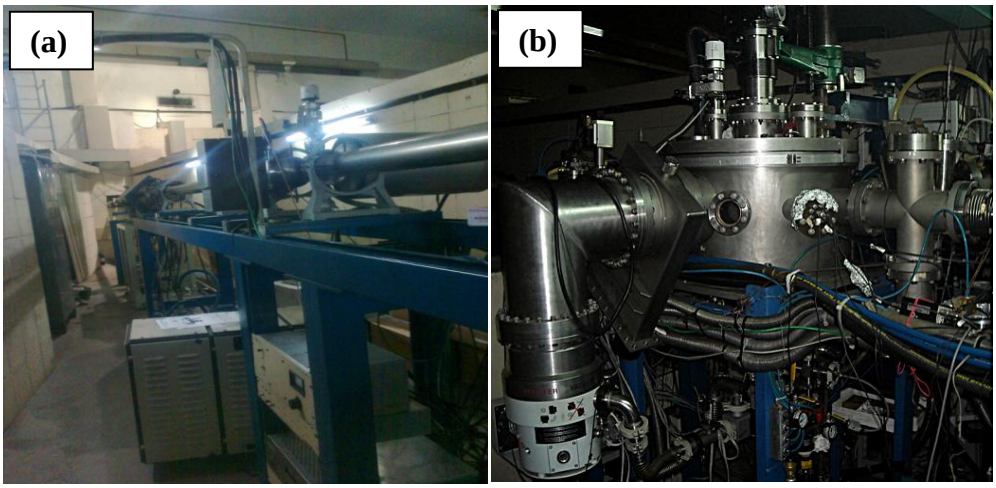

Figure 3.5: *Photographs of (a) Materials Science (MS) beam line and (b) the high vacuum irradiation chamber.*

Fig. 3.5 (a)&(b) shows the Materials Science (MS) beam line and high vacuum irradiation chamber at IUAC, New Delhi used to irradiated the samples for the present work. For SHI irradiation, films of polypyrrole nanostructures (such as nanoparticles, nanotubes and nanofibers) were cut into 1 cm × 1 cm area and fixed on a sample holder (ladder) made up of copper. The ladder in the Material Science (MS) chamber is rectangular and 24 samples can be loaded with six samples on each side at a time. The

ladder with the loaded samples is inserted in the MS vacuum chamber and the vacuum inside the irradiation chamber is maintained at ~ 10^{-6} Torr with the help of a rotary and turbo-molecular pump during irradiation experiment. The different nanostructures of polypyrrole that have chosen in the present work have been irradiated at the normal beam incidence.

3.4. Parameters related to ion irradiation

3.4.1. Fluence (ϕ)

One of the most crucial parameter related to ion beam during swift heavy ion (SHI) irradiation is the fluence. Fluence (ϕ) is defined as the total number of irradiating ions incident per square centimeter (ions/cm^2) on the target sample. The ion fluence was estimated by beam current and the time of irradiation as follows:

$$I = Q/T = Dqe/T = \phi Aqe/T \tag{3.1}$$

$$\therefore \; T = \phi Aqe/I \tag{3.2}$$

where,

I = ion current (nA)

Q = total charge

D = dose = ion fluence (ϕ) in ions cm^{-2} × area (A) of irradiation in cm^{-2}

q = charge state

e = electronic charge = 1.6 × 10^{-19} C

T = time of irradiation (sec)

Since, the number of particles per nano ampere of beam current $= I/qe$ (pnA)

$$\therefore \text{T} = \phi A/\text{beam current (pnA)} \tag{3.3}$$

Using equation (3.3), the required time for a particular fluence was calculated. In the present work five different ion fluence of 1×10^{10}, 5×10^{10}, 1×10^{11}, 5×10^{11} and 1×10^{12} ions/cm^2 were chosen to irradiate PPy nanostructures to study the SHI irradiation induced modification on different physico-chemical properties. During irradiation experiment the beam current was maintained at 0.5 pnA (particle nanoampere) to avoid further heating of the irradiated samples.

3.4.2. Beam energy

The energy of the projectile accelerated ion beam depends on the charge state (q) of ion and the terminal potential V_T as follows:

$$E(MeV) = (q+1)V_T + V_{inj} \quad (3.4)$$

For the 15 UD Pelletron at Inter University Accelerator Centre (IUAC), New Delhi, the terminal potential (V_T) is in the range of 10 MeV to 15 MeV and the Injector potential (V_{inj}) is in the range of 250 to 350 keV. The projected range of 160 MeV Ni^{12+} ion beam used in the present work has been calculated using the SRIM-2007 code (SRIM-Stopping Ranges of Ions in Matter). The incident energy, corresponding electronic energy loss (S_e), nuclear energy loss (S_n) and projected range obtained from SRIM-2007 code for Ni^{12+} ion beam are presented in Table 3.6.

Table 3.6: SRIM data for 160 MeV Ni^{12+} ions in polypyrrole nanostructures.

Sample	**Ion**	**Energy (MeV)**	**S_e (eV/Å)**	**S_n (eV/Å)**	**Projected range (μm)**
PPy nanoparticles	Ni^{12+}	160	4.489×10^{2}	5.135×10^{-1}	42
PPy nanofibers	Ni^{12+}	160	4.489×10^{2}	5.135×10^{-1}	42
PPy nanotubes	Ni^{12+}	160	4.489×10^{2}	5.135×10^{-1}	42

The sample showing the best physico-chemical properties in each system studied in the present work was chosen to irradiate with 160 MeV Ni^{12+} ions with different ion fluence of 1×10^{10}, 5×10^{10}, 1×10^{11}, 5×10^{11} and 1×10^{12} ions/cm^2 to further enhance the properties. The calculated ion range as tabulated in Table 3.6 showed that projected ion range was larger than the film thickness of PPy nanostructures (~30-35 μm) which confirmed that the modifications of different physico-chemical properties in PPy nanostructures was only due to irradiation effect, not because of ion implantation effect.

3.5. Characterization techniques

3.5.1. Transmission electron microscopy

Transmission electron microscopy (TEM) is a special kind of microscopy technique largely used to know about the shape, size, morphology and internal microstructure of different nanoscale objects. In contrast to other microscopes, the electrons that pass through the TEM interact with the atoms of the sample and due to this interaction the electrons are being scattered from the sample. The final image formed by the TEM is a very complicated interference pattern of incident and diffracted beams.

The principal setup of TEM is similar to that of a light microscope. The sample is being illuminated with electrons (light in case of optical microscope) and the image of the sample is then magnified by means of projection lenses and represented on a canvas (screen). However, in case of TEM the electromagnetic lenses are used to guide the projected electron beam through the microscope. The condenser lenses are used in order to focus the electron beam which illuminates the sample. By changing the focal distance of condenser lenses, one can produce parallel or convergent illumination. The parallel beam is usually used in traditional TEM. The convergent beam is typical for STEM mode (Scanning TEM), because one needs to illuminate every point of the sample. The objective lenses of TEM are used for the formation of image. After passing through the objective lens, the electron beams from the sample are focused at the image plane. The objective lenses define the quality of image produced and in that way the resolution of microscope. The projection lenses are used for post-magnification of the image. By using high resolution transmission electron microscope (HRTEM), highest magnification can be obtained up to the order of 10^6 or even higher. The final image can be photographically recorded by exposing a photographic plate directly to the electron beam, or a high-resolution phosphor may be coupled by means of an optical lens system or a fibre optic light-guide to the sensor of a CCD (charge-coupled device) camera. The image detected by the CCD may be displayed on a monitor or computer. In the present work, the TEM studies have been carried out by using JEOL JEM-2100 (200 kV) transmission electron microscope at the Sophisticated Analytical Instrumentation Facility (SAIF), North-Eastern Hill University (NEHU), Shillong, Meghalaya, India shown in Fig. 3.6. The samples have been prepared on carbon coated copper grids for viewing under HRTEM.

Figure 3.6: *Transmission electron microscope (JEOL, JEM-2100, 200 kV) at SAIF, NEHU, Shillong.*

3.5.2. Powder X-ray diffraction

The powder X-ray diffraction (XRD) developed by Debye and Scherrer is a powerful technique to investigate the crystal structure of materials. This technique is based on the scattering of X-rays by crystals following the Bragg's diffraction law. Diffraction occurs when a wave meets a set of regularly spaced scattering objects which is of same order of magnitude with the interplanar spacing. X-ray diffraction pattern gives information about the crystal structure parameters such as crystallite size (domain length or extent of order in case of polymers), interplanar spacing (d-spacing), interchain or hopping distance (R), phase and lattice constants. The diffraction peak intensity and angle of diffraction are related to the atomic arrangement of the crystal. For polymeric materials, XRD is carried out to determine the crystalline and amorphous portions in terms of the degree of crystallinity. It is also used to determine the domain length or extent of order in case of polymers. The X-ray diffraction patterns for polypyrrole nanostructures reported in the present work were recorded using a Rigaku Miniflex X-ray diffractometer using CuK_{α} radiation (λ = 1.5406 Å) as shown in Fig. 3.7.

Figure 3.7: *Rigaku Miniflex X-ray diffractometer installed at the Department of Physics, Tezpur University.*

3.5.3. Fourier transform infrared spectroscopy

Fourier transform infrared spectroscopy (FTIR) is a powerful analytical technique for characterizing and identifying organic molecules, functional groups and molecular structure of different compounds. This technique uses molecular vibrations to characterize a sample. In FTIR spectroscopy, an infrared (IR) radiation is allowed to pass through sample and a part of IR is absorbed by the sample while the rest is transmitted from sample. The absorbed IR at a particular frequency shows a peak which suggests the characteristic of stretching or bending vibration modes of a particular chemical bond of the sample. The suitable frequency range for identification of a chemical compound lies in the near and mid-infrared regions because most of the molecular vibrations lie in these frequency regions. The resulting absorption spectrum represents the molecular fingerprint of the sample with absorption peaks correspond to the frequencies of vibrations between the atomic bonds. Each material has a unique atomic structure due to which two different samples cannot yield the same infrared spectra and hence the infrared spectroscopy can result in qualitative analysis of different kind of materials.

The infrared (IR) spectrum can be divided into three main regions: the far-infrared (< 400 cm^{-1}), the mid-infrared (4000-400 cm^{-1}) and the near-infrared (13000-4000 cm^{-1}). Many infrared applications employ the mid-infrared region, but the near- and far-infrared regions also provide important information about certain materials. A single vibrational energy change is accompanied by a number of rotational energy

changes, consequently the vibrational spectra appear as bands rather than as discrete lines. The band positions in IR spectrum are presented as wave numbers (in cm^{-1}) and consequent band intensities are expressed either as transmittance 'T', the ratio of the radiant power transmitted by the sample or the absorbance 'A', logarithm to the base 10 of the reciprocal of the transmittance, $A = \log_{10}(1/T)$. The frequency at which sample absorbs IR radiation allows direct identification of the sample's chemical composition, since functional groups are known to absorb IR radiation at specific frequencies. The FTIR spectroscopy studies of polypyrrole nanostructures were carried out to understand their structural, compositional and doping studies. The FTIR spectra were recorded using a Perkin Elmer spectrum 100 spectrophotometer installed at Tezpur University, Assam, India, shown in Fig. 3.8.

Figure 3.8: *Perkin Elmer Spectrum 100 spectrophotometer installed at Department of Chemical Sciences, Tezpur University, Assam, India.*

3.5.4. Ultraviolet-visible spectroscopy

Ultraviolet-visible (UV-vis) absorption spectroscopy is a well known characterization technique to study optical property of materials. It is a non-destructive technique and does not require any special preparation and contact. UV-vis spectroscopy provides information about electronic transition and hence electronic structure of materials. There is a linear relationship between absorbance and absorber concentration that makes UV-vis spectroscopy especially attractive for making quantitative measurements. In this technique, absorption of light in the ultraviolet (10-420 nm), visible (420-700 nm) and near-infrared (700-2500 nm) is measured. The absorption of light in UV/vis/NIR region depends on the nature of chemical groups present in the studied

sample. In ground state, a polymer molecule contains two electrons of equal and opposite spin in each filled molecular orbital. One of the electrons in the highest filled π molecular orbital absorbs light and is raised to the lowest unfilled π molecular orbital. The different possible transitions are as followed:

(a) $\sigma - \sigma^*$ transition: In this type of transition, the transition of electron takes place from a bonding sigma orbital to a higher energy antibonding sigma orbital. Since sigma bonds are very strong, this type of transition involves a high energy process.

(b) $n - \sigma^*$ transition: This type of transition is observed in saturated compounds having one hetero atom with unshared pair of electrons. This transition requires less energy than that of the $\sigma - \sigma^*$ transition. In general, $n - \sigma^*$ transitions are sensitive for hydrogen bonding.

(c) $\pi - \pi^*$ transition: Such transition occurs in compounds having unsaturated centres and requires less energy than $n - \sigma^*$ transition.

(d) $n - \pi^*$ transition: In this type of transition an electron of unshared electron pair of a hetero atom is excited to π^* antibonding orbital, which requires the least amount of energy. Transitions from the highest occupied molecular orbital (HOMO) to the lowest unoccupied molecular orbital (LUMO) require the least amount of energy and are therefore usually the most important. This type of transition gives rise to an absorption band at longer wavelength regions.

In organic molecules and polymers, the UV-vis spectrum can help in identifying chromophores and the extent of electronic delocalization [234]. Similarly, for solid materials the UV-vis spectrum can measure the band gap and identify any localized excitations or impurities [235]. The UV-vis spectroscopy studies of polypyrrole nanostructures were carried out to study the optical absorption characteristics and hence to determine the energy band structure using a Shimadzu model UV-2450 spectrophotometer installed at the Department of Physics, Tezpur University, Assam, India as shown in Fig. 3.9.

Figure 3.9: *UV-visible spectrophotometer (ShimadzuUV-2450) installed at Department of Physics, Tezpur University, India.*

3.5.5. Thermogravimetric analysis

Thermogravimetric analysis (TGA) is a powerful technique for thermal characterization of materials. In this technique, weight of a substance is heated in an inert environment at a controlled rate and is recorded as a function of temperature. TGA is widely applied to analyze the characteristic decomposition patterns, studies of degradation mechanisms and reaction kinetics of a sample. A thermogravimetric analyzer consists of a sample pan that is supported by a precision balance and it resides in a furnace which is heated or cooled during the course of experiment. A purge gas such as nitrogen is used to provide the inert atmosphere for heating the sample and mass of the sample is monitored as function of heating temperature during experiment. The thermal stability of a material is the prime aim studied by TGA. A material is thermally stable up to its decomposition temperature (T_d) at which the material starts degrading due to breaking of bonds by thermal energy. Beyond the degradation temperature the material starts to degrade. In the present work, thermal stability of PPy nanostructures was studied using thermogravimetric analyzer (TGA, Perkin Elmer STA 6000) installed at Materials Research Laboratory, Dept. of Physics, Tezpur University as shown in Fig. 3.10.

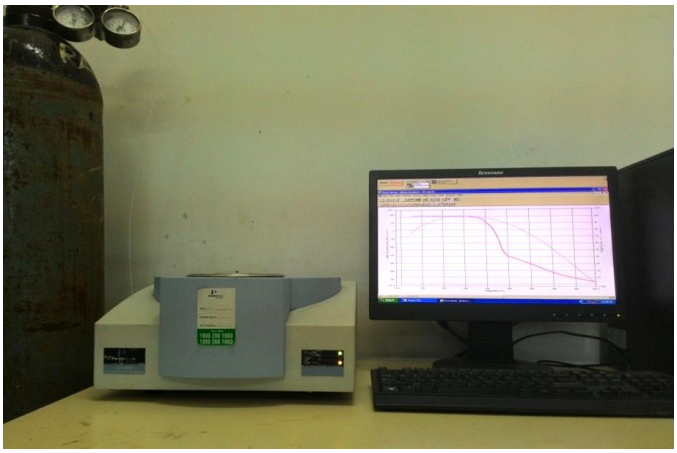

Figure 3.10: *Thermogravimetric analyzer, Perkin Elmer STA 6000 installed at Materials Research Laboratory, Dept. of Physics, Tezpur University.*

3.6. Dielectric relaxation spectroscopy

Dielectric relaxation spectroscopy has been widely used to understand the charge transport and relaxation mechanisms in disordered materials [236, 237]. The measurement of low frequency conductivity and dielectric relaxation have proved to be valuable in providing valuable information on the mechanisms of charge transport that dc conductivity alone does not provide [238, 239]. That is why this technique has been used extensively in many research areas such as in condensed matter physics, polymer science and materials sciences [240, 241]. The overall dielectric behaviour can be studied by employing different formulations such as complex impedance Z^*, complex permittivity ε^* and complex modulus M^*. In the present work, dielectric relaxation and ac conductivity of PPy nanostructures were studied using a Hioki 3532-50 LCR meter connected with stainless steel circular electrodes (radius=0.5 cm) as shown in Fig. 3.11.

Figure 3.11: *HIOKI 3532-50 LCR HiTESTER installed at Materials Research Laboratory, Department of Physics, Tezpur University.*

3.6.1. Impedance formalism

The real (Z') and imaginary (Z'') parts of complex impedance (Z^*) can be calculated as:

$$Z' = |Z|\cos\theta \tag{3.5}$$

$$\text{and } Z'' = |Z|\sin\theta \tag{3.6}$$

where θ $(= \tan^{-1}\frac{Z''}{Z'})$ is the phase angle and $|Z| = \sqrt{Z'^2 + Z''^2}$

The real (Z') and imaginary (Z'') parts of complex impedance (Z^*) were calculated using equations (3.5) and (3.6) using the measured values of $|Z|$ and phase angle (θ) over the frequency range of 42 Hz-5 MHz acquired by the HIOKI LCR meter.

3.6.2. Permittivity formalism

The complex dielectric permittivity (ε^*) of disordered materials can be calculated from the experimentally measured complex impedance $Z^*(\omega)$ data as follows:

$$\varepsilon^*(\omega) = \frac{1}{j\omega C_0 Z^*(\omega)} = \varepsilon'(\omega) - j\varepsilon''(\omega) \tag{3.7}$$

where the real part $\varepsilon'(\omega)$ implies the dielectric permittivity and imaginary part $\varepsilon''(\omega)$ implies the dielectric loss, $C_0 = \varepsilon_0 A/d$ is the capacitance of free space between the electrodes, ω is the angular frequency, A is the area of the electrode, d is the thickness of the sample and ε_0 is the permittivity in free space $(\varepsilon_0 = 8.854\times10^{-12} Nm^{-1})$. The real

(ε') and imaginary (ε'') parts of complex permittivity (ε^*) can be calculated from the measured data of Z' and Z'' using equations 3.8 and 3.9, respectively.

$$\varepsilon'(\omega) = -\frac{1}{C_o\omega}\left[\frac{Z''(\omega)}{Z'^2(\omega) + Z''^2(\omega)}\right] \tag{3.8}$$

$$\varepsilon''(\omega) = \frac{1}{C_o\omega}\left[\frac{Z'(\omega)}{Z'^2(\omega) + Z''^2(\omega)}\right] \tag{3.9}$$

3.6.3. Modulus formalism

The complex electric modulus (M^*) is defined as the inverse of complex permittivity (ε^*) by the following equation,

$$M^* = \frac{1}{\varepsilon^*} = \frac{1}{\varepsilon' - j\varepsilon''} = \frac{\varepsilon'}{\varepsilon'^2 + \varepsilon''^2} + j\frac{\varepsilon''}{\varepsilon'^2 + \varepsilon''^2} = M' + jM'' \tag{3.10}$$

where $j = \sqrt{-1}$ and M' and M'' are the real and imaginary parts of complex modulus M^*, respectively. The values of M' and M'' of PPy nanostructures were calculated by transforming the data obtained for the real and imaginary parts of permittivity using equation (3.10).

3.7. AC conductivity measurements

Studies of ac conductivity provide valuable information about charge transport mechanism in disordered materials. The frequency dependence of total ac conductivity $\sigma'(\omega)$ of PPy nanostructures were obtained using the following equation [242],

$$\sigma'(\omega) = \omega\varepsilon_0\varepsilon'' \tag{3.11}$$

where ω $(= 2\pi f)$ is the angular frequency, ε_0 is the permittivity in free space and ε'' is the dielectric loss and its value can be obtained from equation (3.9).

CHAPTER-IV

Polypyrrole nanoparticles: Dielectric relaxation and electrical transport studies and swift heavy ion irradiation effects

This chapter deals with the synthesis of polypyrrole (PPy) nanoparticles by micro-emulsion polymerization method and their different characterizations. A systematic study on the structure-property relationship of PPy nanoparticles has been established using the sophisticated characterization and measurement techniques and forms a major portion of this chapter. SHI irradiation induced modifications on morphology, structural, optical, thermal, dielectric properties and ac conductivity in PPy nanoparticles have also been discussed.

Conducting polymers with extended π-conjugation structures have received great attention as multifunctional materials due to their potential applications in various scientific and technological areas [243]. Among the family of conducting polymers, polypyrrole (PPy) is one of the most extensively studied conducting polymers due to their high electronic conductivity, environmental and thermal stability, and biocompatibility [244]. PPy has wide range of potential applications such as in drugs delivery, polymeric rechargeable batteries, super-capacitors, electro-chromic windows and displays, bio and gas-sensors, actuators, microwave shielding, corrosion protection etc. [245, 246]. The major drawback of PPy in widespread application is its poor processibility and insolubility. The conducting polymer nanostructures are known to display improved physico-chemical properties due to their large surface to volume ratio, short path lengths for the transport of ions and high electrochemical activity as compared to their bulk counterparts [93, 247]. Recently, a great deal of efforts has been made towards the synthesis of PPy nanoparticles to overcome their inherent intractability, improve its processibility and widen its applications [248]. The smaller dimension of nanoparticles causes dramatic change in their physico-chemical properties as compared to bulk properties. It has been reported that PPy nanoparticles can be more effectively dispersed due to large surface area for reaction and highly porous in solution form [249]. Moreover for application in molecular electronics and microelectronic circuits PPy needs to be developed as nanoparticles. PPy nanoparticles can be

synthesized by taking the advantage of micro-emulsion polymerization method in which particle size is controlled by the micelle reactor size. In previous studies, PPy nanoparticles have been successfully synthesized by using different surfactants or soft templates and surfactant-free methods. Kim et al. [221] reported the size controlled synthesis of unagglomerated PPy nanospheres through a surfactant-free emulsion method. Jang et al. [222] synthesized crystalline supramolecular assemblies of amorphous PPy nanoparticles using octyltrimethylammonium bromide (OTAB) surfactant. Wang et al. [223] synthesized the PPy nanoparticles by micro-emulsion method using ferric chloride ($FeCl_3$) as oxidant and dodecyltrimethylammonium bromide (DTAB) as surfactant and have reported particles size ranging from 50 nm to 100 nm, 100 nm to 200 nm with changing the DTAB surfactant concentration. Jang et al. [105] successfully synthesized PPy nanoparticles via micro-emulsion polymerization approach using various cationic surfactants such as OTAB, DTAB and decyltrimethylammonium bromide (DeTAB) and reported the fabrication of smaller size nanoparticles of diameter 2 nm by the use of OTAB surfactant at low temperature. Ovando-Medina et al. [224] synthesized conductive spherical PPy nanoparticles of sizes lower than 50 nm by micro-emulsion polymerization method using sodium dodecylsulfate (SDS) as anionic surfactant, ethanol as co-surfactant and potassium persulfate (KPS) as oxidant. These achievements indicate that micro-emulsion polymerization method is powerful for the synthesis of conducting polymer nanoparticles. Reung-U-Rai et al. [219] in the micro-emulsion polymerization of pyrrole have studied the influence of surfactant type and polymerization temperature on particle size and conductivity. Also, they reported smaller particle size and higher conductivity at lower temperature (0°C) using n-amyl alcohol as a stabilizer. However, effect of surfactant concentration on the shape, size, stability and morphology of PPy nanoparticles has not been reported.

Swift heavy ion (SHI) irradiation in conducting polymers has proven to be a unique technique for altering their different physico-chemical properties due to tremendous ($\geq$ 10 KeV/nm) amount of electronic energy deposition in the target polymer which is not possible by any other methods [125, 126]. SHI irradiation induced irreversible physico-chemical modifications in conducting polymers results due to large electronic energy deposition into the materials which can be traced as the transformation at the micro-level through the process of cross-linking, chain-

scissioning, bond breaking and emission of gaseous products and cluster formation upon energetic ion beam irradiation [127, 128, 250, 251]. When energetic heavy ions pass through the polymer material, they lose energy during their passage through the material mainly by two different processes: (a) elastic collisions with the nuclei known as nuclear energy loss and (b) inelastic collisions with the atomic electrons of the material known as electronic energy loss [252]. During SHI irradiation the electronic energy loss dominants and the kinetic energy of the ejected electrons is transmitted to the lattice by electron-phonon coupling leading to an increase in local lattice temperature above the melting point of the material. The melting of the material is followed by a rapid quenching resulting in amorphous columnar structure when the melt solidifies and the material's properties get modified. Different physico-chemical modifications of SHI irradiated conducting polymers depend on the ion species, fluence, ion energy and nature of the target materials. In general for polymer irradiation, the ion fluence used is in the range of 10^9-10^{12} ions/cm^2, because the use of higher ion fluence may lead to the destruction of polymer chains and also result in more amorphization of the target polymer [253]. Different studies on SHI irradiation induced effects on conducting polymers reveal modifications in their structural, electrical, optical and thermal properties including their processes such as polymer main chain scission, intermolecular cross-linking, creation of unsaturated bonds, formation of volatile fragments and creation of carbon clusters [130]. The phenomena such as chain-scissioning and cross-linking of the polymer chains depend on the energy loss mechanism during irradiation. The nuclear energy loss (S_n) is mainly responsible for the chain scissioning and electronic stopping (S_e) is responsible for the cross-linking although both the processes can cause cross-linking as well as chain-scissioning of polymer chains. The energetic ion beam produces a latent track described by a cylindrical trajectory of several nanometer diameters within which the phenomena like cross-linking, chain-scissioning, emission of atoms and molecular fragments, free radicals and some gaseous products take place [254, 255]. SHI-conducting polymer interaction mechanism and about electrical transport along with dielectric behavior are available in previous studies [256, 257]. Kaur et al. [258] have reported the 100 MeV Ag^{8+} SHI irradiation effects on the morphology and electrical properties of PPy and found that both crystallinity and electrical conductivity of PPy increase with increasing

the ion fluence. Ramola et al. [256] reported that the conductivity and crystallinity of PPy increase up to a fluence of 10^{12} ions/cm^2 irradiated with 50 MeV Li^{3+} ions.

PPy nanoparticles have been synthesized and various properties have been reported in this chapter. The synthesis procedure has been explained in Chapter-III. Different samples of PPy nanoparticles have been prepared by varying the sodium dodecylsulfate (SDS) concentration as surfactant cum dopant at 0.01 M, 0.05 M, 0.1 M and 0.2 M and the variation in properties with SDS molar concentration has been investigated. The sample with the best properties has been irradiated with 160 MeV Ni^{12+} swift heavy ion (SHI) with different ion fluence of 5×10^{10}, 10^{11}, 5×10^{11}, 10^{12} ions/cm^2 in order to further enhance the properties of PPy nanoparticles. The detailed results on PPy nanoparticles with varying SDS concentration have been presented in Section 4.1 and the results on 160 MeV Ni^{12+} ion irradiated PPy nanoparticles have been discussed in Section 4.2.

4.1. Characterization, dielectric relaxation and ac conductivity of polypyrrole nanoparticles

4.1.1. High resolution transmission electron microscopy studies

Fig. 4.1(a-d) depicts the HRTEM micrographs of PPy nanoparticles synthesized at different SDS concentration using the micro-emulsion polymerization method. The HRTEM micrographs suggest the formation of spherical solid PPy nanoparticles at SDS concentration in between their critical micelle concentration, CMC-I (8×10^{-3} M) and CMC-II (0.2 M) as shown in Fig. 4.1(a-d). The size of the resulting PPy nanoparticles depends on the SDS surfactant concentration. It is observed from the HRTEM micrographs that smaller size PPy nanoparticles results with increasing SDS surfactant concentration. The histograms in Fig. 4.2 show that the average diameters of PPy nanoparticles are 20 nm, 16 nm, 13 nm and 11 nm at SDS concentration of 0.01 M, 0.05 M, 0.1 M and 0.2 M, respectively. The size of PPy nanoparticles can be directly correlated with the size of micelles since the polymerization of pyrrole (Py) monomer is restricted in a localized environment due to encapsulation by surfactant molecules. The increase in surfactant concentration may give rise to smaller micelle dimension with greater stability due to lower value of Gibbs free energy but there is an enormous increase in the number of micelles [259]. Smaller extent of pyrrole monomer can

encapsulate in such micelles resulting in the reduction of nanoparticles size. Thus the size and shape of nanoparticles can be controlled by varying the SDS concentration and smaller size nanoparticles result at higher SDS concentration lower than its CMC-II.

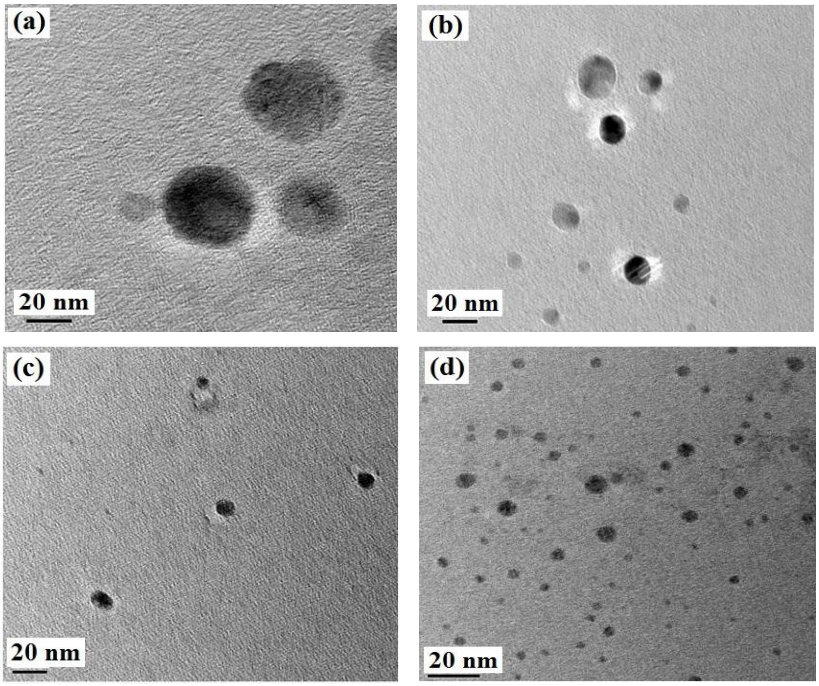

Figure 4.1: *HRTEM micrographs of PPy nanoparticles synthesized at (a) 0.01 M, (b) 0.05 M, (c) 0.1 M and (d) 0.2 M SDS concentration.*

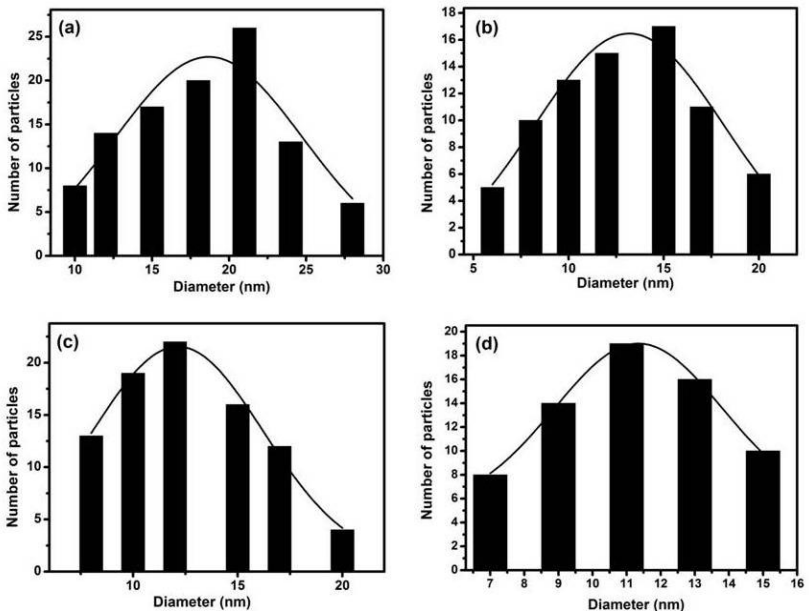

Figure 4.2: *Histograms of PPy nanoparticles synthesized at (a) 0.01 M, (b) 0.05 M, (c) 0.1 M and (d) 0.2 M SDS concentration.*

4.1.2. X-ray diffraction studies

The typical XRD patterns of PPy nanoparticles synthesized at different SDS concentration are shown in Fig. 4.3. A broad diffraction peak in 2θ range of 21°-24° is appeared in the XRD patterns which reveal the amorphous structure and short range arrangement of PPy nanoparticles chains. This broad diffraction peak is related to the interplanar distance of pyrrole-pyrrole and pyrrole-counter ions [260]. The intensity of this diffraction peak increases with increasing SDS concentration which acts as a dopant besides acting as surfactant that suggests the enhancement of crystallinity of PPy nanoparticles chains.

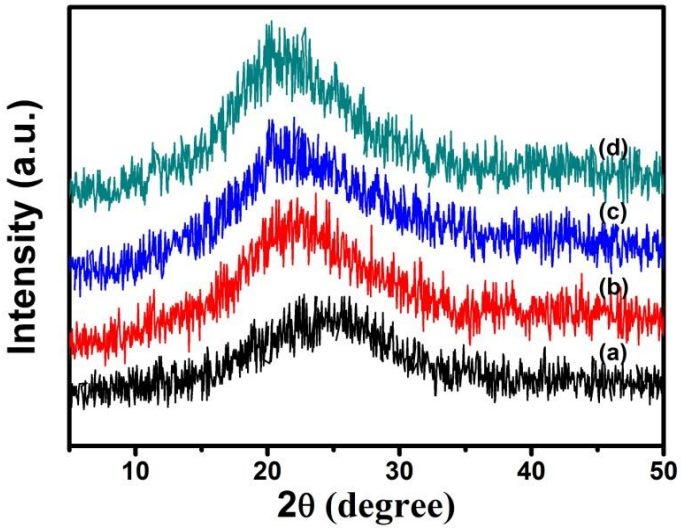

Figure 4.3: *XRD patterns of PPy nanoparticles synthesized at (a) 0.01 M (b) 0.05 M (c) 0.1 M and (d) 0.2 M SDS concentration.*

The degree of ordering of the polymer chains (X_C) can be estimated from the following equation [261],

$$X_C = \frac{A^I}{A^T} \times 100\% \tag{4.1}$$

where A^I is the area of the broad diffraction peak and A^T is the total area of the diffractogram. The enhanced crystallinity of PPy nanoparticles chains can be attributed to the better chain ordering in doped PPy nanoparticles. The extent of order (L) of polymer chains can be estimated using the Scherrer's equation [262],

$$L = \frac{0.9\lambda}{\beta \cos\theta} \tag{4.2}$$

where β is the full width at half maximum (FWHM) of diffraction peak in radian, λ is the X-ray wavelength (λ ~1.5406 Å) and θ is the Bragg's diffraction angle in degree. The interchain separation or hopping distance (R) of polymer chain can be calculated by using the following equation [262, 263],

$$R = \frac{5}{8}\left[\frac{\lambda}{\sin\theta}\right] \tag{4.3}$$

The interplanar spacing (d) of PPy nanoparticles for different SDS molar concentration can be calculated using the Bragg's diffraction formula [264],

$$2d\sin\theta = \lambda \tag{4.4}$$

The calculated values of ordering of chains (X_C), extent of chain order (L), interplanar spacing (d) and hopping distance (R) of PPy nanoparticles synthesized at different SDS molar concentrations are presented in Table 4.1.

Table 4.1: Values of angle of diffraction (2θ), ordering of chains (X_C), extent of chain order (L), interplanar spacing (d) and hopping distance (R) of PPy nanoparticles at different SDS concentrations.

SDS concentration (M)	Angle of diffraction 2θ (degree)	Ordering of chains, X_C (%)	Extent of chain order, L (Å)	Interplanar spacing, d (Å)	Hopping distance, R (Å)
0.01	24.42 ± 0.02	20.18 ± 0.03	6.33 ± 0.006	3.64 ± 0.02	4.50 ± 0.004
0.05	22.44 ± 0.02	23.07 ± 0.05	6.84 ± 0.004	3.96 ± 0.02	4.98 ± 0.003
0.1	21.56 ± 0.03	23.39 ± 0.02	7.54 ± 0.002	4.11 ± 0.03	5.16 ± 0.003
0.2	20.72 ± 0.02	24.60 ± 0.03	7.80 ± 0.004	4.28 ± 0.02	5.16 ± 0.004

It is observed from the Table that the ordering of chains (X_C) and extent of chain order (L) of PPy nanoparticles increase with increasing SDS dopant concentration. However, PPy nanoparticles exhibit highest interplanar spacing (d-spacing) at higher SDS dopant

concentration, which could be attributed to the strong electrostatic interaction between the dopant anions and the polymer chains. The encapsulation of the bulky SDS dopant anions within the PPy chains exerts steric hindrance that resists the polymer chains to come closer resulting in higher interplanar spacing (*d*-spacing) at higher SDS dopant concentration.

The interchain separation between the polymer chains can also be obtained from the determination of hopping distance *R*. It is observed from Table 4.1 that hopping distance increases with increasing SDS concentration with decreasing rate. The calculated value of hopping distance *R* for 0.01 M SDS concentration is 4.50 (± 0.004) Å, which increases to 4.98 (± 0.003) Å for SDS concentration of 0.05 M, which is an increase of 0.5 Å within the experimental error. However, when the SDS concentration is increased to 0.1 M, calculated value of *R* is 5.16 (± 0.003) Å, which is an increase of 0.66 Å. The value of *R* remains almost same, when SDS concentration is doubled to 0.2 M from 0.1M SDS.

4.1.3. Fourier transform infrared spectroscopy analysis

The FTIR spectra of PPy nanoparticles synthesized at SDS molar concentration of 0.01 M, 0.05 M, 0.1 M and 0.2 M are depicted in Fig. 4.4(i). The vibration band in the region of 3000-3500 cm^{-1} is due to the N-H stretching vibration of nitrogen in pyrrole ring [265]. The main vibration bands at 1550 cm^{-1} and 1456 cm^{-1} correspond to the C=C and C-N stretching vibrations, respectively. The vibration band at 1180 cm^{-1} can be attributed to the breathing vibration of pyrrole ring, whereas the medium band at 782 cm^{-1} is attributed to the C-H wagging vibration [266]. The two weak vibration bands at about 2924 cm^{-1} and 2854 cm^{-1} can be attributed to the stretching vibration mode of methylene indicating that the surfactants have been already eliminated from the final PPy nanostructures [267]. The shoulder band at 1296 cm^{-1} is predominantly due to the C-C in-ring stretching and C-N deformation mode [268]. The C-H and C-N in-plane deformation vibrations are located at 1037 cm^{-1} while the C-H out-of-plane deformation vibration is found at 903 cm^{-1}. The expected strong characteristic vibration band of S=O asymmetric stretching vibration of SO_3^- group at 1183 cm^{-1} indicating strong association of the SDS molecules as dopant with PPy nanoparticles which is not clearly observable due to overlapping with pyrrole ring vibration at 1180 cm^{-1} [269].

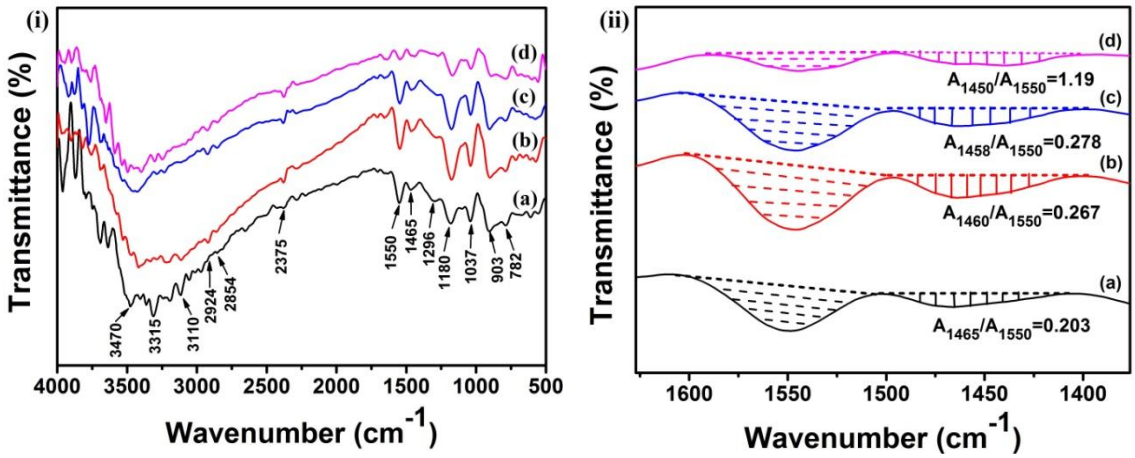

Figure 4.4: *Plots of (i) FTIR spectra and (ii) integrated peak area ratio I_{1465}/I_{1550} (I_{1460}/I_{1550}, I_{1458}/I_{1550}, I_{1450}/I_{1550}) of PPy nanoparticles synthesized at SDS concentrations of (a) 0.01 M (b) 0.05 M (c) 0.1 M and (d) 0.2 M.*

The electronic properties of conducting polymers are strongly dependent on their conjugation length. The IR spectroscopic method can be used for the qualitative measurement of "effective conjugation length" of polymeric materials [78]. This method is based on the theoretical work by Tian and Zerbi, where they predicts that as the conjugation length is increased, the intensity of the asymmetric ring stretching vibration at 1550 cm^{-1} will decrease relative to the symmetric mode vibration at 1474 cm^{-1} [270]. As a result, ratio of the intensities of 1474 and 1563 cm^{-1} bands (I_{1465}/I_{1550}) in FTIR spectra can be used to obtain the relative measure of the "effective conjugation length" [271]. The plots of integrated peak area ratio of I_{1465}/I_{1550} of PPy nanoparticles at different SDS concentrations are shown in Fig. 4.4(ii). It is observed that the peak area ratio I_{1465}/I_{1550} of PPy nanoparticles increases with increasing SDS concentration which indicates enhancement of "effective conjugation length" in PPy nanoparticles. The increase in "effective conjugation length" can result increase in electrical conductivity into PPy nanoparticles at higher SDS concentration.

4.1.4. UV-visible absorption spectroscopy studies

The UV-vis absorption spectra of PPy nanoparticles are shown in Fig. 4.5. There are three absorption bands at around 280 nm, 500 nm and 600 nm. The absorption spectra of all the samples show a strong transition at about 280 nm corresponding to π-π* interband transition i. e. transition from valence band to the conduction band of neutral

state of PPy. The band position in UV-vis spectra reveals the structure of PPy. A single polaronic band centred at about 500 nm lies in the band gap of PPy and hence it indicates the doping state of PPy.

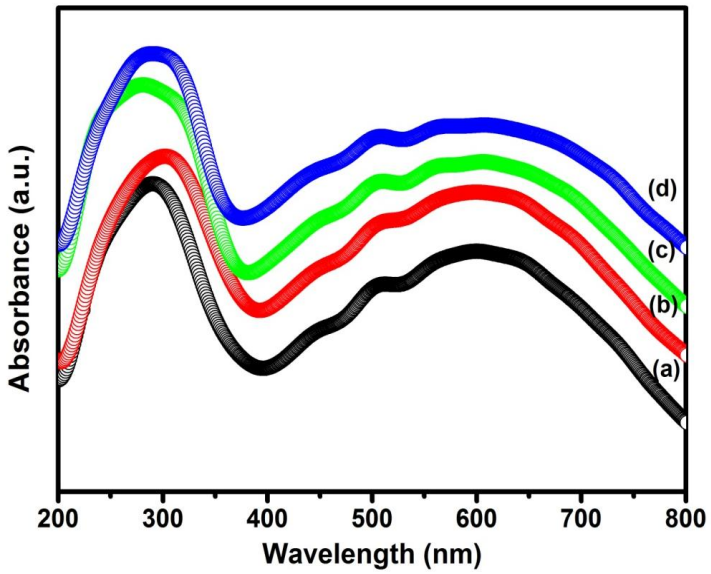

Figure 4.5: *UV-vis absorption spectra of PPy nanoparticles at SDS concentrations of (a) 0.01 M (b) 0.05 M (c) 0.1 M and (d) 0.2 M.*

It is observed that intensity of the polaronic band increases with increasing SDS concentration which can be attributed to the increase in the density of localized defect states in polaronic band with increasing dopant concentration. A broad band above 600 nm indicates the transition from valence band to bipolarons and antibipolarons of the oxidized form of PPy [272].

The optical band gap energy (E_g) of PPy nanoparticles is calculated from its absorption coefficient (α). The absorption coefficient (α) of a material is related to its band gap energy (E_g) by the equation [273],

$$\alpha(\nu) = \frac{B_\alpha (h\nu - E_g)^n}{h\nu} \tag{4.5}$$

where B_α is a constant, E_g is the optical band gap energy and *n* is a number equal to 0.5 for direct band gap and 2 for indirect band gap energy. The value of E_g can be obtained by plotting $(\alpha h\nu)^2$ versus *hν* and then extrapolating the most linear portion of the plot to $(\alpha h\nu)^2$ to zero [273]. Fig. 4.6 depicts such plots for PPy nanoparticles

whose calculated optical band gap energies are found to be 2.75 eV, 2.67 eV, 2.56 eV and 2.43 eV for 0.01 M, 0.05 M, 0.1 M and 0.2 M SDS doped PPy nanoparticles, respectively. It is observed that E_g decreases with increasing SDS concentration and hence one may expect the enhancement of electrical conductivity at higher SDS concentration which can also be correlated with XRD results.

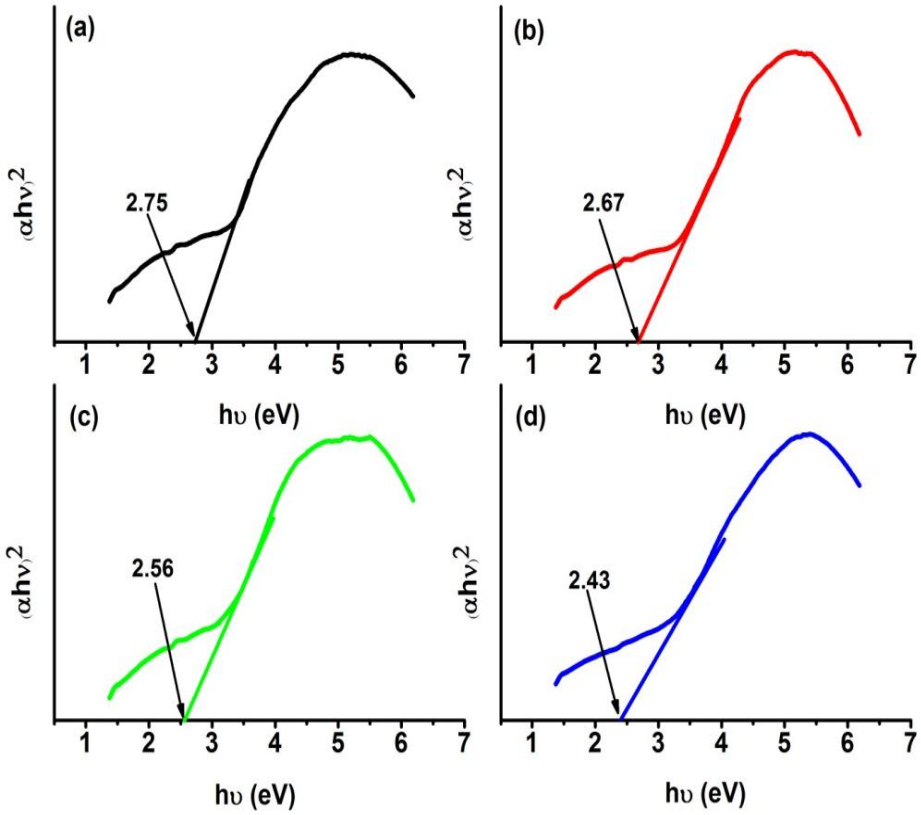

Figure 4.6: *Plots of* $(\alpha h\nu)^2$ *vs.* $h\nu$ *of PPy nanoparticles at SDS concentrations of (a) 0.01 M (b) 0.05 M (c) 0.1 M and (d) 0.2 M.*

4.1.5. Thermogravimetric analysis

The TGA thermographs of PPy nanoparticles at different SDS concentration are depicted in Fig. 4.7. All the thermographs exhibit three stage weight loss or degradation patterns. The first stage of weight loss starts at room temperature and continues to 110 °C which is mainly due to the loss of physically absorbed water molecules. The second weight loss occurs between 170 °C to 320 °C, which is attributed to the loss of dopant

anions bound by weak electrostatic interaction from the inter-chain sites of PPy nanoparticles chains.

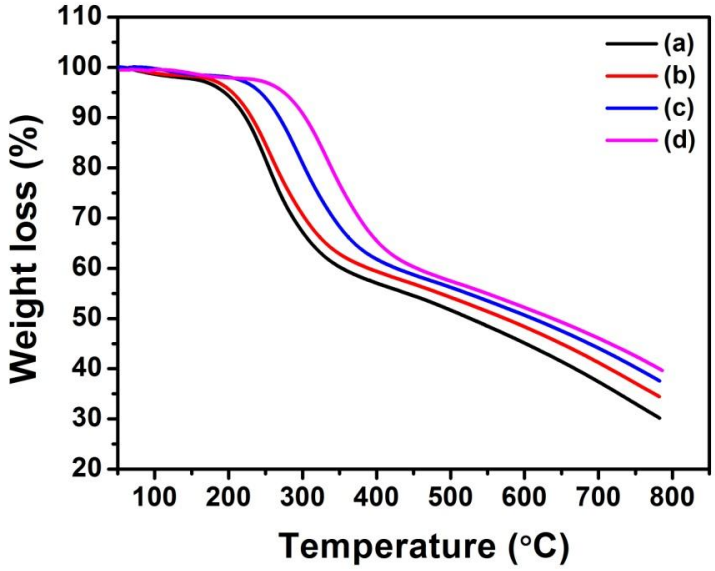

Figure 4.7: *TGA thermographs of PPy nanoparticles at SDS molar concentrations of (a) 0.01 M (b) 0.05 M (c) 0.1 M and (d) 0.2 M.*

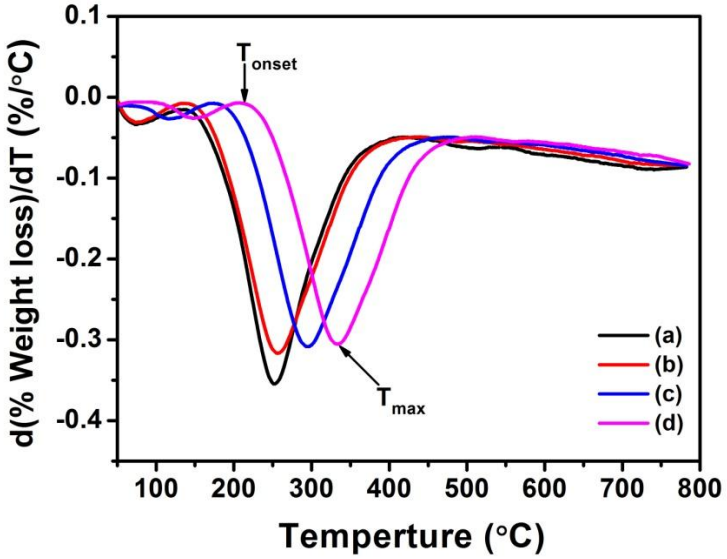

Figure 4.8: *Derivative plots of TGA thermographs for PPy nanoparticles at SDS molar concentrations of (a) 0.01 M (b) 0.05 M (c) 0.1 M and (d) 0.2 M.*

The main weight loss occurs at the third stage in the temperature range of 330 ºC-800 ºC, which is attributed to the exothermic degradation and decomposition of PPy main

chains [274]. In general the free sulfonate groups are thermally active and possibly weaken the thermal degradation of PPy nanoparticles. However higher thermal stability of sulfonate group results when it forms a complex with a counterion [272, 275]. The degradation temperatures at different percentage weight loss of PPy nanoparticles at different SDS concentrations are presented in Table 4.2. It is observed from the table that with increase in SDS concentration, the degradation temperature of PPy nanoparticles increases indicating enhancement of thermal stability of PPy nanoparticles.

The derivative plots of TGA thermographs for PPy nanoparticles at different SDS concentrations are shown in Fig. 4.8. The decomposition and weight loss of the sample are indicated by the negative sign of the derivatives and hence, only the numerical values of the derivatives are taken into account for analysis. The onset decomposition temperature (T_{onset}), maximum decomposition temperature (T_m) and maximum decomposition rate $(dW/dT)_m$ for PPy nanoparticles at different SDS concentrations obtained from the Fig. 4.8 are presented in Table 4.3. The table shows that with increasing SDS molar concentration, the onset decomposition temperature (T_{onset}) and maximum decomposition temperature (T_m) increase, while the maximum decomposition rate $(dW/dT)_m$ decreases implying an increase in thermal stability of PPy nanoparticles with increasing SDS concentration. The improvement in thermal stability that in turn offers thermal processing advantages can also be attributed to the increased alignment of PPy chains, which is supported by the XRD results.

Table 4.2: Degradation temperatures at different percentage weight losses for PPy nanoparticles at different SDS molar concentrations.

SDS concentration (M)	Degradation temperature (°C) at different percentage (%) weight losses				
	10 %	**20 %**	**30 %**	**40 %**	**50 %**
0.01	221	253	285	352	527
0.05	231	263	304	383	571
0.1	267	301	342	430	612
0.2	304	339	375	450	638

Table 4.3: Onset decomposition temperature (T_{onset}), maximum decomposition temperature (T_m) and maximum decomposition rate $(dW/dT)_m$ for PPy nanoparticles at different SDS molar concentrations.

SDS concentration (M)	Onset decomposition temperature, T_{onset} (°C)	Maximum decomposition temperature, T_m (°C)	Maximum decomposition rate, $(dW/dT)_m$ (%/°C)
0.01	135	250	$\|0.353\|$
0.05	141	255	$\|0.317\|$
0.1	172	295	$\|0.308\|$
0.2	212	332	$\|0.306\|$

4.1.6. Dielectric permittivity studies

The complex dielectric permittivity (ε^*) of disordered materials can be calculated from the measured complex impedance $Z^*(\omega)$ data as follows:

$$\varepsilon^*(\omega) = \frac{1}{j\omega C_0 Z^*(\omega)} = \varepsilon'(\omega) - j\varepsilon''(\omega) \tag{4.6}$$

where the real part $\varepsilon'(\omega)$ implies the dielectric permittivity that corresponds to the energy storage and the imaginary part $\varepsilon''(\omega)$ implies the dielectric loss that corresponds to the energy loss in each cycle of electric field, ω is the angular frequency, $C_0 = \varepsilon_0 A/d$ is the capacitance with free space between the electrodes, *A* is the area and *d* is the separation between the electrodes and ε_0 is the permittivity of free space $(\varepsilon_0 = 8.854 \times 10^{-12} Nm^{-1})$. The dielectric permittivity $\varepsilon'(\omega)$ and dielectric loss $\varepsilon''(\omega)$ can be calculated using the following relations [276]:

$$\varepsilon'(\omega) = -\frac{1}{C_o \omega}\left[\frac{Z''(\omega)}{Z'^2(\omega) + Z''^2(\omega)}\right] \tag{4.7}$$

$$\varepsilon''(\omega) = \frac{1}{C_o \omega}\left[\frac{Z'(\omega)}{Z'^2(\omega) + Z''^2(\omega)}\right] \tag{4.8}$$

where $Z'(\omega)$ is the real part of complex impedance Z^* that represents the current through the contact resistor and $Z''(\omega)$ is the imaginary part of Z^* that represents the current through the capacitor.

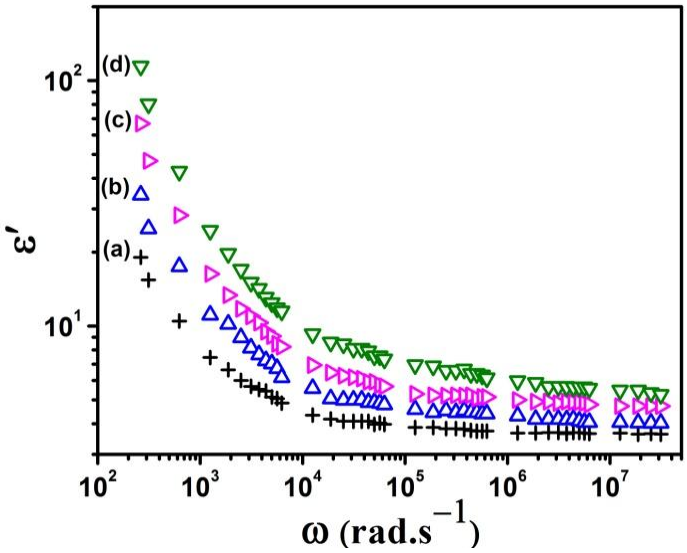

Figure 4.9: *Room temperature (303 K) plots of dielectric permittivity* (ε') *vs. frequency* (ω) *of PPy nanoparticles at SDS concentrations of (a) 0.01 M (b) 0.05 M (c) 0.1 M and (d) 0.2 M.*

Fig. 4.9 depicts the plots of dielectric permittivity (ε') vs. frequency (ω) of PPy nanoparticles synthesized at different SDS concentration at room temperature (303 K). It is observed that the value of $\varepsilon'(\omega)$ for all samples of PPy nanoparticles shows strong frequency dispersion in lower frequencies while in higher frequencies $\varepsilon'(\omega)$ is nearly independent of the frequency. At lower frequencies the response of the charge carriers to the externally applied ac electric field are faster resulting in higher value of ε' which corresponds to ε_s (static value of the dielectric permittivity at lower frequencies). At higher frequencies the applied ac electric field changes so rapidly that the charge carriers are unable to follow the electric field resulting in the lower value of ε' which corresponds to ε_∞ (value of dielectric permittivity at infinite frequencies). The higher value of ε' at lower frequencies can be attributed to the electrode or space charge polarization effect [277]. Moreover, it is also observed that value of $\varepsilon'(\omega)$ increases with increasing SDS concentration. The increase in ε' with increasing SDS

concentration is attributed to the enhancement of electrode polarization effect due to availability of more charge carriers in PPy nanoparticles at higher SDS dopant concentration.

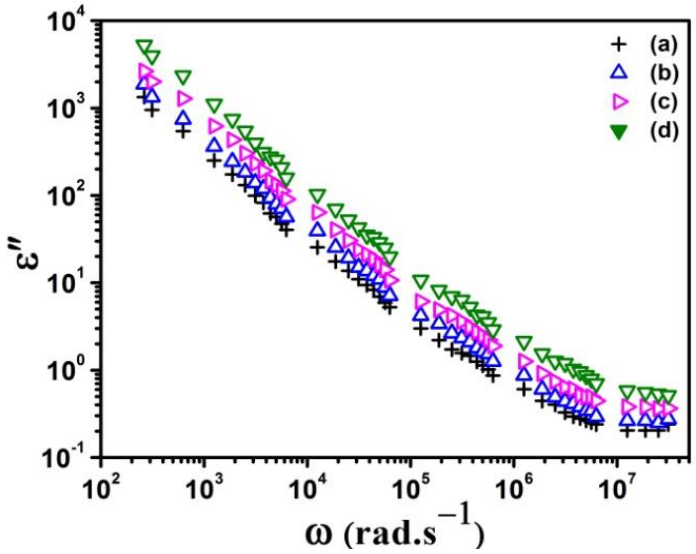

Figure 4.10: *Room temperature (303 K) plots of dielectric loss* (ε'') *vs. frequency* (ω) *of PPy nanoparticles at SDS concentrations of (a) 0.01 M (b) 0.05 M (c) 0.1 M and (d) 0.2 M.*

The plots of dielectric loss (ε'') vs. frequency (ω) of PPy nanoparticles at different SDS molar concentration at room temperature (303 K) are depicted in Fig. 4.10. It is observed that the dielectric loss (ε'') in all the samples of PPy nanoparticles decreases almost linearly with increasing the frequency suggesting the dominant effect of dc loss over the polarization phenomena. Moreover, value of ε'' increases with increasing SDS concentration which can be attributed to the increase in dc conduction due to the movement of large number of charge carriers at higher SDS concentration.

4.1.7. Electric modulus studies

Due to the absence of relaxation peak in dielectric loss spectra, it is difficult to distinguish between the polarization and intrinsic relaxation contributions. However, for materials whose dielectric loss spectra exhibit a dc conduction phenomenon then the dielectric spectra can be analysed using the complex electric modulus formalism [278,

279]. The complex electric modulus (M^*) is defined as the reciprocal of complex dielectric permittivity $(M^* = 1/\varepsilon^*)$, which can be defined as:

$$M^*(\omega) = \frac{1}{\varepsilon^*(\omega)} = \frac{1}{\varepsilon' - j\varepsilon''} = \frac{\varepsilon'}{\varepsilon'^2 + \varepsilon''^2} + j\frac{\varepsilon''}{\varepsilon'^2 + \varepsilon''^2} = M'(\omega) + jM''(\omega) \quad (4.9)$$

where $M'(\omega)$ and $M''(\omega)$ are the real and imaginary parts of complex electric modulus M^*, respectively.

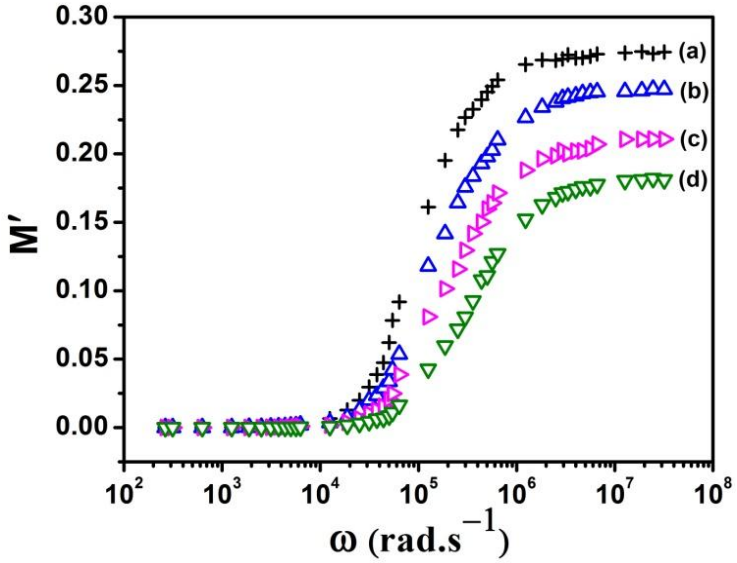

Figure 4.11: *Plots of real part of modulus (M') vs. frequency (ω) of PPy nanoparticles at SDS molar concentrations of (a) 0.01, (b) 0.05, (c) 0.1 M and (d) 0.2 M at room temperature (303 K).*

Fig. 4.11 depicts the plots of real part of modulus (M') vs. frequency (ω) of PPy nanoparticles at different SDS concentrations at room temperature (303 K). It is observed that for each M' spectrum, value of M' increases with increasing frequency and reaches a maximum constant value $(M_\infty = 1/\varepsilon_\infty)$ at higher frequencies due to the relaxation process. At lower frequencies, value of M' approaches to zero indicating removal of the electrode polarization effects [280]. However in between lower and higher frequencies, M' shows frequency dispersive behavior which suggests the occurrence of relaxation of charge carriers. The plots of imaginary part of modulus (M'') vs. frequency (ω) of PPy nanoparticles at different SDS concentrations at room temperature (303 K) are depicted in Fig. 4.12.

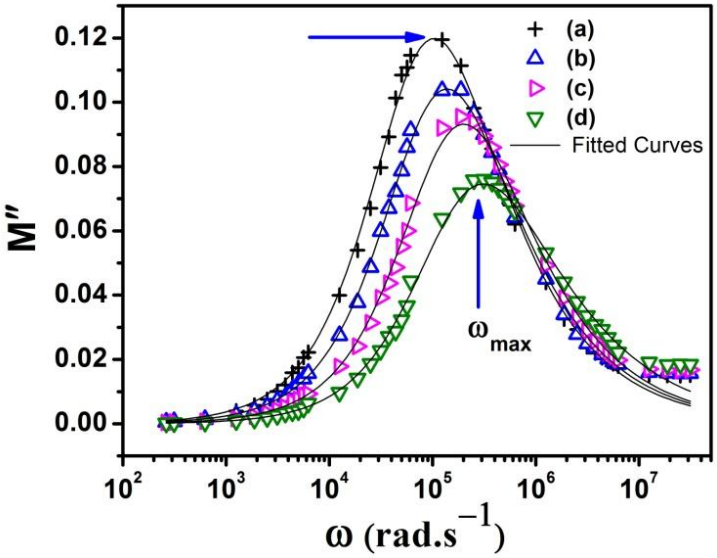

Figure 4.12: *Plots of imaginary part of modulus* (M'') *vs. frequency* (ω) *of PPy nanoparticles at SDS molar concentrations of (a) 0.01, (b) 0.05, (c) 0.1 M and (d) 0.2 M at room temperature (303 K).*

In each M'' spectrum a well defined relaxation peak is appeared corresponding to a particular frequency called the relaxation frequency (ω_{max}). The frequency dispersion of $M''(\omega)$ spectra indicates the distribution of relaxation times for conduction. The relaxation frequency corresponding to each relaxation peak lies in the transition region from dc to ac conduction. The frequencies left to the relaxation peak where the charge carriers are mobile over long distances contributes to dc conduction and frequencies right to the relaxation peak implies that the charge carriers can undergo localized motion which corresponds to ac conduction. The relaxation time (τ) of charge carriers can be estimated by using the following equation:

$$\tau = 1/\omega_{max} \tag{4.10}$$

It is observed that with increasing SDS molar concentration the relaxation peak shifts towards higher frequencies resulting decrease in the relaxation time of charge carrier's motion. However, the relaxation peak also depends on temperature. The temperature dependence of M'' spectra of PPy nanoparticles synthesized at SDS concentration of 0.2 M is shown in Fig. 4.13. As the temperature is increased, the relaxation peak shifts towards higher frequencies indicating shorter relaxation time of charge carrier's motion. At higher temperature the movement of the polymer chains and mobility of the charge

carrier's increase, resulting decrease in relaxation time of charge carriers' with a consequent shifting of the relaxation peak to higher frequencies.

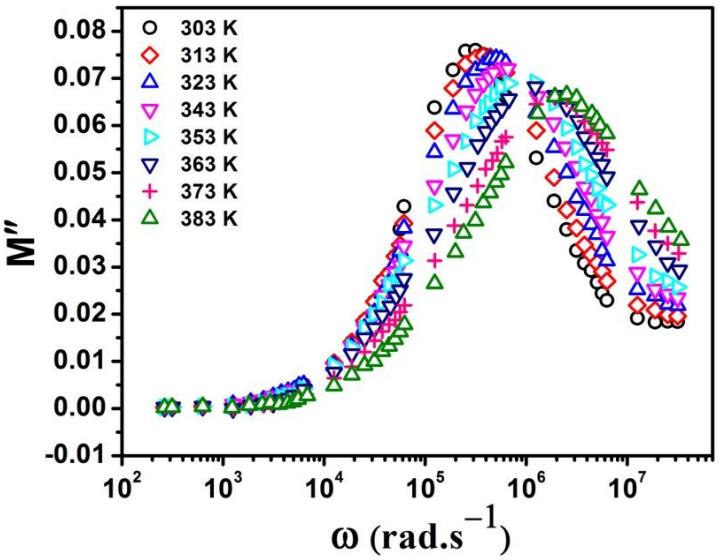

Figure 4.13: *Temperature dependence plots of M'' vs. ω of PPy nanoparticles at 0.2 M SDS concentration.*

The relaxation time (τ) for charge carriers follow the Arrhenius equation [281]:

$$\tau = \tau_{0M} \exp(\frac{E_{aM}}{kT}) \tag{4.11}$$

where τ_{0M} is the high temperature limit of relaxation time and E_{aM} is the activation energy for relaxation of charge carriers. The values of τ_{0M} and E_{aM} can be calculated from the slope and intercept of the best fitted curve of $\ln(\tau)$ vs. $1000/T$ plot. Fig. 4.14 depicts the plot of $\ln(\tau)$ vs. $1000/T$ of PPy nanoparticles at SDS molar concentration of 0.2 M. The points represent the experimentally determined relaxation times of charge carriers and the solid line represents the theoretical best fitted curve using equation (4.11) and calculated values of τ_{0M} and E_{aM} are found as $\tau_{0M} = 11.6 \times 10^{-12}$ s and E_{aM} = 0.33 eV, respectively.

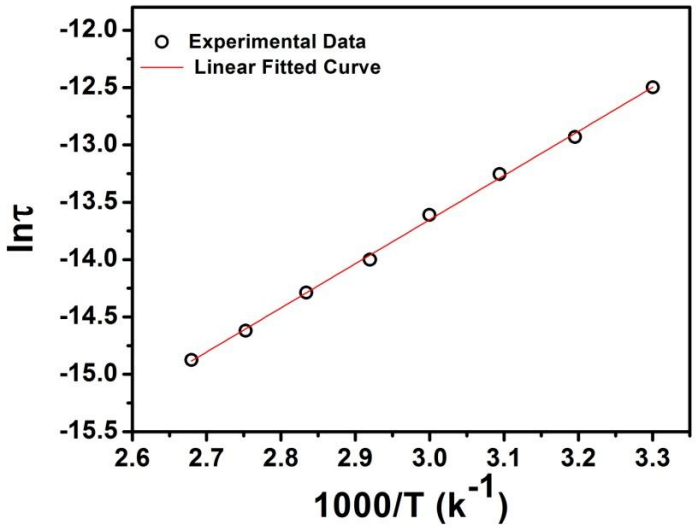

Figure 4.14: *Plots of* $\ln(\tau)$ *vs.* $1000/T$ *of PPy nanoparticles at SDS concentration of 0.2 M.*

The electric modulus can be represented as a Laplace transformation of a relaxation function $\varphi(t)$ [182]:

$$M^* = M_\infty[1-\int_0^\infty e^{-j\omega t}(\frac{d\varphi}{dt})dt] \tag{4.12}$$

where $M_\infty(\omega) = 1/\varepsilon_\infty(\omega)$, $\varepsilon_\infty(\omega)$ is the high frequency asymptotic value of the real part of dielectric permittivity and $\varphi(t)$ is the relaxation function that gives the time evolution of the electric field within the materials. The type of modulus spectra can be expressed by a stretched exponential relaxation function (decay) which can be defined empirically by Kohlrausch-Williams-Watts (KWW) function [282, 283]:

$$\varphi(t) = \exp[-(t/\tau)^\beta], \quad 0 < \beta < 1 \tag{4.13}$$

where τ is the characteristic relaxation time and β is the Kohlrausch relaxation parameter that decreases with increasing the relaxation time distribution. For Debye type relaxation $\beta = 1$ and deviation of β from unity ($0 < \beta < 1$) represents a non-Debye relaxation mechanism. Bergman has modified the KWW function fitting approach allowing direct analysis in the frequency domain. In the frequency approach M'' has been approximated as follows [284]:

$$M''(\omega) = \frac{M''_{\max}}{[(1-\beta)+(\beta/(1+\beta))[\beta(\omega_{\max}/\omega)+(\omega/\omega_{\max})^\beta]]} \tag{4.14}$$

where M''_{max} is the peak maximum in M'' spectrum. As shown in Fig. 4.12 the solid line represents the theoretical best fitted curve of experimentally determined M'' data and the calculated parameters such as M''_{max}, ω_{max} and β are presented in Table 4.4. It is observed that the calculated values of β ranges in 0.61-0.69 which suggests the non-Debye relaxation process of charge carriers in PPy nanoparticles. Furthermore, value of β decreases with increasing SDS concentration, which indicates larger deviation of relaxation process from the ideal Debye relaxation process.

Table 4.4: Room temperature (303 K) values of maximum of imaginary part of modulus (M''_{max}), relaxation frequency (ω_{max}), relaxation time (τ) and Kohlrausch stretched parameter (β) of charge carriers in PPy nanoparticles at different SDS concentrations.

SDS concentration (M)	M''_{max}	ω_{max} (rad.s^{-1})	τ (s)	β
0.01	0.119	111173	8.99×10^{-6}	0.69
0.05	0.104	153847	6.49×10^{-6}	0.67
0.1	0.096	190681	5.24×10^{-6}	0.63
0.2	0.077	301539	3.31×10^{-6}	0.61

4.1.8. AC conductivity studies

The study of ac conductivity provides information about charge transport mechanism in disordered materials. Experimentally the total ac conductivity $\sigma'(\omega)$ can be calculated using the following equation [242]

$$\sigma'(\omega) = \omega\varepsilon_0\varepsilon'' \tag{4.15}$$

where $\omega(=2\pi f)$ is the angular frequency, ε_0 is the permittivity in free space and ε'' is the dielectric loss. Fig. 4.15 shows the plots of total conductivity (σ') vs. frequency (ω) of PPy nanoparticles at different SDS concentrations at room temperature (303 K). Each conductivity plot exhibits two distinct regions: at lower frequencies, $\sigma'(\omega)$ is

independent of frequency i.e. a plateau is present that corresponds to the dc conductivity.

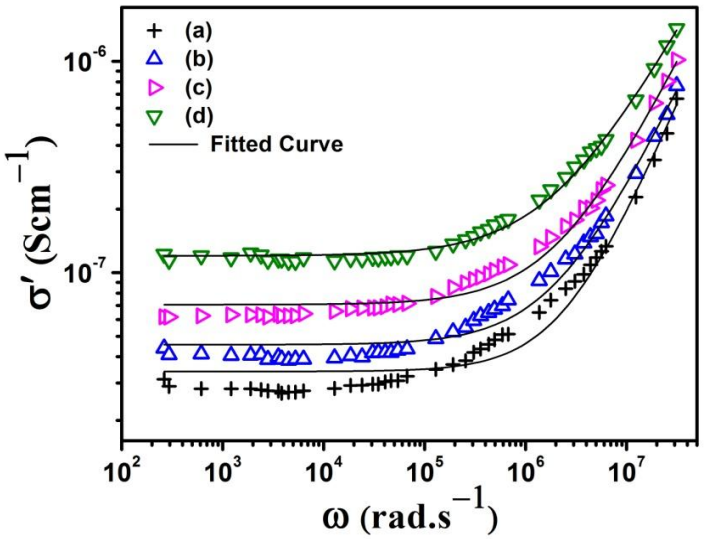

Figure 4.15: *Plots of frequency dependence of total conductivity* $\sigma'(\omega)$ *of PPy nanoparticles at SDS molar concentrations of (a) 0.01 M (b) 0.05 M (c) 0.1 M and (d) 0.2 M at room temperature (303 K).*

Above a characteristic onset frequency called the hopping or critical frequency ω_H the conductivity follows frequency dispersion which corresponds to ac conductivity and it increases with increasing frequency following a universal power law [156],

$$\sigma_{ac}(\omega) = A\omega^s, \text{ with } 0 < s < 1 \tag{4.16}$$

where A is the frequency independent pre-exponential factor that depends only on temperature and s is the dimensionless frequency exponent having value in between 0 and 1. This type of behavior is a characteristic of charge transport in disordered materials and is interpreted by Jonscher as universal dynamic response (UDR) [171]. Experimentally the value of dc conductivity σ_{dc} can be extracted by subtracting the ac conductivity from the total conductivity. The frequency dependence of total conductivity $\sigma'(\omega)$ can be expressed as:

$$\sigma'(\omega) = \sigma_{dc} + A\omega^s \tag{4.17}$$

where σ_{dc} represents the frequency independent conductivity or dc conductivity. The solid line represents the best fitted curve of the experimentally determined total ac

conductivity data. The values of dc conductivity (σ_{dc}) and frequency exponent (s) can be determined from this best fitted curve and are recorded in Table 4.5.

Table 4.5: Room temperature (303 K) dc conductivity (σ_{dc}) and frequency exponent (s) of PPy nanoparticles at different SDS concentrations.

SDS concentration (M)	σ_{dc} (Scm^{-1})	s
0.01	3.38×10^{-8}	0.78
0.05	4.41×10^{-8}	0.76
0.1	6.88×10^{-8}	0.74
0.2	1.18×10^{-7}	0.72

It is observed that the dc conductivity σ_{dc} increases while frequency exponent s decreases with increasing the SDS molar concentration. Also the frequency independent plateau of the total conductivity spectrum increases with increasing SDS concentration which suggests shifting of the hopping frequency towards higher frequencies. In conducting polymers there are no permanent dipoles, instead there is a strong charge trapping [285], the localized motion of which serves as an effective electric dipole under the external electric field [277] and they can hop to neighbouring sites forming a continuous network that allows the charge carriers to travel through the entire physical dimensions of the sample and cause the electrical conduction [157]. Furthermore, total conductivity in PPy nanoparticles increases with increasing SDS concentration. At higher SDS dopant concentration, the incorporation of large number of SDS anions into the PPy nanoparticles chains reduces the charge trapping centres which leads to a large number of charge participations in the conducting process and hence the total conductivity increases.

The microscopic charge transport mechanism in disordered materials is governed by the two physical mechanisms such as the correlated barrier hopping (CBH) and the quantum mechanical tunnelling (QMT). The temperature dependence study of frequency exponent s provides the exact nature of charge transport mechanism in conducting polymers. Fig. 4.16 depicts the plots of temperature dependence of frequency exponent s of PPy nanoparticles at different SDS concentrations. It is

observed that with increasing temperature, value of *s* decreases for all the samples of PPy nanoparticles. At lower temperature the interaction between the neighbouring charge carriers is not strong so enough, resulting higher value of *s*. As temperature is increased, the interaction between the charge carriers increases leading to a decrease in the value of *s*.

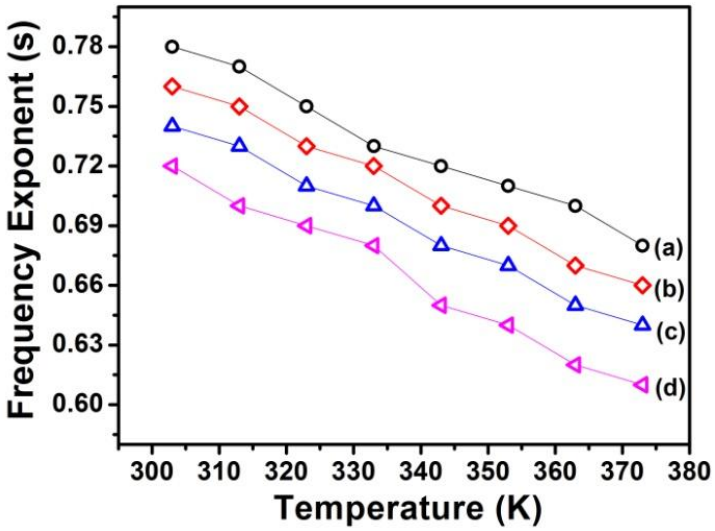

Figure 4.16: *Plots of frequency exponent (s) vs. temperature of PPy nanoparticles at different SDS concentrations.*

In QMT model the frequency exponent *s* can be expressed as follows [286],

$$s = 1 - \frac{4}{\ln(1/\omega\tau)} \tag{4.18}$$

where τ is the relaxation time of charge carriers. In the QMT model, the frequency exponent *s* is temperature independent but frequency dependent. A temperature dependent frequency exponent can be obtained within the framework of QMT model assuming that the charge carriers form non-overlapping small polarons [286], i.e. the total energy of a charge carrier is lowered by the polaron energy resulting from the lattice distortion by a carrier. In this case the frequency exponent *s* can be expressed as:

$$s = 1 - \frac{4}{\ln(1/\omega\tau) - (W_H/kT)} \tag{4.19}$$

The above equation (4.19) predicts that value of *s* is temperature dependent and it increases with increasing temperature. According to the CBH model the charge carriers'

can hop between the neighbouring sites by overcoming the potential barrier [162]. In the framework of CBH model the frequency exponent *s* can be expressed as [155],

$$s = 1 - \frac{6kT}{W_H - kT\ln(\omega\tau)} \tag{4.20}$$

where k is the Boltzmann's constant, W_H is the effective barrier height and τ is the characteristic relaxation time of charge carriers. For small value of (W_H/kT), the expression for *s* reduces to the following expression,

$$s = 1 - \frac{6kT}{W_H} \tag{4.21}$$

The above equation (4.21) predicts that value of *s* decreases with increasing the temperature. Therefore, the decrease in value of *s* with increasing temperature as depicts from Fig. 4.16 suggests that charge carriers follow the correlated barrier hopping (CBH) transport in which the charge carriers hop from one localized site to the others by overcoming the potential barrier between them. The calculated values of barrier activation energy (W_H) of charge carriers in PPy nanoparticles at different SDS concentration are recorded in Table 4.6. The decrease in the value of W_H with increasing SDS concentration reveals reduction in the barrier height of charge carriers' motion which results the enhancement of electrical conduction in PPy nanoparticles.

Table 4.6: Values of barrier activation energy (W_H) for charge carriers in PPy nanoparticles at different SDS concentrations at room temperature (303 K).

SDS concentration (M)	Barrier activation energy, W_H (eV)
0.01	0.71
0.05	0.65
0.1	0.60
0.2	0.56

The ac conductivity in the CBH model due to narrow-band limit is given by,

$$\sigma_{ac}(\omega) = \frac{\pi^3}{24} N^2 \varepsilon' \varepsilon_0 \omega R_\omega^6 \tag{4.22}$$

where N is the density of the pair sites and R_ω is the hopping distance at a frequency ω, which is given by the following relation,

$$R_\omega = \frac{e^2}{\pi\varepsilon'\varepsilon_0[W_m + kT\ln(\omega\tau)]} \tag{4.23}$$

where W_H is the binding energy of the charge carriers in their localized sites.

4.2. 160 MeV Ni^{12+} swift heavy ion irradiation effects on PPy nanoparticles

The detailed studies on PPy nanoparticles with varying SDS molar concentration as discussed in Section 4.1 reveals that the sample of PPy nanoparticles synthesized at 0.2 M SDS concentration has shown the best properties. Therefore this sample of PPy nanoparticles has been chosen to irradiate by 160 MeV Ni^{12+} swift heavy ions (SHI) with a view to further enhance the properties. For SHI irradiation, films of PPy nanoparticles have been prepared by dissolving and ultra-sonicating the dried precipitate into 2 % of PVA (Polyvinyl alcohol) solution. The PVA (M_w = 145000) has been used as plasticizer for making films of PPy nanoparticles for SHI irradiation and the usage of PVA as plasticized did not affect significantly on the properties of PPy nanoparticles. The SHI irradiation on PPy nanoparticles was performed at the 15 UD Pelletron Accelerator available at the Inter University Accelerator Centre (IUAC), New Delhi, India using the Materials Science beam line facilities. Four different ion fluence of 5×10^{10}, 10^{11}, 5×10^{11} and 10^{12} ions/cm^2 were used to irradiated the films of PPy nanoparticles keeping the ion current constant at 0.5 pna (particle nano-ampere). The energy of Ni^{12+} ion beam was chosen at 160 MeV so that the ion beam completely penetrated the PPy films. The projected range of Ni^{12+} ions in PPy films as calculated by using the SRIM (stopping and range of ions in matter) software [286] was found to be 42 μm, which was larger than thickness (~ 30-35 μm) of the PPy films. The results on the 160 MeV Ni^{12+} SHI irradiation induced modifications on the sample of PPy nanoparticles have been discussed under the following sections.

4.2.1. High resolution transmission electron microscopy studies

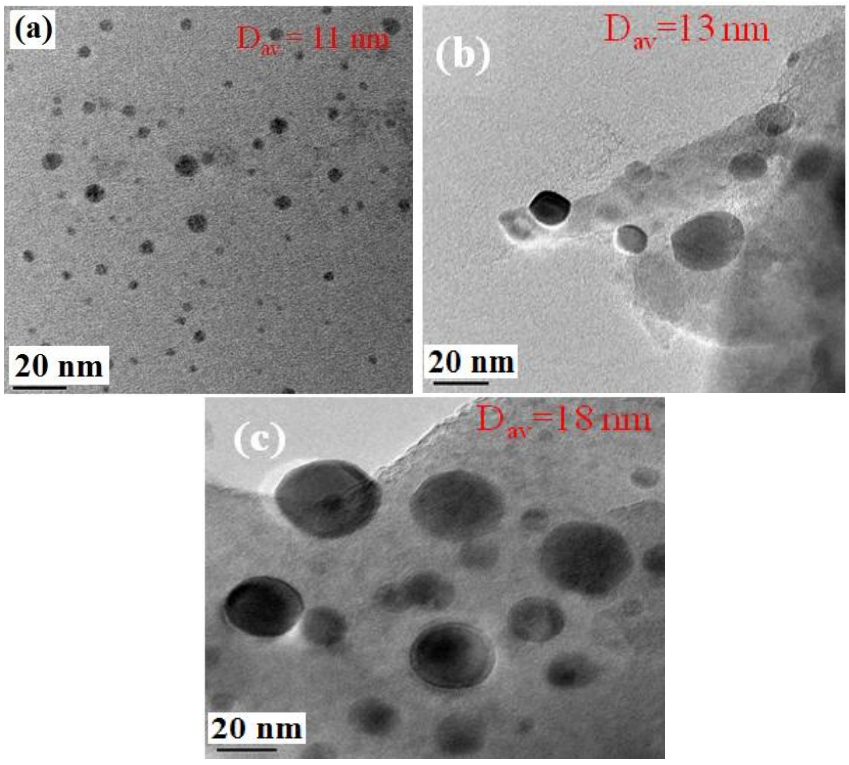

Figure 4.17: *HRTEM micrographs for (a) pristine and irradiated PPy nanoparticles at irradiation fluences of (b) 5×10^{10} and (c) 10^{12} ions/cm^2.*

Fig. 4.17(a-c) depicts the HRTEM micrographs of the pristine and irradiated PPy nanoparticles at different irradiation fluences. It is observed from Fig. 4.17(a) that the pristine PPy nanoparticles are spherical in shape with average diameter of 11 nm. Fig. 4.17(b&c) show the HRTEM micrographs of irradiated PPy nanoparticles with average diameters of 13 and 18 nm at lower and higher irradiation fluences of 5×10^{10} and 10^{12} ions/cm^2, respectively. Upon SHI irradiation, PPy nanoparticles undergo no change in their spherical shape; however the size of the nanoparticles increases to 18 nm at the highest irradiation fluence of 10^{12} ions/cm^2. The irradiated PPy nanoparticles along the ion track are molten due to tremendous electronic energy deposition (~10 KeV/nm) upon SHI irradiation. The diffusion of material in the molten region along the ion track results in the growth of PPy nanoparticles along the ion track. As the irradiation fluence increases, the overlapping of the latent tracks takes place leading to further increase in size of PPy nanoparticles due to enhanced diffusivity within the overlapped ion tracks.

4.2.2. X-ray diffraction studies

The XRD patterns of pristine and irradiated PPy nanoparticles at the irradiation fluences of 5×10^{10}, 10^{11}, 5×10^{11} and 10^{12} ion/cm^2 are depicted in Fig. 4.18. The appearance of the broad diffraction peak in pristine PPy nanoparticles centred about $2\theta = 19.5^{o}$ suggests the amorphous nature and short range arrangement of PPy chains. The origin of this broad diffraction peak is due to the interplanar Vander Walls arrangement of the pyrrole-pyrrole rings in PPy chains. It is observed that upon SHI irradiation, the diffraction peak intensity increases, while the full width at half maximum (FWHM) decreases with increasing the ion fluence from 5×10^{10} ions/cm^2 to 10^{12} ions/cm^2 which suggests the enhancement of crystallinity of PPy nanoparticles chains after SHI irradiation. The ordering of polymer chains (X_C) can be calculated using equation (4.1)

$$X_C = \frac{A^I}{A^T} \times 100\%$$

as mentioned in section 4.1.

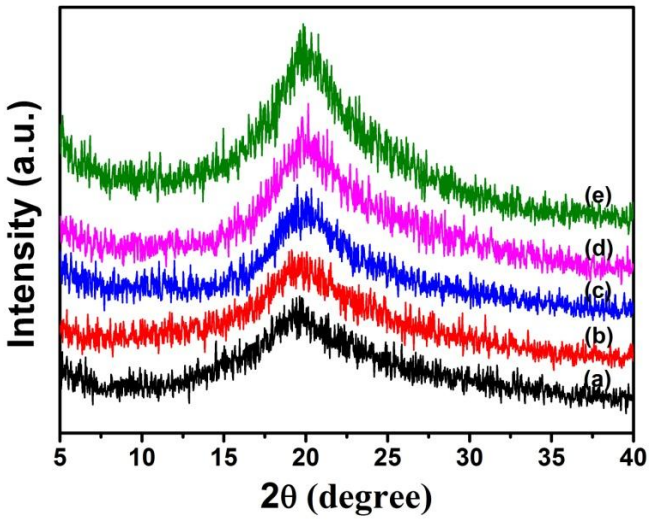

Figure 4.18: *XRD patterns of (a) pristine and irradiated PPy nanoparticles at ion fluences of (b) 5×10^{10}, (c) 10^{11}, (d) 5×10^{11} and (e) 10^{12} ions/cm^2.*

The pristine PPy nanoparticles exhibit 25.12% crystallinity while upon SHI irradiation, crystallinity of PPy nanoparticles increases with increasing the ion fluence. The degree of crystallinity of PPy nanoparticles increases from 25.88% to 28.78% while the ion fluence is increased from 5×10^{10} ions/cm^2 to 10^{12} ions/cm^2, respectively. The increased crystallinity can be ascribed to the systematic alignment of polymer chains by cross-

linking or by formation of single or multiple helices along the ion trajectories due to large electronic energy deposition [288]. The energy loss by SHI irradiation occurs discretely as spurs along the ion track. The spur energy (~30-40 eV) is approximately equal to the energy required to produce one ion pair or radical formation. This energy transfer leads to radical formation, bond scission and cross-linking of the polymer chains. Both cross-linking and scissioning may occur simultaneously during irradiation, but the relative magnitude of cross-linking and chain scissioning depends upon the polymer structure, packing of the polymer chains, characteristics of the radiation sources (ion species and energy), irradiation fluence and linear energy transfer (LET, energy deposited per unit track length). The electronic LET value for Ni^{12+} ion at 160 MeV energy is very high (~4.489×10^2 eV/Å). At such a high LET, huge numbers of radical pairs are created on adjacent polymer chains within the track radius leading to the cross-linking of polymer chains, which in turn gives rise to increased crystallinity. Upon SHI irradiation one can expect increase in electrical conductivity due to decreased scattering of charge carriers [289]. The extent of order (L) of pristine and irradiated PPy nanoparticles can be calculated using equation (4.2)

$$L = \frac{0.9\lambda}{\beta \cos\theta}$$

as mentioned in section 4.1.

As mentioned in section 4.1, the hopping distance (R) and the interplanar spacing (d) of pristine and irradiated PPy nanoparticles have been calculated from equations (4.3) and (4.4), respectively:

$$R = \frac{5}{8}\left[\frac{\lambda}{\sin\theta}\right]$$

$$2d \sin\theta = \lambda$$

The d-spacing for the diffraction peak gives the distance between the pyrrole-pyrrole stacking planes. Also, upon irradiation the broad diffraction peak slightly shifts towards the higher angular positions. The shifting of diffraction peak towards higher angle leads to the contraction of the PPy chains that increase its density which may be due to the cross-linking of polymer chains upon SHI irradiation. This facilitates a tighter packing and bonding of the PPy chain elements and creates volume elements as crystallites. The calculated values of ordering of polymer chains (X_C), full width at half maximum (β),

interplanar spacing (d) and extent of order (L) of pristine and irradiated PPy nanoparticles at different ion fluences are presented in Table 4.7.

Table 4.7: Values of ordering of polymer chains (X_C), full width at half maximum (β), interplanar spacing (d), extent of chain order (L) and hopping distance (R) of pristine and irradiated PPy nanoparticles at different ion fluences.

Fluence (ions/cm^2)	Chain ordering, X_C (%)	FWHM, β (radian)	Interplanar spacing, d (Å)	Extent of chain order, L (Å)	Hopping distance, R (Å)
Pristine	25.12±0.04	0.1562±0.003	4.54±0.04	9.00±0.03	5.68±0.04
5×10^{10}	25.88±0.03	0.1518±0.002	4.49±0.04	9.27±0.02	5.61±0.04
1×10^{11}	26.43±0.05	0.1448±0.003	4.47±0.04	9.72±0.04	5.59±0.04
5×10^{11}	27.97±0.04	0.1404±0.002	4.45±0.04	10.03±0.03	5.56±0.04
1×10^{12}	28.78±0.05	0.1357±0.002	4.45±0.04	10.37±0.04	5.56±0.04

4.2.3. Fourier transform infrared spectroscopy analysis

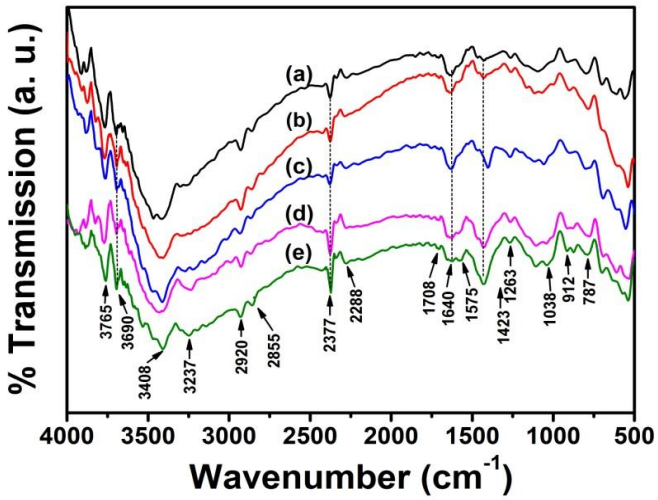

Figure 4.19: *FTIR spectra of (a) pristine and irradiated PPy nanoparticles at irradiation fluences of (b) 5×10^{10}, (c) 10^{11}, (d) 5×10^{11} and (e) 10^{12} ions/cm^2.*

Fig. 4.19 depicts the FTIR spectra of the pristine and irradiated PPy nanoparticles at ion fluences of 5×10^{10}, 10^{11}, 5×10^{11} and 10^{12} ions/cm^2. It is observed that upon SHI irradiation, the vibrational band intensities of N-H, C-H and C-N functional groups

corresponding to the wave numbers of 3695, 2377 and 1423 cm^{-1}, respectively increase with increasing the irradiation fluence. This can be attributed to the cross-linking and successive formation of these functional groups upon SHI irradiation with increasing fluence. On the other hand, the intensity of the vibrational band (C=C) positioned at 1640 cm^{-1} decreases with increasing fluence which suggests bond scission and successive degradation of these functional groups under SHI irradiation. These changes are responsible for the bond cleavage and bond reconstruction during SHI irradiation. However the predominant effect in PPy nanoparticles upon SHI irradiation is the cross-linking processes.

Fig. 4.20 shows the plots of area under the IR active vibrational modes with ion fluence. The increasing (or decreasing) rate of the vibrational peak intensity is different for different peaks, which means that different vibrational modes have different sensitivities to SHI irradiation. According to the saturated track model, the formation or damage of a functional group can be expressed by an exponential relation [290],

$$I(\phi) = I_O \exp(-\sigma\phi) \tag{4.24}$$

where σ is the formation (or damage) cross section of a chemical functional group, $I(\phi)$ is the intensity of the IR active modes at a given fluence and I_o is the normalized peak intensity of the pristine sample. The cross section σ can be determined from the slope of the plot of normalized areal peak intensity $\log_{10}[I(\phi)/I_o]$ vs. ion fluence.

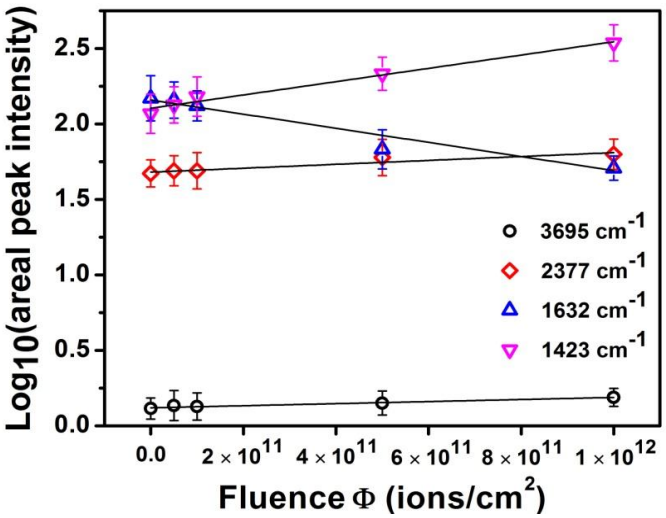

Figure 4.20: *Plots of areas of IR active vibrational modes of pristine and irradiated PPy nanoparticles at different ion fluences.*

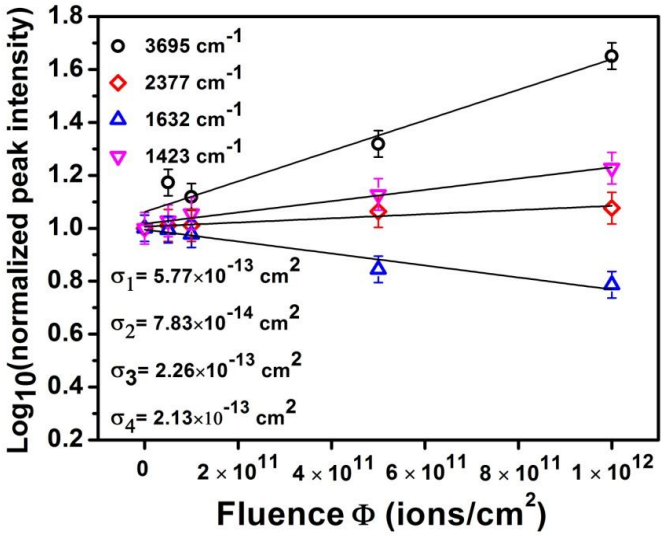

Figure 4.21: *Plots of* $\log_{10}[I(\phi)/I_o]$ *vs. ion fluence* (ϕ) *of the vibrational bands positioned at 3695, 2377, 1632 and 1423 cm^{-1} of PPy nanoparticles.*

Fig. 4.21 depicts the plots of $\log_{10}[I(\phi)/I_o]$ vs. ion fluence (ϕ) for the IR active N-H, C-H, C-N and C=C bands corresponding to the wave numbers of 3695, 2377, 1423, 1640 cm^{-1}, respectively. The linear fits to the FTIR data in Fig. 4.21 yield cross sections of 5.77×10^{-13}, 7.83×10^{-14}, 2.26×10^{-13} and 2.13×10^{-13} cm^2 for the vibrational bands of N-H, C-H, C-N and C=C, respectively positioned at 3695, 2377, 1632 and 1423 cm^{-1}. These results show that the IR active vibrational bands have different cross-sections for SHI irradiation. It is observed that the N-H vibration band positioned at 3695 cm^{-1} has the maximum formation cross-section of 5.77×10^{-13} cm^2 suggesting that this vibration band is most sensitive to SHI irradiation. The effective radius of formation (or damage) cross-section by the ion track can be calculated from $\sigma = \pi r^2$ and it has been calculated 7.58 nm by taking $\sigma = 5.77 \times 10^{-13}$ cm^2.

4.2.4. UV-visible absorption spectroscopy studies

The UV-vis spectra provide information about the electronic structure and type of charge carriers in the PPy nanoparticles. The UV-vis absorption spectra of the pristine and irradiated PPy nanoparticles at the irradiation fluences of 5×10^{10}, 10^{11}, 5×10^{11} and 10^{12} ion/cm^2 are shown in Fig. 4.22. The figure shows a strong absorption band at about 270 nm for pristine PPy nanoparticles corresponding to the π-π* inter-band transition. The absorption band at 440 nm is the polaron absorption band of PPy [291]. A broad

tail above 600 nm in the near infrared (NIR) region corresponds to the transitions from the highest occupied molecular orbitals (HOMO) to bipolaron and antibipolaron bands of the oxidized form of PPy [271].

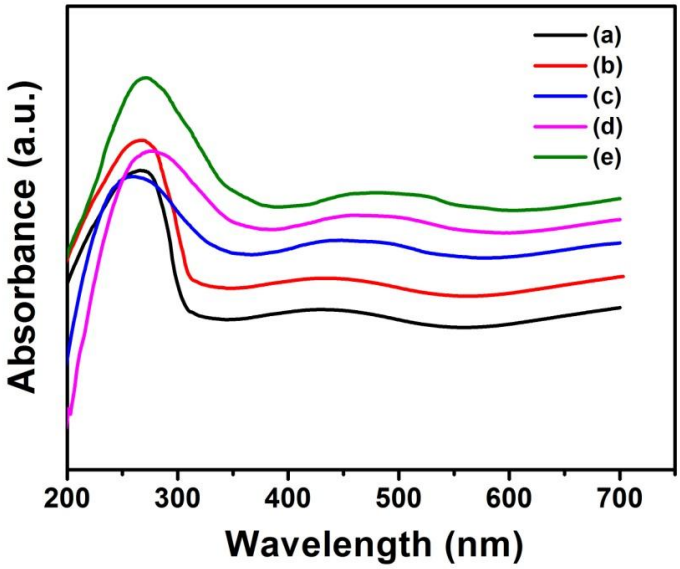

Figure 4.22: *UV-vis absorption spectra of (a) pristine and irradiated PPy nanoparticles at irradiation fluences of (b) 5×10^{10}, (c) 10^{11}, (d) 5×10^{11} and (e) 10^{12} ion/cm^2, respectively.*

Upon SHI irradiation the polaron absorption band gets red shifted towards higher wavelength region with increasing irradiation fluence. This indicates decrease in the optical band gap (E_g) of PPy nanoparticles upon SHI irradiation that gives rise to an increase in their electrical conductivity [292]. This red shifting of the absorption band may be due to the formation of conjugation bonds and generation of free radicals due to the large electronic energy deposition in the polymeric system upon SHI irradiation. Fig. 4.23 shows the plots of $(\alpha h\nu)^2$ vs. $h\nu$ of the pristine and irradiated PPy nanoparticles at the irradiation fluences of 5×10^{10}, 10^{11}, 5×10^{11} and 10^{12} ion/cm^2, respectively. Table 4.8 presents the optical band gap energies (E_g) for PPy nanoparticles at different irradiation fluences. The table shows the optical band gap energy of 2.50 (± 0.03) eV, for pristine PPy nanoparticles, which decreases with increasing irradiation fluence and attains a value of 1.76 (± 0.02) eV upon SHI irradiation with fluence of 10^{12} ion/cm^2. This decrease in the optical band gap energy upon SHI irradiation can be correlated with the formation of crystalline domains and

high conjugation lengths due to large electronic energy deposition in the system. As a result, the electronic disorder decreases that induce a permitted state in the forbidden band or deformation of the valence band of PPy nanoparticles [293]. The decrease in optical band gap energy of the SHI irradiated PPy nanoparticles is consistent with the XRD where crystallinity increases upon SHI irradiation.

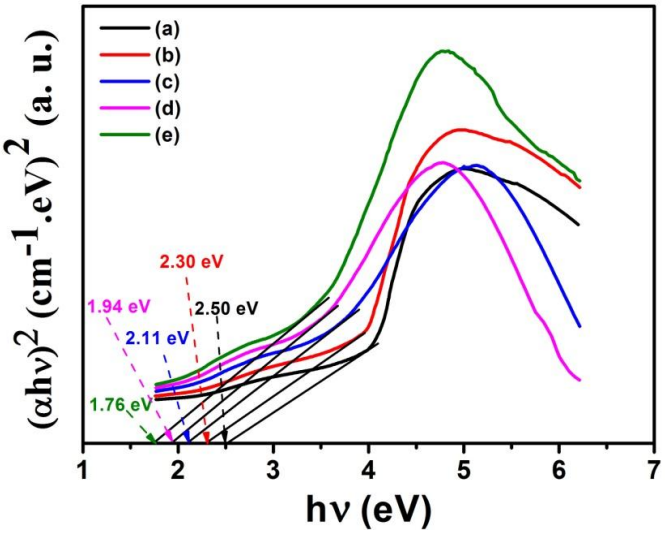

Figure 4.23: *Plots of* $(\alpha h\nu)^2$ *vs.* $h\nu$ *of (a) pristine and irradiated PPy nanoparticles at irradiation fluences of (b)* 5×10^{10}*, (c)* 10^{11}*, (d)* 5×10^{11} *and (e)* 10^{12} *ion/cm*^{2}*, respectively.*

Table 4.8: Values of optical band gap energies (E_g) of pristine and irradiated PPy nanoparticles at different ion fluences.

Fluence (ions/cm^2)	Optical band gap energy, E_g (eV)
Pristine	2.50 ± 0.03
5×10^{10}	2.30 ± 0.02
1×10^{11}	2.11 ± 0.03
5×10^{11}	1.94 ± 0.02
1×10^{12}	1.76 ± 0.02

4.2.5. Thermogravimetric analysis

Information regarding thermal stability of materials can be obtained by studying their TGA thermographs. The TGA thermographs of pristine and irradiated PPy nanoparticles at the ion fluences of 5×10^{10}, 10^{11}, 5×10^{11} and 10^{12} ion/cm^2 are shown in Fig. 4.24. It is observed that the TGA thermograph of 0.2 M SDS doped PPy nanoparticles in powder form (Fig. 4.7) does not match with the TGA thermograph of 0.2 M SDS doped PPy nanoparticles (2 wt % in powder form) dispersed in PVA matrix (Fig. 4.24). The difference between the two TGA thermographs of the same sample arises due to its two different forms. The SHI irradiation cannot be done in powder form at atmospheric pressure without making a film in an inert polymer matrix. For SHI irradiation the sample in thin film form is placed in a vacuum chamber (~10^{-5} Torr). 2 wt % of sample of each morphology was dispersed in an inert PVA matrix to make a film of 30-35 μm for SHI irradiation.

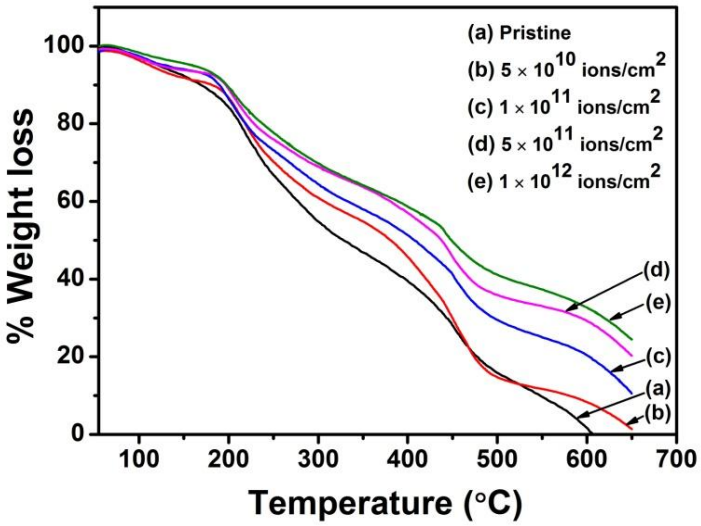

Figure 4.24: *TGA thermographs of (a) pristine and irradiated PPy nanoparticles at ion fluences of (b) 5×10^{10}, (c) 10^{11}, (d) 5×10^{11} and (e) 10^{12} ion/cm^2.*

The TGA thermographs show that the weight loss of the pristine and irradiated PPy nanoparticles occurs through three different stages. For the pristine PPy nanoparticles the first stage of weight loss occurs in the temperature range of 50-120 °C which is due to the removal of moisture and undesired reactants present in the sample [294]. The second stage of weight loss occurs in the temperature range of 180-440 °C which can be attributed to the loss of dopant anions from the PPy chains. The third and final stage of

weight loss occurs above 450 °C which is mainly due to the degradation or decomposition of the main polymer chains. It is observed that the degradation temperature of SHI irradiated PPy nanoparticles increases with increasing the irradiation fluence. The degradation temperature of both pristine and irradiated PPy nanoparticles at different percentage weight loss determined from the TGA plots are presented in Table 4.9. The increase in degradation temperature with increasing ion fluence reveals the enhancement of thermal stability of PPy nanoparticles upon SHI irradiation.

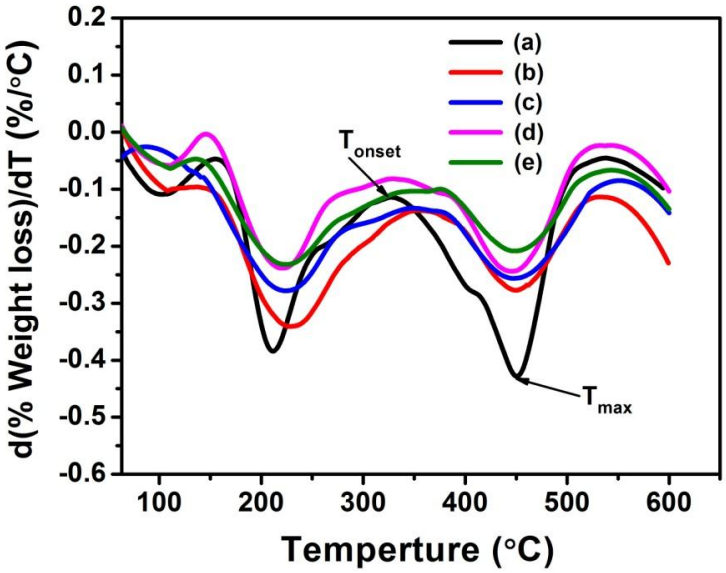

Figure 4.25: *Derivative plots of TGA thermographs for (a) pristine and irradiated PPy nanoparticles at different irradiation fluences of (b) 5×10^{10}, (c) 10^{11}, (d) 5×10^{11} and (e) 10^{12} ions/cm^2, respectively.*

The derivative plots of TGA thermographs for pristine and irradiated PPy nanoparticles at different irradiation fluences are shown in Fig. 4.25. The negative sign of the derivatives signifies the decomposition and weight loss of the sample. Therefore, only the numerical (without minus sign) values of the derivatives are relevant for analysis. It is observed from the figure that upon SHI irradiation, the onset decomposition temperature (T_{onset}) increases, while the maximum decomposition rate $(dW/dT)_m$ for PPy nanoparticles decreases as compared to that of the pristine PPy nanoparticles. Moreover, T_{onset} shifts towards higher temperature and $(dW/dT)_m$ shows decreasing trend with increasing irradiation fluence. The results further lead to the

conclusion that the thermal stability of the irradiated PPy nanoparticles increases with increasing fluence upon SHI irradiation. The onset decomposition temperature (T_{onset}) and maximum decomposition rate $(dW/dT)_m$ for PPy nanoparticles at different SDS concentrations are presented in Table 4.9. The enhanced thermal stability can be assigned to the better ordering of PPy chains which produces more crystalline structures upon SHI irradiation. The TGA studies are consistent with the XRD results where the crystallinity of PPy nanoparticles increases with increasing the irradiation fluence.

Table 4.9: Degradation temperatures at different percentage weigh losses, onset decomposition temperature, T_{onset} and maximum decomposition rate, $(dW/dT)_m$ for both pristine and irradiated PPy nanoparticles at different irradiation fluences.

Irradiation fluence (ions/cm^2)	Degradation temperature (°C) at different percentage (%) weight losses					Onset decomposition temperature, T_{onset} (°C)	Maximum decomposition rate, $(dW/dT)_m$ (%/°C)
	10 %	**30 %**	**50 %**	**70 %**	**90 %**		
Pristine	169	238	328	443	548	326	$\lvert 0.425 \rvert$
5×10^{10}	197	255	385	452	592	355	$\lvert 0.281 \rvert$
1×10^{11}	189	269	407	598	652	355	$\lvert 0.258 \rvert$
5×10^{11}	197	297	440	600	> 680	375	$\lvert 0.243 \rvert$
1×10^{12}	197	297	446	616	> 680	381	$\lvert 0.208 \rvert$

4.2.6. Dielectric permittivity studies

The dielectric relaxation spectroscopy has been used to investigate the molecular dynamics by studying the effect of applied ac electric field on the pristine and irradiated PPy nanoparticles. Fig. 4.26 depicts the plots of dielectric permittivity (ε') vs. frequency (ω) of both pristine and irradiated PPy nanoparticles at the ion fluences of 5×10^{10}, 10^{11}, 5×10^{11} and 10^{12} ions/cm^2 at room temperature (303 K). It is observed that value of dielectric permittivity (ε') of SHI irradiated PPy nanoparticles is higher as

compared to the pristine sample of PPy nanoparticles and its value increases with increasing the irradiation fluence.

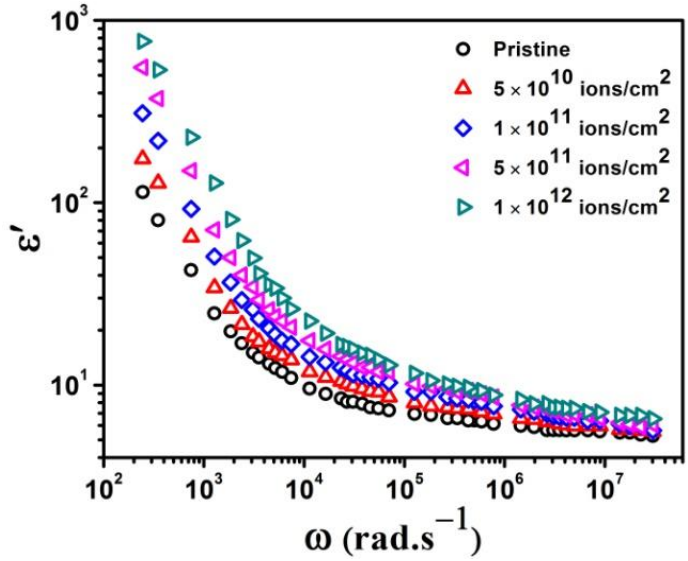

Figure 4.26: *Plots of dielectric permittivity* (ε') *vs. frequency* (ω) *of both pristine and irradiated PPy nanoparticles at different ion fluences at room temperature (303 K).*

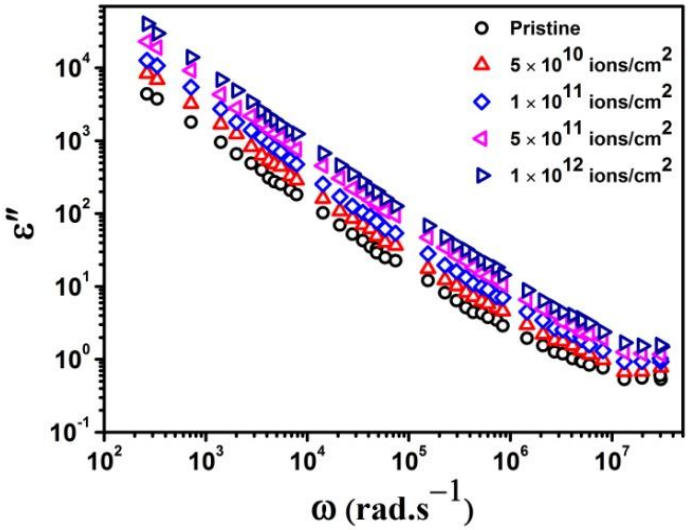

Figure 4.27: *Plots of dielectric loss* (ε'') *vs. frequency* (ω) *of both pristine and irradiated PPy nanoparticles at different ion fluences at room temperature (303 K).*

For a given ion fluence, in lower frequencies ε' decreases with increasing frequency and ε' attains a constant value in higher frequencies. In lower frequencies ($\omega << 1/\tau$, τ is the relaxation time), one can make the approximation $\varepsilon' \approx \varepsilon_s$ where ε_s is the low frequency value of ε', which can be attributed to the large electrode polarization

effects. The charge carriers migrating through the dielectric get trapped in the defects and induce opposite charges in their vicinity producing induced dipoles [295]. At the characteristic frequency $(\omega = 1/\tau)$, the induced dipoles exhibit a relaxation process. At higher frequencies $(\omega >> 1/\tau)$, the induced dipoles are not able to respond to the applied electric field and ε' approaches the lowest saturation value ε_∞. The increase in the value of ε' with increasing irradiation fluence can be attributed to the increase contribution of electrode polarization after SHI irradiation on PPy nanoparticles due to the generation of large number of charge carriers. Fig. 4.27 depicts the room temperature plots of dielectric loss (ε'') vs. frequency (ω) of both pristine and irradiated PPy nanoparticles at the ion fluences of 5×10^{10}, 10^{11}, 5×10^{11} and 10^{12} ions/cm^2. The linear increase in ε'' with decreasing frequency reveals that the dc conduction loss is more prominent over the polarization effect. However, at a particular frequency the value of ε'' increases with increasing irradiation fluence which can be attributed to increased dc conduction in PPy nanoparticles as a result of generation of large number of free charge carriers.

4.2.7. Electric modulus studies

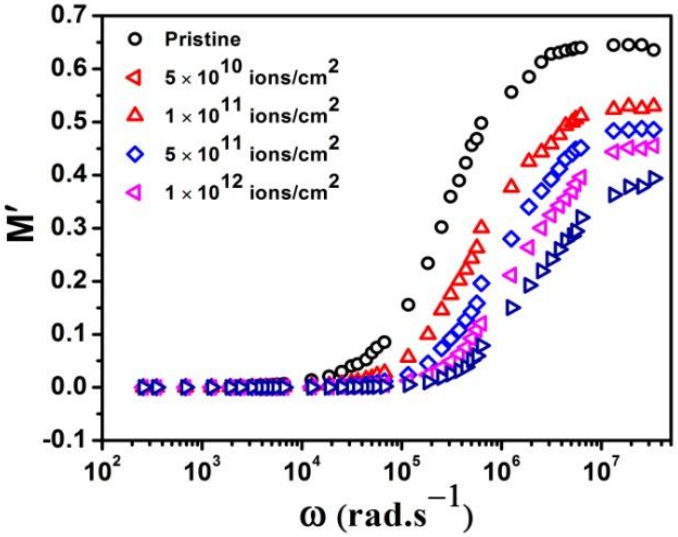

Figure 4.28: *Plots of real part of modulus* (M') *vs. frequency* (ω) *of pristine and irradiated PPy nanoparticles at different ion fluences at room temperature (303 K).*

The plots of real part of modulus (M') vs. frequency (ω) of pristine and irradiated PPy nanoparticles at different ion fluences at room temperature (303 K) are shown in Fig. 4.28. Each M' spectrum shows a sigmoid type behavior i.e. value of M' increases with increasing frequency and reaches a constant maximum value in higher frequencies. At lower frequencies, value of M' approaches zero suggesting elimination of the electrode polarization effect and hence the conductivity relaxation of charge carriers can be best studied [296]. The increase in value of M' with increasing frequency suggests that the conduction process is due to the long range mobility of the charge carriers. In the higher frequency limit, value of M' reaches a maximum and approaches to $M_{\infty}(\omega \to \infty)$ for all the samples which suggests that conduction is due to the short range mobility of charge carriers [297].

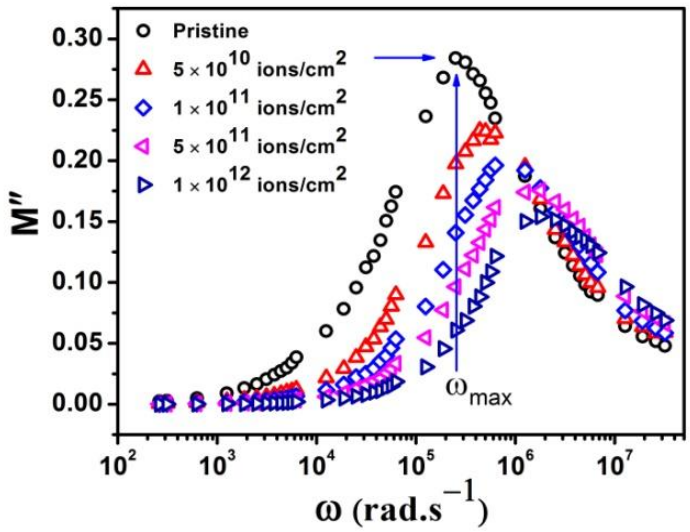

Figure 4.29: *Plots of imaginary part of modulus* (M'') *vs. frequency* (ω) *of pristine and irradiated PPy nanoparticles at different ion fluences at room temperature (303 K).*

Information regarding conductivity relaxation mechanism in SHI irradiated PPy nanoparticles can be extracted from the M'' plots as function of frequency and temperature. Fig. 4.29 shows the plots of imaginary part of modulus (M'') vs. frequency (ω) of pristine and irradiated PPy nanoparticles at different ion fluences at room temperature (303 K). Each M'' spectrum shows a relaxation peak that indicates transition of the motion of charge carriers from long range to the short range with increasing frequency. It is observed that the relaxation peak of both pristine and irradiated PPy is asymmetrical which suggests a non-Debye relaxation process of

charge carriers. The frequencies left to the M'' relaxation peak suggest range of frequencies in which charge carriers undergo long range hopping motion and frequencies right to the M'' relaxation peak represent the short range localized motion of the charge carriers [298]. It is observed from Fig. 4.29 that upon SHI irradiation, the relaxation peak shifts towards higher frequencies with increasing irradiation fluence. This can be ascribed to the fact that more and more trapped charges are released and move a longer distance in the newly formed crystalline domains by the process of interchain cross-linking and formation of single or multiple helices upon SHI irradiation with increasing fluence. This result is in good agreement with the XRD results which shows that crystallinity of PPy chains increases upon SHI irradiation. However the relaxation time $\tau(=1/\omega_{max})$ of charge carriers decreases upon SHI irradiation that reveals easy hopping of charge carriers between two energetically localized regions by overcoming the potential barriers between them.

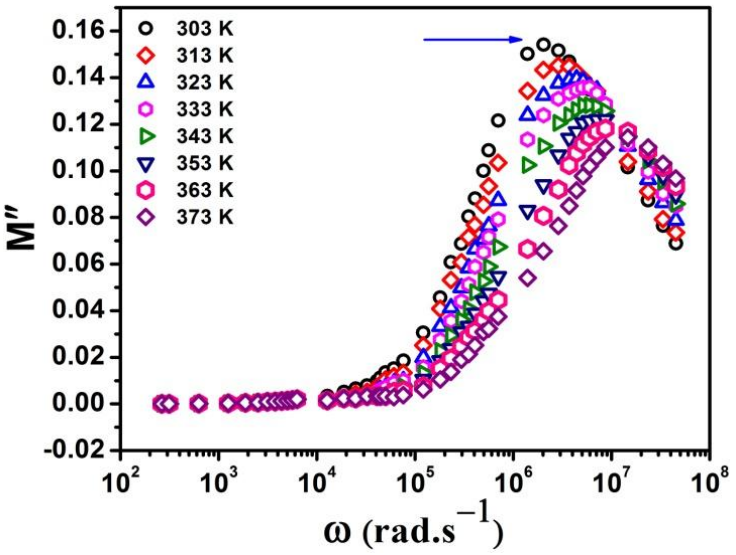

Figure 4.30: *Temperature dependent plots of imaginary part of modulus* (M'') *vs. frequency* (ω) *of irradiated PPy nanoparticles at ion fluence of* 10^{12} *ions/cm*^{2}.

Fig. 4.30 shows the temperature dependent plots of M'' vs. ω of irradiated PPy nanoparticles at ion fluence of 10^{12} ions/cm^2. The plots show asymmetric behavior with respect to the relaxation peak and it is observed that the relaxation peak shifts towards higher frequencies with increasing temperature. This shifting of relaxation peak towards the higher frequencies indicates long range movement of charge carriers in SHI

irradiated PPy nanoparticles due to their thermally activated motion. The temperature dependent relaxation time (τ) follows the Arrhenius relation given by equation (4.11)

$$\tau = \tau_{0M} \exp(\frac{E_{aM}}{kT})$$

as mentioned in section 4.1. The values of τ_0 and (E_{aM}) can be calculated from the intercept and slope of the plot of $\ln\tau$ vs. $1000/T$.

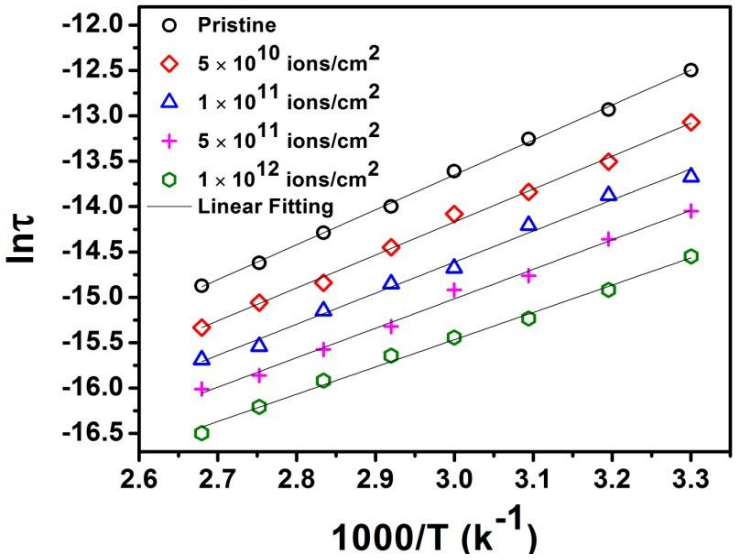

Figure 4.31: *Plots of* $\ln(\tau)$ *vs.* $1000/T$ *for both pristine and irradiated PPy nanoparticles at different fluences.*

Fig. 4.31 depicts the plots of $\ln\tau$ vs. $1000/T$ of pristine and irradiated PPy nanoparticles at different irradiation fluences. The calculated relaxation time (τ) and hopping activation energy (E_{aM}) of both pristine and irradiated PPy nanoparticles at different ion fluences are recorded in Table 4.10. For pristine PPy nanoparticles values of ω and τ are found to be 2.54×10^5 rad.s^{-1} and 3.92×10^{-6} s at room temperature (303 K), while upon SHI ion irradiation, value of ω increases to 17.03×10^5 rad.s^{-1} and τ decreases to 5.87×10^{-7} s at the highest ion fluence of 1×10^{12} ions/cm^2. Moreover, the calculated hopping activation energy E_{aM} of pristine PPy nanoparticles is 0.33 eV while the activation energy of charge carriers decreases upon SHI irradiation and E_{aM} decreases to 0.25 eV at the highest irradiation fluence of 10^{12} ions/cm^2. Thus the SHI

irradiation on PPy nanoparticles decreases the thermal activation energy of charge carriers resulting in enhanced electrical conduction.

Table 4.10: Values of relaxation time (τ) and hopping activation energy (E_{aM}) of both pristine and irradiated PPy nanoparticles at different ion fluences.

Fluence (ions/cm^2)	Relaxation time, τ (s)	Hopping activation energy, E_{aM} (eV)
Pristine	3.92×10^{-6}	0.33
5×10^{10}	2.04×10^{-6}	0.31
1×10^{11}	1.15×10^{-6}	0.29
5×10^{11}	8.53×10^{-7}	0.28
1×10^{12}	5.87×10^{-7}	0.25

4.2.8. AC conductivity studies

The plots of total conductivity (σ') vs. frequency (ω) of both pristine and irradiated PPy nanoparticles at the ion fluences of 5×10^{10}, 10^{11}, 5×10^{11} and 10^{12} ions/cm^2 are shown in Fig. 4.32. The figure shows that the total conductivity (σ') of both pristine and irradiated PPy nanoparticles can be expressed as the sum of dc conductivity (σ_{dc}) and ac conductivity (σ_{ac}) and ac conductivity can be expressed by equation (4.16)

$$\sigma_{ac}(\omega) = A\omega^{s}$$

as discussed in section 4.1. In lower frequencies, the frequency independent conductivity corresponds to dc conductivity (σ_{dc}) is due to the long range motion of charge carriers. In higher frequencies, the conductivity corresponds to ac conductivity (σ_{ac}) and it increases with increasing frequency following the power law equation (4.16) as $\sigma_{ac}(\omega) = A\omega^{s}$. It is observed that upon SHI ion irradiation the conductivity of PPy nanoparticles increases with increasing the irradiation fluence. The increase of ac conductivity with increasing ion fluence can be attributed to the introduction of defects due to high deposition of electronic energy into the PPy chains that produces the free radicals, unsaturations and other defects upon SHI irradiation.

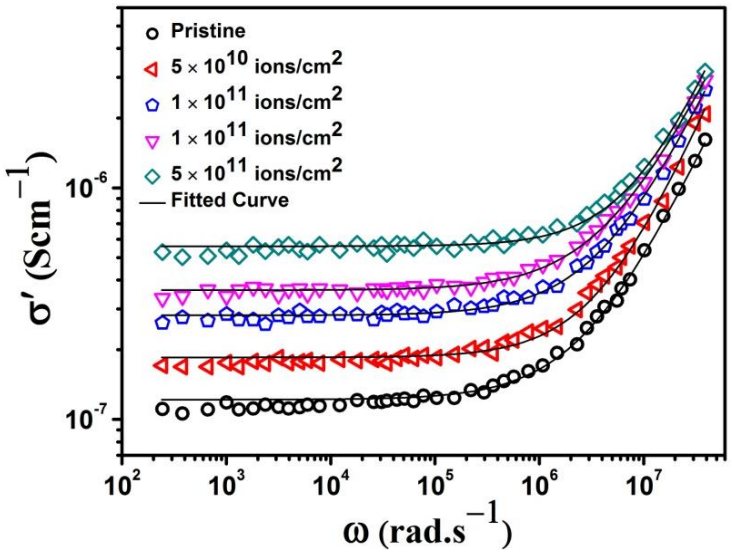

Figure 4.32: *Plots of total conductivity (σ') vs. frequency (ω) of pristine and irradiated PPy nanoparticles at ion fluences of 5×10^{10}, 10^{11}, 5×10^{11} and 10^{12} ions/cm^2 at room temperature (303 K).*

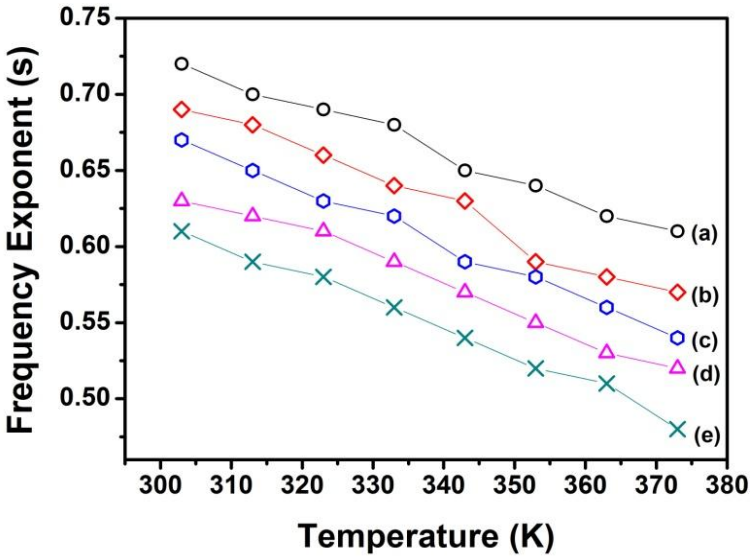

Figure 4.33: *Temperature dependence of frequency exponent (s) of (a) pristine and irradiated PPy nanoparticles at ion fluences of (b) 5×10^{10}, (c) 10^{11}, (d) 5×10^{11} and (e) 10^{12} ions/cm^2.*

The temperature dependence of frequency exponent *s* is crucial in elucidating the microscopic origin of conductivity relaxation mechanism in disordered polymeric materials. Fig. 4.33 shows the temperature dependent plots of frequency exponent *s* of both the pristine and irradiated PPy nanoparticles at the ion fluences of 5×10^{10}, 10^{11}, 5×10^{11} and 10^{12} ions/cm^2. It is observed that value of *s* for both pristine and irradiated

PPy nanoparticles decreases as the temperature is increased. The decrease in value of *s* with increasing temperature reveals that charge carriers in both the pristine and irradiated PPy nanoparticles follow the correlated barrier hopping (CBH) model as the dominant charge transport mechanism in which the charge carriers hop from one localized site to the other neighbouring localized sites by overcoming the potential barrier between them. The activation energy W_H of charge carriers of both pristine and irradiated PPy nanoparticles has been calculated using equation (4.21)

$$s = 1 - \frac{6kT}{W_H}$$

as mentioned in section 4.1. Table 4.11 presents the calculated values of frequency exponent (*s*) and barrier activation energy (W_H) of charge carriers in both pristine and irradiated PPy nanoparticles at different ion fluences at room temperature (303 K*).*

Table 4.11: Values of frequency exponent (*s*) and barrier activation energy (W_H) for charge carriers in both pristine and irradiated PPy nanoparticles at room temperature (303 K).

Fluence (ions/cm^2)	Frequency Exponent, *s*	Barrier activation energy, W_H (eV)
Pristine	0.72	0.56
5×10^{10}	0.69	0.50
1×10^{11}	0.67	0.47
5×10^{11}	0.63	0.42
1×10^{12}	0.61	0.40

Upon SHI irradiation the values of *s* and W_H at a particular temperature decrease as compared to the pristine sample of PPy nanoparticles. The calculated values of *s* and W_H at room temperature for pristine PPy nanoparticles are found as 0.72 and 0.56 eV, respectively while upon SHI irradiation, both the values of *s* and W_H decrease to 0.61 and 0.40 eV, respectively at the highest ion fluence of 10^{12} ions/cm^2. The fact that value of W_H lies between 0.40-0.56 eV indicates that the polarons and not the bipolarons are

the majority charge carriers in PPy nanoparticles since W_H is about four times higher for the bipolaronic transport [155].

4.3. Summary

PPy nanoparticles with average diameters ranging from 11 nm to 22 nm have been synthesised by the micro-emulsion polymerization method in sodium dodecylsulfate (SDS) micellar solution, in which SDS acts both as surfactant and dopant. The SDS micelles behave as nano-reactors for polymerization of pyrrole. Spherical PPy nanoparticles form at SDS surfactant concentration between its CMC-I (8×10^{-3} M) and CMC-II (0.2 M). The HRTEM results show that size of PPy nanoparticles decrease from 22 nm to 11 nm when SDS concentration is increased from 0.01 M to 0.2 M. The crystallinity of PPy nanoparticles increases with increasing SDS concentration. The FTIR results reveal that effective conjugation length of PPy chains increases with increasing SDS concentration which provides a direct consequence of enhanced electrical conductivity at higher SDS molar concentration. TGA results show that the thermal stability of the PPy nanoparticles increases with increasing the SDS concentration. The higher value of dielectric permittivity (ε') at lower frequencies is due to the electrode polarization effects. At a given frequency, the increase in the value of ε' with increasing SDS concentration is attributed to the enhancement of electrode polarization due to availability of more charge carriers in PPy nanoparticles at higher SDS dopant concentration. The linear decrease in the value of dielectric loss (ε'') with increasing frequency suggests the dominant effect of dc loss over the polarization phenomena. Studies of modulus spectra reveal that charge carriers in PPy nanoparticles obey the non Debye relaxation mechanism and relaxation time (τ) decreases with increasing SDS dopant concentration. The ac conductivity of PPy nanoparticles increases with increasing SDS concentration and charge carriers follow the correlated barrier hopping (CBH) model as the dominant transport phenomena.

PPy nanoparticles synthesized at SDS concentration of 0.2 M that shows the best properties has been irradiated with 160 MeV Ni^{12+} ions with four different irradiation fluence of 5×10^{10}, 10^{11}, 5×10^{11} and 10^{12} ions/cm^2. HRTEM results show that upon SHI irradiation the average diameter of PPy nanoparticles increases with

increasing irradiation fluence. XRD results depict that the crystallinity of SHI irradiated PPy nanoparticles increases with increasing the irradiation fluence which is attributed to the cross-linking and formation of single or multiple helices in the PPy nanoparticles after SHI irradiation. FTIR spectra reveal that the IR active vibrational bands have different cross sections for SHI irradiation and the N-H vibrational band at 3695 cm^{-1} is most sensitive to SHI irradiation with formation cross section of 5.77×10^{-13} cm^2 and effective radius of 7.58 nm. Upon SHI irradiation the thermal stability of PPy nanoparticles increases with increasing the irradiation fluence, which can be attributed to the alignment of polymer chains upon SHI irradiation as confirmed by XRD results. The modulus studies reveal that the relaxation peak shifts towards higher frequencies with increasing ion fluence. These results indicate that the long range motion of charge carriers increases upon SHI irradiation. Upon SHI irradiation, the ac conductivity of PPy nanoparticles increases with increasing irradiation fluence following the universal power law equation $\sigma_{ac} = A\omega^s$. The calculated values of frequency exponent *s* of the pristine and irradiated PPy nanoparticles lie in the range of 0.61-0.72 and the value of *s* decreases with increasing temperature. The decrease in frequency exponent *s* with increasing temperature reveals that the correlated barrier hopping (CBH) is the dominant charge transport mechanism in both pristine and irradiated PPy nanoparticles. Binding energy calculations (0.40-0.56 eV) indicate that polarons are the majority charge carriers in both pristine and irradiated PPy nanoparticles.

CHAPTER-V

Polypyrrole nanofibers: Dielectric relaxation and electrical transport studies and swift heavy ion irradiation effects

This chapter deals with the synthesis of different alkylbenzenesulfonic acid (ABSA) doped polypyrrole (PPy) nanofibers by interfacial polymerization method and their different characterizations. A systematic study on the structure-property relationship of the synthesized PPy nanofibers has been established using the sophisticated characterization techniques and studies on the dielectric relaxation and ac conductivity in PPy nanofibers have been discussed. SHI irradiation induced enhancement on the structural, optical and thermal properties along with the dielectric relaxation and ac conductivity in the irradiated PPy nanofibers has also been discussed.

Conducting polymers are well known for their excellent electronic and optical properties with conductivity ranging from insulator to metallic regions along with the additional properties of retaining lightweight, flexibility, good mechanical properties and processing advantages [299]. Compared with the bulk counterparts conducting polymer nanostructures are expected to display high performance in various potential devices because of unique properties caused by their nanometer dimension: high conductivity, large surface area and light weight [300]. Among the various conducting polymers, polypyrrole (PPy) is studied most extensively because of its potential application in various fields such as in chemical and biosensors, actuators, drugs delivery devices, advanced polymeric batteries, electro-chromic windows and displays, corrosion protection etc. due to their easy fabrication processes, good environmental stability and biocompatibility, flexibility, low toxicity, reversible redox property, tenable electrical and optical properties [301-304]. Various synthesis methods have been developed for fabrication of conducting polymer nanostructures which can be used as the building blocks for nano-electronic devices. In recent years, synthesis of one dimensional (1-D) PPy nanostructures including nanofibers and nanotubes has brought considerable attention in fundamental research and industrial applications owing to their application as molecular wires and comparable metallic conductivity [305]. Since

synthesis method is the fundamental and most important issue in the field of conducting polymer nanostructures, various methods such as template method [225], interfacial polymerization [93], seeding polymerization [58] etc. have been developed for fabrication of PPy nanofibers. However, each currently used method has its own advantages as well as disadvantages. Template guided synthesis method uses structural directing agents such as zeolite, alumina, polycarbonate, porous membranes and surfactants as templates [226, 227] and needs post polymerization step to remove externally applied templates. Henceforth the template guided method produces lower yields with less reproducibility that limits their industrial applicability. Electrospinning method can produce good quality nanofibers without use of the external templates but production scale are very limited [100]. A relatively new synthesis method known as interfacial polymerization [94, 306] has been developed for synthesis of conducting polymer nanofibers as one of the effective alternative chemical route. The polymerization occurs at the interface of two immiscible aqueous-organic biphasic medium and resulting product diffuse away from the interface to the aqueous solution because of their hydrophilic nature. In particular the interfacial polymerization approach requires equal volume of organic solvent to the aqueous water. However, the major drawback of this method is that the organic solvents immiscible to water are typically very toxic to the environment and also makes the synthesis procedure costly. Therefore to design and synthesis of multifunctional PPy nanofibers it is crucial to find out a novel, reliable, cost effective, less toxic synthesis approach to realize their practical applications in nanodevices. Synthesis of π-conjugated polymers with different dopants affect on their electrical, optical and structural properties [307]. The presence of an extended π-conjugation structure however confers the required mobility to the charges that generates during doping process into the polymer backbones which makes them electrically conducting [308]. The process of doping generates charge carriers viz. polarons and bipolarons into the conjugated chains of conducting polymers. Doping into the conducting polymers can be influenced by many factors viz. chain length, polaron length, charge transfer to adjacent molecules and conjugation length [309]. Furthermore the properties of doped conducting polymers depend on the type and molecular size of the dopants [310]. The conducting polymers doped with functional organic acids exhibit improved properties due to their easy incorporation as dopant into the polymer chains. However, the inherently poor solubility of PPy in many common

solvents that results from strong intra and inter-chain interactions can be improved using organic acids as dopants into the PPy chains. Despite the technological importance, reports on the effects of alkyl chain length in bulky dopant molecules on the various properties of PPy nanofibers are very rare.

The physico-chemical properties of materials can be altered in a controlled manner by irradiation induced processes. SHI irradiation in materials induces various improvements to the mechanical, optical and electrical properties of polymers [208, 311-314]. Materials modifications by SHI irradiation have several potential applications in electronics, medical devices, energy storage devices and many more [206, 315]. The modifications of polymer structure and properties induced by SHI irradiation are caused by the deposition of energy when the irradiated ion passes through the materials. In case of polymers, the high energetic heavy ions lose their energy mainly through the electronic processes and the energy is deposited in a very small cylindrical region around the ion trajectory [316]. A variety of modifications in the structure and chemical composition including many elementary processes such as production of primary and secondary free radicals, displacing atoms, carbonization, creation of unsaturated bonds, formation of volatile fragments and creation of carbonaceous clusters, which induce cross-linking and chain scission that gradually modify the properties of the polymers [317-319]. The structural modifications in SHI irradiated polymers may produce new electronic levels in the forbidden gap of the electronic structure. SHI irradiation on conducting polymers can enhance their electrical conductivity and hence this technique produces opportunities for use of the ion bean irradiation in producing special materials for electronic applications.

In this chapter, synthesis of PPy nanofibers doped with alkylbenzenesulfonic acids (ABSA) by interfacial polymerization have been reported and the effects of alkyl chain lengths of ABSA dopants on the morphology, structural, optical and thermal properties of PPy nanofibers have been analysed using the state-of-art characterization techniques. Studies on the dielectric relaxation and ac conductivity have also been carried out to understand the transport mechanism in different ABSA doped PPy nanofibers. The synthesis procedure of ABSA doped PPy nanofibers have been explained in Chapter-III. Four different samples viz., *p*-tolunesulfonic acid (*p*-TSA), camphorsulfonic acid (CSA), dodecylbenzenesulfonic acid (DBSA) and octylbenzenesulfonic acid (OBSA) doped PPy nanofibers have been synthesized by

interfacial polymerization method and effects of alkyl chain lengths of different ABSA dopants on various properties have been investigated. The samples with the best properties have been irradiated with 160 MeV Ni^{12+} swift heavy ions (SHI) with different ion fluence of 10^{10}, 5×10^{10}, 10^{11}, 5×10^{11} and 10^{12} ions/cm^2 in order to further enhance the properties of PPy nanofibers. The detailed results of different ABSA doped PPy nanofibers have been presented in Section 5.1 and the results of 160 MeV Ni^{12+} ion irradiated PPy nanofibers have been discussed in Section 5.2.

5.1. Characterization, dielectric relaxation and ac conductivity of polypyrrole nanofibers

5.1.1. High resolution transmission electron microscopy studies

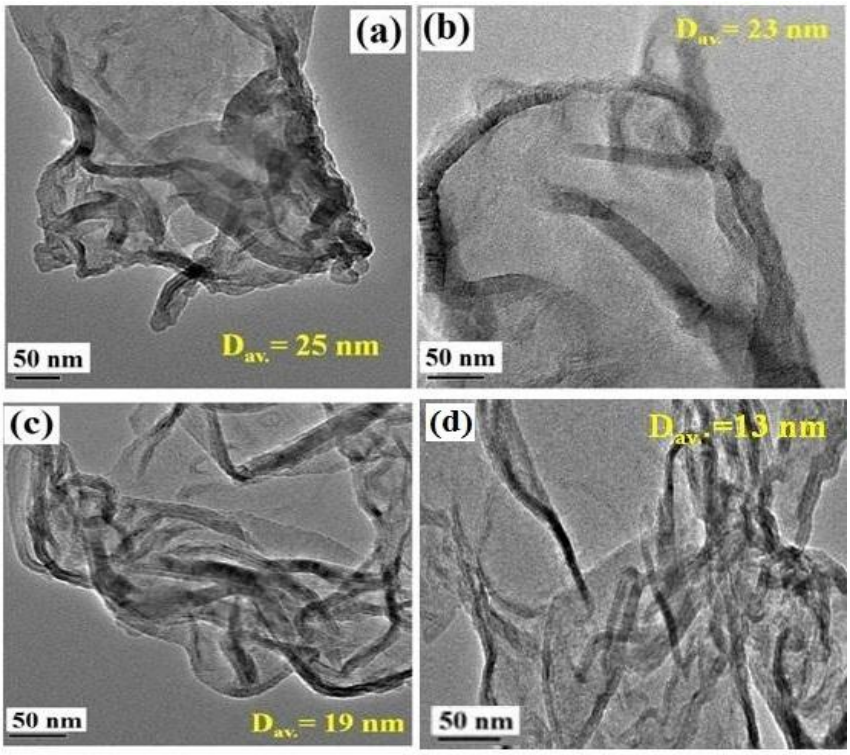

Figure 5.1: *HRTEM micrographs of (a) DBSA, (b) OBSA, (c) CSA and (d) p-TSA doped PPy nanofibers.*

The HRTEM micrographs of different ABSA doped PPy nanofibers are depicted in Fig. 5.1. It is observed that uniform PPy nanofibers result with average diameter ranging from 13 nm to 25 nm and length of nanofibers are in micrometer scale. The morphology and diameter of ABSA doped PPy nanofibers are strongly affected by dopant structure

i.e. alkyl chain length of dopant. Smaller diameter PPy nanofibers result for short alkyl chain *p*-TSA doped PPy nanofibers and increasing order of diameter for different ABSA doped PPy nanofibers is as follows: PPy-(*p*-TSA) < PPy-(CSA) < PPy-(OBSA) < PPy-(DBSA). Furthermore, HRTEM micrographs confirm the twisted structure of PPy nanofibers which suggests that alkylbenzenesulfonic acid (ABSA) doped PPy nanofibers is also highly flexible.

5.1.2. X-ray diffraction studies

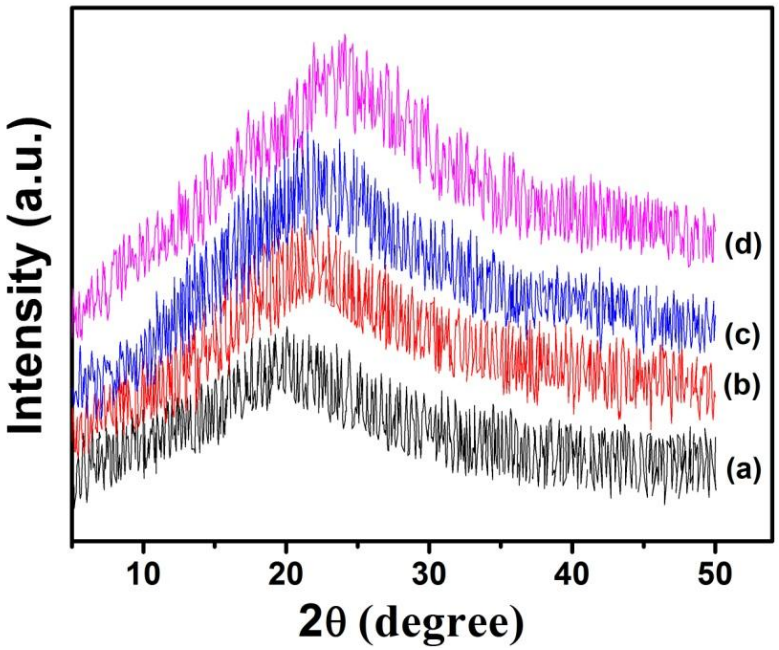

Figure 5.2: *XRD patterns of (a) DBSA (b) OBSA (c) CSA and (d) p-TSA doped PPy nanofibers.*

The chain ordering and chain packing of different ABSA doped PPy nanofibers have been investigated by recording their XRD patterns. Fig. 5.2 depicts the XRD patterns of different ABSA doped PPy nanofibers at room temperature. A broad diffraction peak in 2θ range $20° \leq 2\theta \leq 23.46°$ is appeared for all samples of PPy nanofibers where the intensity and peak position depend on the nature of dopant structure and this is related to the interplanar distance of pyrrole-pyrrole and pyrrole-counter ions [260, 320]. It is observed that for short alkyl chain *p*-TSA doped PPy nanofibers, the diffraction peak intensity is maximum suggesting higher ordering of polymer chains as compared to the other ABSA doped PPy nanofibers. The ordering of short alkyl chain ABSA doped PPy

nanofibers can result from the short range arrangement of polymer chains due to strong electrostatic interaction of the dopant anions with the polymer chains. The ordering of chains (X_C) of PPy nanofibers has been calculated using the following equation [261]:

$$\text{Ordering of polymer chains, } X_C = \frac{A^I}{A^T} \times 100\% \qquad (5.1)$$

where A^I and A^T are the area of the broad diffraction peak and the total area under the diffractogram, respectively. The origin of different crystallinity of ABSA doped PPy nanofibers depends on (a) type of dopant (b) size of the corresponding dopant anions and (c) electrostatic interaction between dopant anions and polymer chains. It is observed that for *p*-TSA doped PPy nanofibers the broad diffraction peak appears at slightly higher angle $2\theta = 23.46^o$ that suggest decrease in interplanar spacing between the polymer chains. The structural properties of PPy nanofibers can also be correlated with their electrical properties. Higher crystallinity of polymer chains is a favourable factor for the intra-molecular mobility of charge carriers along the polymer chains and in some extent the intermolecular hopping due to better and close packing. Hence one can expect increase value of electrical conductivity in *p*-TSA doped PPy nanofibers as compared to the other ABSA doped PPy nanofibers. The interplanar spacing or *d*-spacing can be calculated using the Bragg's diffraction formula [263]:

$$2d \sin\theta = \lambda \qquad (5.2)$$

The calculated *d*-spacing shows that *p*-TSA doped PPy nanofibers exhibit smaller *d*-spacing of 3.78 Å, while DBSA doped PPy nanofibers exhibit higher *d*-spacing of 4.44 Å. The hopping distance (*R*) between the polymer chains can be calculated from the relation given by Klung and Alexender [262, 263]:

$$R = \frac{5}{8}\left[\frac{\lambda}{\sin\theta}\right] \qquad (5.3)$$

The calculation of hopping distance of different ABSA doped PPy nanofibers suggest that *p*-TSA doped PPy nanofibers exhibit smaller hopping distance of $R = 4.73$ Å, while long alkyl chain DBSA doped PPy nanofibers exhibit higher hopping distance of $R = 5.54$ Å. The decrease in *d*-spacing increases the probability of increasing interchain hopping of charge carriers, which consequently results increase in electrical conductivity in short alkyl chain doped PPy nanofibers. The net electrical conductivity arises both from the intra and inter chain mobility of charge carriers. The increase in crystallinity of different ABSA doped PPy nanofibers is of the order of PPy-(DBSA)<

PPy-(OBSA)< PPy-(CSA)< PPy-(*p*-TSA), while their ordering of *d*-spacing is opposite to that of their crystallinity order. However, chain length of different ABSA dopants is in the order of DBSA > OBSA > CSA > *p*-TSA. The dopant with longer chain length exerts more force that resists the alignment and close packing of PPy nanofibers chains resulting lower crystallinity. Hence from the structural analysis it is expected that *p*-TSA doped PPy nanofibers can exhibit higher electrical conductivity than that of other ABSA doped PPy nanofibers. The calculated values of diffraction peak position (2θ), ordering of chains (X_C), interplanar spacing (d) and hopping distance (R) of different ABSA doped PPy nanofibers are presented in Table 5.1.

Table 5.1: Values of diffraction peak position (2θ), ordering of chains (X_C), interplanar spacing (d) and hopping distance (R) of different ABSA doped PPy nanofibers.

ABSA dopant	Diffraction peak, 2θ (degree)	Ordering of chains, X_C (%)	Interplanar spacing, d (Å)	Hopping distance, R (Å)
DBSA	20 ± 0.04	17.40 ± 0.3	4.44 ± 0.04	5.54 ± 0.04
OBSA	21.48 ± 0.03	19.70 ± 0.2	4.13 ± 0.03	5.16 ± 0.03
CSA	22.17 ± 0.02	21.40 ± 0.3	4.00 ± 0.02	5.01 ± 0.02
p-TSA	23.46 ± 0.03	23.25 ± 0.2	3.78 ± 0.03	4.73 ± 0.03

5.1.3. Fourier transform infrared spectroscopy analysis

The chemical structure of different ABSA doped PPy nanofibers have been investigated by recording their FTIR spectra. The FTIR spectra of different ABSA doped PPy nanofibers are depicted in Fig. 5.3. A strong vibration band is appeared in the wave number region of 3100-3600 cm^{-1} which ascribes to the N-H stretching vibration mode of PPy [321]. The characteristic vibration bands at 1544 and 1464 cm^{-1} correspond to the C-C and C-N stretching vibration, respectively which represent the antisymmetric and symmetric pyrrole ring stretching modes [322]. The vibration bands at 1278 cm^{-1} and 1034 cm^{-1} are attributed to the C-H and C-N in-plane-deformation mode [323]. The vibration band at 1194 cm^{-1} is attributed to the SO_3^- aromatic ring-doped state of PPy

nanofibers [324]. The vibration band at 774 cm^{-1} is ascribed to the C-H out-of-plane-bending vibration while the vibration band at 905 cm^{-1} ascribes to C-H out-of-plane deformation vibration and the band of C-H stretching vibration is located at 2929 cm^{-1}.

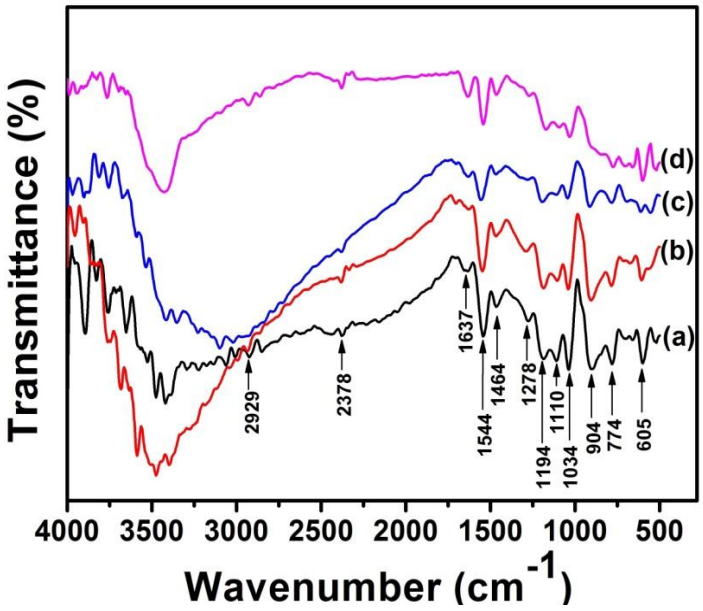

Figure 5.3: *Plots of FTIR spectra of PPy nanofibers doped with (a) DBSA (b) OBSA (c) CSA and (d) p-TSA.*

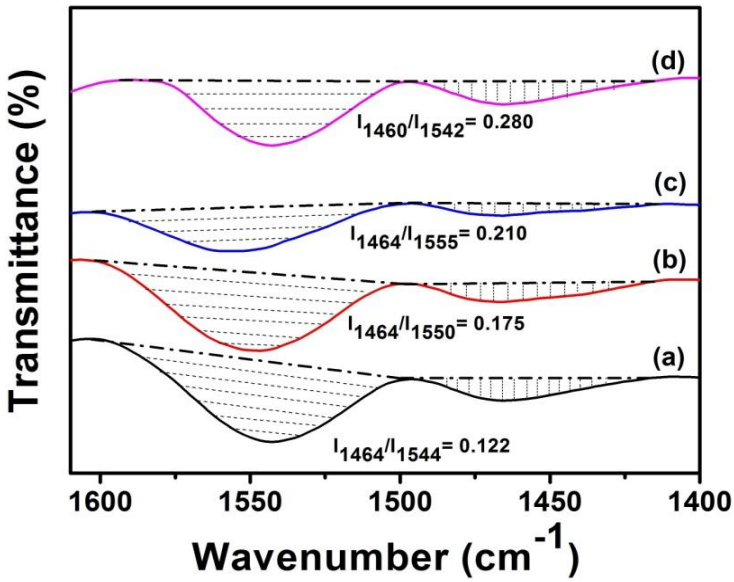

Figure 5.4: *Plots of peak area ratio of I_{1464}/I_{1544} (I_{1464}/I_{1550}, I_{1464}/I_{1555}, I_{1460}/I_{1542}) of PPy nanofibers doped with (a) DBSA (b) OBSA (c) CSA and (d) p-TSA.*

The variation in electrical conductivity of different ABSA doped PPy nanofibers can be understood qualitatively from their respective FTIR spectra. The electrical conductivity of PPy nanofibers is related to their "effective conjugation length" which can be estimated by measuring the degree of delocalization. The degree of delocalization or "effective conjugation length'' of polymer chain is directly proportional to the integrated peak area ratio of I_{1464}/I_{1544} [270]. Fig. 5.4 depicts the plots of integrated peak area ratio of I_{1464}/I_{1544} of different ABSA doped PPy nanofibers and the calculated values of I_{1464}/I_{1544} are presented in Table 5.2. It is observed that peak area ratio of I_{1464}/I_{1544} of PPy nanofibers increases according to the following order: PPy-(DBSA)< PPy-(OBSA)< PPy-(CSA)< PPy-(*p*-TSA), which is directly proportional to increase in electrical conductivity into PPy nanofibers chains. Therefore studies of FTIR spectra suggest conjugation length dominated electrical conductivity in ABSA doped PPy nanofibers.

Table 5.2: Values of integrated peak area ratio of I_{1464}/I_{1544} (I_{1464}/I_{1550}, I_{1464}/I_{1555}, I_{1460}/I_{1542}) of different ABSA doped PPy nanofibers.

ABSA dopants	Peak area ratio of I_{1464}/I_{1544} (I_{1464}/I_{1550}, I_{1464}/I_{1555}, I_{1460}/I_{1542})	Optical band gap energy, E_g (eV)
DBSA	0.122 ± 0.002	2.89 ± 0.003
OBSA	0.175 ± 0.003	2.85 ± 0.002
CSA	0.210 ± 0.002	2.74 ± 0.003
p-TSA	0.280 ± 0.002	2.64 ± 0.003

5.1.4. UV-visible absorption spectroscopy studies

Information about electronic structure and optical band gap energy of materials can be extracted by studying their UV-vis absorption spectra. Fig. 5.5 depicts the UV-vis absorption spectra of different ABSA doped PPy nanofibers at room temperature. The π orbital produces the valence band and π* orbital forms the conduction band. The energy difference between these two bands is called the optical band gap energy which determines the optical properties of semiconducting polymeric materials. The smaller value of optical band gap energy allows easy π-π* electronic transition and hence

results higher value of electrical conductivity. It is observed that UV-vis absorption spectra of different ABSA doped PPy nanofibers exhibit three characteristic absorption bands at 330 nm, 466 nm and a trail band above 700 nm.

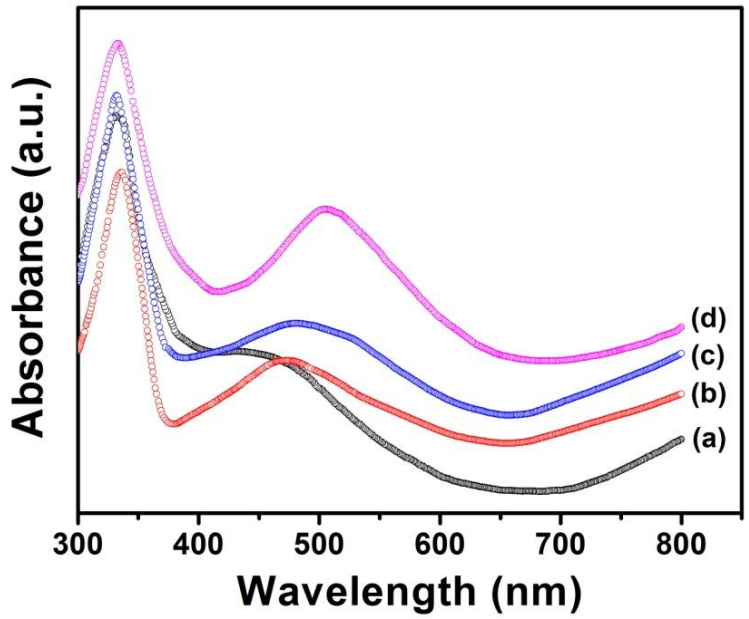

Figure 5.5: *UV-vis absorption spectra of (a) DBSA (b) OBSA (c) CSA and (d) p-TSA doped PPy nanofibers at room temperature.*

Upon doping with ABSA into PPy nanofibers chains, the electrons extract from PPy backbones and then electric charges become delocalize and form a polaron. A polaron induces two localized electronic levels in the band gap: an occupied bonding polaron level (BPL) and an unoccupied antibonding polaron level (APL). In general the two polarons are usually unstable and hence combine together to form a stable bipolaron. The two electronic levels of bipolarons i.e. bonding/antibonding bipolaron levels, BBL and ABL, get closer and the bonding bipolaron state are empty which is dissimilar to the polaron case. Therefore the absorption band at 330 nm is attributed to the interband π-π^* transition, i.e. transition from top of the valence band to bottom of the conduction band in PPy nanofibers. The absorption band at about 466 nm is assigned to the transition from valence band to the antibonding polaron state because of polaron absorption. The third absorption band above 700 nm can be attributed to the transition from valence band to the bipolaron band due to bipolaron absorption [325, 326]. The band position in UV-vis absorption spectra reveals the corresponding structure of PPy nanofibers. It is observed that polaron absorption band makes a red shift for PPy

nanofibers doped with short alkyl chain *p*-TSA dopant and this red shifting is attributed to the reduction in optical band gap energy. The decrease in optical band gap energy can result increase in electrical conductivity of short alkyl chain doped PPy nanofibers.

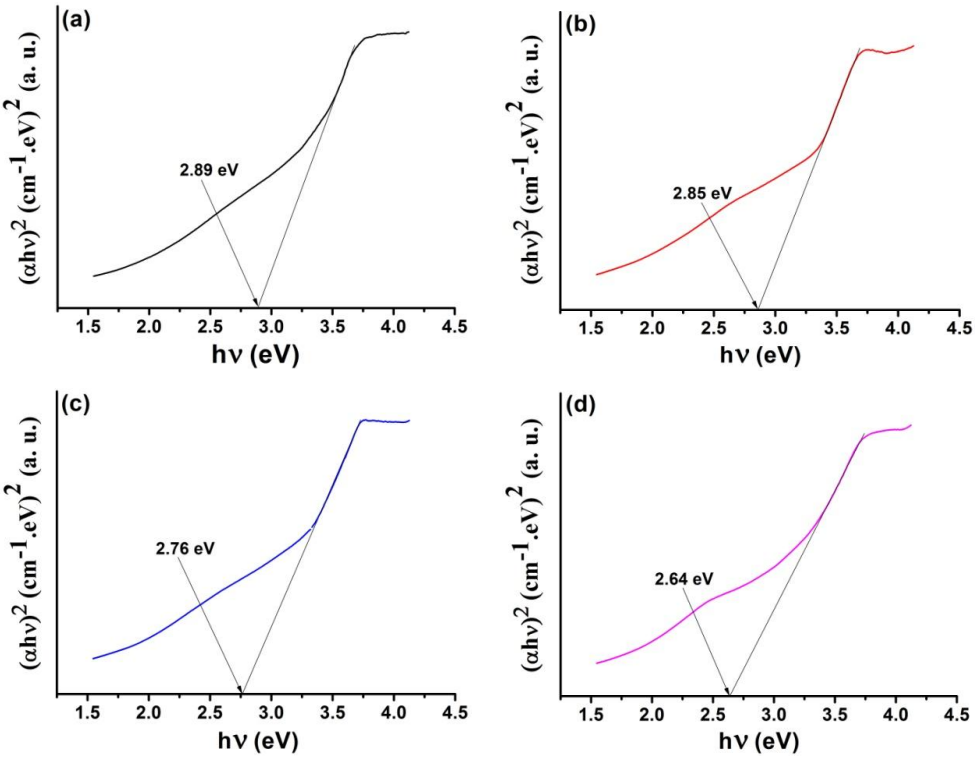

Figure 5.6: *Plots of* $(\alpha h\nu)^2$ *vs.* $h\nu$ *of (a) DBSA (b) OBSA (c) CSA and (d) p-TSA doped PPy nanofibers.*

The optical band gap energy (E_g) of PPy nanofibers has been calculated using the Tauc's equation [272],

$$\alpha(\nu) = \frac{B_\alpha (h\nu - E_g)^n}{h\nu} \tag{5.4}$$

where α is the absorption coefficient, B_α is the proportionality constant and the index *n* represents the corresponding optical transition such that $n = 0.5$ for allowed direct transition, $n = 1.5$ for direct forbidden transition, $n = 2$ for allowed indirect transition and $n = 3$ for forbidden indirect transition. By plotting $(\alpha h\nu)^{1/n}$ vs. $h\nu$ and extrapolating the most linear portion of the plot $(\alpha h\nu)^{1/n}$ to zero, the value of optical band gap energy (E_g) of the material can be determined. Fig. 5.6 depicts the plots of $(\alpha h\nu)^2$ vs. $h\nu$ of different ABSA doped PPy nanofibers and the calculated values of

E_g are recorded in Table 5.2. Calculation of E_g shows that the short alkyl chain *p*-TSA doped PPy nanofibers exhibit smaller optical band gap energy of 2.64 eV, while the long alkyl chain DBSA doped PPy nanofibers exhibit higher optical band gap energy of 2.89 eV among other ABSA doped PPy nanofibers.

5.1.5. Thermogravimetric analysis

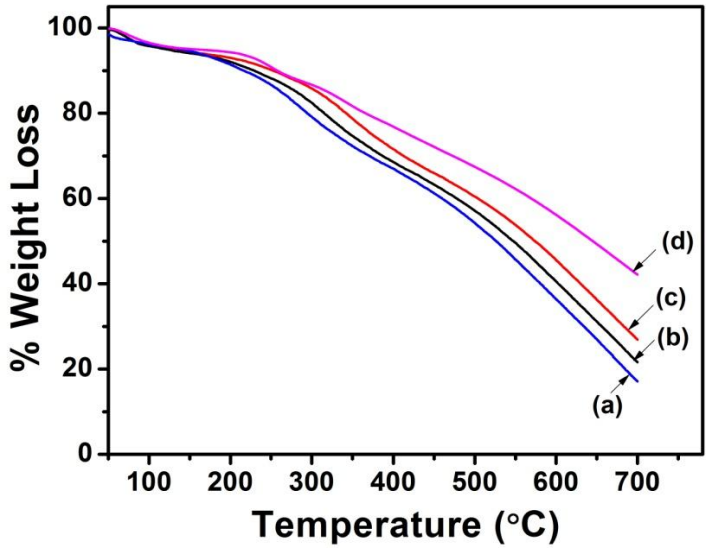

Figure 5.7: *TGA thermographs of PPy nanofibers doped with (a) DBSA (b) OBSA (c) CSA and (d) p-TSA.*

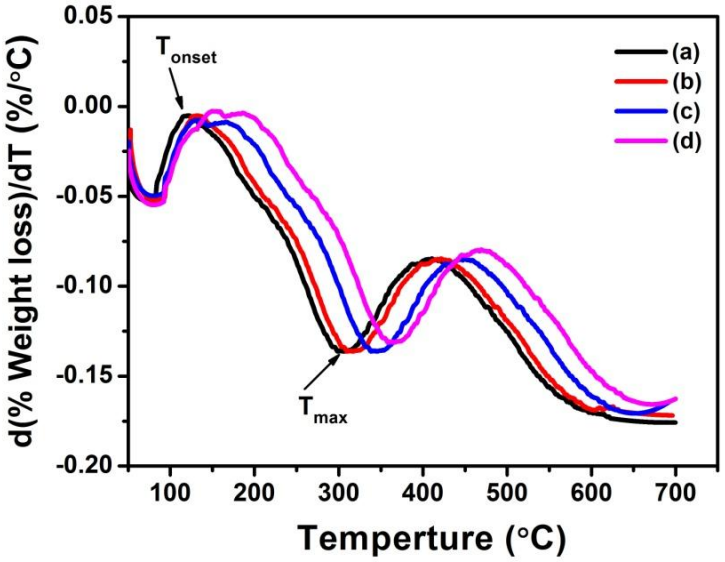

Figure 5.8: *Derivative plots of TGA thermographs for PPy nanofibers doped with (a) DBSA (b) OBSA (c) CSA and (d) p-TSA.*

The TGA thermographs of different ABSA doped PPy nanofibers are shown in Fig. 5.7. The Figure shows that the weight loss of ABSA doped PPy nanofibers takes place in three different stages. The first stage of weight loss occurs from room temperature to 160 °C, which is attributed to the loss of moisture and low molecular weight oligomers. The second stage of weight loss begins at about 180 °C and continues up to 410 °C, which occurs due to the elimination of dopant anions from the PPy nanofibers chains. The third and most remarkable weight loss above the temperature 410 °C takes place due to the exothermic thermal degradation of PPy nanofibers chains. However, the degradation temperature of different ABSA doped PPy nanofibers increases, while their weight loss decreases according to the following order: PPy-(DBSA) <PPy-(OBSA) <PPy-(CSA) <PPy-(*p*-TSA). The degradation temperature at different percentage weight losses for different ABSA doped PPy nanofibers are presented in Table 5.3. The derivative plots of TGA thermographs for different ABSA doped PPy nanofibers are shown in Fig. 5.8. The figure depicts the onset decomposition temperature (T_{onset}) and maximum decomposition temperature (T_m), at which the decomposition (degradation) rate is rapidest, which are tabulated in Table 5.4. The table shows that T_{onset} and T_m increase with decreasing length of the alkyl chain of the ABSA dopant. The T_{onset} and T_m for the long alkyl chain DBSA doped PPy nanofibers that occur at 120 °C and 303 °C, respectively are shifted to 182 °C and 365 °C, respectively for the short alkyl chain *p*-TSA doped PPy nanofibers. These results confirm the higher thermal stability of short alkyl chain *p*-TSA doped PPy nanofibers than that of the long alkyl chain DBSA doped PPy nanofibers. The increase in thermal stability of short alkyl chain ABSA doped PPy nanofibers can also be correlated with their structural properties i.e. higher thermal stability of *p*-TSA doped PPy nanofibers originates because of the ordered arrangement of PPy nanofibers chains.

Table 5.3: Degradation temperature at different percentage weight losses for PPy nanofibers doped with different ABSA dopants.

ABSA dopant	Degradation temperature (°C) at different percentage weight losses						
	10 %	**20%**	**30%**	**40 %**	**50 %**	**60 %**	**70 %**
DBSA	215	293	368	458	523	577	631
OBSA	227	316	389	478	546	605	657
CSA	250	345	417	504	577	626	682
p-TSA	255	362	474	570	644	---	---

Table 5.4: Onset decomposition temperature, T_{onset} and maximum decomposition temperature, T_m for PPy nanofibers doped with different ABSA dopants.

ABSA dopant	Onset decomposition temperature, T_{onset} (°C)	Maximum decomposition temperature, T_m (°C)
DBSA	120	303
OBSA	130	314
CSA	165	346
p-TSA	182	365

5.1.6. Dielectric permittivity studies

The frequency dependence of complex permittivity $\varepsilon^*(\omega)$ can be expressed as:

$$\varepsilon^*(\omega) = \varepsilon'(\omega) - j\varepsilon''(\omega) \quad (5.5)$$

where the real part $\varepsilon'(\omega)$ is known as the dielectric permittivity that represents the energy stored and the imaginary part $\varepsilon''(\omega)$ is known as the dielectric loss that represents the energy loss in each cycle of electric field. To study the dielectric relaxation mechanism, the frequency dependence of dielectric permittivity $\varepsilon'(\omega)$ and

dielectric loss $\varepsilon''(\omega)$ of different ABSA doped PPy nanofibers at room temperature are shown in Figs. 5.9 and 5.10, respectively.

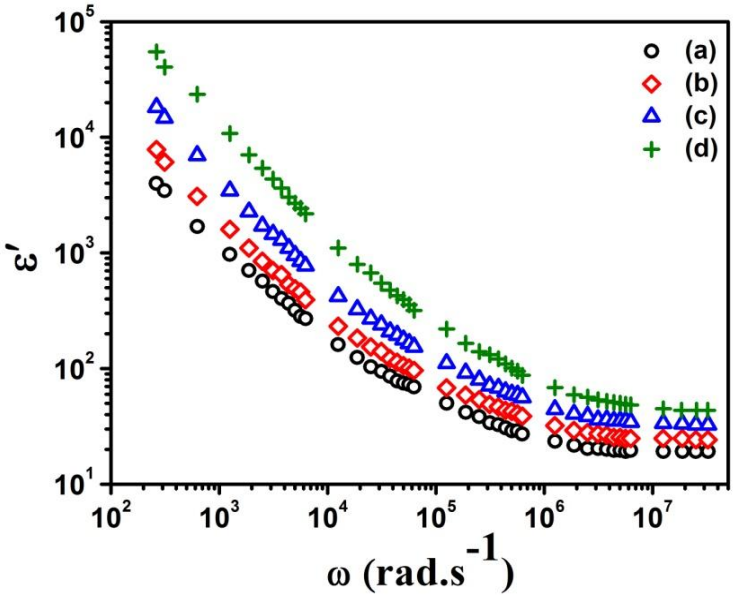

Figure 5.9: *Plots of dielectric permittivity* (ε') *vs. frequency* (ω) *of PPy nanofibers doped with (a) DBSA (b) OBSA (c) CSA and (d) p-TSA at room temperature (303 K).*

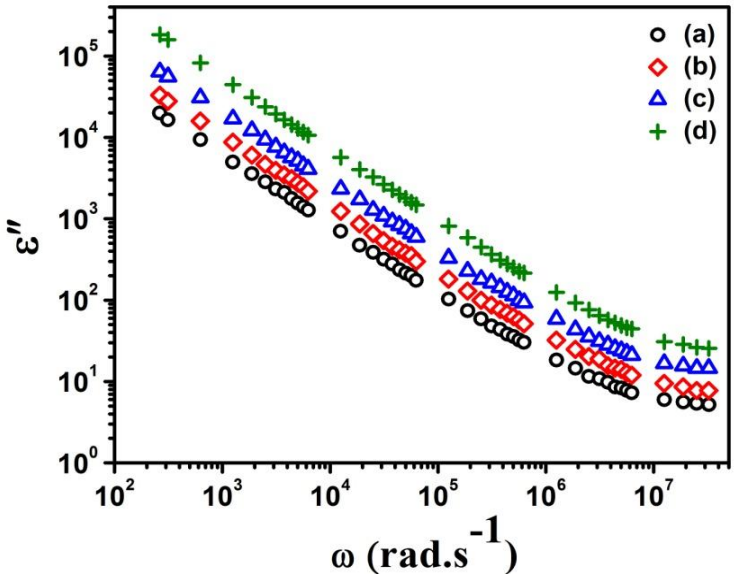

Figure 5.10: *Plots of dielectric loss* (ε'') *vs. frequency* (ω) *of PPy nanofibers doped with (a) DBSA (b) OBSA (c) CSA and (d) p-TSA at room temperature (303 K).*

The ABSA doped PPy nanofibers show a strong frequency dispersion at low frequencies followed by a nearly frequency independent behavior in high frequencies. The increased value of $\varepsilon'(\omega)$ at low frequencies ($\leq 10^4$ Hz) may be ascribed to the electrode i.e. Maxwell-Wagner-Sillars (MWS) polarization effects. Also, value of $\varepsilon'(\omega)$ at a given frequency is different for different ABSA doped PPy nanofibers. The value of ε' is higher for short alkyl chain *p*-TSA doped PPy nanofibers, while the PPy nanofibers doped with long alkyl chain DBSA exhibit smaller value of ε' among the other ABSA doped PPy nanofibers. As shown in Fig. 5.10, $\varepsilon''(\omega)$ of different ABSA doped PPy nanofibers increases almost linearly as frequency is decreased at a particular temperature. The magnitude of $\varepsilon''(\omega)$ may be regarded as the contribution from three distinct effects [241]: dc conductance, Maxwell-Wagner or interfacial polarization and usual dipole orientation or Debye loss.

$$\varepsilon'' = \varepsilon''_{dc} + \varepsilon''_{MW} + \varepsilon''_{D} \tag{5.6}$$

Considering the polymer sample as parallel resistor-capacitor circuit system [239], a mathematical framework has been developed to distinguish the loss ε''_{dc} that arises from the dc conductivity process from other processes. The loss factor ε''_{dc} due to dc conductance can be obtained from the following equation,

$$\varepsilon''_{dc} = \frac{2\pi \times 1.8 \times 10^{12}[G_{spec}]}{\omega} \tag{5.7}$$

where G_{spec} is the specific conductivity (Scm^{-1}) of the sample. The loss factor due to Maxwell-Wagner-Sillars (MWS) relaxation ε''_{MW} can be obtained from the following equation [327],

$$\varepsilon''_{MW} = \varepsilon_{\infty}\left(1 + \frac{K}{1+\omega^2\tau^2}\right) \tag{5.8}$$

where ε_{∞} and K are the constants calculated considering two different dielectric permittivity of the sample at the interfaces and τ is the relaxation time of polarization process. Expressing equations (5.7) and (5.8) in logarithmic scale and plotting of ε''_{dc} vs. ω and ε''_{MW} vs. ω, two different curves can be obtained. The plot of ε''_{dc} vs. ω represents a straight line, whereas the plot of ε''_{MW} vs. ω represents a sigmoid curve.

The linear increase of ε'' with decreasing frequency suggests that the dc conductivity process is more significant than that of the electrode polarization effect. Also, it is observed that value of dielectric loss ε'' is different for different ABSA dopants. The value of ε'' is higher in short alkyl chain *p*-TSA doped PPy nanofibers while the DBSA doped PPy nanofibers exhibits smaller ε'' than that of the other ABSA doped PPy nanofibers. The high value of ε'' may be attributed to the generation of increased concentration of charge carriers that increases ε'' which results from the strong doping reaction with the short alkyl chain doped ABSA into the PPy nanofibers chains.

5.1.7. Electric modulus studies

To study the conductivity relaxation in depth, the modulus formalism is used. The main advantage of using modulus formalism over the permittivity formalism for studying the relaxation mechanism is that the electrode polarization effects which dominate the permittivity formalism are suppressed in this formalism [328, 329]. The modulus formalism provides greater insight into the charge transport processes such as mechanism of conductivity relaxation and charge dynamics as a function of frequency and temperature [330]. In modulus formalism, the complex electric modulus M^* is defined as the reciprocal of complex permittivity ε^*.

$$M^*(\omega) = 1/\varepsilon^*(\omega) = M'(\omega) + jM''(\omega) \tag{5.9}$$

where $M'(\omega)$ and $M''(\omega)$ are the real and imaginary parts of complex electric modulus M^*. The real and imaginary parts of M^* are given by,

$$M' = \frac{\varepsilon'}{(\varepsilon')^2 + (\varepsilon'')^2} \tag{5.10}$$

$$M'' = \frac{\varepsilon''}{(\varepsilon')^2 + (\varepsilon'')^2} \tag{5.11}$$

The plots of real part of modulus M' vs. frequency of different ABSA doped PPy nanofibers at room temperature are shown in Fig. 5.11. It is observed that for each sample, M' attains a constant value at high frequencies while in the intermediate frequencies M' increases as frequency is increased suggesting the evidence of electrode

polarization effects. However at low frequencies, M' approaches to zero suggesting the suppression of electrode polarization effects in lower frequency region [331].

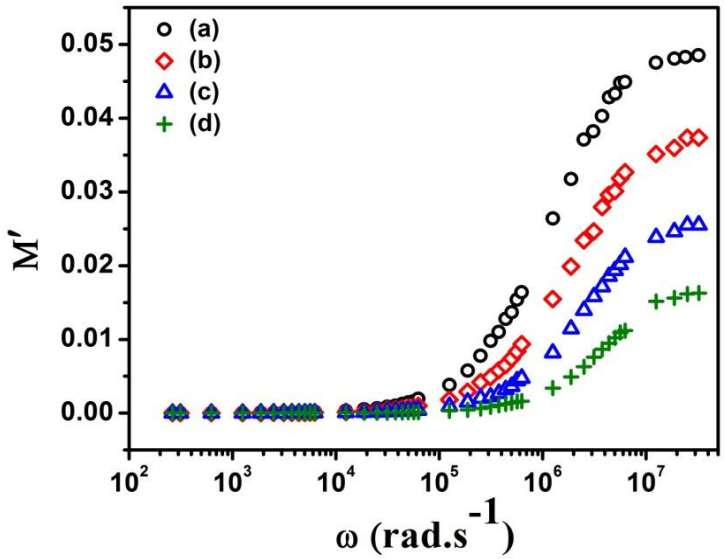

Figure 5.11: *Plots of real part of modulus* (M') *vs. frequency* (ω) *of PPy nanofibers doped with (a) DBSA (b) OBSA (c) CSA and (d) p-TSA at room temperature (303 K).*

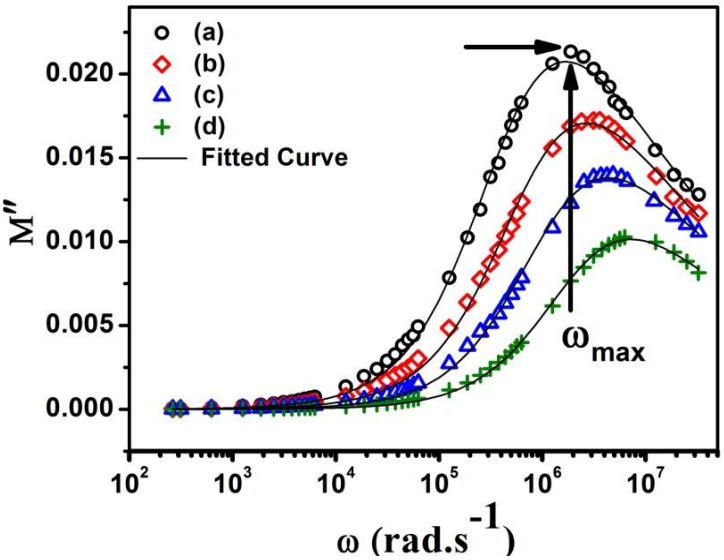

Figure 5.12: *Plots of imaginary part of modulus* (M'') *vs. frequency* (ω) *of PPy nanofibers doped with (a) DBSA (b) OBSA (c) CSA and (d) p-TSA at room temperature (303 K).*

Fig. 5.12 depicts the plots of imaginary part of modulus M'' vs. frequency of PPy nanofibers doped with different ABSA doped PPy nanofibers at room temperature (303 K). The M'' spectra for each sample exhibits a single relaxation peak centred at the frequency dispersion region of M' spectra. The frequency region left to the relaxation peak corresponds to the motion of localized charge carriers, while that to the right of the relaxation peak signifies the long range motion of charge carriers. The conductivity relaxation frequency ω_0 corresponding to $M''_{\max}$ gives the conductivity relaxation time τ that can be calculated by the following relation [332],

$$\tau = \frac{1}{\omega_{\max}} \tag{5.12}$$

It is observed that the relaxation frequency $\omega_{\max}$ of PPy nanofibers is dopant dependent at a given temperature. For short alkyl chain *p*-TSA doped PPy nanofibers, the relaxation frequency shifts towards higher frequencies as compared to the other ABSA doped PPy nanofibers. Therefore, charge carriers in *p*-TSA doped PPy nanofibers exhibit short range to long range motion with smallest relaxation time τ. The asymmetric shape of M'' spectra indicates that the relaxation process deviates from the ideal Debye behavior and there exists a distribution of relaxation times. This distribution may originate from the non-homogeneity of the doping process [184] implying different environments for the charge carriers. To further analyze the conductivity relaxation mechanism, the experimentally obtained M'' data are fitted with the modified Kohlrausch-Williams-Watts (KWW) fitting function in the frequency domain as proposed by Bergman [283]. In the frequency approach M'' can be approximated as follows:

$$M''(\omega) = \frac{M''_{\max}}{[(1-\beta)+(\beta/(1+\beta))[\beta(\omega_{\max}/\omega)+(\omega/\omega_{\max})^{\beta}]]} \tag{5.13}$$

where $M''_{\max}$ is the peak maximum of the imaginary part of electric modulus, β is the Kohlrausch stretched parameter that describes the distribution of relaxation times. Debye relaxation is obtained for $\beta = 1$ and deviation of β from unity indicates non-Debye relaxation mechanism and a distribution of relaxation times. The value of stretched parameter β can be defined empirically by Kohlrausch-Williams-Watts (KWW) function as follows [281, 282]:

$$\varphi(t) = \exp[-(t/\tau)^{\beta}] \tag{5.14}$$

where τ is the relaxation time for charge carriers. Fig. 5.12 depicts that the experimental data of M'' spectra are well fitted with equation (5.13). Values of maximum of imaginary part of modulus (M''_{max}), relaxation frequency (ω_{max}), relaxation time (τ) and Kohlrausch stretched parameter (β) for charge carriers of different ABSA doped PPy nanofibers at room temperature (303 K) are presented in Table 5.5.

Table 5.5: Values of maximum of imaginary part of modulus (M''_{max}), relaxation frequency (ω_{max}), relaxation time (τ) and Kohlrausch stretched parameter (β) for charge carriers of different ABSA doped PPy nanofibers at room temperature (303 K).

ABSA dopants	M''_{max}	(ω_{max}) (rad.s^{-1})	τ (s)	β
DBSA	0.021	1.83×10^{6}	5.45×10^{-7}	0.65
OBSA	0.017	2.98×10^{6}	3.35×10^{-7}	0.63
CSA	0.014	3.89×10^{6}	2.57×10^{-7}	0.60
p-TSA	0.010	7.85×10^{6}	1.27×10^{-7}	0.56

The values of β are less than unity $(0.56 \le \beta \le 0.65)$, which indicates that the relaxation mechanism of charge carriers follows the non-Debye relaxation process. Moreover, value of β in *p*-TSA doped PPy nanofibers is smaller than that of the other ABSA doped PPy nanofibers suggesting a broader distribution of the relaxation times of the charge carriers. The temperature also affects the relaxation frequency and hence the relaxation time of ABSA doped PPy nanofibers. Fig. 5.13 depicts the variation of M'' vs. ω for *p*-TSA doped PPy nanofibers at different temperatures. As the temperature increases, M''_{max} shifts towards higher frequencies resulting in smaller relaxation time of charge carriers. The increase in the movement of polymer chains and mobility of charge carriers with increasing temperature facilitates the charge transfer process that results in the decrease in the relaxation time. This suggests thermally

activated relaxation and hopping of charge carriers. The similar temperature dependence of M'' vs. ω can be observed for the other ABSA doped PPy nanofibers.

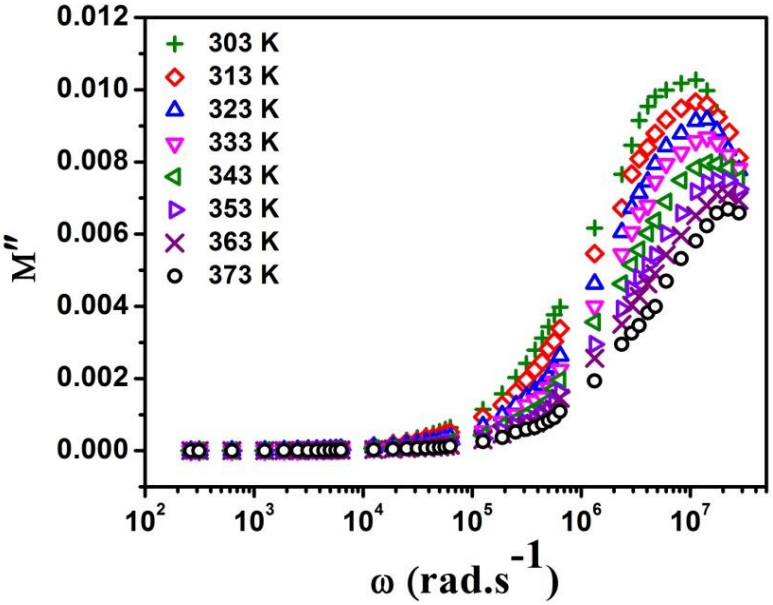

Figure 5.13: *Temperature dependence plots of imaginary part of modulus* (M'') *vs. frequency* (ω) *for p-TSA doped PPy nanofibers.*

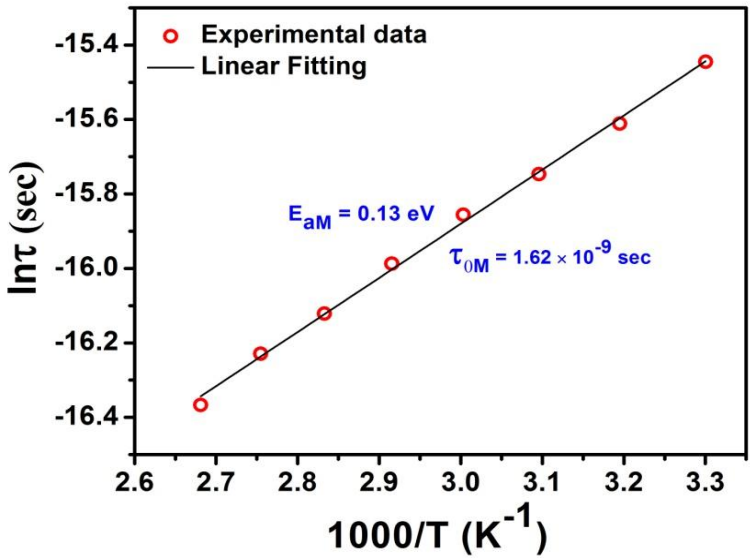

Figure 5.14: *Plot of* $\ln(\tau)$ *vs.* $1000/T$ *for p-TSA doped PPy nanofibers.*

The activation energy E_{aM} of relaxation process can be evaluated using the Arrhenius equation given below:

$$\tau = \tau_{0M} \exp\left(\frac{E_{aM}}{kT}\right) \tag{5.15}$$

where τ_{0M} is the pre-exponential factor that represents the higher temperature limit of relaxation time. The slope and intercept of the plot of $\ln(\tau)$ vs. $1000/T$ gives the value of τ_{0M} and E_{aM}, respectively. The experimental data are best fitted with Arrhenius equation (5.15) as shown in Fig. 5.14 and the calculated values of τ_{0M} and E_{aM} are found to be 1.62×10^{-9} sec and 0.13 eV, respectively.

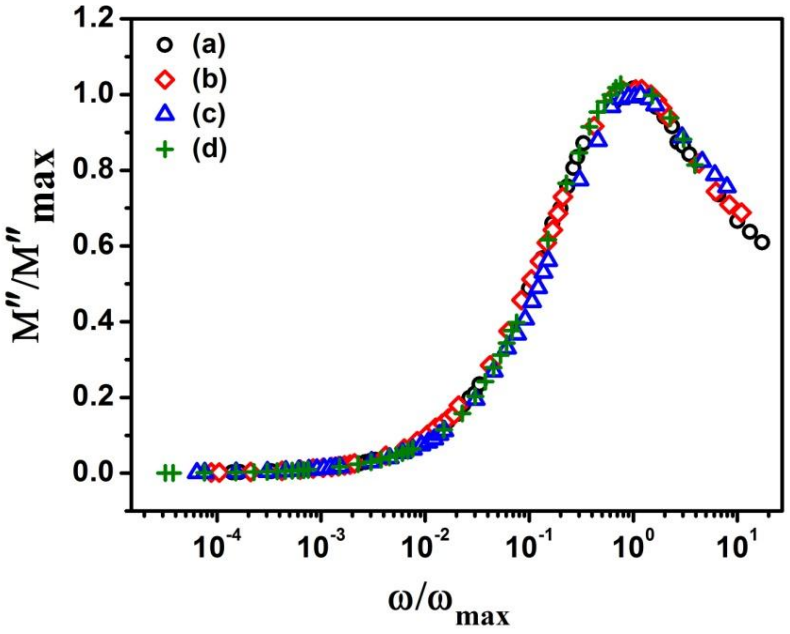

Figure 5.15: *Room temperature scaling plots of imaginary part of modulus* (M'') *of PPy nanofibers doped with (a) DBSA (b) OBSA (c) CSA and (d) p-TSA.*

The scaling behavior of modulus spectra is used to obtain better insight into the relaxation dynamics of charge carriers [333]. The imaginary part of modulus, M'' spectra are scaled by $M''_{\max}$ while the frequency axis is scaled by the relaxation frequency $\omega_{\max}$. The scaling plots of different ABSA doped PPy nanofibers at room temperature are shown in Fig. 5.15. The perfect overlap of all the individual M'' spectra onto a single master curve indicates that the conductivity relaxation process in PPy nanofibers is independent of the dopants. The scaling of M'' spectra can also be done at different temperatures. After scaling it is observed that all the individual M'' spectra at various temperatures fall onto a single master curve, which suggests the temperature independent relaxation dynamics of charge carriers.

5.1.8. AC conductivity studies

Fig. 5.16 depicts the frequency variation of total conductivity of different ABSA doped PPy nanofibers at room temperature (303 K). The measured total conductivity $\sigma'(\omega)$ can be expressed as:

$$\sigma'(\omega) = \sigma_{dc} + \sigma_{ac} \tag{5.16}$$

where σ_{dc} is the frequency independent or dc conductivity and σ_{ac} is the frequency dependent or ac conductivity. The general behavior of σ_{ac} can be described by the Jonscher relation [334],

$$\sigma_{ac} = A\omega^{s} \tag{5.17}$$

i. e. the ac conductivity is proportional to ω^{s}, where the value of frequency exponent *s* is less than unity and A is the temperature dependent pre-exponential factor. The particular frequency where the onset of ac conductivity takes place is known as the critical or hopping frequency ω_H that represents the change of conductivity mechanism from long range to the short range conduction [335].

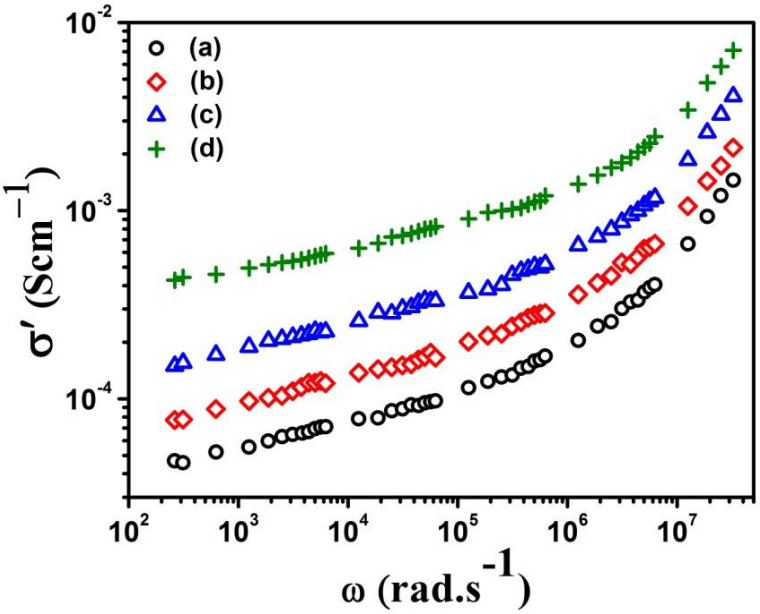

Figure 5.16: *Plots of total conductivity $\sigma'(\omega)$ vs. frequency (ω) of PPy nanofibers doped with (a) DBSA (b) OBSA (c) CSA and (d) p-TSA at room temperature (303 K).*

At low frequencies (< 10^4 Hz), the conductivity remains almost constant and corresponds to the dc conductivity. The random diffusion of free charge carriers via the

activated hopping gives rise to the dc conduction. Experimentally value of dc conductivity can be extracted from the frequency independent plateau by extrapolating the data to the static frequency [169]. At high frequencies (> 10^4 Hz), $\sigma'(\omega)$ corresponds to σ_{ac} and follows a universal power law $\sigma_{ac} = A\omega^s$ with $0 < s < 1$ characteristics of the disordered materials where the hopping of charge carriers takes place [172, 336]. At higher frequencies, probability of charge carriers to go to the other favourable sites and come back to the original site increases. This results in increase in the conductivity showing strong frequency dispersion. It is observed that the *p*-TSA doped PPy nanofibers exhibit higher conductivity than that of the other ABSA doped PPy nanofibers. The increase in conductivity is due to the generation of increased number of charge carriers (polarons) during the doping reaction in short alkyl chain *p*-TSA doped PPy nanofibers. Moreover, the hopping frequency ω_H is also dopant dependent. For *p*-TSA doped PPy nanofibers, hopping frequency shifts towards higher frequency suggesting higher contribution of dc conductivity than that for the other ABSA doped PPy nanofibers. The temperature dependence of total conductivity for a particular ABSA doped PPy nanofibers are shown in Fig. 5.17.

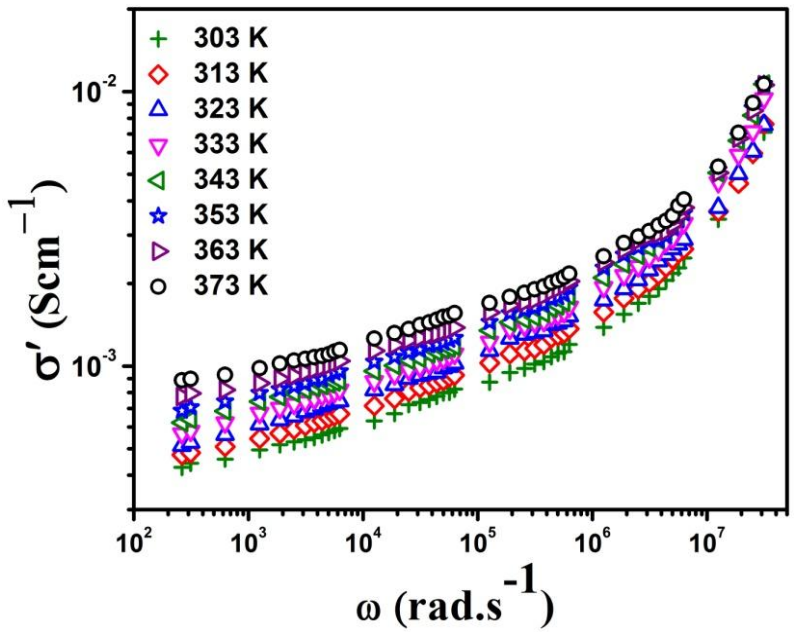

Figure 5.17: *Temperature dependence plots of total conductivity* $\sigma'(\omega)$ *vs. frequency* (ω) *of PPy nanofibers doped with p-TSA.*

It is observed that as the temperature is increased, the dc conductivity increases and a cross-over from the frequency independent to the frequency dependent regions mark the onset of the conductivity relaxation. Moreover hopping frequency ω_H shifts towards higher frequency with increasing temperature that also suggests the large contribution of dc conductivity with increasing temperature. The increase of σ_{dc} with increasing temperature is attributed to the increase in mobility of the free charge carriers.

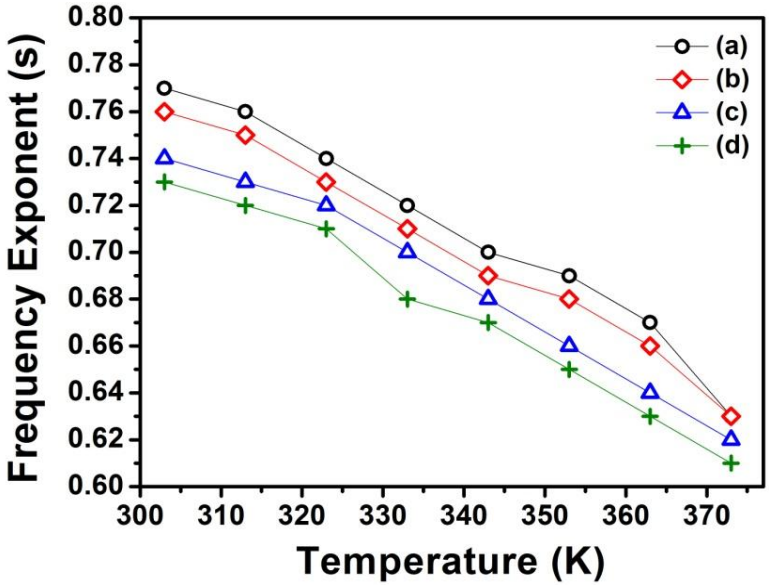

Figure 5.18: *Plots of frequency exponent (s) vs. temperature of PPy nanofibers doped with (a) DBSA (b) OBSA (c) CSA and (d) p-TSA.*

Further information regarding conductivity mechanism can be obtained by analyzing the temperature dependence of the frequency exponent *s*. The variation of frequency exponent *s* with temperature for different ABSA doped PPy nanofibers are shown in Fig. 5.18. The value of *s* decreases with increasing temperature, which reveals that the correlated barrier hopping (CBH) is the dominant charge transport mechanism in different ABSA doped PPy nanofibers, wherein the charge carriers can hop from one localized region to the other localized regions by overcoming the potential barrier. Pike [162] explains the temperature dependence of frequency exponent *s* by suggesting the following relation,

$$s = 1 - \frac{6kT}{W_H} \tag{5.18}$$

where W_H is the barrier activation energy for the charge carriers. The *p*-TSA doped PPy nanofibers exhibit small activation energy of 0.58 eV, while the DBSA doped PPy nanofibers possess higher activation energy of 0.68 eV. Due to small activation energy the charge carriers can easily hop from one localized site to the other localized sites in *p*-TSA doped PPy nanofibers resulting in higher electrical conductivity than that for the other ABSA doped PPy nanofibers. The calculated values of frequency exponent (*s*) and barrier activation energy (W_H) of PPy nanofibers doped with different ABSA at room temperature (303 K) are presented in Table 5.6.

Table 5.6: Values of frequency exponent (*s*) and barrier activation energy (W_H) of different ABSA doped PPy nanofibers at room temperature (303 K).

ABSA dopant	Frequency exponent, '*s*' at 303 K	Barrier activation energy, W_H (eV) at 303 K
DBSA	0.77	0.68
OBSA	0.76	0.65
CSA	0.74	0.60
p-TSA	0.73	0.58

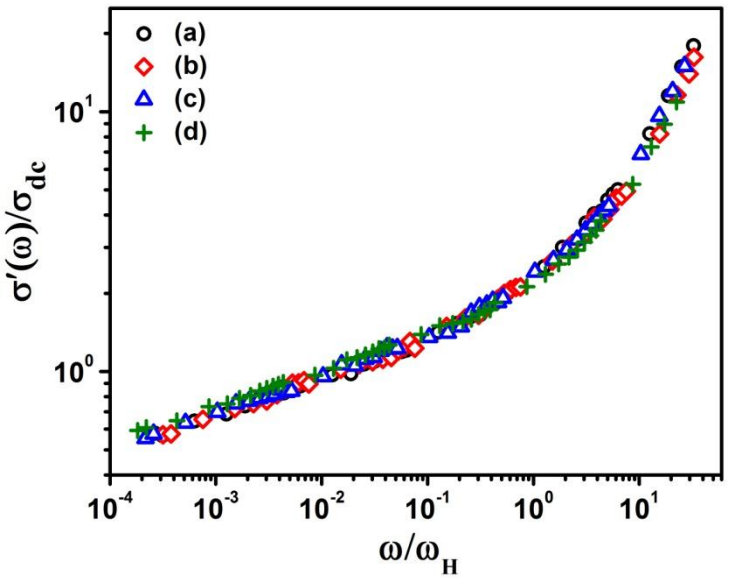

Figure 5.19: *Scaling plots of total conductivity spectra of PPy nanofibers doped with (a) DBSA (b) OBSA (c) CSA and (d) p-TSA at room temperature (303 K).*

The scaling behavior of conductivity spectra provides an insight into the charge carriers' dynamics. The scaling of the conductivity data is done using the procedure outlined elsewhere [337]. The room temperature scaling plots of different ABSA doped PPy nanofibers are shown in Fig. 5.19. The perfect overlap of all the individual conductivity spectra into a single master curve indicates that the charge transport in different alkylbenzenesulfonic acid doped PPy nanofibers is independent of dopant. Similar scaling behavior of conductivity spectra can also be obtained for different temperatures for different ABSA doped PPy nanofibers. These results suggest that the relaxation dynamics of charge carriers' in ABSA doped PPy nanofibers follow a common conduction mechanism at different temperatures for different dopants.

5.2. 160 MeV Ni^{12+} swift heavy ion irradiation effects on PPy nanofibers

The detailed results on different ABSA doped PPy nanofibers synthesized by interfacial polymerization method as discussed in Section 5.1 reveal that the sample of PPy nanofibers doped *p*-TSA has shown the best properties. Therefore this sample has been chosen to irradiate by 160 MeV Ni^{12+} swift heavy ions (SHI) with a view to further improve its different properties. For SHI irradiation, films of PPy nanofibers doped with *p*-TSA have been prepared by dissolving and ultra-sonicating the dried precipitate into 2 % of PVA (Polyvinyl alcohol) solution. The PVA (M_w = 145000) has been used as plasticizer for making films of PPy nanofibers for SHI irradiation purpose and the usage of PVA as plasticized did not affect significantly on the properties of PPy nanofibers. The SHI irradiation on PPy nanofibers was performed at the 15 UD Pelletron Accelerator available at the Inter University Accelerator Centre (IUAC), New Delhi, India using the Materials Science beam line facilities. Five different ion fluences of 10^{10}, 5×10^{10}, 10^{11}, 5×10^{11} and 10^{12} ions/cm^2 were used to irradiated the films of PPy nanofibers keeping the ion current constant at 0.5 pna (particle nano-ampere). The energy of the Ni^{12+} ion beam was chosen as 160 MeV so that the ion beam completely penetrated the polymer films to undergo uniform irradiation effects as the projected ion range of 42 μm, as calculated by using SRIM (stopping and range of ions in matter)

software [286], was larger than the thickness (~30-35 μm) of the films. The results on the effects of swift heavy ions have been discussed under the following sections.

5.2.1. High resolution transmission electron microscopy studies

Fig. 5.20 shows the HRTEM micrographs for pristine and irradiated PPy nanofibers at different irradiation fluences. It is observed that the pristine PPy nanofibers are uniform nanofibers with average diameter of 13 nm and length of the nanofibers are in the micrometer scale. It is observed that the SHI irradiation does not affect the diameter and length of the pristine PPy nanofibers, while the PPy nanofibers become dense after SHI irradiation and density increases with increasing the irradiation fluence. This may be attributed to the cross-linking of PPy chains upon SHI irradiation due to generation of free radicals and formation of bonds between adjacent chains in PPy nanofibers.

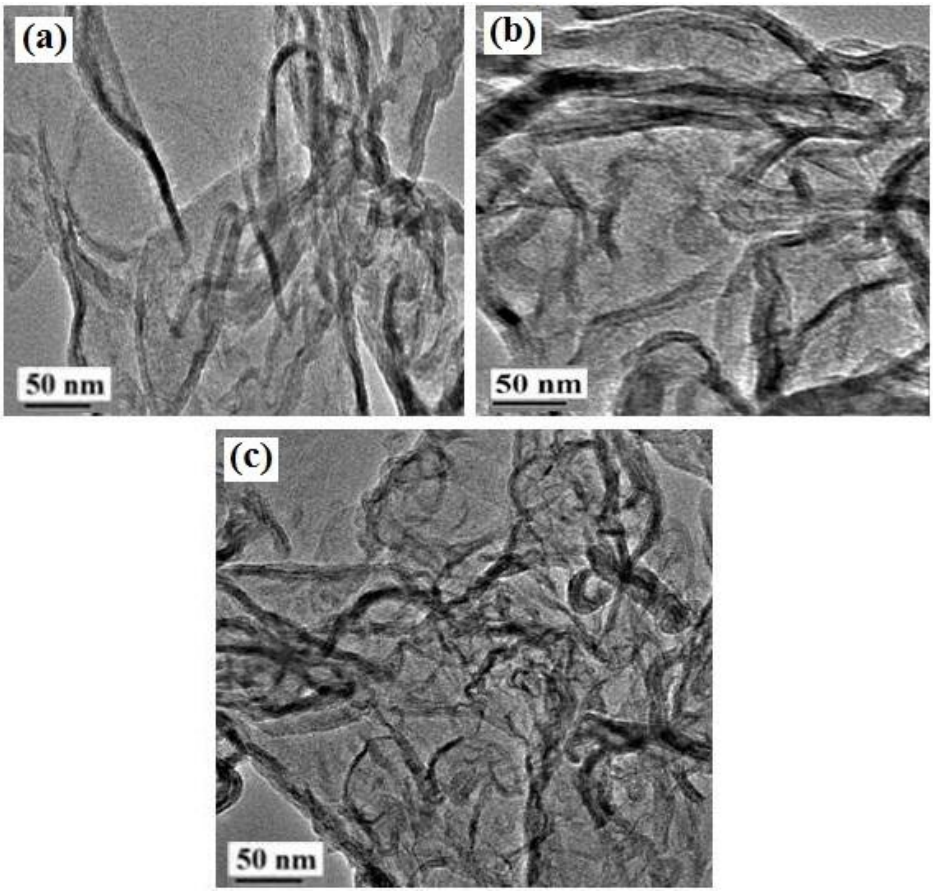

Figure 5.20: *HRTEM micrographs for (a) pristine and irradiated PPy nanofibers at irradiation fluences of (b) 5×10^{10} (c) 10^{12} ions/cm^2.*

5.2.2. X-ray diffraction studies

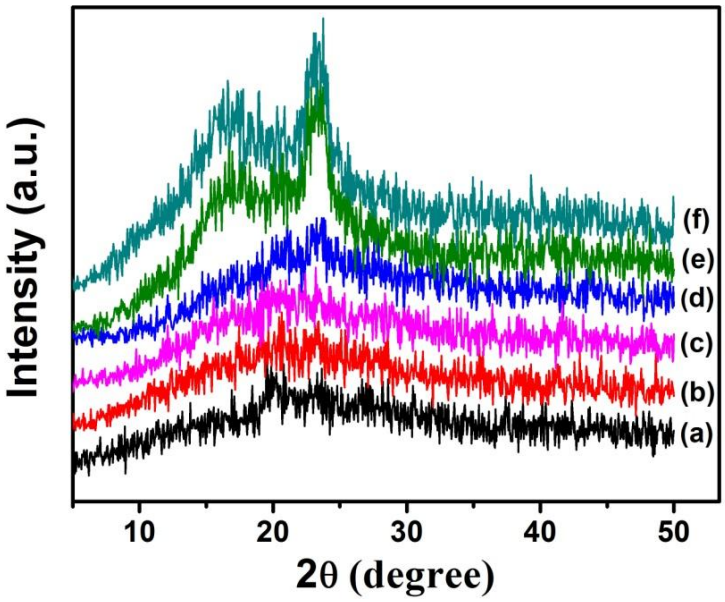

Figure 5.21: *XRD patterns of (a) pristine and irradiated PPy nanofibers at ion fluences of (b) 10^{10} (c) 5×10^{10} (d) 10^{11} (e) 5×10^{11} and (f) 10^{12} ions/cm^2.*

The XRD diffraction patterns of pristine and irradiated PPy nanofibers at ion fluences of 10^{10}, 5×10^{10}, 10^{11}, 5×10^{11} and 10^{12} ions/cm^2 are depicted in Fig. 5.21. A characteristic broad diffraction peak at $2\theta = 22^{o}$ occurs for pristine PPy nanofibers. Upon SHI irradiation position of the diffraction peak changes slightly, while the intensity increases with increasing irradiation fluence. The alignment of the PPy nanofibers chains by chain folding or formation of single or multiple helices along the ion track due to electronic energy deposition upon SHI irradiation leads to the enhancement in crystallinity of the irradiated PPy nanofibers as compared to that in the pristine sample. Moreover, at higher irradiation fluences (5×10^{11}-10^{12} ions/cm^2), the diffraction peak shifts to slightly higher angular position $2\theta = 23.10^{o}$ and intensity of this diffraction peak increases sharply as compared to pristine PPy nanofibers indicating that PPy nanofibers have highly crystalline structure after SHI irradiation. Also, at higher ion fluences (5×10^{11} -10^{12} ions/cm^2), a new diffraction peak appears at $2\theta = 17^{o}$ which reveals the formation of new crystalline regions in SHI irradiated PPy nanofibers. The increase in crystallinity upon SHI irradiation provides easy conduction path for charge carriers giving rise to the increase in electrical conduction in SHI irradiated PPy nanofibers [338].

Moreover, density of SHI irradiated PPy nanofibers increases after SHI irradiation that makes the PPy nanofibers more compact and as a result produces closely packed regions by chain folding, cross-linking of the polymer chains due to the high deposition of electronic energy along their trajectories. The interplanar spacing (*d*) and hopping distance (*R*) of the pristine and irradiated PPy nanofibers have been calculated using equations (5.2)

$$2d\sin\theta = \lambda$$

and (5.3),

$$R = \frac{5}{8}\left[\frac{\lambda}{\sin\theta}\right]$$

respectively as discussed in section 5.1. Upon SHI irradiation, the *d*-spacing of PPy nanofibers decreases as compared to that of the pristine PPy nanofibers. The decrease in *d*-spacing upon SHI irradiation can facilitate easy hopping of charge carriers, which can leads to higher electrical conductivity in the irradiated PPy nanofibers. The calculated values of diffraction peak (2θ), chain ordering (X_C), interplanar spacing (*d*) and hopping distance (*R*) of pristine and irradiated PPy nanofibers at different ion fluences are presented in Table 5.7.

Table 5.7: Values of diffraction peak (2θ), chain ordering (X_C), interplanar spacing (d) and hopping distance (*R*) of pristine and irradiated PPy nanofibers at ion fluences of 10^{10}, 5×10^{10}, 10^{11}, 5×10^{11} and 10^{12} ions/cm^2.

Fluence (ions/cm^2)	Diffraction peak, 2θ (degree)		Chain ordering, X_C (%)			Interplanar spacing, *d* (Å)		Hopping distance, *R* (Å)	
	$2\theta_1$	$2\theta_2$	X_{C1}	X_{C2}	X_C	d_1	d_2	R_1	R_2
Pristine	---	22	---	22.50	22.50	---	4.07	---	5.04
1×10^{10}	---	22	---	22.80	22.80	---	4.07	---	5.04
5×10^{10}	---	22	---	23.30	23.30	---	4.07	---	5.04
1×10^{11}	---	23	---	25.00	25.00	---	3.86	---	4.83
5×10^{11}	17	23.10	10.50	27.78	38.28	5.21	3.84	6.51	4.80
1×10^{12}	17	23.10	12.00	28.30	40.30	5.21	3.84	6.51	4.80

N. B.: $2\theta_1$: broad diffraction peak at lower angle, $2\theta_2$: broad diffraction peak at higher angle, X_{C1}: chain ordering corresponding to diffraction peak at $2\theta_1$, X_{C2}: chain ordering corresponding to diffraction peak at $2\theta_2$, d_1: interplanar spacing due to $2\theta_1$, d_2: interplanar spacing due to $2\theta_2$, R_1: hopping distance due to $2\theta_1$, R_2: hopping distance due to $2\theta_2$.

5.2.3. Fourier transform infrared spectroscopy analysis

The chemical modification of PPy nanofibers under SHI irradiation can be studied using FTIR spectroscopy. The relative changes in the vibrational bands have been estimated from the relative increase or decrease in the intensity of the bands associated with the functional groups present in PPy nanofibers. The FTIR spectra of pristine and irradiated PPy nanofibers at ion fluences of 10^{10}, 5×10^{10}, 10^{11}, 5×10^{11} and 10^{12} ions/cm^2 are shown in Fig. 5.22.

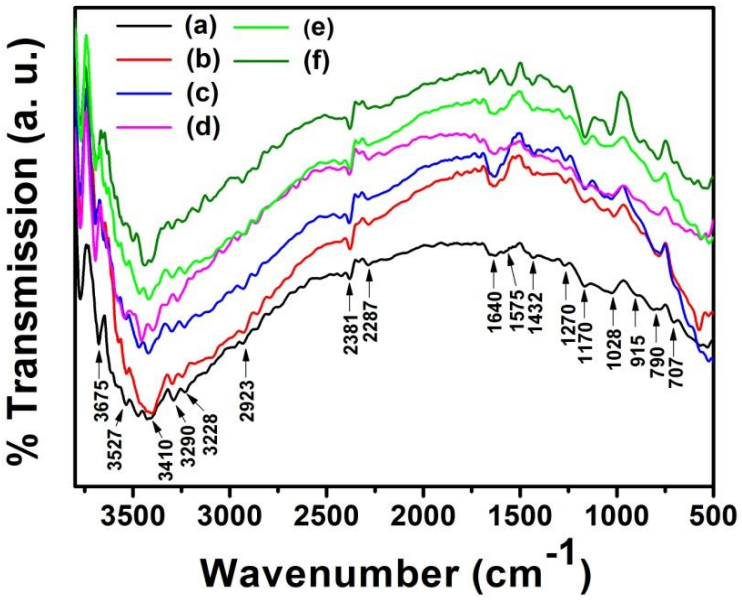

Figure 5.22: *FTIR spectra of (a) pristine and irradiated PPy nanofibers at ion fluences of (b) 10^{10}, (c) 5×10^{10}, (d) 10^{11}, (e) 5×10^{11}, and (f) 10^{12} ions/cm^2.*

The FTIR spectra upon SHI irradiation show an overall increase in intensity of some of the characteristic vibration bands of pristine PPy nanofibers. With increasing the irradiation fluence the intensity of the vibration bands at 1575, 1170 and 1028 cm^{-1} increase as compared to pristine PPy nanofibers. However the vibration band at 1575 cm^{-1} corresponding to C=C stretching vibration in pristine PPy nanofibers shifts to 1554 cm^{-1} at the highest ion fluence of 10^{12} ions/cm^2 and the large increase in intensity of this

vibration band suggests the formation of conjugated C=C bonds after SHI irradiation. Also, the increase in the band intensity at 1170 and 1028 cm^{-1} after SHI irradiation suggests the formation of C-C and C-H groups. The formation of the different functional groups such as C=C, C-C, C-H etc. upon SHI irradiation suggests that the dominant mechanism in the irradiated PPy nanofibers is the cross-linking, which is also corroborated from the UV-vis studies. SHI irradiation deposits tremendous amount of energy in the cylindrical ion track of few nanometer diameter within an extremely short interval of time of about 10^{-15} s generating huge number of radical pairs on adjacent polymer chains within the track radius leading to the cross-linking of the polymer chains. In general, the energy density of the ion track is several KeV/nm^3 and considering that the energy of carbon bonds is of few eV, this high energy deposition is sufficient to break the chemical bonds and reorganise themselves within the ion track core of polymer materials. Furthermore the increase of particular vibration bands intensity reveals the enhancement of crystallinity of PPy nanofibers upon SHI irradiation which is corroborated with the XRD results.

5.2.4. UV-visible absorption spectroscopy studies

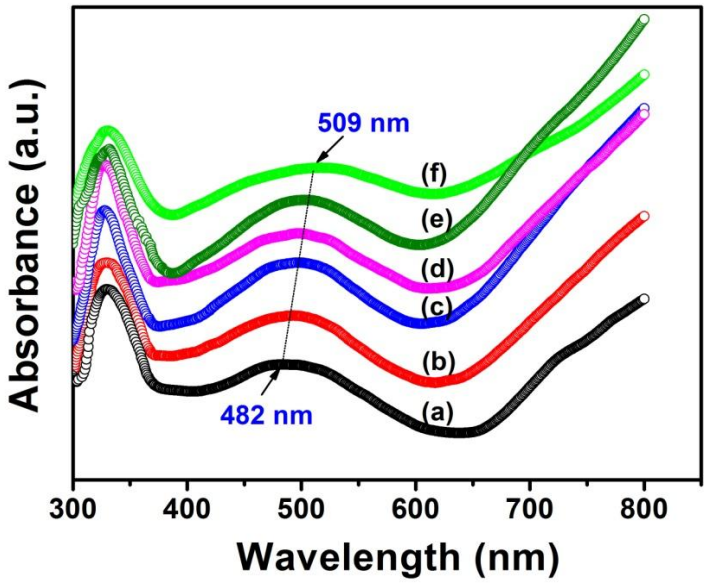

Figure 5.23: *UV-vis absorption spectra of (a) pristine and irradiated PPy nanofibers at ion fluences of (b) 10^{10}, (c) 5×10^{10}, (d) 10^{11}, (e) 5×10^{11} and (f) 10^{12} ions/cm^2.*

The UV-vis absorption spectra of pristine and irradiated PPy nanofibers at ion fluences of 10^{10}, 5×10^{10}, 10^{11}, 5×10^{11} and 10^{12} ions/cm^2 are depicted in Fig. 5.23. The absorption spectra reveal a strong absorption band at 330 nm for both pristine and irradiated PPy nanofibers which can be assigned to the interband π-π^* transition. For pristine PPy nanofibers the second absorption band appears at about 482 nm which is attributed to the transition from valence band to the polaron band and a free tail above 680 nm is attributed to the transition from the valence band to the bipolaron band or anti-bipolaron states of oxidized PPy nanofibers. It is observed that the polaron absorption band in PPy nanofibers after SHI irradiation makes a red shift which is highest for PPy nanofibers irradiated at the ion fluence of 10^{12} ions/cm^2. In the irradiated polymers, the processes of ionization and electronic excitation are considered to give rise to the chain scissioning and cross-linking. Cross-linking occurs when two free dangling ions or radical pairs on neighbouring chain join to form a bond, whereas double or triple bonds are formed if two neighbouring radicals in the same chain unite. Thus the breaking of atomic bonds and the rearrangement of polymer chains around the ion trajectory result in lattice deformation along the path of the ion. The red shifting of the polaron absorption band with increasing irradiation fluence can be attributed to the formation of the conjugated systems of carbon bonds as a consequence of bond breaking and reconstruction (cross-linking) of the polymer chains induced by SHI irradiation which leads to the formation of carbon clusters. SHI irradiation induces the cleavage of C-C bonds and dehydrogenation of the polymer chains i.e. evolution of hydrogen atoms from the adjacent chains leading to the formation of conjugated -C=C- bonds due to cross-linking. During SHI irradiation the polymeric material gradually loses gas atoms and enrichment of carbon atoms leads to the formation of a hydrogenated amorphous carbon with optical band gap depending on the H/C atom ratio [339]. It is known that both pristine and irradiated PPy nanofibers obey the rule of direct and indirect band transition. In direct transition the electron is simply transferred vertically from top of the valence band to the bottom of the conduction band with changing the momentum [340]. However in case of indirect transition the irradiation produces species (band rapture, free radicals etc.) which increases the electronic disorder thereby creating permitted state in the forbidden band or deformation of the valence band [341].

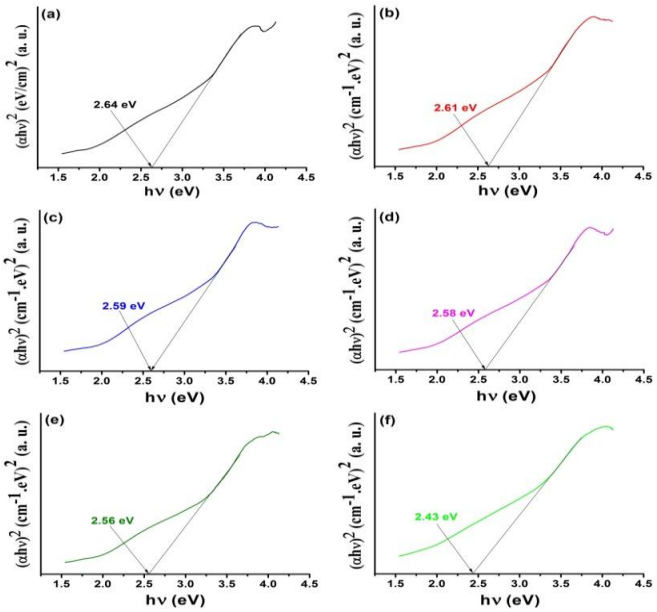

Figure 5.24: *Plots of* $(\alpha h\nu)^2$ *vs.* $h\nu$ *of (a) pristine and irradiated PPy nanofibers at ion fluences of (b)* 10^{10}*, (c)* 5×10^{10}*, (d)* 10^{11}*, (e)* 5×10^{11} *and (f)* 10^{12} *ions/cm*^{2}.

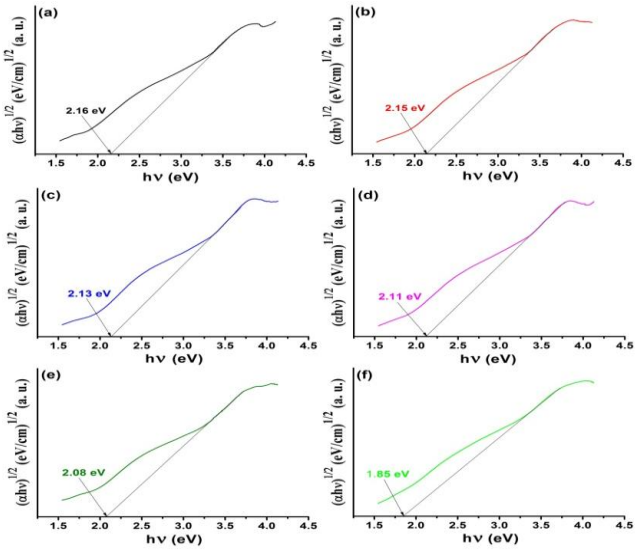

Figure 5.25: *Plots of* $(\alpha h\nu)^{1/2}$ *vs.* $h\nu$ *of (a) pristine and irradiated PPy nanofibers at ion fluences of (b)* 10^{10}*, (c)* 5×10^{10}*, (d)* 10^{11}*, (e)* 5×10^{11} *and (f)* 10^{12} *ions/cm*^{2}.

Figs. 5.24 and 5.25 show the variation of $(\alpha h\nu)^2$ vs. $h\nu$ and $(\alpha h\nu)^{1/2}$ vs. $h\nu$ for both pristine and irradiated PPy nanofibers at different ion fluences. The calculated direct and indirect optical band gap energies of pristine and irradiated PPy nanofibers at different ion fluences are presented in Table 5.8. The calculation of optical band gap energy depicts that both direct and indirect optical band gap energy of the SHI irradiated PPy nanofibers decrease as compared to that of the pristine PPy nanofibers.

Furthermore, value of indirect band gap energy is found to be lower than that of their corresponding direct band gap of pristine as well as irradiated PPy nanofibers. For a linear structure the number of carbon atoms per conjugation length (N) is correlated to the optical band gap energy E_g and is given by the following formula [293],

$$N = \frac{2\beta\pi}{E_g} \tag{5.19}$$

where 2β gives the band structure energy for a pair of adjacent π sites. The value of β is taken to be -2.9 eV which is associated with the π-π* optical transition in -C=C- structure. The calculated number of carbon atoms per conjugation length (N) for pristine and irradiated PPy nanofibers are recorded in Table 5.8.

Table 5.8: Optical band gap energy (E_g), number of carbon atoms per conjugation length (N) and number of carbon atoms per cluster (M) of the pristine and irradiated PPy nanofibers at ion fluences of 10^{10}, 5×10^{10}, 10^{11}, 5×10^{11} and 10^{12} ions/cm^2.

Fluence (ions/cm^2)	Band gap energy, E_g (eV)		Number of carbon atoms per conjugation length (N)		Number of carbon atoms per cluster (M)	
	direct	indirect	direct	indirect	direct	indirect
Pristine	2.64 ±0.002	2.16 ±0.002	~ 6.90 ±0.002	~ 8.43 ±0.002	~ 168.79 ±0.002	~ 252.47 ±0.002
1×10^{10}	2.61 ±0.003	2.15 ±0.003	~ 6.98 ±0.003	~ 8.47 ±0.003	~ 172.76 ±0.003	~ 254.65 ±0.003
5×10^{10}	2.59 ±0.002	2.13 ±0.002	~ 7.03 ±0.002	~ 8.55 ±0.002	~ 175.60 ±0.002	~ 259.14 ±0.002
1×10^{11}	2.58 ±0.001	2.11 ±0.001	~ 7.05 ±0.001	~ 8.63 ±0.001	~ 176.65 ±0.001	~ 264.38 ±0.001
5×10^{11}	2.56 ±0.003	2.08 ±0.003	~ 7.11 ±0.003	~ 8.75 ±0.003	~ 179.62 ±0.003	~ 272.34 ±0.003
1×10^{12}	2.43 ±0.002	1.85 ±0.002	~ 7.49 ±0.002	~ 9.84 ±0.002	~ 199.40 ±0.002	~ 344.00 ±0.002

It is observed that value of N increases with increasing ion fluence and for PPy nanofibers irradiated at the ion fluence of 10^{12} ions/cm^2, the number of carbon atoms per conjugation length is more than that of the others. Furthermore, the number of carbon atoms per conjugation length (N) involved in the indirect transition of both pristine and irradiated PPy nanofibers is higher than that in direct band transition. Also, the number of carbon hexagon rings (R) in the cluster can be calculated from the Robertson's relation [342],

$$E_g \approx \frac{2|\beta|}{\sqrt{R}} \tag{5.20}$$

where 2β is the band structure energy for a pair of adjacent π sites and the value of β is taken to be -2.9 eV for a six-membered carbon ring. Fink *et al.* [343] reported that the Robertson equation (5.19) underestimate the cluster size in irradiated polymers and they considered the structure of cluster to be like a buckminsterfullerence, i.e. a C_{60} ring instead of C_6 arriving at the following relation:

$$E_g \approx \frac{34.3}{\sqrt{M}} \tag{5.21}$$

The number of carbon atoms per cluster (M) of both pristine and irradiated PPy nanofibers is presented in the above Table 5.8. It is also observed that the number of carbon atoms per cluster (M) in PPy nanofibers increases after SHI irradiation.

5.2.5. Thermogravimetric analysis

The TGA thermographs of pristine and irradiated PPy nanofibers at ion fluences of 10^{10}, 5×10^{10}, 10^{11}, 5×10^{11} and 10^{12} ions/cm^2 are depicted in Fig. 5.26. It is observed that all the thermographs show three stage weight loss patterns. The first weight loss of both pristine and irradiated PPy nanofibers begins at room temperature and continues to 180 °C which can be attributed to the evaporation of moistures and other volatiles present in the samples. The second weight loss occurs in the temperature region of 210-330 °C which can be ascribed to the removal of dopant molecules (*p*-TSA anions) from the PPy nanofibers chains. The third and final weight loss occurs above 330-500 °C, which is attributed to the complete degradation or decomposition of the PPy nanofibers chains. It is observed that the degradation temperature of PPy nanofibers upon SHI irradiation is enhanced and increases with increasing the irradiation fluence. The degradation

temperature of pristine and irradiated PPy nanofibers at different percentage weight losses is calculated and is presented in Table 5.9. The degradation temperature at any percentage weight loss is found to increase with increasing the irradiation fluence form 10^{10} ions/cm^2 to 10^{12} ions/cm^2 as compared to the pristine sample, which is a direct evidence of improvement of thermal stability of PPy nanofibers after SHI irradiation.

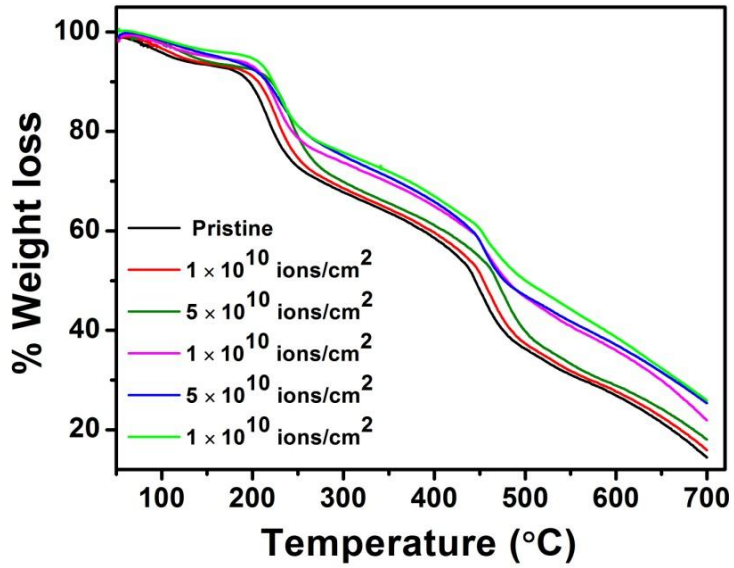

Figure 5.26: *TGA thermographs of pristine and irradiated PPy nanofibers at different ion fluences.*

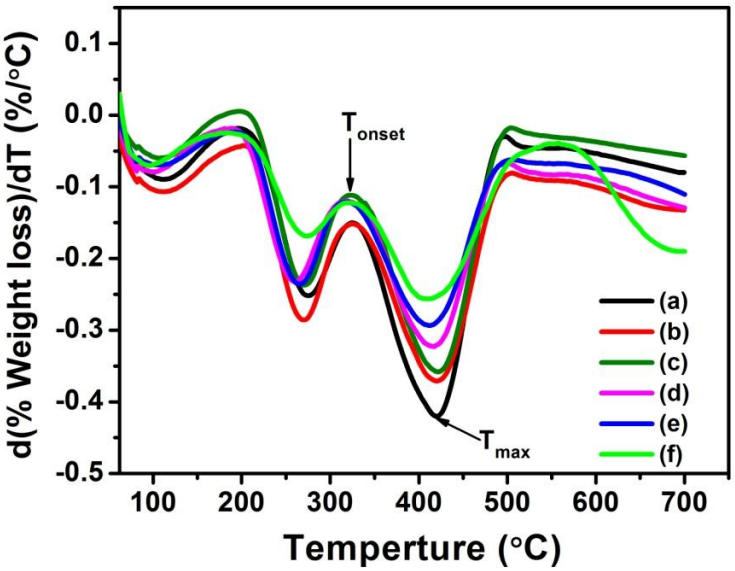

Figure 5.27: *Derivative plots of TGA thermographs for (a) pristine and irradiated PPy nanofibers at irradiation fluences of (b) 10^{10}, (c) 5×10^{10}, (d) 10^{11}, (e) 5×10^{11} and (e) 10^{12} ions/cm^2, respectively.*

Fig. 5.27 shows the derivative plots of TGA thermographs for pristine and irradiated PPy nanofibers at different irradiation fluences. As the negative sign of the derivatives represents the decomposition and weight loss of the sample, only the numerical (without minus sign) values of the derivatives are considered for analysis. The rate of decomposition (as observed from Fig. 5.27) for the pristine and irradiated PPy nanofibers at different irradiation fluences are presented in Table 5.9. The onset decomposition temperature (T_{onset}= 323°C) and maximum decomposition temperature (T_m= 420 °C) do not change significantly for different SHI irradiation fluences. However, the rate of maximum decomposition $(dW/dT)_m$ significantly decreases with increasing irradiation fluence upon SHI irradiation as compared to that of the pristine PPy nanofibers. Table 5.9 shows that $(dW/dT)_m$ is $|0.421|$ %/°C for the pristine PPy nanofibers, whereas it decreases to $|0.255|$ %/°C for the irradiated PPy nanofibers with fluence 10^{12} ions/cm^2. The decrease in decomposition rate with increasing fluence indicates the enhancement in thermal stability of the irradiated PPy nanofibers upon SHI irradiation, which increases with increasing irradiation fluence.

Table 5.9: Degradation temperature at different percentage weight losses and maximum decomposition rate, $(dW/dT)_m$ for pristine and irradiated PPy nanofibers at different ion fluences.

Fluence (ions/cm^2)	Degradation temperature (°C) at different percentage (%) weight losses							Maximum decomposition rate, $(dW/dT)_m$ (%/°C)
	10 %	**20 %**	**30 %**	**40 %**	**50 %**	**60 %**	**70 %**	
Pristine	195	220	273	383	444	473	562	$\|0.421\|$
1×10^{10}	201	232	279	395	454	481	565	$\|0.369\|$
5×10^{10}	211	242	296	408	468	496	576	$\|0.356\|$
1×10^{11}	211	242	346	438	475	557	649	$\|0.321\|$
5×10^{11}	211	257	352	438	475	569	661	$\|0.290\|$
1×10^{12}	220	257	366	449	498	583	662	$\|0.255\|$

5.2.6. Dielectric permittivity studies

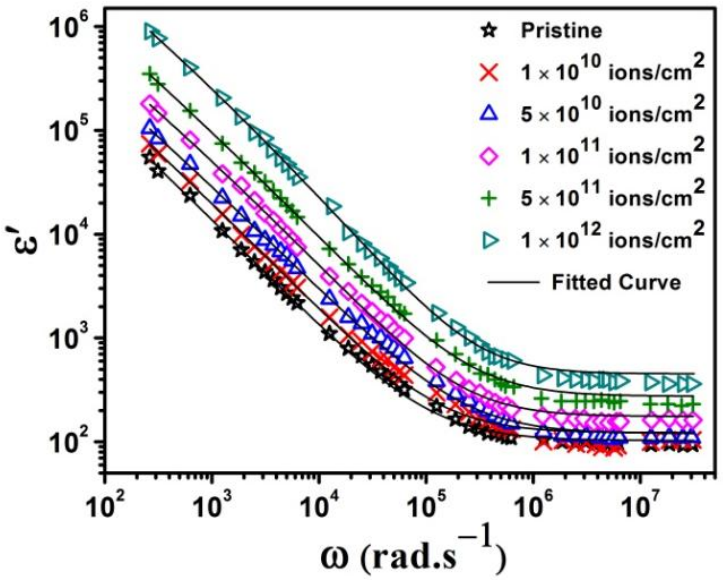

Figure 5.28: *Plots of dielectric permittivity* (ε') *vs. frequency* (ω) *of both pristine and irradiated PPy nanofibers at different ion fluences at room temperature (303 K).*

Fig. 5.28 depicts the plots of dielectric permittivity (ε') vs. frequency (ω) of both pristine and irradiated PPy nanofibers at irradiation fluences of 10^{10}, 5×10^{10}, 10^{11}, 5×10^{11} and 10^{12} ions/cm^2 at room temperature (303 K). The dielectric permittivity (ε') of SHI irradiated PPy nanofibers is higher as compared to the pristine PPy nanofibers and its value increases with increasing the irradiation fluence. In lower frequencies, ε' decreases with increasing frequency and at higher frequencies, ε' attains a constant value. The higher value of ε' at lower frequencies is attributed to the electrode polarization effects [344]. The increase in the value of ε' with increasing irradiation fluence can be attributed to the increase contribution of electrode polarization after SHI irradiation on PPy nanofibers due to the generation of large number of charge carriers.

Fig. 5.29 depicts the room temperature plots of dielectric loss (ε'') vs. frequency (ω) of both pristine and irradiated PPy nanofibers at the ion fluences of 10^{10}, 5×10^{10}, 10^{11}, 5×10^{11} and 10^{12} ions/cm^2. The linear increase in ε'' with decreasing frequency reveals that the dc conduction loss is more prominent over the polarization effect. However at a particular frequency, value of ε'' increases with increasing irradiation fluence which can be attributed to increased dc conduction in PPy nanofibers as a result of generation of more number of free charge carriers due to large electronic energy deposition.

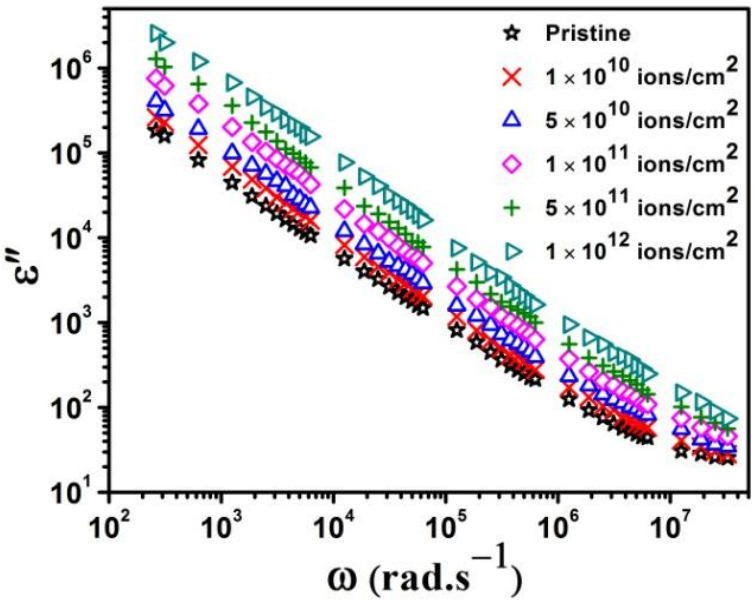

Figure 5.29: *Plots of dielectric loss* (ε'') *vs. frequency* (ω) *of both pristine and irradiated PPy nanofibers at different ion fluences at room temperature (303 K).*

5.2.7. Electric modulus studies

Fig. 5.30 depicts the plots of real part of modulus (M') vs. frequency (ω) of pristine and irradiated PPy nanofibers at different ion fluences at room temperature. It is observed that the M' spectrum of both pristine and irradiated PPy nanofibers shows sigmoid type behavior i.e. value of M' increases with increasing frequency and reaches a constant maximum value in higher frequencies. For both the pristine and irradiated PPy nanofibers, at lower frequencies ($\leq 10^4$ Hz) the values of M' approach to zero indicating the suppression of electrode polarization effects [296]. In the intermediate frequency range, the values of M' increase with increasing frequency, which suggests that the conduction process is due to the long range motion of charge carriers. At higher frequencies ($\geq 10^7$ Hz), M' attains a constant maximum value of M_∞ suggesting that conduction at higher frequencies involves the short range motion of charge carriers [297]. More information about the conductivity relaxation in SHI irradiated PPy nanofibers can be obtained by studying the M'' plots as function of frequency and temperature. Fig. 5.31 shows the plots of imaginary part of modulus (M'') vs. frequency (ω) of pristine and irradiated PPy nanoparticles at different ion fluences at room temperature (303 K). The appearance of a relaxation peak in each M'' spectrum

of both pristine and irradiated PPy nanofibers indicates the transition of charge carriers' motion from long range to short range with increasing frequency. However, the presence of asymmetric relaxation peak indicates the non-Debye relaxation mechanism of charge carriers in both the pristine and SHI irradiated PPy nanofibers.

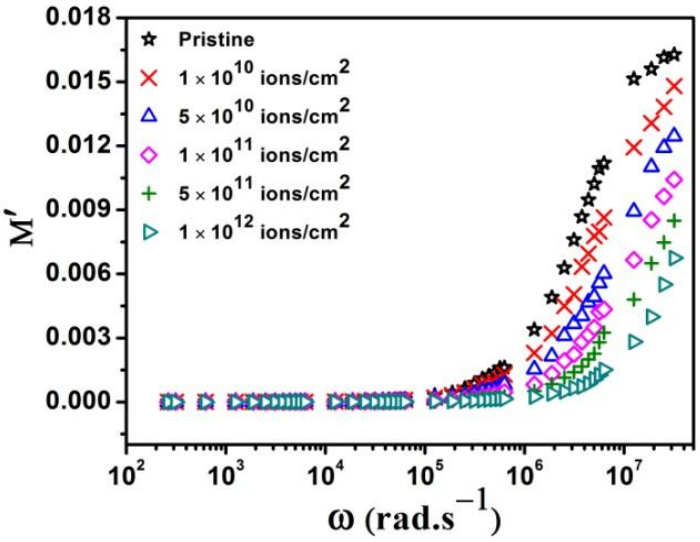

Figure 5.30: *Plots of real part of modulus* (M') *vs. frequency* (ω) *of pristine and irradiated PPy nanofibers at different ion fluences at room temperature (303 K).*

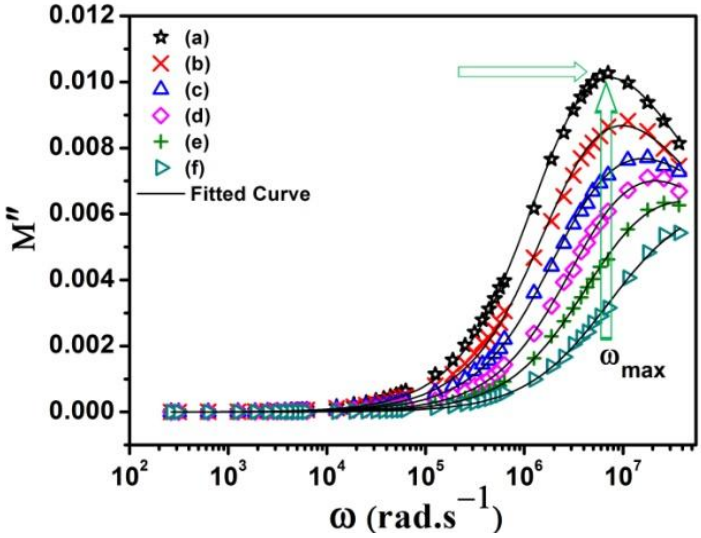

Figure 5.31: *Room temperature (303 K) plots of imaginary part of modulus* (M'') *vs. frequency* (ω) *of (a) pristine and irradiated PPy nanofibers at ion fluences of (b)* 10^{10}*, (c)* 5×10^{10}*, (d)* 10^{11}*, (e)* 5×10^{11} *and (f)* 10^{12} *ions/cm*^{2}*, respectively.*

Upon SHI irradiation the relaxation peak shifts towards higher frequencies with increasing the irradiation fluences which indicates increase in long range motion of

charge carriers in SHI irradiated PPy nanofibers. As a result the relaxation time (τ) of charge carriers' motion in SHI irradiated PPy nanofibers decreases with increasing the irradiation fluences. The calculated relaxation frequency (ω) and relaxation time (τ) for charge carriers in both pristine and irradiated PPy nanofibers are recorded in Table 5.10.

Table 5.10: Relaxation frequency (ω) and relaxation time (τ) for charge carriers in both pristine and irradiated PPy nanofibers at different ion fluences.

Fluence (ions/cm^2)	Relaxation frequency, ω_{max} (rad.s^{-1})	Relaxation time, τ (s)
Pristine	6.67×10^{6}	1.49×10^{-7}
1×10^{10}	8.75×10^{6}	1.14×10^{-7}
5×10^{10}	14.30×10^{6}	6.99×10^{-8}
1×10^{11}	19.78×10^{6}	5.05×10^{-8}
5×10^{11}	30.57×10^{6}	3.27×10^{-8}
1×10^{12}	---	---

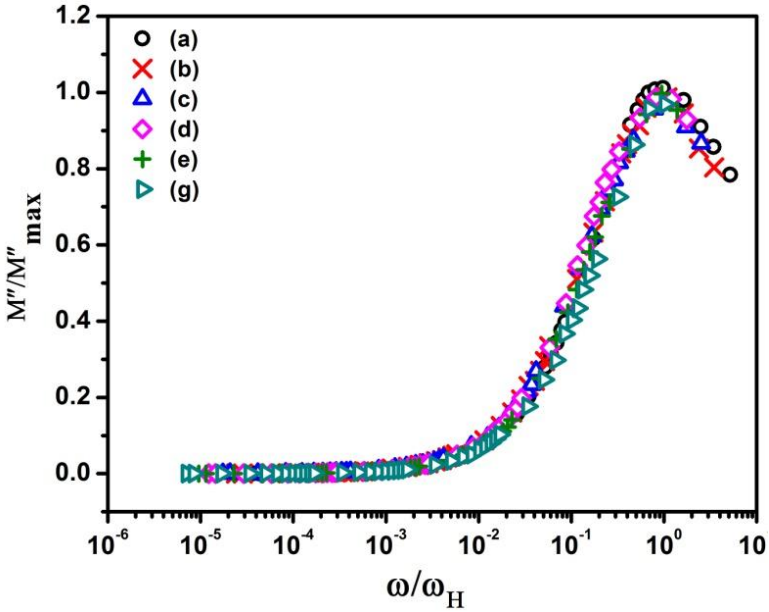

Figure 5.32: *Room temperature (303 K) scaling plots of M'' spectra of (a) pristine and irradiated PPy nanofibers at ion fluences of (b) 10^{10}, (c) 5×10^{10}, (d) 10^{11}, (e) 5×10^{11} and (f) 10^{12} ions/cm^2, respectively.*

The scaling behavior of modulus spectra provides an insight into the irradiation fluence dependence of relaxation dynamics of charge carriers in irradiated PPy nanofibers. The scaling plots of M'' spectra of the pristine and irradiated PPy nanofibers at room temperature (303 K) are shown in Fig. 5.32. The scaling is done by dividing M'' with $M''_{\max}$, while the frequency axis is scaled by the relaxation frequency $(\omega_{\max})$. The M'' spectra of the pristine and irradiated PPy nanofibers at different ion fluences merge on a single master curve which indicates that the relaxation dynamics of charge carriers in SHI irradiated PPy nanofibers are independent of the ion fluence.

5.2.8. AC conductivity studies

Fig. 5.33 depicts the variation of total conductivity $\sigma'(\omega)$ with frequency ω of pristine and irradiated PPy nanofibers at room temperature (303 K). The total ac conductivity plots of pristine as well as irradiated PPy nanofibers exhibit a frequency independent plateau in the lower frequencies and show a dispersive behavior at the higher frequency regions. Hence the frequency independent plateau of the total ac conductivity curve corresponds to the dc conductivity σ_{dc} and frequency dependent conductivity at the high frequency domain represents the ac conductivity $\sigma_{ac}(\omega)$ which follows an universal power law, $\sigma_{ac}(\omega) = A\omega^{s}$ where A is the pre-exponential factor that depends only on temperature not on frequency and *s* is the frequency exponent that lies between 0 and 1. Upon SHI irradiation, the onset of the conductivity relaxation, which represents the transformation from frequency-independent to the frequency-dependent conductivity, shifts towards the higher frequency in the irradiated PPy nanofibers. Moreover, the shift to higher frequency increases with increasing the irradiation fluence. Furthermore, upon SHI irradiation the ac conductivity of PPy nanofibers increases as compared to the pristine PPy nanofibers and the increase in conductivity can be attributed to the formation of defects (free radicals, unsaturations, carbon clusters etc.) besides formation of the conjugated double bonds.

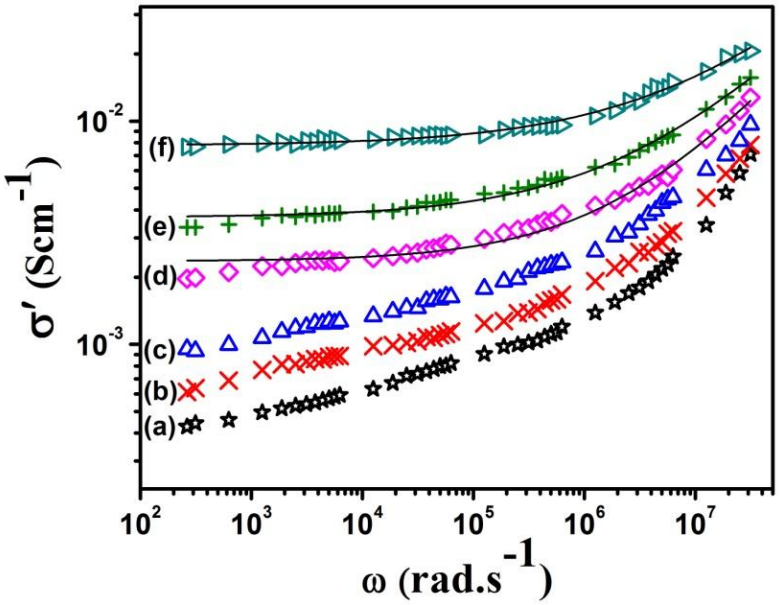

Figure 5.33: *Plots of total conductivity (σ') of (a) pristine and irradiated PPy nanofibers at ion fluences of (b) 10^{10}, (c) 5×10^{10}, (d) 10^{11}, (e) 5×10^{11} and (f) 10^{12} ions/cm^2 at room temperature (303 K).*

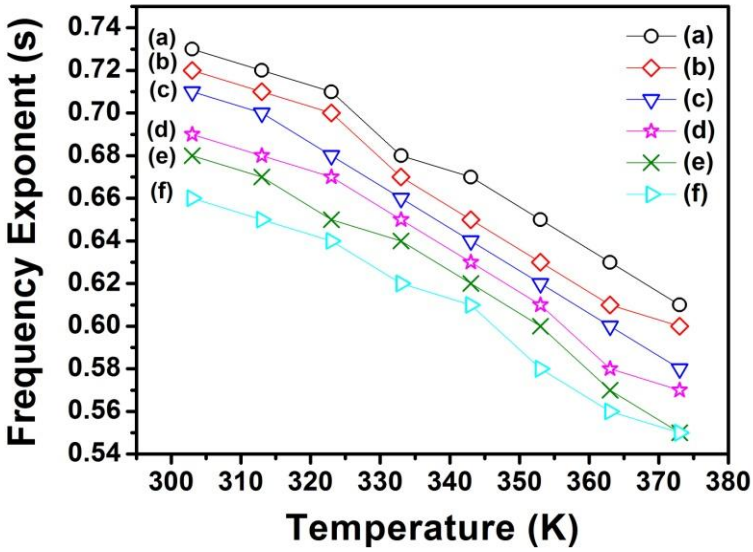

Figure 5.34: *Temperature variation of frequency exponent 's' of (a) pristine and irradiated PPy nanofibers at ion fluences of (b) 10^{10}, (c) 5×10^{10}, (d) 10^{11}, (e) 5×10^{11} and (f) 10^{12} ions/cm^2.*

The temperature dependence studies of frequency exponent *s* helps in elucidating the charge transport mechanism in SHI irradiated PPy nanofibers. Fig. 5.34 depicts the plots of frequency exponent (*s*) vs. temperature for both the pristine and irradiated PPy nanofibers. It is observed that the value of *s* decreases with increasing temperature for

pristine and irradiated PPy nanofibers at different ion fluences. The decrease in the value of *s* with increasing temperature suggests that the charge carriers in both the pristine and irradiated PPy nanofibers at different irradiation fluences follow the correlated barrier hopping (CBH) model as the dominant charge transport mechanism i.e. the charge carriers hop from one localized site to other localized site by overcoming the potential barrier height. Also, value of W_H decreases upon SHI irradiation suggesting reduction in barrier height for charge carriers' motion which in turn can increase the electrical conductivity in SHI irradiated PPy nanofibers. The smaller values (0.288-0.362 eV) of W_H suggest that polarons are majority charge carriers in pristine as well as irradiated PPy nanofibers since W_H is about four times higher for bipolaronic transport [155]. The calculated values of frequency exponent (*s*) and effective barrier height (W_H) for charge carriers of pristine and irradiated PPy nanofibers at room temperature are presented in Table 5.11.

Table 5.11: Room temperature (303 K) values of frequency exponent (*s*) and barrier activation energy (W_H) of pristine and irradiated PPy nanofibers at different ion fluences.

Fluence (ions/cm^2)	Frequency exponent, *s*	Barrier activation energy W_H (eV) at 303 K
Pristine	0.73	0.362
1×10^{10}	0.72	0.350
5×10^{10}	0.71	0.338
1×10^{11}	0.69	0.316
5×10^{11}	0.68	0.306
1×10^{12}	0.66	0.288

The scaling of ac conductivity in disordered materials provides deep insight about the conductivity relaxation mechanism. In the present work, the ac conductivity spectra have been scaled by the scaling process reported by Gosh *et. al*. [337]: the conductivity is scaled by σ_{dc} while the frequency axis is scaled by the cross-over or cut-off frequency ω_{max}. The master plots of ac conductivity of pristine and irradiated

PPy nanofibers at different ion fluences at room temperature are shown in Fig. 5.35. It is observed that the plots fall onto a single master curve, which indicates that the conductivity relaxation mechanism of charge carriers in SHI irradiated PPy nanofibers is independent of irradiation fluence.

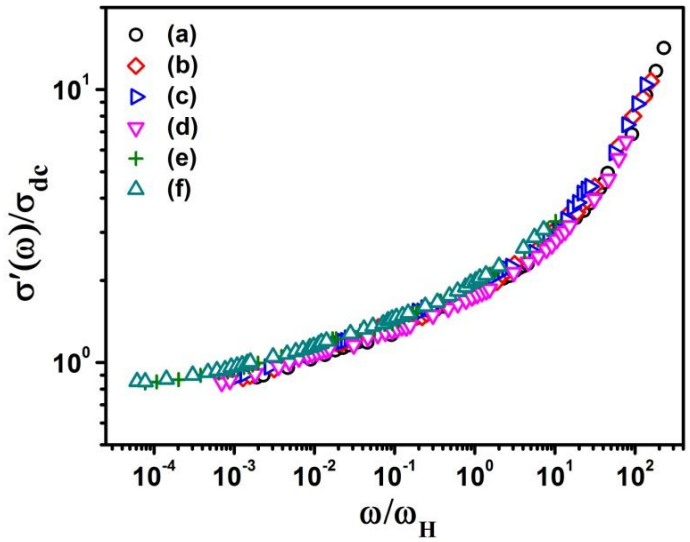

Figure 5.35: *Scaling plots of total conductivity of (a) pristine and irradiated PPy nanofibers at ion fluences of (b) 10^{10}, (c) 5×10^{10}, (d) 10^{11}, (e) 5×10^{11} and (f) 10^{12} ions/cm^2 at room temperature (303 K).*

5.3. Summary

High quality PPy nanofibers doped with different alkylbenzenesulfonic (ABSA) acids have been synthesized by controlled interfacial polymerization approach. PPy nanofibers doped with short alkyl chain ABSA dopant shows smaller diameter and diameter of the PPy nanofibers increases in the order of PPy-(*p*-TSA)< PPy-(CSA)< PPy-(OBSA)< PPy-(DBSA). Among the different ABSA doped PPy nanofibers, the short alkyl chain *p*-TSA doped PPy nanofibers exhibit higher value of crystallinity that can be attributed to strong electrostatic interaction between SO_4^{2-} anions and PPy nanofibers chains. The calculated "effective conjugation length" of PPy nanofibers increases in the order of PPy-(DBSA) < PPy-(OBSA) < PPy-(CSA) < PPy-(*p*-TSA). The increase in "effective conjugation length" gives rise to increase in electrical conductivity in short alkyl chain *p*-TSA doped PPy nanofibers i.e. conjugation length dominated electrical conductivity in ABSA doped PPy nanofibers. The optical band gap

energy (E_g) is smaller for short alkyl chain *p*-TSA doped PPy nanofibers, while thermal stability in different ABSA doped PPy nanofibers increases in the order of PPy-(DBSA)< PPy-(OBSA)< PPy-(CSA)< PPy-(*p*-TSA) which in turn predicts that short alkyl chain ABSA doped PPy nanofibers are thermally and structurally more stable. The studies of complex dielectric permittivity depict that the dielectric permittivity $\varepsilon'(\omega)$ of different ABSA doped PPy nanofibers increases with decreasing frequency which can be attributed to the electrode polarization effects. The linear increase of the dielectric loss $\varepsilon''(\omega)$ with decreasing frequency suggests the dominant effect of dc conductivity than that of the electrode polarization effects. The modulus formalism provides a powerful method to study the relaxation mechanism in materials where dc loss is dominant. This method helps to eliminate the dc loss and distinguish the relaxation peak that is not observed in dielectric loss (ε'') spectra. The small value of stretched exponent β $(0.56 \leq \beta \leq 0.65)$ indicates deviation of the relaxation process from the ideal Debye relaxation and wide distribution of relaxation times of the charge carriers. The decrease in frequency exponent (*s*) with increasing temperature suggests the correlated barrier hopping (CBH) mechanism for transport of charge carriers in different ABSA doped PPy nanofibers. The scaling of modulus spectra indicates a common relaxation dynamics. The scaling of ac conductivity conductivity spectra provides a common conductivity relaxation mechanism of the charge carriers for different dopants in PPy nanofibers at different temperatures.

Enhancement of the structural, optical and thermal properties along with the dielectric properties and ac conductivity in 160 MeV Ni^{12+} SHI irradiated PPy nanofibers have been observed. Upon SHI irradiation the ordering of PPy nanofibers chains increases, while the value of *d*-spacing decreases with increasing the irradiation fluence. The polaron absorption band in SHI irradiated PPy nanofibers makes a red shift and accordingly both the direct and indirect optical band gap energies (E_g) decrease significantly with increasing ion fluence. Moreover upon SHI irradiation, the number of carbon atoms per conjugation length (N) and number of carbon atoms per cluster (M) in PPy nanofibers increase. The increase in vibrational band intensity upon SHI irradiation reveals the formation of characteristic functional groups viz. C=C, C-H and C-H in PPy nanofibers. Also, the thermal stability of PPy nanofibers increases with increasing the irradiation fluence which may be attributed to the formation of more ordered structure

after SHI irradiation. The increase in the value of ε' with increasing irradiation fluence can be attributed to the increased contribution of electrode polarization after SHI irradiation on PPy nanofibers due to the generation of increased number of charge carriers. The asymmetric relaxation peak indicates the non-Debye relaxation of charge carriers in both the pristine and SHI irradiated PPy nanofibers. Upon SHI irradiation the relaxation peak shifts towards higher frequency with increasing ion fluence indicating increase in the long range motion of charge carriers in SHI irradiated PPy nanofibers. The scaling of M'' spectra at different ion fluences indicates that the relaxation dynamics of charge carriers in SHI irradiated PPy nanofibers are independent of the ion fluence. Upon SHI irradiation, ac conductivity of PPy nanofibers increases and the decreased value of frequency exponent *s* with increasing temperature suggest that the correlated barrier hopping (CBH) is the dominant charge transport mechanism in both pristine and irradiated PPy nanofibers. The effective barrier height calculations show that polarons are the majority charge carriers in pristine as well as irradiated PPy nanofibers. The scaling of ac conductivity at different ion fluences suggests that conductivity relaxation in irradiated PPy nanofibers is independent of the ion fluences.

CHAPTER-VI

Polypyrrole nanotubes: Dielectric relaxation and electrical transport studies and swift heavy ion irradiation effects

This chapter deals with the synthesis of polypyrrole (PPy) nanotubes by self assembly polymerization method with varying dopant/monomer molar ratio and their different characterizations. A systematic study of the dielectric relaxation and ac conductivity of PPy nanotubes has been discussed and forms a major portion of this chapter. SHI irradiation induced modifications on morphology, structural, optical, thermal, dielectric properties and ac conductivity in PPy nanotubes have also been discussed.

Conducting polymers with extended π-conjugation structure are organic conductors with their advantage of flexible chemical functionalization that can replace the traditional metallic conductors. The common feature of conducting polymers is the tenability of their electrical conductivity that can be raised up to several orders of magnitude upon doping [43]. Owing to high electrical conductivity, ease of synthesis, excellent optical properties, good thermal stability, biocompatibility, solubility and processibility [304], conducting PPy has wide range of potential applications including biosensors [7], drug delivery devices [345], corrosion protection [346], polymeric rechargeable batteries [347] etc. The conducting polymer nanostructures are known to display improved physico-chemical properties due to their high electrical conductivity, large surface to volume ratio, short path lengths for the transport of ions and high electrochemical activity as compared to their bulk counterparts [300]. In recent studies, it has been reported that the conducting polymer nanotubes can be used as promising functional materials for futuristic applications in molecular electronics, molecular wires and devices [348, 349]. There have been more recent applications of PPy nanotubes for biosensors that include high-performance field-effect transistor-type glucose biosensor based on nanohybrids of carboxylated polypyrrole nanotube wrapped graphene sheet transducer [350] and PPy nanotubes embedded reduced graphene oxide transducer for field-effect transistor-type H_2O_2 biosensor [351]. Different synthesis methods such as template synthesis [78], reactive self-degradation [124], electrochemical [229] and self-

assembly polymerization [230] methods have been used to fabricate nanotubes of conducting polymers. Nanotubes with controlled morphology can be synthesized by hard template method but this method suffers from the disadvantages of dissolution of the external hard template after polymerization, which can damage the resulting nanotubes and hence limits their applicability. The reactive self-degrade approach needs a reactive template for polymerization which makes the synthesis costlier. Therefore, the template free self-assembly method has received more attention due to its simplicity, cost effectiveness and large-scale production. Another aspect of self-assembly method is that the dopant used during polymerization also acts as soft template in the process of formation of nanotubes [231, 232]. Previous studies have reported the successful self-assembly synthesis of conducting polymer nanotubes doped with different protonic acids viz. naphthalene sulfonic acid (NSA) [352], azobenzene sulfonic acid [353] and *p*-toluene sulfonic acid (*p*-TSA) [352]. The morphology, diameter and length of the nanotubes can be controlled by controlling the synthesis conditions such as dopant type, dopant to monomer ratio, dopant concentration and reaction temperature [352]. However, use of organic macromolecules as dopant has shown easy incorporation into the polymer chains during synthesis and can confer added functionality to the material.

In the recent years, swift heavy ion (SHI) irradiation induced modifications in the properties of conducting polymers have been a subject of great interest for researchers. SHI irradiation in conducting polymers can produce irreversible changes in their electrical, structural, chemical, mechanical and optical properties [316, 354]. The remarkable modifications in properties of materials have been observed with SHI irradiation, which cannot be observed by irradiation with conventional e-beam or γ-rays irradiation. During SHI irradiation, the chemical modifications like electronic excitation, ionization, cross-linking, bond breaking and formation of new chemical bonds as well as mass losses are accepted as the basic causes that give rise to the observed macroscopic changes in the materials [355]. In this process, the knocked out target electrons dissipate their energy into the polymeric material in a very small cylindrical zone around the ion path, referred to as ion track [316] either by collisions with other electrons or by electron-phonon coupling mode. The results show that the cross-linking and chain-scissioning phenomena during SHI irradiation depend on the ion beam type and energy used as well as on target polymeric structure [356]. In

polymers the ionization and electronic excitation processes are considered to cause chain-scissioning and cross-linking phenomena. The cross-linking occurs when two free dangling ions or radical pairs are on neighbouring chain unit, whereas double or triple bonds are formed when two neighbouring radicals are formed in the same chain unit. The cross-linking results in increasing the molecular weight while the chain scission leads to decreasing molecular weight. Both the effects change the polymer phase, chemical structure, crystallinity and molecular weight [125]. Hussain *et al.* [357] have studied SHI irradiation effects on PPy using 160 MeV Ni^{12+} ions and have observed a significant increase of crystallinity after SHI irradiation. Moreover, upon SHI irradiation the absorption edge shifted to the higher wavelength region resulting in reduction in optical band gap energy. Kaur *et al.* [258] have studied SHI irradiation effects on morphology and electrical properties of PPy and reported that upon SHI irradiation, the surface structure of PPy films became smoother and electrical conductivity of the PPy films doubled as compared to that of the pristine sample.

Highlighting these research finding, PPy nanotubes at different dopant/monomer (CSA/Py) molar ratio have been synthesized by the self-assembly polymerization method with a view to enhance structural, optical and thermal properties. Also, the dielectric properties and ac conductivity of synthesized PPy nanotubes have been investigated to understand the relaxation mechanism and charge dynamics of PPy nanotubes. The synthesis procedure of PPy nanotubes by the self assembly polymerization approach has been explained in Chapter-III. Four different samples of PPy nanotubes have been synthesized by varying the molar ratios of CSA/Py at 0.1:1, 0.5:1, 1:1 and 2:1 keeping Py (monomer) and APS (oxidant) molar concentration fixed at 0.15 M. The variation in the properties of PPy nanotubes with CSA/Py molar ratio has been investigated. The sample with the best properties has been irradiated with 160 MeV Ni^{12+} swift heavy ion (SHI) with different ion fluences of 10^{10}, 5×10^{10}, 10^{11}, 5×10^{11}, 10^{12} ions/cm^2 in order to further improve the properties of PPy nanotubes. The detailed results on PPy nanotubes with varying CSA/Py molar ratio have been presented in Section 6.1 and the results on 160 MeV Ni^{12+} ion irradiated PPy nanotubes have been discussed in Section 6.2.

6.1. Characterization, dielectric relaxation and ac conductivity of polypyrrole nanotubes

6.1.1. High resolution transmission electron microscopy studies

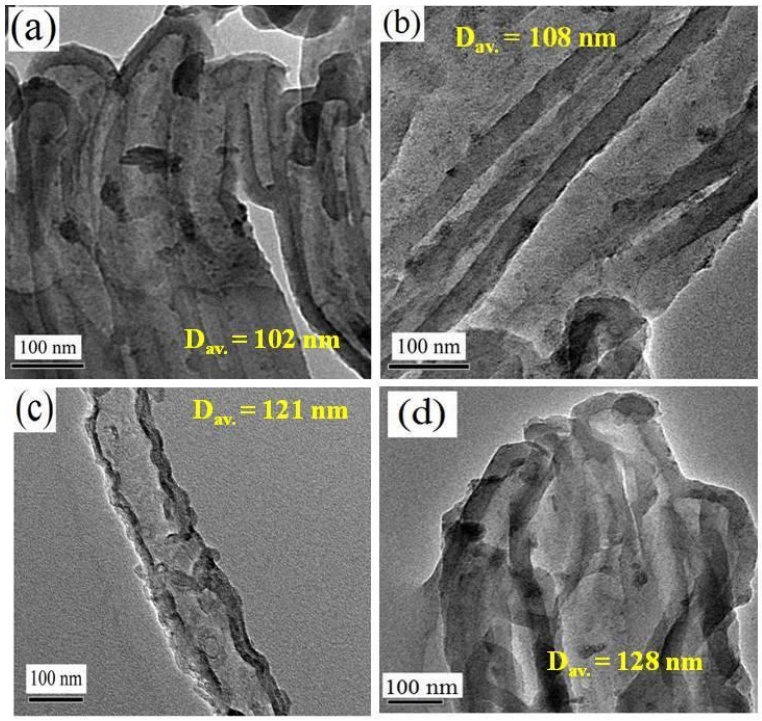

Figure 6.1: *HRTEM micrographs of PPy nanotubes synthesized at CSA/Py molar ratios of (a) 0.1:1, (b) 0.5:1, (c) 1:1 and (d) 2:1.*

Figs. 6.1(a-d) depict the HRTEM micrographs of PPy nanotubes synthesized at CSA/Py molar ratios of 0.1:1, 0.5:1, 1:1 and 2:1, respectively. All the HRTEM micrographs confirm the formation of PPy nanotubes with length in micrometer scale. As observed from Figs. 6.1 (a-d), the dopant/monomer (CSA/Py) molar ratio effects the diameter of PPy nanotubes synthesized by the self-assembly polymerization method. With increasing CSA/Py molar ratio from 0.1:1 to 2:1, the average outer diameter of the PPy nanotubes increases from 102 nm to 128 nm. The effect of dopant/monomer ratio on the diameter of PPy nanotubes can be explained by the "template like" model [63, 358]: the pyrrole salt formed with CSA during polymerization acts as soft "template" and the tubular nanotubes are formed by the elongation of micelles at the polymerization reaction and size of the micelle increases with increasing dopant concentration.

6.1.2. Formation mechanism of PPy nanotubes

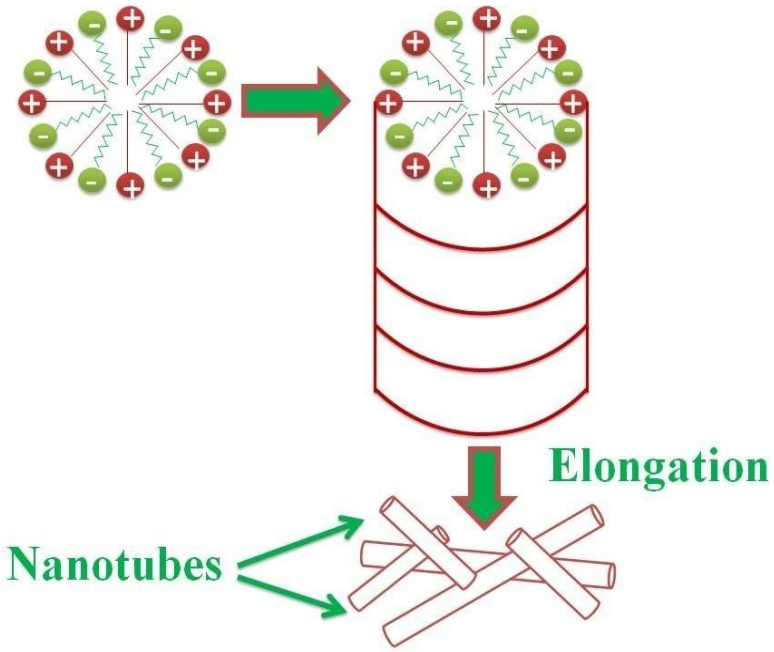

Figure 6.2: *Schematic of formation of PPy nanotubes by self-assembly method.*

The self-assembly formation mechanism of PPy nanotubes can be understood as follows: In the initial stage of polymerization reaction, CSA and Py form CSA/Py salt through the acid base reaction before the oxidative polymerization. Due to the presence of a polar head group (hydrophilic $-SO_3H$ group) and a non-polar tail (hydrophobic $C_{10}H_5O-$ group), the CSA/Py salt can self-assemble into the micelles in the aqueous solution that can act as soft template during polymerization. The micelles consisting of CSA anions and Py cations coexist and form a double layer. The free Py monomer can diffuse into the micelles to form pyrrole filled micelles which act as soft template during the self-assembly and the Py cations may solubilise into the micelle/water interface as depicted in Fig. 6.2. When APS oxidant is added into the reaction solution, the polymerization proceeds which takes place only at the micelle/water interface adjacent to the polar head groups of CSA, since the hydrophilic APS molecules cannot penetrate into the micelle surface [359]. During the course of polymerization the self-assembled micelles become bigger by accretion [360] or tubular/fibrilar structure by elongation [361] depending on the local concentration of the surfactant. In this

synthesis procedure, the elongation of micelles dominates the reaction thereby confirming the formation of PPy nanotubes as observed from the HRTEM micrographs.

6.1.3. *X-ray diffraction studies*

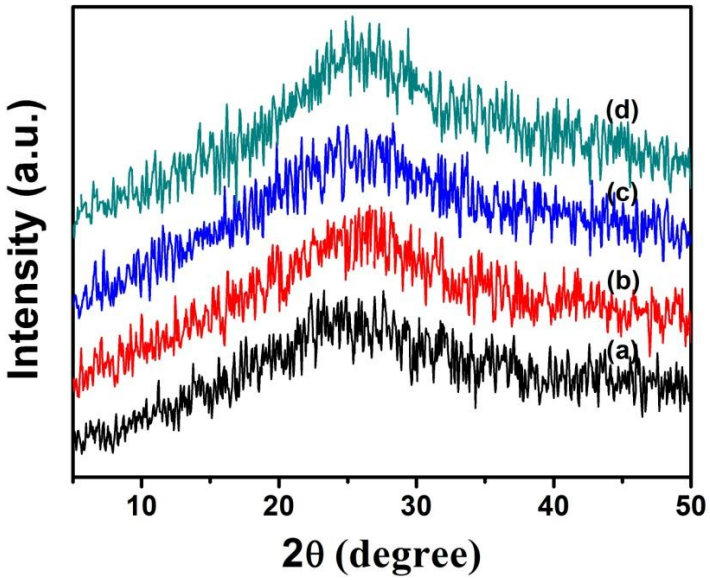

Figure 6.3: *XRD patterns of PPy nanotubes synthesized at CSA/Py molar ratios of (a) 0.1:1, (b) 0.5:1, (c) 1:1 and (d) 2:1.*

The XRD patterns of PPy nanotubes synthesized at various CSA/Py molar ratios are depicted in Fig. 6.3. The appearance of a broad diffraction peak reveals the amorphous structure of PPy nanotubes and the origin of this broad diffraction peak can be ascribed to the reflections from the pyrrole-counterions or pyrrole-pyrrole interplanar distance [362]. In general, PPy is a highly rigid conducting polymer due to its linear structure and less flexible chain folding to induce crystalline domains. On addition of dopant CSA with PPy nanotubes, the polymer undergoes electrostatic interaction which organise the PPy chains in ordered fashion. Furthermore, the dopant/monomer molar ratio also affects the nature of the diffraction peak. With increasing CSA/Py ratio, the intensity of diffraction peak increases suggesting enhancement of crystallinity of PPy nanotubes. The crystallinity has the direct affect on electrical conductivity, where one can expect higher value of electrical conductivity at a higher crystallinity. The ordering of chains (X_C) of the PPy nanotubes has been determined by using the equation (6.1) given below [261]:

$$\text{Ordering of chains, } X_C = \frac{A^I}{A^T} \times 100\% \tag{6.1}$$

where A^I is the area under the diffraction peak and A^T is the total area covered under the diffractogram.

The extent of chain order (L) of PPy nanotubes has been calculated using the Scherrer's formula [262]:

$$L = \frac{K\lambda}{\beta \cos\theta} \tag{6.2}$$

where K is the proportionality constant equal to 0.9 for unknown structures, β is the full width at half maxima (FWHM) expressed in radian, λ (=1.5406 Å) is the wavelength of X-rays used.

Also, the hopping distance (*R*) of PPy nanotubes has been calculated using equation (6.3) as follows [262, 263]:

$$R = \frac{5}{8}\left[\frac{\lambda}{\sin\theta}\right] \tag{6.3}$$

The calculated values of angle of diffraction (2θ), full width at half-maximum *(β)*, ordering of chains (X_C), extent of chain order (*L*) and hopping distance (*R*) of PPy nanotubes synthesized at various molar ratios of CSA/Py are presented in Table 6.1.

Table 6.1: Values of angle of diffraction (2θ), full width at half-maximum (β), ordering of chains (X_C), extent of chain order (*L*) and hopping distance (*R*) of PPy nanotubes at different CSA/Py molar ratios.

CSA/Py molar ratio	Diffraction peak position, 2θ (degree)	Full width at half-maximum, β (in radians)	Ordering of chains, X_C (%)	Extent of chain order, *L* (Å)	Hopping distance, *R* (Å)
0.01:1	25.28±0.03	0.2412±0.0003	17.35±0.10	5.78±0.03	4.40±0.03
0.05:1	25.96±0.02	0.2492±0.0002	19.20±0.12	6.07±0.02	4.28±0.02
1:1	26.05±0.03	0.2406±0.0003	20.45±0.08	6.41±0.03	4.27±0.03
2:1	25.96±0.04	0.2179±0.0004	23.65±0.11	6.65±0.04	4.28±0.04

The table shows that with increasing CSA/Py molar ratio, both the crystallinity and extent of chain order of PPy nanotubes increase. Extent of chain order (L) has been determined from the theta (θ) and beta (β) values as other parameters are constant in the Scherrer formula. The value of beta (β) for each diffraction peak has been measured using the calculating program for FWHM. It is observed that FWMH for the diffraction peak of PPy nanotubes decreases and L increases with increasing the CSA/Py molar ratio. Moreover, the diffraction peak (2θ) shifts towards higher theta (θ) at higher CSA/Py molar ratio of 2:1. The higher value L results from the smaller value of β and higher value of θ for PPy nanotubes with higher CSA/Py molar ratio of 2:1.

6.1.4. Fourier transform infrared spectroscopy analysis

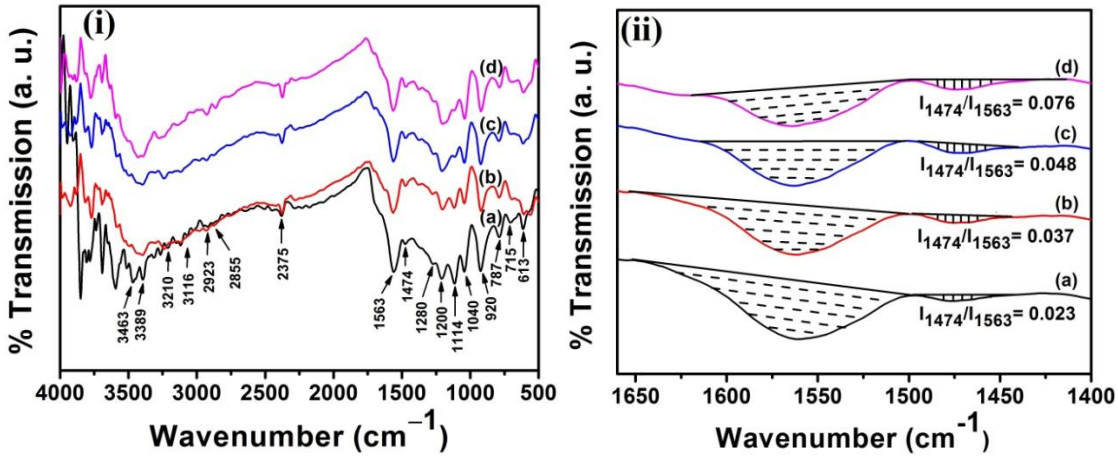

Figure 6.4: *Plots of (i) FTIR spectra and (ii) peak area ratio of I_{1474}/I_{1563} of PPy nanotubes at CSA/Py molar ratios of (a) 0.1:1, (b) 0.5:1, (c) 1:1 and (d) 2:1.*

Information about the molecular structure of PPy nanotubes can be obtained by studying their FTIR spectra. Fig. 6.4(i) depicts FTIR spectra of PPy nanotubes at different molar ratios of CSA/Py. The main vibration bands at 1563 and 1474 cm^{-1} are assigned to the C=C and C-N stretching vibration in pyrrole rings, respectively. The strong vibration bands at 1040 and 920 cm^{-1} are ascribed to the C-H and C-N in-plane deformation vibration, respectively. The C-H wagging vibration is due to the vibration band at 787 cm^{-1}, whereas the vibration at 1280 cm^{-1} is assigned to the C-H or C-N in-plane-deformation modes [301]. The strong vibration bands in the range of 3000-3500 cm^{-1} are assigned to the presence of N-H stretching vibration and the band at 1200 cm^{-1}

corresponds to the C-C breathing vibration of pyrrole rings. The expected vibration band at 1183 cm^{-1} due to S=O stretching vibration of SO_3^- group of CSA dopant is not observed clearly due to overlapping with the pyrrole ring vibration at 1200 cm^{-1} [219]. The incorporation of the dopant counter anions into the PPy chains can further be confirmed from the presence of vibration bands at 2923 and 2855 cm^{-1} which can be attributed to the vibration of aliphatic $-CH_3$ and $-CH_2$ groups related to the sulfonate anions supplied from CSA dopant [363]. The vibration bands at 715 and 613 cm^{-1} correspond to the C-S and S-O stretching vibration, respectively which also indicate the doping of CSA into the PPy nanotubes.

The electronic properties of conducting polymers can be explained in terms of their "effective conjugation length" which can be determined from their FTIR spectra. The presence of the conjugated double bonds in their backbone structure give rise to electrical conductivity as it allows the efficient transfer of charges along the polymer backbone chains [364]. The defects that interrupt the conjugation include sp^3 carbons, carbonyl groups, cross-links etc. The qualitative information regarding the "effective conjugation length" can be obtained from the theoretical work done by Tian and Zerbi [78], according to which as the conjugation length increases, the intensity of asymmetric ring stretching vibration of PPy nanotubes at 1563 cm^{-1} decreases with respect to the symmetric mode vibration at 1474 cm^{-1} [270]. Thus, the effective conjugation lengths of the PPy nanotubes for different CSA/Py molar ratios have been determined from the ratio of the peak intensities of 1474 and 1563 cm^{-1} peaks in their respective FTIR spectra [269]. Fig. 6.4(ii) depicts the plots of integrated peak area ratio of I_{1474}/I_{1563} of PPy nanotubes at different molar ratio of CSA/Py. The calculated peak area ratios of I_{1474}/I_{1563} of PPy nanotubes at various molar ratios of CSA/Py are presented in Table 6.2. The integrated peak area ratio I_{1474}/I_{1563} is 0.023 for PPy nanotubes at CSA/Py molar ratio of 0.01:1, wherein I_{1474}/I_{1563} increases to 0.076 at the CSA/Py molar ratio of 2:1 suggesting higher conjugation length in the PPy nanotubes. The increase in conjugation length can increase the delocalization of charge carriers over several PPy chains leading to a higher value of electrical conductivity in PPy nanotubes.

Table 6.2: Values of integrated peak area ratios of I_{1476}/I_{1563} of PPy nanotubes synthesized at different CSA/Py molar ratios.

CSA/Py molar ratio	Peak area ratio of I_{1476}/I_{1563}
0.01:1	0.023 ± 0.002
0.05:1	0.037 ± 0.001
1:1	0.048 ± 0.002
2:1	0.076 ± 0.003

6.1.5. UV-vis absorption spectroscopy studies

The UV-vis absorption spectra of PPy nanotubes at different CSA/Py molar ratios are depicted in Fig. 6.5. The UV-vis absorption spectra of PPy nanotubes show three absorption bands at 340 nm, 478 nm and a free trail centred above 680 nm in near infrared (NIR) region.

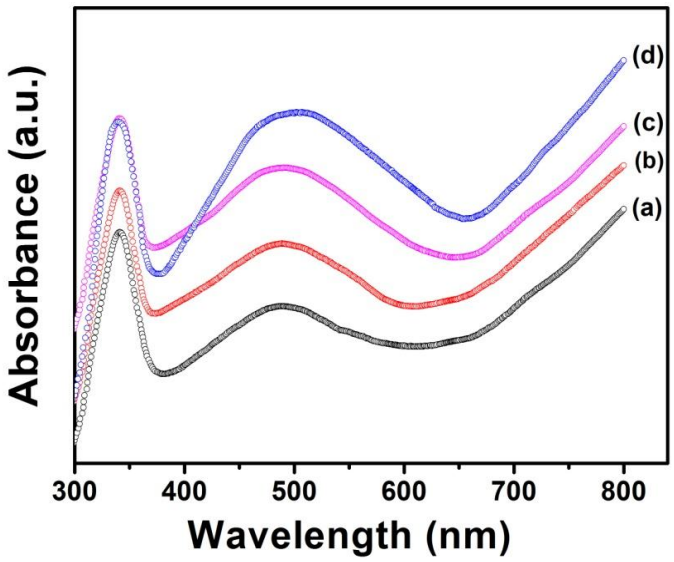

Figure 6.5: *UV-vis absorption spectra of PPy nanotubes at CSA/Py molar ratios of (a) 0.1:1, (b) 0.5:1, (c) 1:1 and (d) 2:1.*

The origin of three different absorption bands can be explained as follows: The neutral PPy is an insulator whose electronic band is characterized by a band gap of energy 3.2 eV [325]. Upon doping with CSA, the electrons extracted from the PPy backbone chains and as a result the polaronic states are introduced within the neutral band gap of

PPy. The formation of polarons induces two localized electronic bands into the energy gap: an occupied bonding polaron level (BPL) and an empty antibonding polaron level (APL). The two polarons combine together and form a stable bipolaron. The bonding bipolaron level (BBL) and antibonding bipolaron level (ABL) get closer and the bipolaron bonding state is empty unlike the polaron states. Therefore the absorption band at 340 nm corresponds to the interband π-π* transition whose intensity is related to the PPy content. The band at about 478 nm is attributed to the transition from valence band to the antibonding polaron or bipolaron state because of the polaron absorption. The broad tail absorption band centred on 680 nm corresponds to the transition from valence band to antibonding polaron or bipolaron state mainly due to the bipolaron absorption [365, 366]. Moreover, information regarding the optical band gap energy of materials can be obtained from their respective UV-vis spectra. It is observed that with increasing CSA/Py molar ratio, the polaron absorption band makes a red shift and this red shifting of absorption band with increasing dopant/monomer ratio reveals a decrease in the optical band gap energy which is a direct consequence of enhancement of conjugation length in PPy nanotubes. As a result, the increase in the conjugation length can lead to increase in electrical conductivity in PPy nanotubes with increasing the dopant/monomer molar ratio. Thus the UV-vis results corroborate the conclusion drawn from the FTIR analysis that the PPy nanotubes with extended π-conjugation exhibit higher value of electrical conductivity.

The optical band gap energy (E_g) for disordered materials can be calculated using the Tauc's equation which relates the absorption coefficient (α) and incident photon energy $(h\nu)$ as follows [272],

$$\alpha(\nu) = \frac{B_\alpha (h\nu - E_g)^n}{h\nu} \tag{6.4}$$

where B_α is the constant of proportionality and the exponent *n* characterizes the nature of electronic transition whether it is direct or indirect band transition. For the value of *n* = 1/2, 3/2, 2 and 3, the corresponding band transition represents the direct allowed, direct forbidden, indirect allowed and indirect forbidden transitions, respectively. The optical band gap energy of materials can be determined from the plot of $(\alpha h\nu)^{1/n}$ vs. $h\nu$ and extrapolation of the linear portion of the plot to $(\alpha h\nu)^{1/n} = 0$ gives the value of

band gap energy. The plots of $(\alpha h\nu)^2$ vs. $h\nu$ of PPy nanotubes at different CSA/Py molar ratios are depicted in Fig. 6.6. The calculated values of optical band gap energy (E_g) of PPy nanotubes at different CSA/Py ratios are presented in Table 6.3. With increasing CSA/Py ratio, the optical band gap energy of PPy nanotubes decreases. The decrease in the value of optical band gap energy confirms reduction in the disorder and increase in the density of the defect states in the system which results from the high level of CSA doping into the PPy nanotubes chains.

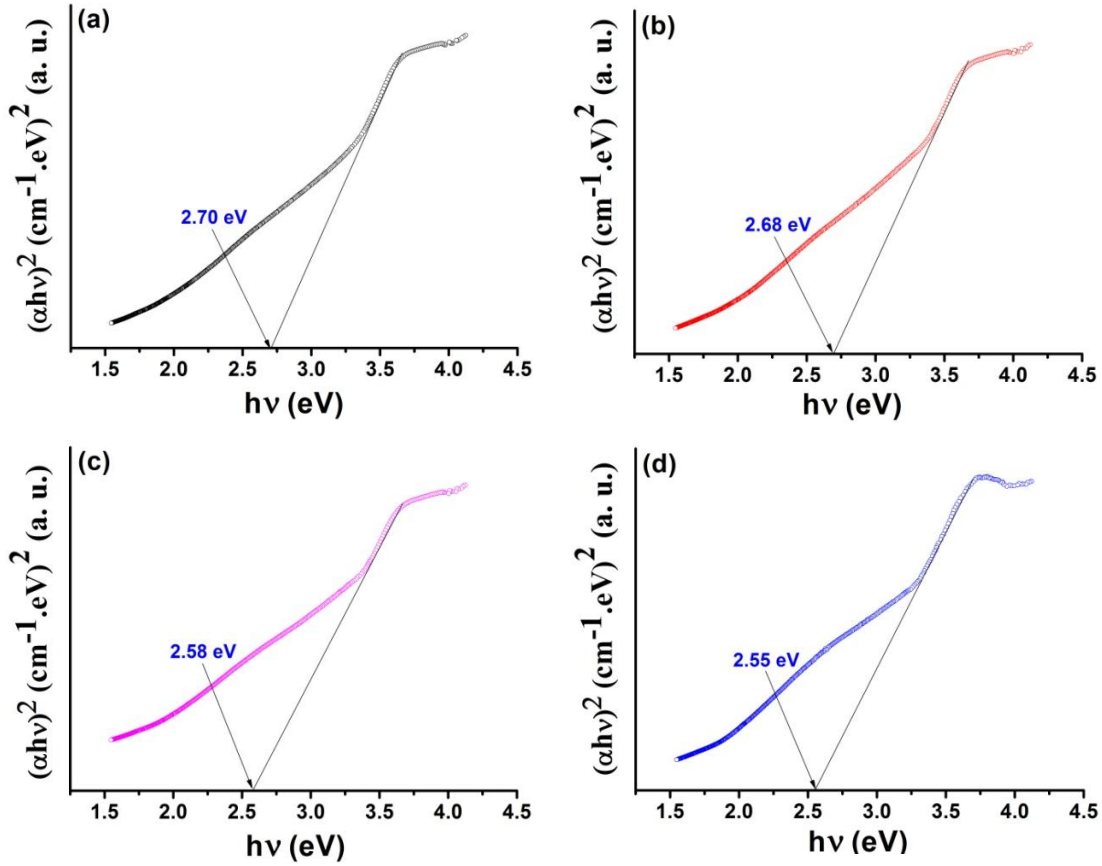

Figure 6.6: *Plots of $(\alpha h\nu)^2$ vs. $h\nu$ of PPy nanotubes at CSA/Py molar ratios of (a) 0.1:1, (b) 0.5:1, (c) 1:1 and (d) 2:1.*

Table 6.3: Values of optical band gap energies (E_g) of PPy nanotubes at different CSA/Py molar ratios.

CSA/Py molar ratio	Optical band gap energy, E_g (eV)
0.01:1	2.70 ± 0.002
0.05:1	2.68 ± 0.003
1:1	2.58 ± 0.003
2:1	2.55 ± 0.002

6.1.6. *Thermogravimetric analysis*

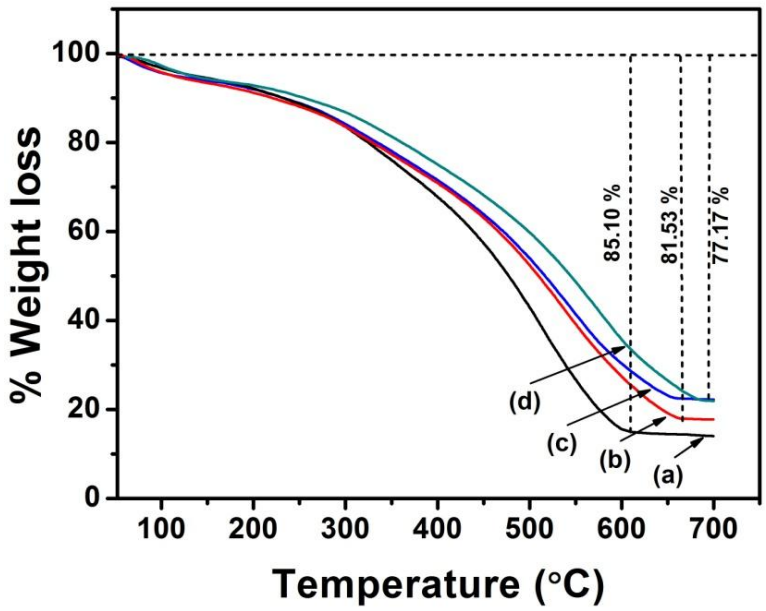

Figure 6.7: *Plots of TGA thermographs of PPy nanotubes at CSA/Py molar ratios of (a) 0.1:1, (b) 0.5:1 (c) 1:1 and (d) 2:1.*

The thermogravimetric analysis is a common technique for determination of the thermal stability of materials and to find out their degradation/decomposition at various temperatures. The TGA thermographs for PPy nanotubes at various CSA/Py molar ratios are shown in Fig. 6.7. All the thermographs exhibit three stage weight loss patterns in the investigated temperature region of 50-700 ºC. The first stage of weight loss occurs from room temperature to 130 °C, which can be attributed to the release of moisture and other volatiles from the polymer chains [294]. The second weight loss

stage in the temperature region of 250-380 °C occurs due to the degradation of dopant molecules from the polymer chains. The third and final stage of weight loss above 380 °C can be attributed to the degradation and/or decomposition of the PPy backbone chains [367]. It is observed that the degradation temperature of PPy nanotubes shifts to higher temperatures with increasing CSA/Py molar ratio. In general the free sulfonate groups are thermally active which possibly leads to thermal degradation of PPy. However, the sulfonate groups become thermally stable when they form complex with countercations. Thus incorpation of sulfonate anions from the CSA dopant increases the thermal stability of PPy nanotubes. At higher dopant concentration, due to more availability of dopant anions into the PPy chains the interaction between the dopant and polymer chains increases which aligns the polymer chains in an ordered fashion. The ordered alignment of the polymer chains results more crystalline structure and hence the degradation temperature of PPy nanotubes at higher CSA/Py molar ratio increases. Thus the TGA studies reveal that thermal stability of PPy nanotubes increases with increasing dopant/monomer ratio, which is consistent with the XRD results.

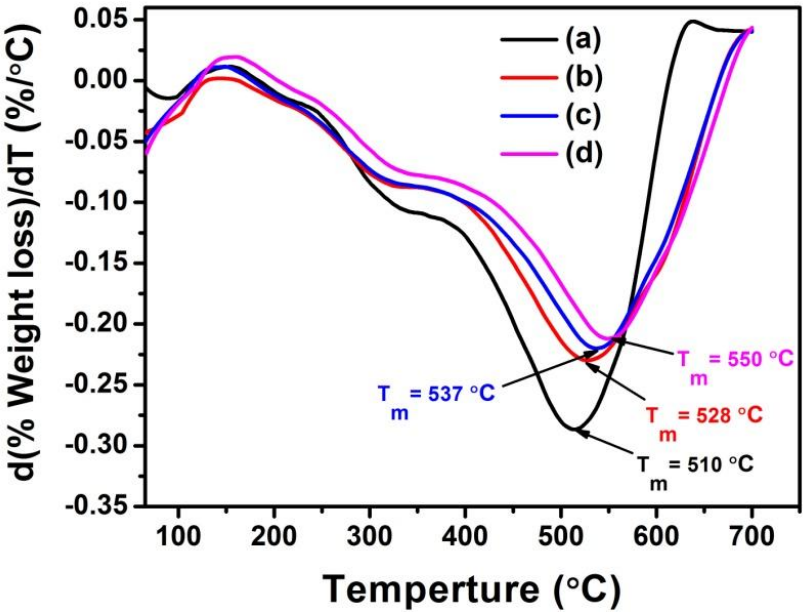

Figure 6.8: *Derivative plots of TGA thermographs for PPy nanotubes at CSA/Py molar ratios of (a) 0.1:1, (b) 0.5:1 (c) 1:1 and (d) 2:1.*

Fig. 6.8 depicts the derivative plots of TGA thermographs for PPy nanotubes at various CSA/Py molar ratios. The negative sign of the derivatives means the decomposition and weight loss of the sample. Therefore, only the numerical (without minus sign) values of

the derivatives are relevant for analysis. The maximum decomposition temperature (T_m), at which the rate of weight loss is maximum, and the maximum decomposition rate $(dW/dT)_m$ for PPy nanotubes with different CSA/Py molar ratios (obtained from the figure 6.8) are recorded in Table 6.4. The table shows that the maximum decomposition temperature (T_m) increases, while the maximum decomposition rate $(dW/dT)_m$ decreases with increasing CSA/Py molar ratio. For PPy nanotubes with CSA/Py molar ratio of 0.01:1, T_m increases from 510 °C to 550 °C with CSA/Py molar ratio of 2:1 suggesting that the sample can sustain a higher temperature. Moreover, the rate of maximum decomposition $(dW/dT)_m$ is $|0.288|$ %/°C for PPy nanotubes with CSA/Py molar ratio of 0.01:1, which decreases to $|0.212|$ %/°C when the CSA/Py molar ratio is increased to 2:1. It shows that the sample with higher CSA/Py molar ratio is decomposing at a lower rate meaning thereby that it is more thermally stable. The increase in T_m and decrease in $(dW/dT)_m$ with increasing CSA/Py molar ratio strongly support that the thermal stability of PPy nanotubes increases with increasing CSA/Py molar ratio. This may be ascribed to the increased degree of crystallinity due to polymer chain ordering with increasing CSA/Py molar ratio.

Table 6.4: Degradation temperatures at different percentage weigh losses (%), maximum decomposition temperature, (T_m) and maximum decomposition rate, $(dW/dT)_m$ for PPy nanotubes at various CSA/Py molar ratios.

CSA/Py molar ratio	Degradation temperature (°C) at different percentage (%) weight losses					Maximum decomposition temperature, T_m (°C)	Maximum decomposition rate, $(dW/dT)_m$ (%/°C)
	10 %	**20%**	**30%**	**50 %**	**70 %**		
0.01:1	215	317	387	474	539	510	$\|0.288\|$
0.05:1	215	320	408	510	588	528	$\|0.231\|$
1:1	215	320	408	516	588	537	$\|0.218\|$
2:1	250	362	439	547	629	550	$\|0.212\|$

6.1.7. Dielectric permittivity studies

The complex dielectric permittivity (ε^*) of disordered materials can be determined from the experimentally measured complex impedance $Z^*(\omega)$ data by using the following equation (6.5),

$$\varepsilon^*(\omega) = \frac{1}{j\omega C_0 Z^*(\omega)} = \varepsilon'(\omega) - j\varepsilon''(\omega) \tag{6.5}$$

where the real part $\varepsilon'(\omega)$ represents the dielectric permittivity that corresponds to the energy storage and the imaginary part $\varepsilon''(\omega)$ represents the dielectric loss corresponding to the energy loss in each cycle of electric field, $C_0 = \varepsilon_0 A/d$ represents the capacitance of free space between the electrodes, ω represents the angular frequency, *A* is the area of the electrode, *d* is the thickness of the sample and ε_0 is the permittivity in free space ($\varepsilon_0 = 8.854 \times 10^{-12} Nm^{-1}$). The dielectric permittivity $\varepsilon'(\omega)$ and dielectric loss $\varepsilon''(\omega)$ have been calculated from equations (6.6) and (6.7), respectively given below:

$$\varepsilon'(\omega) = -\frac{1}{C_o \omega}\left[\frac{Z''(\omega)}{Z'^2(\omega) + Z''^2(\omega)}\right] \tag{6.6}$$

$$\varepsilon''(\omega) = \frac{1}{C_o \omega}\left[\frac{Z'(\omega)}{Z'^2(\omega) + Z''^2(\omega)}\right] \tag{6.7}$$

where $Z'(\omega)$ is the real part of complex impedance (Z^*) corresponds to the current through the contact resistor, and $Z''(\omega)$ is the imaginary part of Z^* corresponds to the current through the capacitor.

To determine the nature of each of the relaxation, a least square fit of the experimental data to the Havriliak-Nigami (HN) function giving the complex dielectric permittivity for a single relaxation process is used [180],

$$\varepsilon^*(\omega) = \varepsilon_\infty + \frac{\Delta\varepsilon}{[1 + (i\omega\tau)^{\alpha_{HN}}]^{\gamma_{HN}}}, \tag{6.8}$$

where $\Delta\varepsilon = \varepsilon_s - \varepsilon_\infty$ is the dielectric relaxation strength, ε_s and ε_∞ are the dielectric constant at very low and high frequencies, respectively and τ is the average relaxation time, α_{HN} and γ_{HN} are the symmetrical and asymmetrical distribution parameters for the relaxation peak, which can assume values such that $0 \le \alpha_{HN}\gamma_{HN} \le 1$. This

expression reduces to Cole-Cole (CC) function for γ_{HN} =1, Davison-Cole (DC) for α_{HN} =1 and ideal Debye type for $\alpha_{HN} = \gamma_{HN} = 1$. From equation (6.9), the real part of permittivity $\varepsilon'(\omega)$ is given by:

$$\varepsilon'(\omega) = \varepsilon_\infty + \mathrm{Re}\{\frac{\Delta\varepsilon}{[1+(i\omega\tau)^{\alpha_{HN}}]^{\gamma_{HN}}}\} \tag{6.9}$$

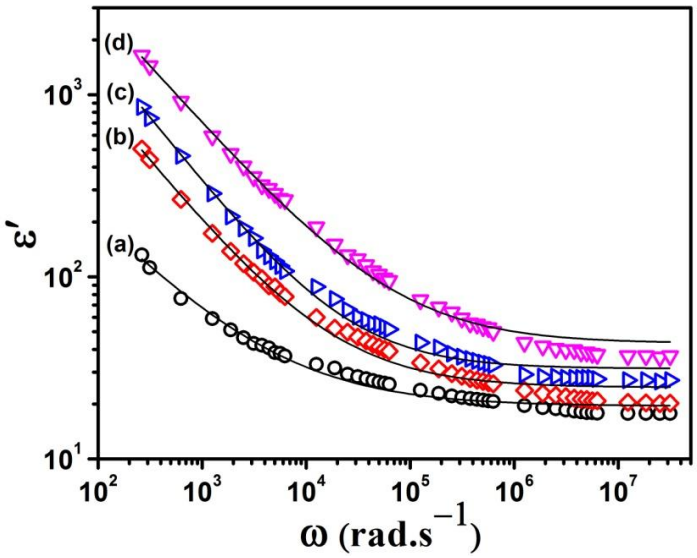

Figure 6.9: *Room temperature plots of dielectric permittivity* (ε') *vs. frequency* (ω) *of PPy nanotubes at CSA/Py molar ratios of (a) 0.1:1, (b) 0.5:1, (c) 1:1 and (d) 2:1.*

The plots of dielectric permittivity (ε') vs. frequency (ω) of PPy nanotubes at different molar ratio of CSA/Py at room temperature (303 K) are shown in Fig. 6.9. The figure shows that at lower frequencies, ε' exhibits stronger frequency dispersion and follows nearly frequency-independent behavior at higher frequencies. The response of the charge carriers to the externally applied ac electric field is faster at lower frequencies ($\leq 10^4$ Hz) giving rise to higher value of ε' corresponding to ε_s (static value of dielectric permittivity). At higher frequencies ($\geq 10^7$ Hz), the applied electric field changes rapidly and the charge carriers are unable to respond to the ac electric field giving lower value of ε' corresponding to ε_∞ (dielectric permittivity at infinite frequencies). The higher value of ε' at lower frequencies can be attributed to the electrode or space charge polarization effect [276]. To extract information about the dielectric relaxation, the experimental permittivity data in Fig. 6.9 are fitted using equation (6.9) by the non

linear curve fitting method. The solid line represents the best fitted curve for the experimental data of dielectric permittivity and values of various parameters such as ε_∞ , $\Delta\varepsilon$, α_{HN} and γ_{HN} can be estimated from the fitted curve. The calculated values of ε_∞ , $\Delta\varepsilon$, α_{HN} and γ_{HN} of PPy nanotubes at different CSA/Py molar ratios at room temperature are recorded in Table 6.5. The value of α_{HN} lies in 0.54-0.63, while the value of γ_{HN} lies in 0.89-0.93 suggesting the non-Debye dielectric relaxation in PPy nanotubes. Furthermore, the dielectric strength $(\Delta\varepsilon)$ of PPy nanotubes increases with increasing the CSA/Py molar ratio.

Table 6.5: Different dielectric relaxation parameters for PPy nanotubes using Havriliak -Nigami (HN) equation.

CSA/Py molar ratio	ε_∞	$\Delta\varepsilon$	α_{HN}	γ_{HN}
0.1:1	18	118	0.63	0.89
0.5:1	23	483	0.61	0.90
1:1	31	863	0.58	0.92
2:1	44	1633	0.54	0.93

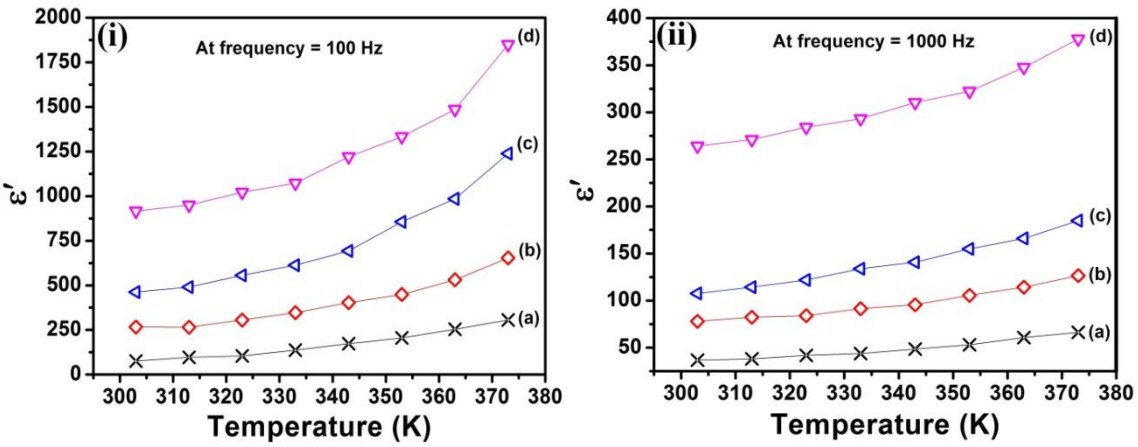

Figure 6.10: *Temperature dependence of dielectric permittivity* (ε') *of PPy nanotubes at frequencies of (i) 100 Hz and (ii) 1000 Hz at CSA/Py molar ratios of (a) 0.1:1, (b) 0.5:1, (c) 1:1 and (d) 2:1.*

Fig. 6.10 compares the dielectric permittivity (ε') of different samples of PPy nanotubes at different temperatures and frequencies. It is observed that ε' at a particular frequency increases with increasing the temperature. The orientation of the dipoles gets facilitated at higher temperatures which as a result increase the value of dielectric permittivity of PPy nanotubes. However, increase of dielectric permittivity is more prominent at lower frequencies than that of the higher frequencies.

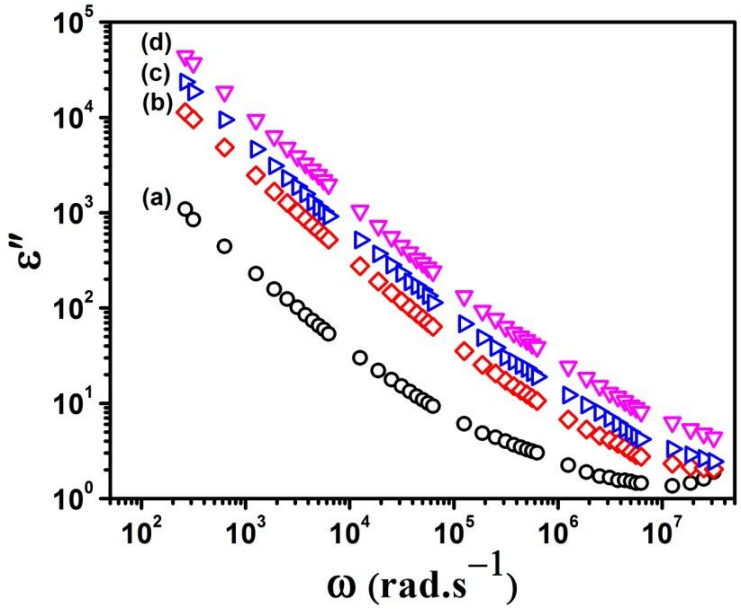

Figure 6.11: *Plots of dielectric loss (ε'') vs. frequency (ω) of PPy nanotubes at CSA/Py molar ratios of (a) 0.1:1, (b) 0.5:1, (c) 1:1 and (d) 2:1 at room temperature.*

The plots of dielectric loss (ε'') vs. frequency (ω) of PPy nanotubes at different molar ratios of CSA/Py at room temperature are depicted in Fig. 6.11. Three distinct effects given in the following equation contribute to the total dielectric loss ε'' [368, 369]:

$$\varepsilon'' = \varepsilon''_{dc} + \varepsilon''_{MW} + \varepsilon''_{D} \qquad (6.10)$$

where ε''_{dc} is due to dc conductance, ε''_{MW} comes from the Maxwell-Wagner polarization or electrode polarization effect and ε''_{D} is contributed by the dipolar orientation or Debye loss factor. To distinguish between the different losses arising from the dc conductivity process and from the other processes, different equations have been developed by considering the sample as parallel resistor-capacitor circuit [370]. The dielectric loss due to dc conductance (ε''_{dc}) can be expressed as [239],

$$\varepsilon''_{dc} = \frac{2\pi \times 1.8 \times 10^{12}[G_{spec}]}{\omega} \tag{6.11}$$

where G_{spec} is the specific conductivity (Scm^{-1}) of the sample. The dielectric loss due to the Maxwell-Wagner polarization or electrode polarization (ε''_{MW}) can be expressed as [327],

$$\varepsilon''_{MW} = \varepsilon_{\infty}(1 + \frac{K}{1+\omega^2\tau^2}) \tag{6.12}$$

where ε_{∞} and K are the constants calculated considering two different dielectric permittivity of the sample at the interfaces and τ is the relaxation time. In logarithmic scale, plot of ε''_{dc} vs. ω using equation (6.11) represents a straight line, while plot of ε''_{MW} vs. ω using equation (6.12) represents a sigmoid curve. It is observed that dielectric loss (ε'') decreases linearly with increasing frequency for all the samples of PPy nanotubes, which suggests that the dc loss is dominant over the polarization effect. However in the measured frequency range (42 Hz-5 MHz), there appears no relaxation peak in ε'' spectra, which can be believed that the electrical conduction process may mask the relaxation process. Also with increasing the molar ratio of CSA/Py, value of ε'' increases which can be attributed to increase contribution to the dc electrical conduction due to the more availability of free charge carriers at higher dopant/monomer ratio.

6.1.8. Electric modulus studies

It is difficult to distinguish between the polarization and conductivity relaxation contributions since the dielectric loss spectra of PPy nanotubes do not show any relaxation peak. However, the dielectric spectra can be analysed using the complex electric modulus formalism for the materials whose loss spectra exhibit a dc conduction phenomenon [277]. The complex electric modulus (M^*) defined as the reciprocal of complex dielectric permittivity ($M^* = 1/\varepsilon^*$), can be expressed as:

$$M^*(\omega) = \frac{1}{\varepsilon^*(\omega)} = \frac{1}{\varepsilon' - j\varepsilon''} = \frac{\varepsilon'}{\varepsilon'^2 + \varepsilon''^2} + j\frac{\varepsilon''}{\varepsilon'^2 + \varepsilon''^2} = M'(\omega) + jM''(\omega) \tag{6.13}$$

where $M'(\omega)$ and $M''(\omega)$ are the real and imaginary parts of M^*, respectively can be written as:

$$M' = \frac{\varepsilon'}{(\varepsilon')^2 + (\varepsilon'')^2} \tag{6.14}$$

$$M'' = \frac{\varepsilon''}{(\varepsilon')^2 + (\varepsilon'')^2} \tag{6.15}$$

The plots of real part of modulus (M') vs. frequency (ω) and imaginary part of modulus (M'') vs. frequency (ω) of PPy nanotubes at different CSA/Py molar ratios at room temperature are depicted in Figs. 6.12 and 6.13, respectively. Fig. 6.12 shows that for each M' spectrum, M' increases with increasing frequency and attains a maximum constant value $(M_\infty = 1/\varepsilon_\infty)$ at high frequencies due to the conductivity relaxation process. At lower frequencies, value of M' approaches to zero which suggests the suppression of electrode polarization effects [279]. On the other hand, in Fig. 6.13 each M'' plot shows a well defined loss peak corresponding to a particular frequency called the relaxation frequency (ω_{max}) at which charge carriers undergo the relaxation process. The dispersion of both M' and M'' with frequency indicates the presence of relaxation time distribution for conduction. The relaxation frequency corresponding to each relaxation peak signifies the transition region from dc to ac conduction, the frequencies left to the relaxation peak wherein the charge carriers are mobile over long distances contributes to dc conduction and frequencies right to the relaxation peak implies that the charge carriers are spatially confined to their potential wells that corresponds to ac conduction. The relaxation time (τ) for the charge carriers can be calculated as follows:

$$\tau = 1/\omega_{max} \tag{6.16}$$

It is observed that the relaxation peak shifts towards higher frequencies with increasing CSA/Py molar ratio indicating a decrease in the relaxation time for charge carrier motion in PPy nanotubes.

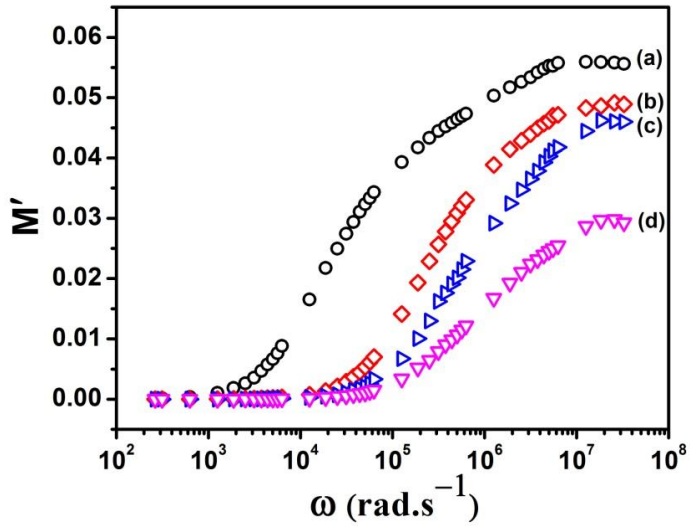

Figure 6.12: *Plots of real part of modulus* (M') *vs. frequency* (ω) *of PPy nanotubes at CSA/Py molar ratios of (a) 0.1:1, (b) 0.5:1, (c) 1:1 and (d) 2:1 at room temperature (303 K).*

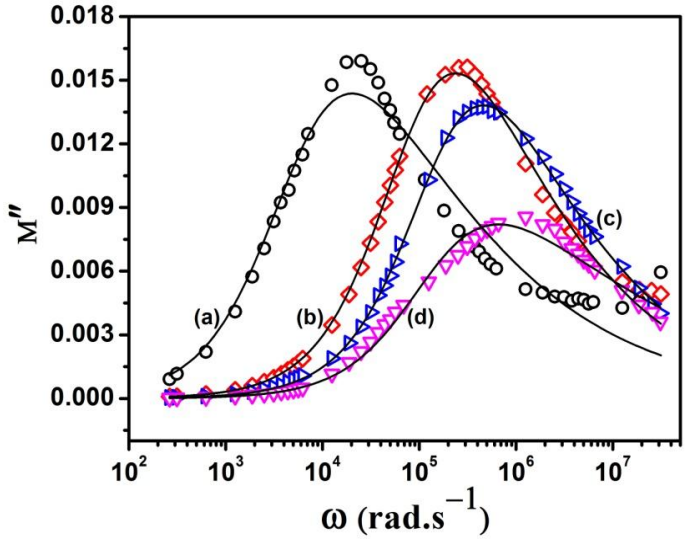

Figure 6.13: *Plots of imaginary part of modulus* (M'') *vs. frequency* (ω) *of PPy nanotubes at CSA/Py molar ratios of (a) 0.1:1, (b) 0.5:1, (c) 1:1 and (d) 2:1 at room temperature (303 K).*

However, the temperature also affects the position of the relaxation peak in M'' spectra. For example, Fig. 6.14 depicts the temperature dependent plots of M'' vs. ω of PPy nanotubes at CSA/Py molar ratio of 2:1. The figure shows that with increasing temperature, the relaxation peak shifts towards higher frequencies indicating smaller relaxation time for the charge carrier motion. At higher temperature the polymer chains

movement and the charge carrier's mobility increase giving rise to a decrease in relaxation time resulting in shifting of the relaxation peak to higher frequencies.

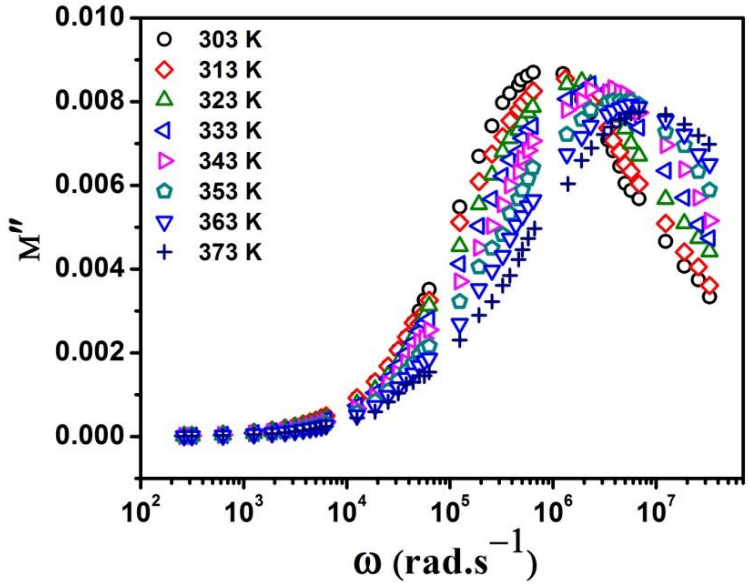

Figure 6.14: *Temperature dependence of M'' spectra of PPy nanotubes at CSA/Py molar ratio of 2:1.*

These results predict that the relaxation time depends on both the temperature and dopant/monomer ratio. The relaxation time (τ) determined from M'' spectra follow the Arrhenius equation [280]:

$$\tau = \tau_{0M} \exp(\frac{E_{aM}}{kT}) \qquad (6.17)$$

where τ_{0M} is the high temperature limit of relaxation time and E_{aM} is the activation energy for relaxation of charge carriers. The values of relaxation frequency $(\omega_{\max})$ and relaxation time (τ) of PPy nanotubes at CSA/Py molar ratio of 2:1 corresponding to each measured temperature are presented in Table 6.6. The plots of $\ln(\tau)$ vs. $1000/T$ of PPy nanotubes at CSA/Py molar ratio of 2:1 are depicted in Fig. 6.15. The plot shows a linear relationship between $\ln(\tau)$ vs.$1000/T$, where the points represent the experimentally determined relaxation time and the solid line represents the theoretical best fitted curve for the calculated relaxation times using equation (6.17). The slope and intercept of the best fitted curve gives the value of τ_{0M} = 6.82 × 10^{-12} s and E_{aM} = 0.31 eV, respectively.

Table 6.6: Values of relaxation frequency (ω_{max}) and relaxation time (τ) of PPy nanotubes for CSA/Py molar ratio of 2:1 at different temperatures.

Temperature (K)	Relaxation frequency (ω_{max}) (rad.s^{-1})	Relaxation time (τ) $\times 10^{-7}$ (s)
303	8.13×10^5	12.30
313	11.68×10^5	8.56
323	17.33×10^5	5.77
333	25.70×10^5	3.89
343	32.67×10^5	3.06
353	43.66×10^5	2.29
363	59.88×10^5	1.67
373	80.00×10^5	1.25

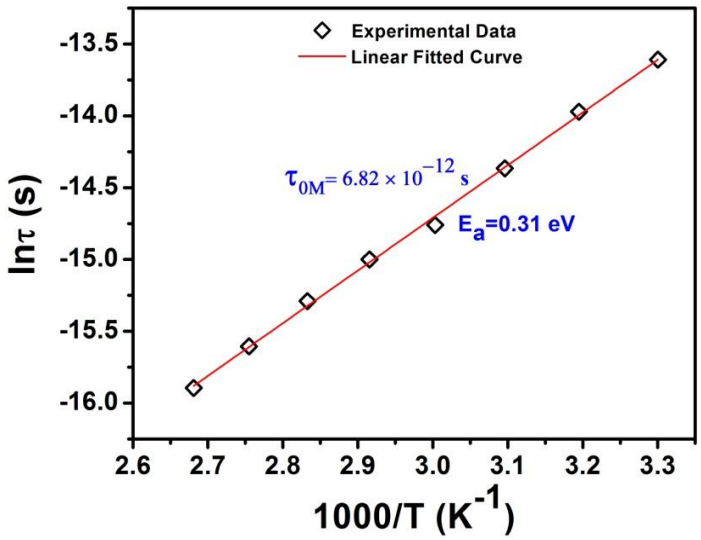

Figure 6.15: *Plots of* $\ln(\tau)$ *vs.* $1000/T$ *of PPy nanotubes at CSA/Py molar ratio of 2:1.*

The electric modulus can be written as Laplace transformation of a relaxation function $\varphi(t)$ [182]:

$$M^* = M_\infty[1-\int_0^\infty e^{-j\omega t}(\frac{d\varphi}{dt})dt] \qquad (6.18)$$

where $M_\infty(\omega)=1/\varepsilon_\infty(\omega)$, $\varepsilon_\infty(\omega)$ is the asymptotic value of the real part of dielectric

permittivity at high frequency and $\varphi(t)$ is the relaxation function that gives the time evolution of the electric field within the materials. This type of modulus spectra can be expressed by a stretched exponential relaxation function (decay) empirically defined by Kohlrausch-Williams-Watts (KWW) function [281, 282]:

$$\varphi(t) = \exp[-(t/\tau)^{\beta}], \quad 0 < \beta < 1 \tag{6.19}$$

where τ is the characteristic relaxation time and β is the Kohlrausch relaxation parameter that decreases with increasing relaxation time distribution. In particular, value of β ranges in between $0 < \beta < 1$ that represents departure from the Debye relaxation process $(\beta = 1)$. In the frequency approach, M'' can be approximated with equation (6.19) as follows [283]:

$$M''(\omega) = \frac{M''_{\max}}{[(1-\beta) + (\beta/(1+\beta))[\beta(\omega_{\max}/\omega) + (\omega/\omega_{\max})^{\beta}]]} \tag{6.20}$$

where $M''_{\max}$ is the peak maximum of the imaginary part of electric modulus. The frequency dependence of M'' spectra at various CSA/Py molar ratios (Fig. 6.13) are fitted using equation (6.20) and the calculated parameters such as $M''_{\max}$, $\omega_{\max}$ and β from the best fitted curves are tabulated in Table 6.7. The calculated values of β lie in 0.60-0.69 which suggests the non-Debye relaxation process of charge carriers. Furthermore, with increasing the CSA/Py molar ratio the value of β decreases suggesting more deviation from the idealized Debye relaxation.

Table 6.7: Values of maximum imaginary modulus $(M''_{\max})$, relaxation frequency $(\omega_{\max})$, relaxation time (τ) and stretched exponent (β) of PPy nanotubes at various CSA/Py molar ratios at room temperature (303 K).

CSA/Py molar ratio	$M''_{\max}$	$\omega_{\max}$ (rad.s^{-1})	τ (s)	β
0.1:1	0.0143	1.97×10^{4}	5.05×10^{-5}	0.69
0.5:1	0.0153	2.63×10^{4}	3.80×10^{-6}	0.66
1:1	0.0136	4.39×10^{4}	2.27×10^{-6}	0.64
2:1	0.0082	8.13×10^{4}	1.23×10^{-6}	0.60

The scaling behavior of modulus spectra provides an insight into the temperature and dopant/monomer ratio dependence of relaxation dynamics [371, 372]. The scaling plots of M'' spectra of PPy nanotubes at various CSA/Py molar ratios at room temperature (303 *K*) are shown in Fig. 6.16. The scaling is done by dividing M'' with M''_{max}, while the frequency axis is scaled by the relaxation frequency ω_{max}. The M'' spectra at different CSA/Py ratios merge on a single master curve indicating that the relaxation dynamics of charge carriers are independent of dopant/monomer molar ratio. Furthermore, such scaling behavior of M'' spectra of PPy nanotubes is also observed at various temperatures. Fig. 6.17 depicts the scaling plots of M'' spectra of PPy nanotubes at CSA/Py molar ratio of 2:1 for different temperatures. The individual M'' spectrum at different temperatures superimpose on a single master curve, which indicates that the dynamical processes occurring at different temperature are independent of temperature. These results suggest that the relaxation dynamics of charge carriers follow a common relaxation mechanism throughout the temperature range and dopant/monomer ratio.

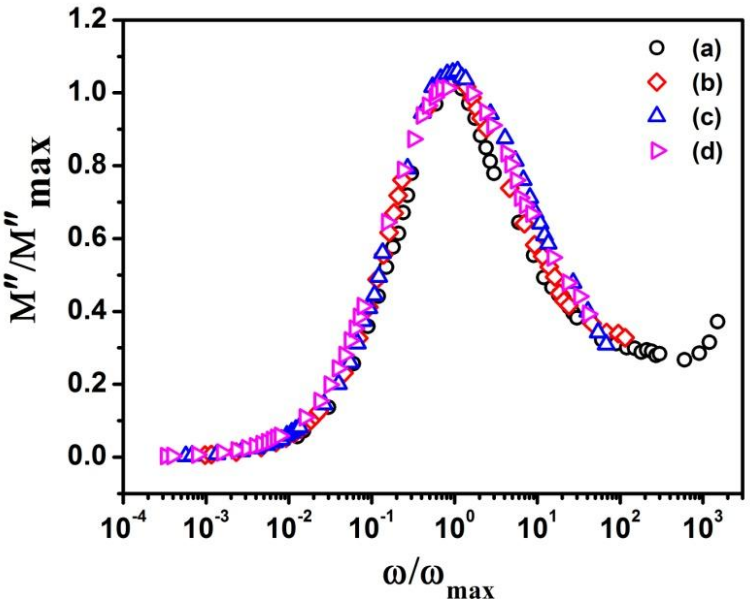

Figure 6.16: *Scaling of M'' spectra of PPy nanotubes at CSA/Py molar ratios of (a) 0.1:1, (b) 0.5:1, (c) 1:1 and (d) 2:1 at room temperature (303 K).*

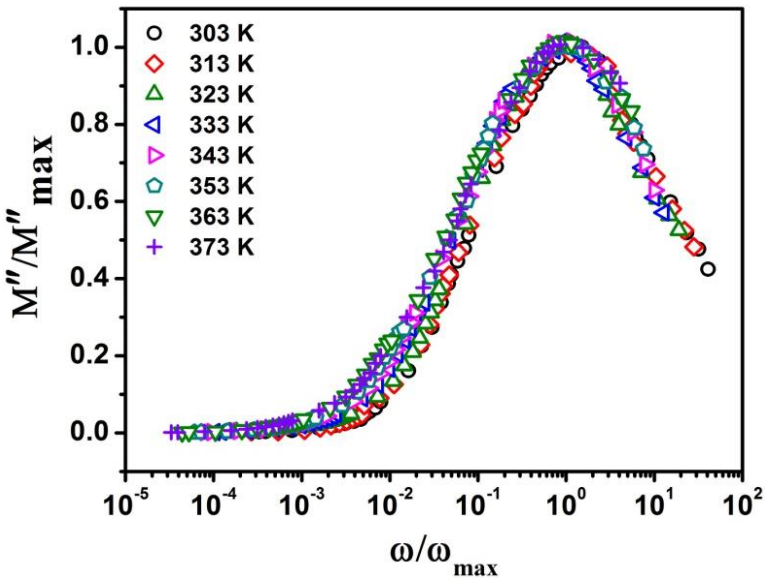

Figure 6.17: *Scaling of M'' spectra of PPy nanotubes at CSA/Py molar ratio of 2:1 at different temperatures.*

6.1.9. AC conductivity studies

The ac conductivity study provides vital information about the charge transport mechanism in disordered materials. The frequency dependence of total ac conductivity $\sigma'(\omega)$ can be expressed using the following equation [242],

$$\sigma'(\omega) = \omega\varepsilon_0\varepsilon'' \tag{6.21}$$

where ω is the frequency, ε_0 is the permittivity in free space and ε'' represents the dielectric loss. The plots of total ac conductivity σ' vs. frequency (ω) of PPy nanotubes at different CSA/Py molar ratios at room temperature are depicted in Fig. 6.18. Each conductivity plot shows frequency-independent and frequency-dependent regions in the measured frequency region. The transition from the frequency-independent to the frequency-dependent region represents the onset of conductivity relaxation phenomena. The corresponding onset frequency is called the hopping (ω_H) above which conductivity follows frequency dispersion with a power law equation as follows [156],

$$\sigma_{ac}(\omega) = A\omega^s, \text{ with } 0 < s < 1 \tag{6.22}$$

where the frequency independent pre-exponential factor *A* depends on temperature only and *s* represents the frequency exponent whose value lies between 0 and 1. Jonscher

[171] interpreted this characteristic behavior of charge transport in disordered materials as universal dynamic response (UDR). The dc conductivity (σ_{dc}) can be obtained by subtracting the ac conductivity from the total conductivity.

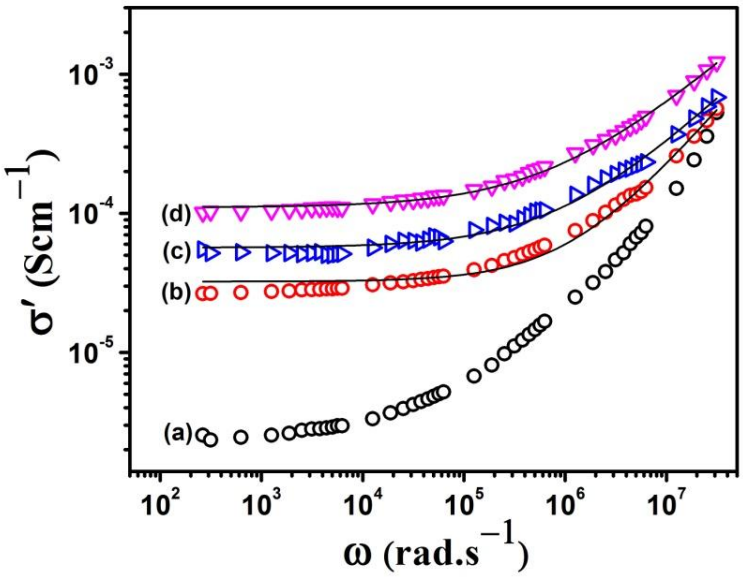

Figure 6.18: *Plots of total conductivity* (σ') *vs. frequency* (ω) *of PPy nanotubes at different CSA/Py molar ratios of (a) 0.1:1, (b) 0.5:1, (c) 1:1 and (d) 2:1 at room temperature (303 K).*

The frequency dependence of total ac conductivity $\sigma'(\omega)$ can be expressed as follows:

$$\sigma'(\omega) = \sigma_{dc} + A\omega^{s} = \sigma_{dc}[1 + (\frac{\omega}{\omega_H})^{s}] \qquad (6.23)$$

From the theoretical best fitted curve of the experimentally determined conductivity data in Fig. 6.18 using equation (6.23), the values of different parameters such as σ_{dc}, ω_H and *s* can be extracted and are tabulated in Table 6.8. The values of σ_{dc} and ω_H increase whereas the frequency exponent *s* decreases with increasing the CSA/Py molar ratio. The decreased value of *s* with increasing dopant/monomer molar ratio indicates that dispersion of ac conductivity with frequency reduces. Also with increasing CSA/Py ratio, contribution of the dc conductivity to the total conductivity increases, wherein the hopping frequency shifts to high frequencies. The conducting polymers do not possess permanent dipoles, however the localized motion of the strongly trapped charges in them [284, 373] acts as an effective electric dipole under the externally applied electric

field [276]. Charges can hop to neighbouring sites forming a continuous network which allows the charge carriers to travel through the sample and contribute to electrical conductivity [157]. Moreover, total conductivity increases with increasing CSA/Py molar ratio. The incorporation of dopant anions into the PPy chains reduces the charge trapping centres, thereby leading to a large number of charge participations in conducting process. With increasing dopant/monomer ratio, number of charge carriers increases which can hop into the neighbouring sites resulting increase in electrical conduction.

Table 6.8: Room temperature values of dc conductivity (σ_{dc}), hopping frequency (ω_H), frequency exponent (*s*) and barrier activation energy (W_H) for PPy nanotubes at different CSA/Py molar ratios.

CSA/Py molar ratio	σ_{dc} (Scm^{-1})	ω_H $\times10^5$ (rad.s^{-1})	*s*	W_H $\times10^{-4}$ (eV)
0.1:1	2.38×10^{-6}	4.43	0.94	86.16
0.5:1	3.23×10^{-5}	5.40	0.85	34.46
1:1	5.67×10^{-5}	7.38	0.69	16.67
2:1	1.10×10^{-4}	8.44	0.65	14.77

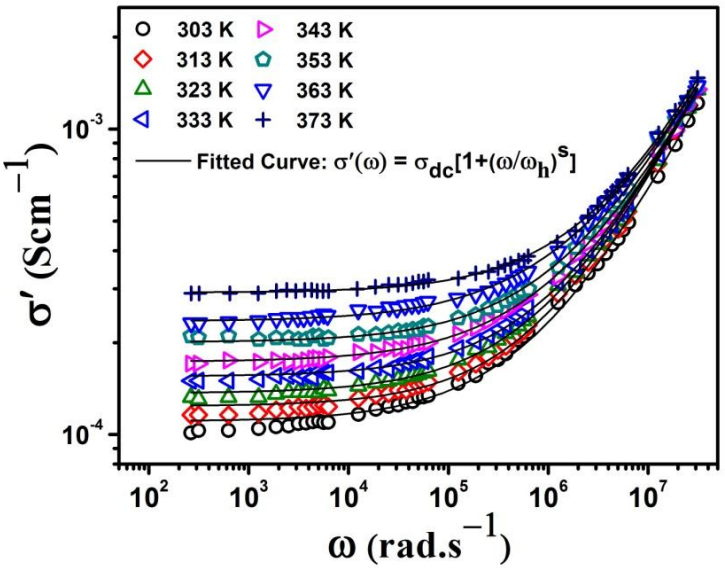

Figure 6.19: *Plots of total conductivity* $\sigma'(\omega)$ *of PPy nanotubes at CSA/Py molar ratio of 2:1 at different temperatures.*

Fig. 6.19 depicts the plots of total conductivity for PPy nanotubes at CSA/Py molar ratio of 2:1 at different temperatures. The σ_{dc} increases with increasing the temperature obeying the temperature dependent Arrhenius relation,

$$\sigma_{dc} = \sigma_0 \exp(-\frac{E_\sigma}{kT}) \tag{6.24}$$

where σ_0 is the pre-exponential factor and E_σ is the activation energy for dc conduction. Fig. 6.20(i) shows the plot of $\ln\sigma_{dc}$ vs. $1000/T$ for PPy nanotubes at CSA/Py molar ratio of 2:1. The intercept and slope of the best fitted linear curve using equation (6.24) gives the values of the pre-exponential factor, σ_0 =1.48×10^{-2} Scm^{-1} and activation energy, E_σ = 0.21 eV, respectively. To correlate between the dc and ac conduction, the temperature dependence of hopping frequency is compared with that of the dc conductivity behavior as shown in Fig. 6.20(ii). The temperature dependence of hopping frequency (ω_H) is thermally activated and obeys also the Arrhenius relation:

$$\omega_H = \omega_0 \exp(-E_H/kT) \tag{6.25}$$

where ω_0 is the pre-exponential factor and E_H is the hopping activation energy.

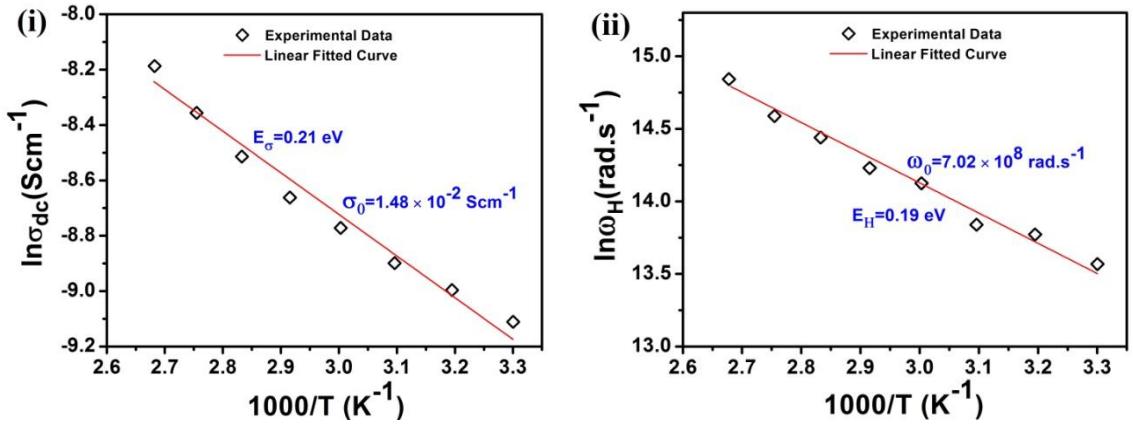

Figure 6.20: *Plots of (i)* $\ln\sigma_{dc}$ *vs.* $1000/T$ *and (ii)* $\ln\omega_H$ *vs.* $1000/T$ *of PPy nanotubes at CSA/Py molar ratio of 2:1.*

The hopping frequency shifts towards high frequencies with increasing temperature i.e. at higher temperature the dc conductivity is dominant below this hopping frequency. The best fitted linear curve using equation (6.25) gives the value of ω_0 = 7.02 ×10^8 rad.s^{-1} and E_H = 0.19 eV, respectively. Both the calculated values of E_H and E_σ are

nearly same suggesting the same transport mechanism, i.e. the thermally activated nearest neighbour hopping.

Several theoretical models based on the relaxation caused by the hopping or tunnelling of charge carriers between equilibrium sites have been proposed to explain the frequency and temperature dependence of ac conductivity and *s*: the two most widely used models are the correlated barrier hopping (CBH) and quantum mechanical tunnelling (QMT) models. The exact nature of charge transport mechanism can be obtained by the experimental studies of the temperature dependence of the frequency exponent (*s*). Fig. 6.21 depicts the temperature dependence of *s* for PPy nanotubes at various CSA/Py ratios. The value of *s* decreases with increasing temperature for all samples of PPy nanotubes, which can be attributed to weak interaction among the charge carriers on the neighbouring chains giving higher value of *s* at lower temperatures. As the temperature increases, interaction between the charge carriers on the neighbouring chains increases leading to a decrease in the value of *s*.

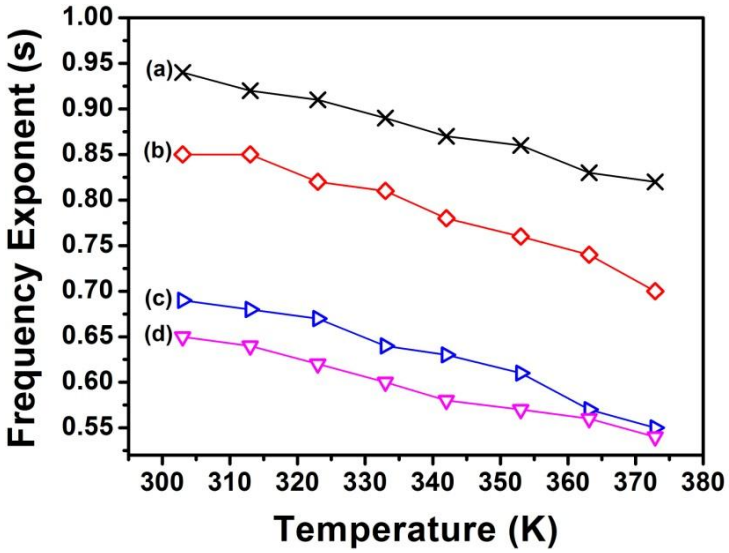

Figure 6.21: *Temperature dependence of frequency exponent (s) of PPy nanotubes at CSA/Py ratios of (a) 0.1:1, (b) 0.5:1, (c) 1:1 and (d) 2:1.*

In the QMT model, frequency exponent (*s*) can be written as [286],

$$s = 1 - \frac{4}{\ln(1/\omega\tau)} \tag{6.26}$$

where τ is the characteristic relaxation time. In the QMT model, the exponent *s* is temperature independent but depends on the frequency. In the QMT model, a

temperature dependent frequency exponent can be obtained assuming that the charge carriers form non-overlapping small polarons [286], i.e. the total energy of a charge carrier is lowered by the polaron energy resulting from the lattice distortion by a carrier. In this case the frequency exponent *s* can be expressed as:

$$s = 1 - \frac{4}{\ln(1/\omega\tau) - (W_H/kT)} \tag{6.27}$$

This means that the exponent *s* is temperature dependent which increases with the increasing temperature. According to the CBH model as proposed by Pike [162], the charge carrier's can hop between the neighbouring sites over the potential barrier separating them. The frequency exponent (s) in this model can be expressed as [155],

$$s = 1 - \frac{6kT}{W_H - kT\ln(\omega\tau)} \tag{6.28}$$

where k is the Boltzmann's constant, W_H is the effective barrier height and τ is the characteristic relaxation time. For small values of (W_H/kT), the expression for *s* yields,

$$s = 1 - \frac{6kT}{W_H} \tag{6.29}$$

The above equation (6.29) predicts that the value of *s* decreases with increasing temperature. Hence, decrease in value of *s* with increasing temperature suggests that the charge carriers in PPy nanotubes follow the CBH model i.e. the charge carriers make short range hopping motion between the localized sites separated by energy barriers of varying height. It is observed that the value of W_H decreases with increasing the dopant/monomer ratio suggesting reduction in the barrier height for the charge carrier's motion, thereby resulting increased electrical conduction in PPy nanotubes. According to the CBH model, the ac conductivity is given by the following relation:

$$\sigma_{ac}(\omega) = \frac{\pi^3}{24} N^2 \varepsilon' \varepsilon_0 \omega R_\omega^6, \tag{6.30}$$

where *N* is the density of the pair sites and R_ω is the hopping distance at a frequency ω, which is given as:

$$R_\omega = \frac{e^2}{\pi\varepsilon'\varepsilon_0[W_H + kT\ln(\omega\tau)]}, \tag{6.31}$$

where W_H is the binding energy of the charge carriers in their localized sites.

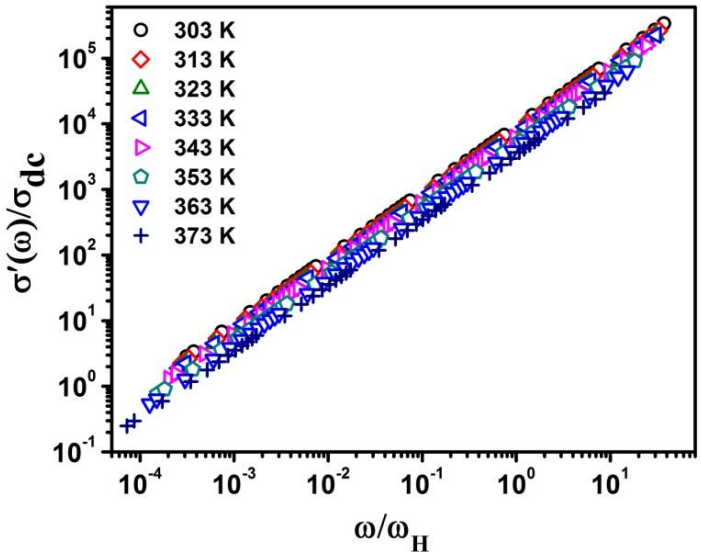

Figure 6.22: *Scaling plots of total conductivity of PPy nanotubes for CSA/Py molar ratio of 2:1 at different temperatures.*

The scaling behavior of ac conductivity in disordered materials is a unique property which provides a deeper insight about the conductivity mechanism. The scaling is done by scaling the ac conductivity axis with respect to σ_{dc} and the angular frequency axis with respect to the characteristic relaxation frequency $\omega_{\max}$ [161]. Fig. 6.22 depicts the scaling plots of total conductivity spectra of PPy nanotubes at CSA/Py molar ratio of 2:1 in the temperature range of 303-373 K. It is observed that the individual conductivity spectrum falls into a single master plot indicating that the relaxation dynamics of charge carriers are temperature independent. Also, such master plot implies the existence of the universal relaxation processes in disordered systems, in which the motion of the localized charge carriers at higher frequencies executes a sequence of forward-backward hops, while at low frequencies the charge carrier's transport over longer distances contributing to the net conduction.

6.2. 160 MeV Ni^{12+} swift heavy ion irradiation effects on PPy nanotubes

The detailed results on PPy nanotubes synthesized at different CSA/Py molar ratios as discussed in Section 6.1 reveal that the sample of PPy nanotubes at CSA/Py molar ratio of 2:1 has shown the best properties. Therefore this sample has been chosen to irradiate by 160 MeV Ni^{12+} swift heavy ions (SHI) with a view to further improve its different physico-chemical properties. The SHI irradiation on PPy nanotubes was performed at

the 15 UD Pelletron Accelerator available at the Inter University Accelerator Centre (IUAC), New Delhi, India using the Materials Science beam line facilities. Five different ion fluence of 10^{10}, 5×10^{10}, 10^{11}, 5×10^{11} and 10^{12} ions/cm^2 were used to irradiated the films of PPy nanotubes keeping the ion current constant at 0.5 pna (particle nano-ampere). The energy of Ni^{12+} ion beam was chosen as 160 MeV so that the ion beam could completely penetrated the PPy nanotube's films and the films undergo uniform irradiation effects as the projected ion range was of 42 μm, as calculated by using SRIM (stopping and range of ions in matter) software [287], which was larger than the film's thickness (~30-35 μm). The results on the effects of swift heavy ion beam irradiation have been discussed under the following sections.

6.2.1. High resolution transmission electron microscopy studies

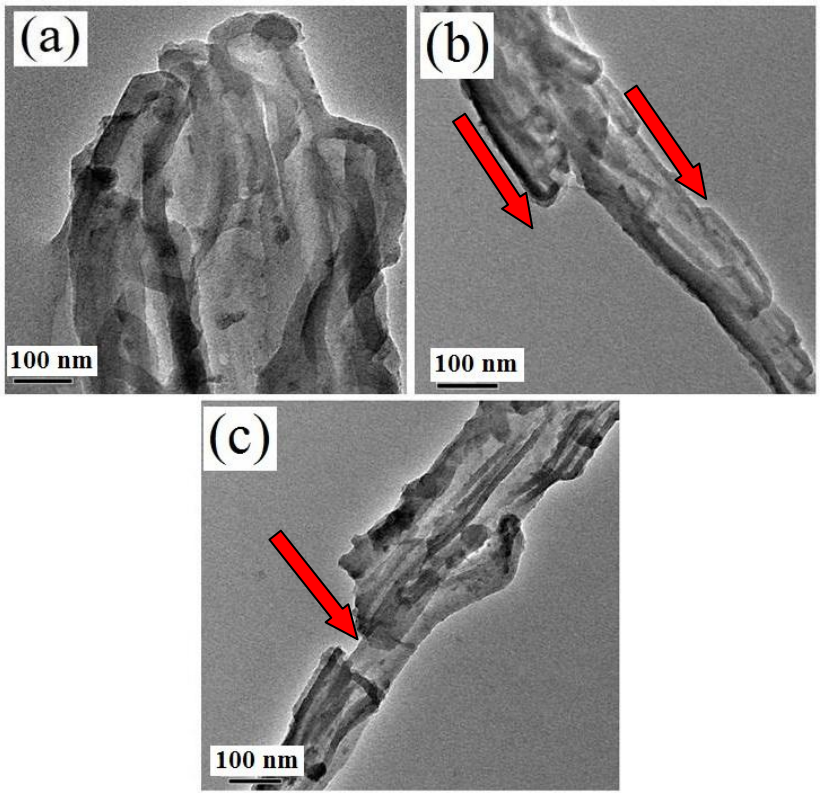

Figure 6.23: *HRTEM micrographs of (a) pristine and irradiated PPy nanotubes at ion fluences of (b) 5×10^{11} and (c) 10^{12} ions/cm^2.*

The HRTEM micrographs of the pristine and irradiated PPy nanotubes are depicted in Fig. 6.23. It is observed that upon SHI irradiation, the PPy nanotubes irradiated at the

ion fluence of 5×10^{11} ions/cm^2 become more align and denser as compared to the pristine PPy nanotubes. However, PPy nanotubes irradiated at the highest ion fluence of 10^{12} ions/cm^2 show the breaking or degradation of PPy nanotubes, which results in the random alignments of PPy nanotubes.

6.2.2. X-ray diffraction studies

The XRD diffraction patterns of the pristine and irradiated PPy nanotubes at the ion fluence of 10^{10}, 5×10^{10}, 10^{11}, 5×10^{11} and 10^{12} ions/cm^2, respectively are depicted in Fig. 6.24. The characteristic broad diffraction peak of the pristine PPy nanotubes is observed at around $2\theta = 19.96^{o}$.

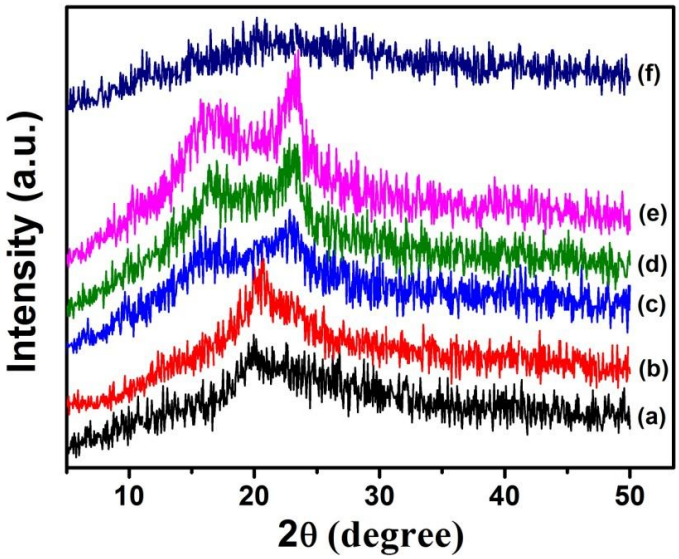

Figure 6.24: *XRD diffraction patterns of (a) pristine and irradiated PPy nanotubes at ion fluences of (b) 10^{10}, (c) 5×10^{10}, (d) 10^{11}, (e) 5×10^{11} and (f) 10^{12} ions/cm^2.*

It is observed that upon SHI irradiation, a new peak begin to appear at $2\theta = 15.90^{o}$ at the irradiation fluence of 5×10^{10} ions/cm^2, which grows in intensity with increasing fluence up to 5×10^{11} ions/cm^2. The appearance of the new peak suggests the formation of new crystalline domains with higher d-spacing (~5.41 Å) in the irradiated PPy nanotubes. Upon SHI irradiation, the characteristic diffraction peak of pristine PPy nanotubes at $2\theta = 19.96^{o}$ shifts towards higher angle around 2θ=22.95° at the ion fluence of 5×10^{10} ions/cm^2. This indicates the formation of denser crystalline domains in the PPy nanotubes upon SHI irradiation. However, with further increase in irradiation

fluence up to 5×10^{11} ions/cm^2, the diffraction peak position remains almost same, which suggest that the density of the PPy nanotubes irradiated with ion fluence of 5×10^{11} ions/cm^2 does not increase further but intensity of the peak increases with increasing the ion fluence up to 5×10^{11} ions/cm^2 indicating the increase in volume of the denser crystalline domains. The formation of crystalline domains of two different *d*-spacings in the irradiated PPy nanotubes at the moderate and higher irradiation fluence (5×10^{10}-5×10^{11} ions/cm^2) could be attributed to the hollow tubular morphology of the PPy nanotubes. Two different crystallinine domains with larger *d*-spacing (low density) and lower *d*-spacing (high density) may form in PPy nanotubes upon SHI irradiation. High density crystalline domain with lower *d*-spacing may form due to rearrangement of the adjacent PPy nanotubes by cross-linking between the polymer chains on adjacent PPy nanotubes. Low density with higher *d*-spacing crystalline domain may form by the formation of single or multiple helices along the ion trajectories through the nanotubes resulting in intra-chain periodicity of the PPy nanotubes.

At the highest irradiation fluence of 10^{12} ions/cm^2 employed in the present work, the degradation or breaking of PPy nanotubes occurs due to deposition of huge electronic energy (~ 4.5×10^2 eV/Å) along the ion track and whole crystalline domain structure is disrupted. The broad hump showing amorphous structure is observed, which is also corroborated by the HRTEM studies. This can originate from either the ion beam generated defects and dislocations or the grain splitting effect at the highest irradiation fluence of 10^{12} ions/cm^2, which dominates over the induced crystallization process. Upon SHI irradiation at the low and moderate ion fluences, there is an increase in total intensity of the diffraction peak with increasing the irradiation fluence which reveals the enhancement of crystallinity of PPy nanotubes. But there is a sudden decrease in intensity (less than the pristine sample) of the diffraction peak at the ion fluence of 10^{12} ions/cm^2 which is a direct consequent of reduction of crystallinity of irradiated PPy nanotubes at highest fluence. The ordering of the polymer chains (X_C) can be calculated using equation (6.1)

$$X_C = \frac{A^I}{A^T}\times100\%$$

as mentioned in section 6.1. The increase in crystallinity of PPy nanotubes after SHI irradiation can be attributed to the systematic alignment of polymer chains by chain

folding or by formation of single or multiple helices, for at least along their lengths. However, the decrease in crystallinity at the highest ion fluence can be thought of the scissioning of polymer chains due to tremendous electronic energy deposition. Upon SHI irradiation, the shifting of the diffraction peak towards higher angular side is due to the contraction of polymer lattice [374]. The increase density makes the polymer chains more compact and produces closely packed regions by chain folding, cross-linking of the polymer chains or due to formation of single or multiple helices resulting PPy nanotubes more crystalline. The increase crystallinity provides an easy path for charge carrier's transport and thereby resulting increase in electrical conduction into the PPy nanotubes. The extent of order (L) of pristine and irradiated PPy nanotubes has been calculated using equation (6.2),

$$L = \frac{K\lambda}{\beta \cos\theta}$$

as discussed in section 6.1. The calculation shows that after irradiation, the extent of polymer chain (L) in PPy nanotubes increases with increasing the irradiation fluence up to 5×10^{11} ions/cm^2. However beyond this ion fluence, extent of polymer chains decreases as compared to the pristine sample. The decrease in extent of chain order at the highest ion fluence of 10^{12} ions/cm^2 leads to the formation of disordered structure in the irradiated PPy nanotubes [375].

The hopping distance (R) of both pristine and irradiated PPy nanotubes has been calculated using equation (6.3),

$$R = \frac{5}{8}\left[\frac{\lambda}{\sin\theta}\right]$$

as discussed in section 6.1.

The d-spacing of both pristine and irradiated PPy nanotubes can be calculated using the Bragg's diffraction formula [264],

$$2d\sin\theta = \lambda \qquad (6.32)$$

It is also observed that the d-spacing of irradiated PPy nanotubes decreases with increasing the irradiation fluence up to 5×10^{11} ions/cm^2, however at the highest ion fluence of 10^{12} ions/cm^2, the d-spacing of the irradiated PPy nanotubes increases as compared to the pristine PPy nanotubes. The values of angle of diffraction (2θ),

ordering of chains (X_C), inter-planar spacing (d) and extent of chain order (L) of the pristine and irradiated PPy nanotubes at different ion fluences are recorded in Table 6.9.

Table 6.9: Angle of diffraction (2θ), ordering of chains (X_C), inter-planar spacing (d), hopping distance (R) and extent of chain order (L) of pristine and irradiated PPy nanotubes at different ion fluences.

Fluence (ions/ cm^2)	Diffraction peak 2θ (°)		Ordering of chains X_C (%)		Inter-planar spacing d (Å)		Hopping distance R (Å)		Extent of chain order L (Å)	
	$2\theta_1$	$2\theta_2$	X_{c1}	X_{c2}	d_1	d_2	R_1	R_2	L_1	L_2
Pristine	---	19.96	---	25.72	---	4.44	---	5.56	---	5.57
1×10^{10}	---	20.45	---	26.20	---	4.34	---	5.42	---	7.71
5×10^{10}	15.90	22.95	3.0	24.19	5.57	3.87	6.96	4.83	20.56	6.50
1×10^{11}	16.37	22.95	3.6	27.15	5.41	3.87	6.77	4.84	21.26	6.67
5×10^{11}	16.37	23.10	7.5	24.44	5.41	3.85	6.77	4.81	18.73	8.32
1×10^{12}	---	20.75	---	23.40	---	4.28	---	5.34	---	4.12

N. B.: $2\theta_1$: broad diffraction peak at lower angle, $2\theta_2$: broad diffraction peak at higher angle, X_{C1}: ordering of chains calculated taking peak position at $2\theta_1$, X_{C2}: ordering of chains calculated taking peak position at $2\theta_2$, d_1: inter-planar spacing due to $2\theta_1$, d_2: inter-planar spacing due to $2\theta_2$, R_1: hopping distance due to $2\theta_1$, R_2: hopping distance due to $2\theta_2$, L_1: extent of chain order due to $2\theta_1$, L_2: extent of chain order due to $2\theta_2$.

6.2.3. *Fourier transform infrared spectroscopy analysis*

The FTIR spectral analysis has been carried out to investigate the structural changes induced in the SHI irradiated PPy nanotubes. The changes have been estimated from the relative increase or decrease in the band intensity associated with the functional groups. Fig. 6.25 depicts the FTIR spectra of the pristine and irradiated PPy nanotubes at different ion fluences. The presence of the same main vibrational bands in the SHI irradiated PPy nanotubes at all the ion fluence indicate that the structure of PPy nanotubes is not destroyed upon SHI irradiation. However, it is observed that upon SHI irradiation, the intensity of the vibrational bands increases as compared to the pristine PPy nanotubes up to the ion fluence of 5×10^{11} ions/cm^2, while at the highest ion fluence

of 10^{12} ions/cm^2 the intensity of the vibration bands again decreases. The increase in vibration band intensity of the SHI irradiated PPy nanotubes indicate the irradiation induced cross-linking which as a result increase their crystallinity. The decrease in vibration band intensity at the highest irradiation fluence of 10^{12} ions/cm^2 indicates the breaking of bonds and degradation of PPy nanotubes upon SHI irradiation.

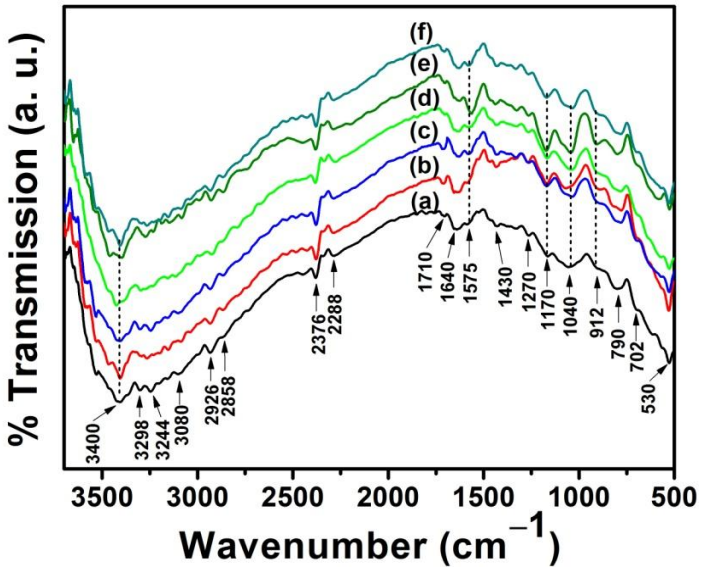

Figure 6.25: *FTIR spectra of (a) pristine and irradiated PPy nanotubes at ion fluences of (b) 10^{10}, (c) 5×10^{10}, (d) 10^{11}, (e) 5×10^{11} and (f) 10^{12} ions/cm^2.*

6.2.4. UV-vis absorption spectroscopy studies

Fig. 6.26 depicts the UV-vis absorption spectra of the pristine and irradiated PPy nanotubes at ion fluences of 10^{10}, 5×10^{10}, 10^{11}, 5×10^{11} and 10^{12} ions/cm^2, respectively. The UV-vis absorption spectra of pristine PPy nanotubes shows three absorption bands: the band at 340 nm is due to π-π* transition, band at 484 nm is ascribed to the transition from valence band to polaron band and a free tail above 670 nm is correspond to the transition from valence band to bipolaron or anti-bipolaron state of oxidized form of PPy nanotubes. It is observed that upon SHI irradiation, the position of π-π* band remains unaffected, while at the low and moderate ion fluence (10^{10} - 5×10^{11} ions/cm^2) the polaron absorption band makes a red shift with increasing the irradiation fluence up to 5×10^{11} ions/cm^2. However at the highest ion fluence of 10^{12} ions/cm^2, the polaron band makes a blue shift i.e. to the smaller wavelength region.

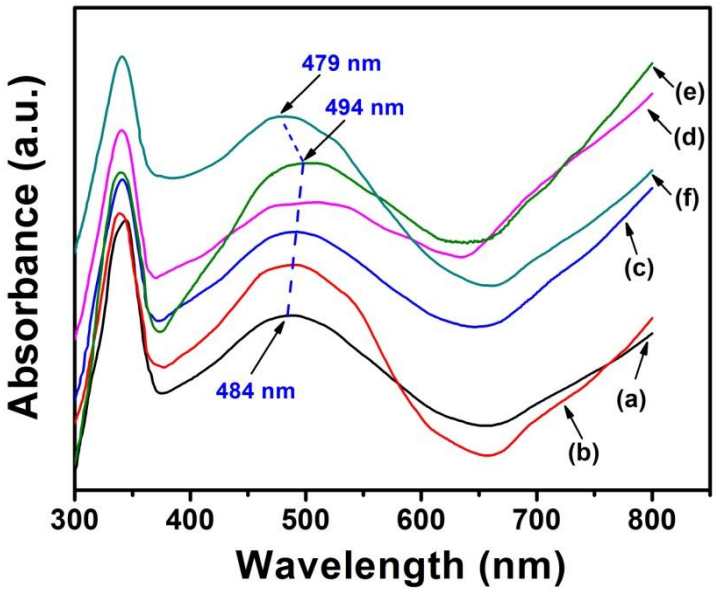

Figure 6.26: *UV-vis absorption spectra of (a) pristine and irradiated PPy nanotubes at ion fluences of (b) 10^{10}, (c) 5×10^{10}, (d) 10^{11}, (e) 5×10^{11} and (f) 10^{12} ions/cm^2.*

The red shifting of the absorption band with increasing ion fluence can be related to the structure of the energy gap of the polymer [376], namely the irradiation with SHI induces cleavage of -C-C- bonds and dehydrogenation of the PPy chains i.e. evaluation of the hydrogen atoms as hydrogen molecules and this in turns produces conjugated -C=C- bonds. During SHI irradiation, the polymeric material gradually loses gas atoms and the enhancement of carbon atoms leads to the formation of a hydrogenated amorphous carbon with optical band gap energy depending on the H/C atom ratio [339]. The shifting in the absorption edge as function of ion fluence can be correlated with the optical band gap energy. The optical band gap energy for materials represents the most common optical parameter that explains the optical transitions, which can be defined as the difference between the bottom of the conduction band and top of the valence band. The optical band gap energy for materials can be determined using equation (6.4)

$$\alpha(\nu) = \frac{B_\alpha (h\nu - E_g)^n}{h\nu}$$

as mentioned in section 6.1.

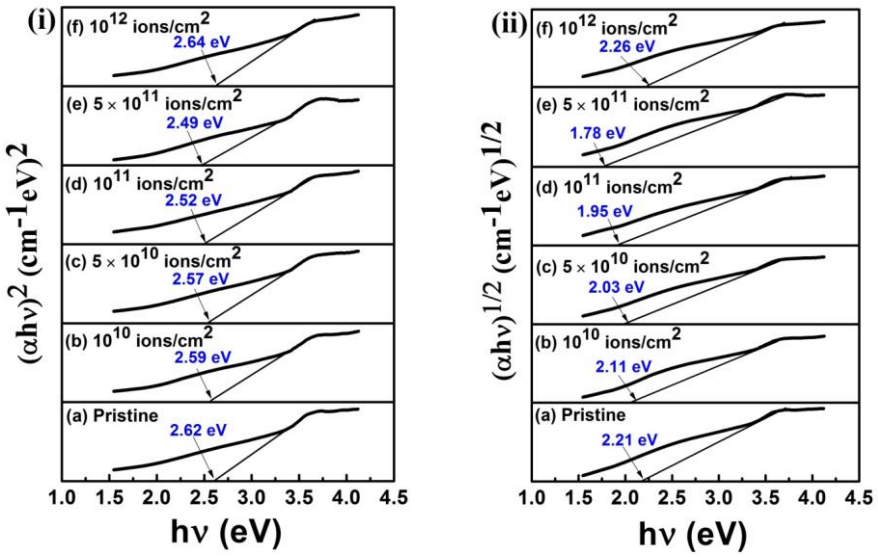

Figure 6.27: *Plots of variation of (i) $(\alpha h\nu)^2$ vs. $h\nu$ and (ii) $(\alpha h\nu)^{1/2}$ with $h\nu$ of pristine and irradiated PPy nanotubes at different ion fluences.*

The variation of $(\alpha h\nu)^2$ with $h\nu$ and $(\alpha h\nu)^{1/2}$ with $h\nu$ of the pristine and irradiated PPy nanotubes are depicted in Fig. 6.27 (i)&(ii), respectively. The optical band gap energy E_g can be calculated from the intersection of the extrapolated lines from the linear portion of the curves, from the photon energy axis. For direct transition, the electron is simply transferred vertically from the top of the valence band to the bottom of conduction band without the change in momentum [340], while in case of indirect transition the irradiation with SHI produces species (bond rapture, free radicals etc.) which increases the electronic disorder that produces a permitted state in the forbidden band or the deformation of valence band.

Fig. 6.28 compares the values of direct and indirect band gap energies both for the pristine and irradiated PPy nanotubes at irradiation fluences of 10^{10}, 5×10^{10}, 10^{11}, 5×10^{11} and 10^{12} ions/cm^2. For the irradiated PPy nanotubes, both the direct and indirect band gap energies decrease with increasing the ion fluence up to 5×10^{11} ions/cm^2, however at the highest ion fluence of 10^{12} ions/cm^2 both direct and indirect band gap energies increase to a value higher than that of pristine PPy nanotubes. This in turn indicates the simultaneous existence of direct and indirect band gaps in PPy nanotubes with a decreasing tendency at low and moderate ion fluence (10^{10} - 5×10^{11} ions/cm^2) and increasing tendency at the highest ion fluence (10^{12} ions/cm^2). Moreover, value of indirect band gap energy is found to be lower than its corresponding direct band gap

energy for the pristine and irradiated PPy nanotubes. The decrease in the optical band gap energy can be attributed to the formation of defects upon SHI irradiation and/enrich carbon clusters due to partial evaluation of hydrogen molecules. These clusters influence the optical properties of the irradiated PPy nanotubes.

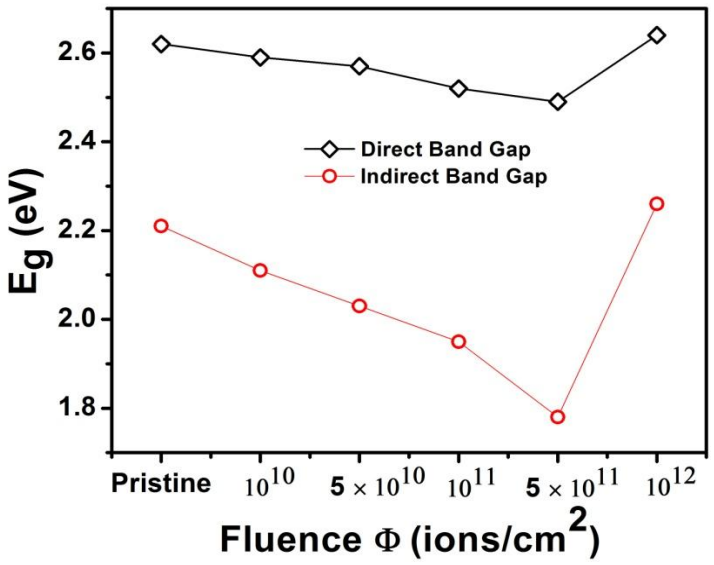

Figure 6.28: *Comparison of direct and indirect band gap energies of pristine and irradiated PPy nanotubes at different irradiation fluences.*

The number of carbon atoms per conjugation length (N) for linear structure is correlated with the optical band gap energy (E_g) which can be determined from the modified Tauc's equation [376];

$$N = 2\beta\pi / E_g \tag{6.33}$$

where 2β gives the band structure energy of a pair of adjacent π sites. The value of β is taken to be -2.9 eV as it is associated with the π-π* optical transitions in -C=C- structure. The red shifting of the absorption edge can be attributed to the increase in conjugation length. Upon SHI irradiation the number of carbon atoms per conjugation length (N) and number of carbon atoms per cluster (M) increase with increasing the irradiation fluence from 10^{10} to 5×10^{11} ions/cm^2, while at the highest ion fluence of 10^{12} ions/cm^2 both the values of N and M decrease. The increase in electrical conduction with increasing irradiation fluence can also be corroborated with the increase in conjugation lengths, thereby allowing easy transports of charge carriers along the

conjugated structures of PPy nanotubes chains. The direct and indirect band gap energies (E_g) and number of carbon atoms per conjugation length (N) of the pristine and irradiated PPy nanotubes are presented in Table 6.10. The carbon enriched domains created in the SHI irradiated PPy nanotubes is mainly responsible for the reduction in the optical band gap energy [318, 377].

Table 6.10: Direct and indirect band gap energies (E_g), number of carbon atoms per conjugation length (N) of the pristine and irradiated PPy nanotubes at different ion fluences.

Fluence (ions/cm^2)	Band gap energy, E_g (eV)		Number of carbon atoms per conjugation length (N)	
	direct	indirect	direct	indirect
Pristine	2.62 ± 0.002	2.21 ± 0.002	~ 6.95 ± 0.002	~ 8.24 ± 0.002
1×10^{10}	2.59 ± 0.002	2.11 ± 0.002	~ 7.03 ± 0.002	~ 8.63 ± 0.002
5×10^{10}	2.57 ± 0.001	2.03 ± 0.001	~ 7.08 ± 0.001	~ 8.97 ± 0.001
1×10^{11}	2.52 ± 0.002	1.95 ± 0.002	~ 7.22 ± 0.002	~ 9.33 ± 0.001
5×10^{11}	2.49 ± 0.001	1.78 ± 0.001	~ 7.31 ± 0.001	~ 10.23 ± 0.001
1×10^{12}	2.64 ± 0.003	2.26 ± 0.003	~ 6.89 ± 0.003	~ 8.05 ± 0.003

6.2.5. Thermogravimetric analysis

The TGA thermographs for the pristine and irradiated PPy nanotubes at different irradiation fluences are shown in Fig. 6.29. At room temperature the weight loss of the pristine and irradiated PPy nanotubes at different ion fluences is negligible. The first weight loss at 110 °C for the pristine and irradiated PPy nanotubes is due to the loss of moisture. The second weight loss occurs in between temperature 210-330 °C which may be due to the evaporation of dopant molecules from the polymer chains. The third and final weight loss of both the pristine and irradiated PPy nanotubes occurs in between temperature 330-500 °C which can be attributed to the degradation and/or decomposition of the PPy backbone chains. It is observed that upon SHI irradiation, the

weight loss of PPy nanotubes decreases gradually with increasing ion fluence from 10^{10} to 5×10^{11} ions/cm^2, while at the highest ion fluence of 10^{12} ions/cm^2 the weight loss decreases to a value smaller than that of the pristine sample.

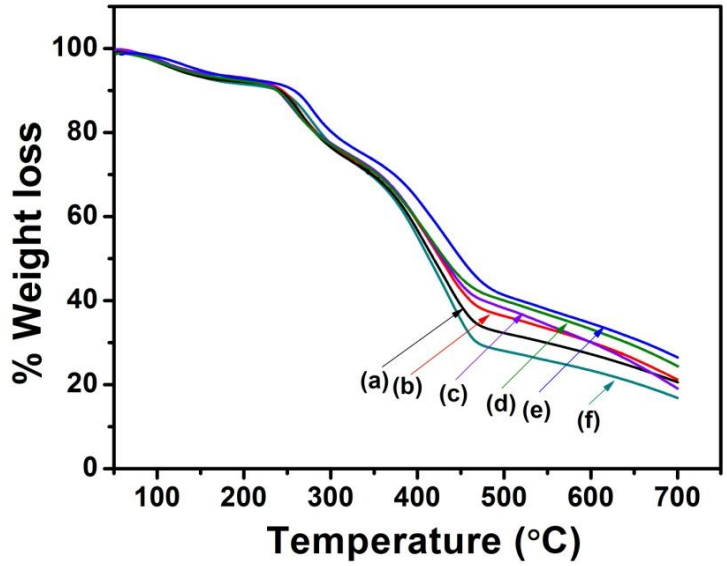

Figure 6.29: *TGA thermographs of (a) pristine and irradiated PPy nanotubes at ion fluences of (b) 10^{10}, (c) 5×10^{10}, (d) 10^{11}, (e) 5×10^{11} and (f) 10^{12} ions/cm^2.*

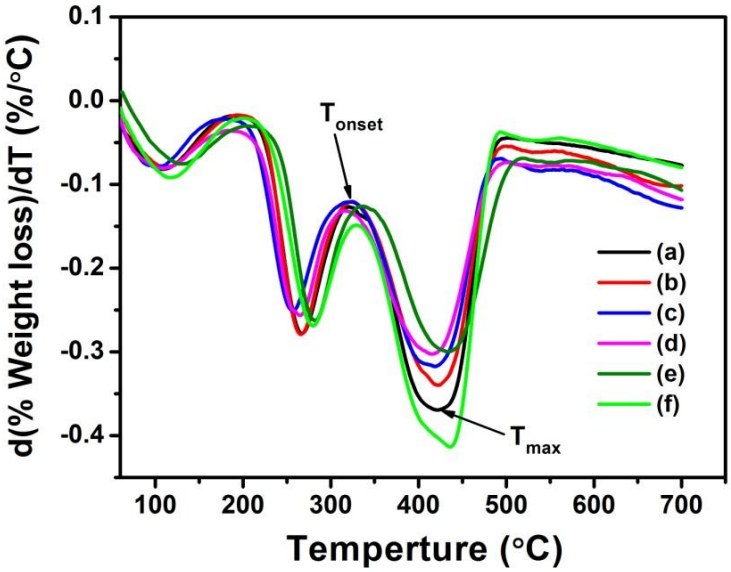

Figure 6.30: *Derivative plots of TGA thermographs for (a) pristine and irradiated PPy nanotubes at irradiation fluences of (b) 10^{10}, (c) 5×10^{10}, (d) 10^{11}, (e) 5×10^{11} and (f) 10^{12} ions/cm^2.*

Fig. 6.30 shows the derivative plots of TGA thermographs for the pristine and irradiated PPy nanotubes. The negative values of the derivatives plots of TGA thermographs mean the weight loss i.e. decomposition of the sample and hence the modulus values of the derivatives are considered. The values of maximum decomposition temperature (T_{max}) and maximum decomposition rate $(dW/dT)_m$ for the pristine and irradiated PPy nanotubes obtained from Fig. 6.30 are presented in Table 6.11.

Table 6.11: Values of maximum decomposition rate, $(dW/dT)_m$ for pristine and irradiated PPy nanotubes at irradiation fluences of 10^{10}, 5×10^{10}, 10^{11}, 5×10^{11} and 10^{12} ions/cm^2.

Ion Fluence (ions/cm^2)	Maximum decomposition rate, $(dW/dT)_m$, (%/°C)
Pristine	$\lvert 0.367 \rvert$
1×10^{10}	$\lvert 0.339 \rvert$
5×10^{10}	$\lvert 0.315 \rvert$
1×10^{11}	$\lvert 0.300 \rvert$
5×10^{11}	$\lvert 0.298 \rvert$
1×10^{12}	$\lvert 0.411 \rvert$

In the third weight loss stage (330-500 °C), the onset decomposition temperature (T_{onset} = 322 °C) and maximum decomposition temperature (T_{max}= 421 °C) do not change significantly for PPy nanotubes upon irradiation with different ion fluences. However, as observed from the Fig. 6.30 and Table 6.11, the rate of decomposition for PPy nanotubes decreases as compared to pristine PPy nanotubes upon SHI irradiation with increasing irradiation fluence. The pristine PPy nanotubes exhibit the maximum decomposition rate $(dW/dT)_m$ of $\lvert 0.367 \rvert$ %/°C, which decreases to $\lvert 0.298 \rvert$ %/°C upon SHI irradiation with fluence of 5×10^{11} ions/cm^2 indicating an enhancement in thermal stability of the irradiated PPy nanotubes. This may be attributed to the cross-linking occurring at the lower fluence. However, at higher irradiation fluence of 10^{12} ions/cm^2,

$(dW/dT)_m$ increases to $|0.411|$ %/°C (which is higher than that of the pristine $(dW/dT)_m$ value) implying faster decomposition rate for PPy nanotubes irradiated at fluence of 10^{12} ions/cm^2. This indicates decrease in thermal stability of PPy nanotubes irradiated at the fluence of 10^{12} ions/cm^2, which may be attributed to the chain scissoning or breaking of bonds and decrease in the molecular weight at the highest irradiation fluence. It can be inferred from the TGA and differential thermographs results that PPy nanotubes irradiated with low and moderate ion fluence are thermally and structurally more stable as compared to the PPy nanotubes irradiated with higher (1×10^{12} ions/cm^2) ion fluence.

6.2.6. Dielectric permittivity studies

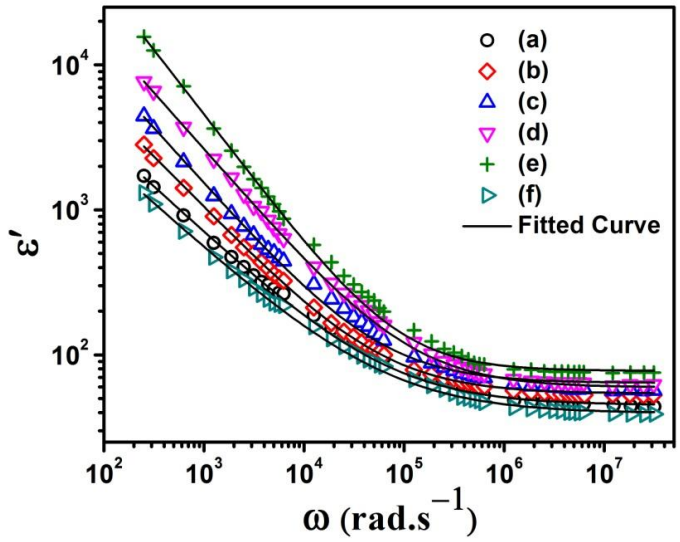

Figure 6.31: *Plots of dielectric permittivity* (ε') *vs. frequency* (ω) *of (a) pristine and irradiated PPy nanotubes at ion fluences of (b)* 10^{10}*, (c)* 5×10^{10}*, (d)* 10^{11}*, (e)* 5×10^{11} *and (f)* 10^{12} *ions/cm*^{2} *at room temperature (303 K).*

The plots of dielectric permittivity (ε') vs. frequency (ω) of both pristine and irradiated PPy nanotubes at ion fluences of 10^{10}, 5×10^{10}, 10^{11}, 5×10^{11} and 10^{12} ions/cm^2 at room temperature (303 K) is depicted in Fig. 6.31. It is observed that in lower frequencies, ε' shows strong frequency dispersion and its value decreases with increasing frequency and at higher frequencies, ε' attains a nearly constant value. The higher value of ε' at lower frequencies can be attributed to the electrode polarization effects [344]. Upon

SHI irradiation, ε' increases with increasing ion fluence which can be attributed to the increased contribution of electrode polarization effects in the irradiated PPy nanotubes due to the generation of more charge carriers during SHI irradiation. It is observed that at the highest ion fluence of 10^{12} ions/cm^2, value of ε' at a particular frequency decreases as compared to the pristine PPy nanotubes which can be attributed to the decrease in electrode polarization effects at lower frequencies.

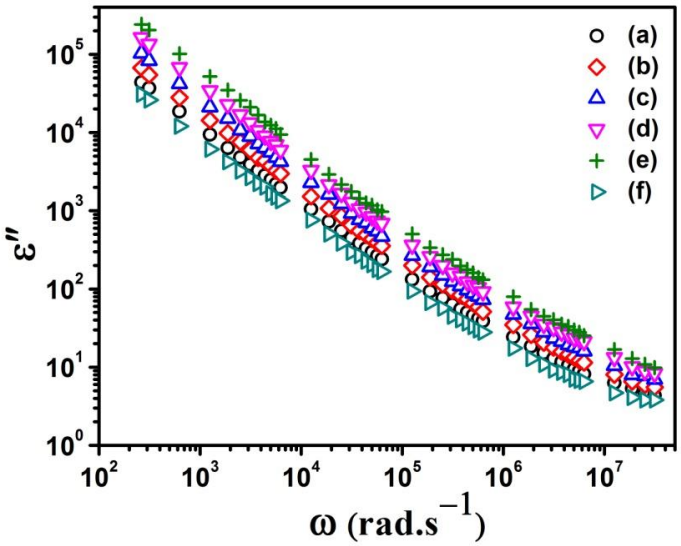

Figure 6.32: *Plots of dielectric loss (ε'') vs. frequency (ω) of (a) pristine and irradiated PPy nanotubes at ion fluences of (b) 10^{10}, (c) 5×10^{10}, (d) 10^{11}, (e) 5×10^{11} and (f) 10^{12} ions/cm^2 at room temperature (303 K).*

Fig. 6.32 depicts the plots of dielectric loss (ε'') vs. frequency (ω) of both pristine and irradiated PPy nanotubes at ion fluences of 10^{10}, 5×10^{10}, 10^{11}, 5×10^{11} and 10^{12} ions/cm^2 at room temperature (303 K). The linear increase in the value of ε'' with decreasing frequency indicates that the dc conduction loss is more prominent over the polarization effect. However, upon SHI irradiation, the value of ε'' at a given frequency increases with increasing irradiation fluence, which can be attributed to increased dc conduction in irradiated PPy nanotubes as a result of generation of more number of free charge carriers, while at the highest ion fluence of 10^{12} ions/cm^2 the value of ε'' at a given frequency decreases as compared to the pristine PPy nanotubes.

6.2.7. Electric modulus studies

The room temperature (303 K) plots of real part of modulus (M') vs. frequency (ω) of both pristine and irradiated PPy nanotubes at different ion fluences are depicted in Fig. 6.33. Each of M' spectrums exhibits a sigmoid type behavior i.e. the value of M' increases with increasing frequency and reaches a constant maximum value in higher frequencies. The elimination of the electrode polarization from the pristine and irradiated samples of PPy nanotubes can be confirmed from the zero value of M' at lower frequencies [296]. At the higher frequency, M' approaches to $M_{\infty}(\omega \to \infty)$ for both the pristine and SHI irradiated PPy nanotubes suggesting that the conduction process is due to the short range motion of charge carriers [297].

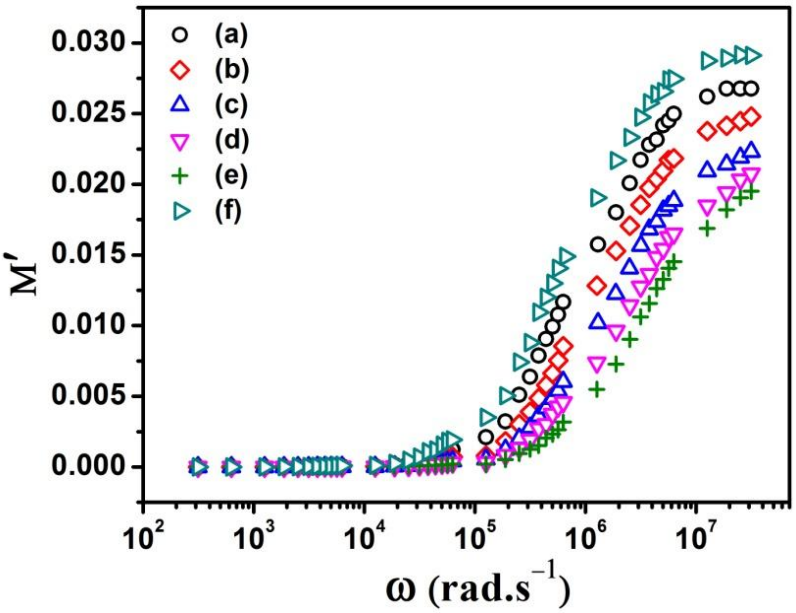

Figure 6.33: *Plots of real part of modulus (M') vs. frequency (ω) of (a) pristine and irradiated PPy nanotubes at ion fluences of (b) 10^{10}, (c) 5×10^{10}, (d) 10^{11}, (e) 5×10^{11} and (f) 10^{12} ions/cm^2 at room temperature (303 K).*

To get more information about the conductivity relaxation mechanism in SHI irradiated PPy nanotubes, the frequency dependence behavior of M'' spectra have been studied. Fig. 6.34 depicts the room temperature plots of imaginary part of modulus (M'') vs. frequency (ω) of both pristine and irradiated PPy nanotubes at different ion fluences. A single relaxation peak is observed in each M'' spectrum of both pristine and irradiated PPy nanotubes which suggests the transition of charge carriers' motion from long range

to short range with increasing frequency. At low and moderate irradiation fluence (10^{10}-5×10^{11} ions/cm^2), the relaxation peak in M'' spectra shifts towards higher frequency indicating increase in long range motion of charge carriers in the SHI irradiated PPy nanotubes. As a result the relaxation time (τ) of charge carriers' motion decreases with increasing the irradiation fluences. However, the M'' peak shifts towards lower frequencies as compared to the pristine PPy nanotubes at the irradiated highest ion fluence of 10^{12} ions/cm^2 resulting increase in the relaxation time (τ) of charge carriers. Table 6.12 presents the calculated values of the relaxation frequency (ω) and relaxation time (τ) of charge carriers in both pristine and irradiated PPy nanofibers at different irradiation fluence at room temperature (303 K). Moreover, the asymmetric relaxation peak in M'' plots indicates the non-Debye relaxation mechanism of charge carriers in the irradiated PPy nanotubes.

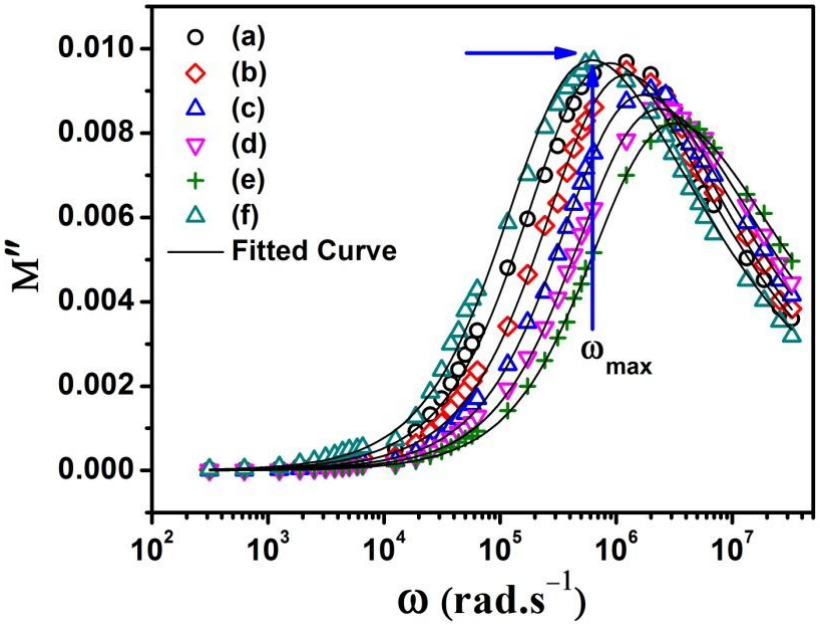

Figure 6.34: *Plots of imaginary part of modulus (M'') vs. frequency (ω) of (a) pristine and irradiated PPy nanotubes at ion fluences of (b) 10^{10}, (c) 5×10^{10}, (d) 10^{11}, (e) 5×10^{11} and (f) 10^{12} ions/cm^2 at room temperature (303 K).*

Table 6.12: Relaxation frequency (ω_{max}) and relaxation time (τ) for charge carriers in pristine and irradiated PPy nanotubes at room temperature (303 *K*).

Fluence (ions/cm^2)	Relaxation frequency, ω_{max} (rad.s^{-1})	Relaxation time, τ (s)
Pristine	1.19×10^{6}	8.35×10^{-7}
1×10^{10}	1.43×10^{6}	6.94×10^{-7}
5×10^{10}	1.87×10^{6}	5.33×10^{-7}
1×10^{11}	2.44×10^{6}	4.09×10^{-7}
5×10^{11}	3.44×10^{6}	2.90×10^{-7}
1×10^{12}	9.95×10^{5}	1.00×10^{-6}

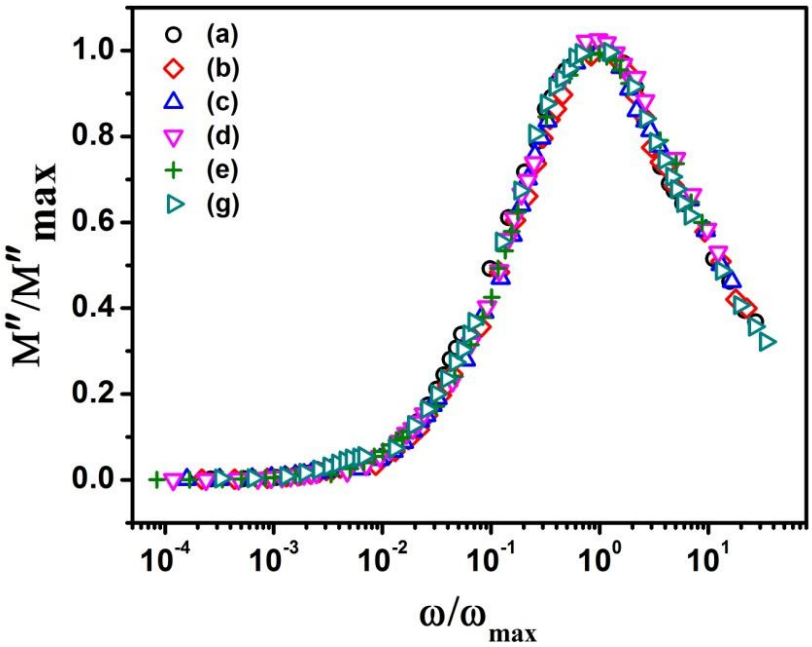

Figure 6.35: *Room temperature scaling plots of imaginary part of modulus (M'') of (a) pristine and irradiated PPy nanotubes at ion fluences of (b) 10^{10}, (c) 5×10^{10}, (d) 10^{11}, (e) 5×10^{11} and (f) 10^{12} ions/cm^2.*

Fig. 6.35 depicts the room temperature scaling plots of M'' spectra of both pristine and irradiated PPy nanotubes at different ion fluences. The scaling of modulus spectra can provide a deep insight into the ion fluence dependence of relaxation dynamics in the irradiated PPy nanotubes. The scaling is done by dividing M'' with

M''_{max}, while the frequency axis is scaled by the relaxation frequency ω_{max}. It is observed that each of the individual M'' spectra at different ion fluences merge on a common master curve indicating the ion fluence independent of relaxation dynamics of charge carriers in SHI irradiated PPy nanotubes.

6.2.8. AC conductivity studies

The room temperature (303 K) frequency variation of total conductivity $\sigma'(\omega)$ of pristine and irradiated PPy nanotubes at different ion fluences is depicted in Fig. 6.36. It is observed that in lower frequency region, the conductivity of both the pristine and irradiated PPy nanotubes is frequency independent which corresponds to the dc conductivity σ_{dc} and at higher frequency region; the conductivity follows a frequency dispersive behavior which corresponds to the ac conductivity $\sigma_{ac} = A\omega^s$, $0 < s < 1$ and *A* is the pre-exponential factor that depends only on temperature not on frequency.

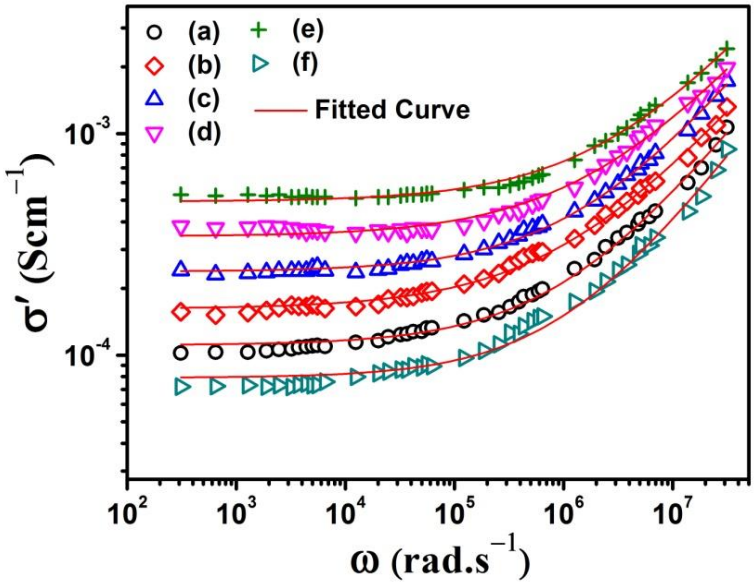

Figure 6.36: *Room temperature plots of total conductivity* (σ') *of (a) pristine and irradiated PPy nanotubes at ion fluences of (b)* 10^{10}*, (c)* 5×10^{10}*, (d)* 10^{11}*, (e)* 5×10^{11} *and (f)* 10^{12} *ions/cm*^{2}.

The transformation from the frequency-independent to the frequency-dependent region marks the onset of the conductivity relaxation, which shifts to the higher frequency region with increasing the irradiation fluence. Upon SHI irradiation, the total

conductivity of PPy nanotubes gets enhanced than that of the pristine PPy nanotubes. The increase in conductivity upon SHI irradiation can be ascribed to the formation of crystalline structure besides formation of the conjugated double bonds. However, at the highest irradiation fluence of 10^{12} ions/cm^2, the total conductivity decreases as compared to the pristine PPy nanotubes which can be attributed to the decreased crystallinity of the irradiated PPy nanotubes than that of the pristine sample.

To understand the charge transport mechanism in the SHI irradiated PPy nanotubes, the temperature dependent studies of frequency exponent *s* has been carried out. The temperature dependent plots of frequency exponent of both the pristine and irradiated PPy nanotubes at different ion fluences are depicted in Fig. 6.37. It is observed that the frequency exponent *s* of both pristine and irradiated PPy nanotubes decreases with increasing temperature. The decreased nature of *s* with increasing temperature suggests that charge carriers in both the pristine and irradiated PPy nanotubes follow the correlated barrier hopping (CBH) model as the dominant charge transport mechanism.

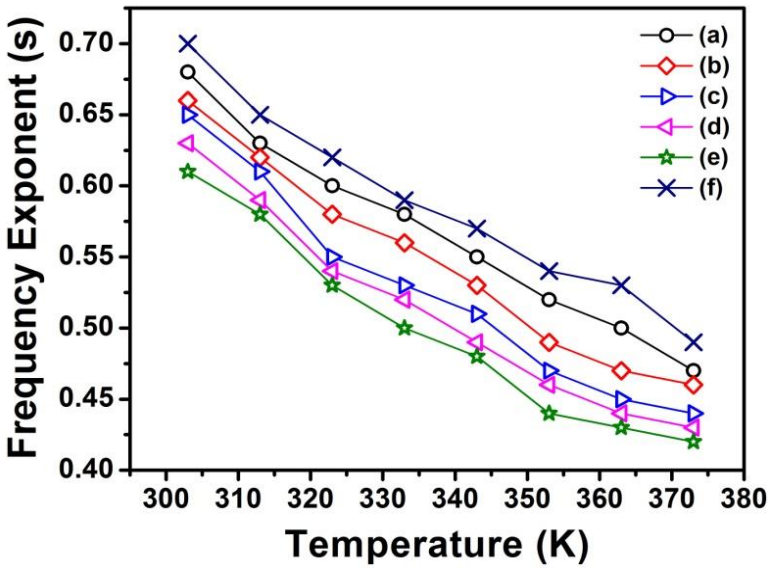

Figure 6.37: *Temperature variation of frequency exponent 's' of (a) pristine and irradiated PPy nanotubes at ion fluences of (b) 10^{10}, (c) 5×10^{10}, (d) 10^{11}, (e) 5×10^{11} and (f) 10^{12} ions/cm^2.*

The values of barrier activation energy (W_H) for charge carriers of both pristine and irradiated PPy nanotubes has been calculated using equation (6.29),

$$s = 1 - \frac{6kT}{W_H}$$

as mentioned in section 6.1 and values are presented in Table 6.13. Upon SHI irradiation, at low and moderate irradiation fluence (10^{10} - 5×10^{11} ions/cm^2), value of W_H for charge carriers' decreases which suggests reduction in barrier height for charge carriers' motion and as a result the electrical conductivity in SHI irradiated PPy nanotubes get enhanced. However, at the highest irradiation fluence of 10^{12} ions/cm^2, barrier activation energy increases as compared to the pristine sample, thereby resulting decrease in electrical conductivity of PPy nanotubes at the highest irradiation fluence.

Table 6.13: Frequency exponent (s) and barrier activation energy (W_H) of pristine and irradiated PPy nanotubes at different irradiation fluences at room temperature (303 K).

Fluence (ions/cm^2)	Frequency exponent, s	Barrier activation energy W_H (eV) at 303 K
Pristine	0.68	0.49
1×10^{10}	0.66	0.46
5×10^{10}	0.65	0.44
1×10^{11}	0.63	0.42
5×10^{11}	0.61	0.40
1×10^{12}	0.70	0.52

Fig. 6.38 depicts the room temperature scaling plots of total conductivity of the pristine and irradiated PPy nanotubes at different ion fluences. The ac conductivity spectra of both the pristine and irradiated PPy nanotubes have been scaled by the scaling process as reported by Gosh *et al*. [337] in which the total conductivity $\sigma'(\omega)$ is scaled by σ_{dc} while the frequency axis is scaled by the cross-over or cut-off frequency $\omega_{\max}$. It is observed that all the conductivity spectra after the scaling process fall onto a single master curve, which indicates the irradiation fluence independent conductivity relaxation in the irradiated PPy nanotubes.

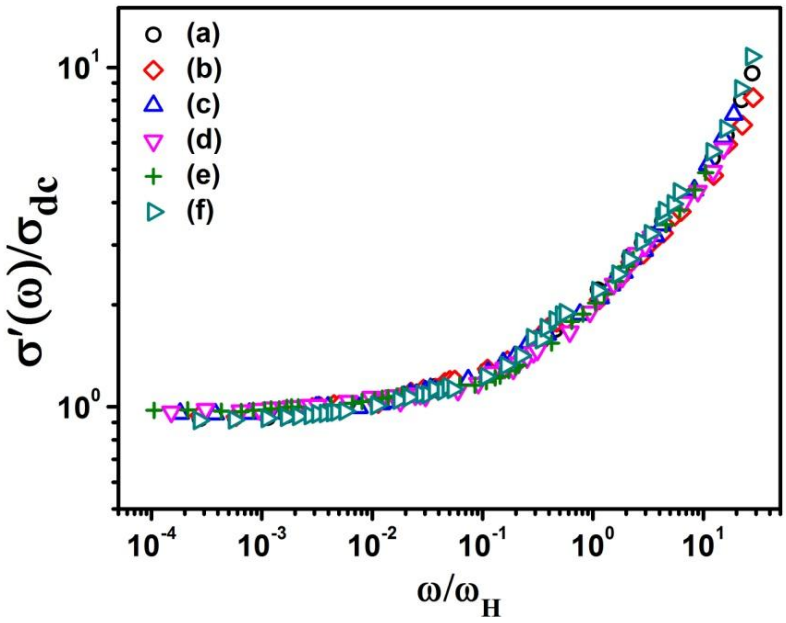

Figure 6.38: *Room temperature scaling plots of total conductivity of (a) pristine and irradiated PPy nanotubes at ion fluences of (b) 10^{10}, (c) 5×10^{10}, (d) 10^{11}, (e) 5×10^{11} and (f) 10^{12} ions/cm^2.*

6.3. Summary

PPy nanotubes with controlled morphology have been synthesized using the self assembly polymerization method. The average diameter of the PPy nanotubes increases with increasing the dopant/monomer molar ratio. The micelles formed by the CSA surfactant molecules and pyrrole cations act as soft templates during the formation of PPy nanotubes. The PPy nanotubes exhibit higher crystallinity at higher dopant/monomer ratio due to the favourable role of CSA counter ions in reordering of the polymer chains. FTIR results reveal that "effective conjugation length" of PPy nanotubes increases with increasing CSA/Py ratio confirming increased electrical conductivity in PPy nanotubes at higher dopant/monomer molar ratio. The presence of polaron and bipolaron bands in UV-vis absorption spectra confirms the doping of CSA into the PPy chains. The optical band gap energy of PPy nanotubes decreases with increasing CSA/Py ratio. PPy nanotubes are thermally and structurally more stable at higher dopant/monomer ratio and the degradation temperature shifts towards higher temperature limit with increasing the dopant/monomer ratio. The higher value of dielectric permittivity (ε') at lower frequencies is attributed to the electrode

polarization affects. The increased dielectric loss $\varepsilon''(\omega)$ with increasing dopant/monomer ratio is due to the increased dc electrical conduction. The frequency dependence of imaginary modulus (M'') shows a single relaxation peak, which indicates increasing the long range motion over short range motion of charge carriers with decreasing frequency. The relaxation time (τ) of the charge carriers' motion decreases with increasing both the dopant/monomer ratio and temperature. The lower values of non-exponential parameter β suggest the non-Debye relaxation of charge carriers in PPy nanotubes. The temperature variation of M'' peak predicts that the observed relaxation is a thermally activated process. The scaling of modulus spectra M'' at different dopant/monomer ratio and temperature reveal the same relaxation dynamics of charge carriers in PPy nanotubes. The frequency dependence of ac conductivity for PPy nanotubes at different dopant/monomer ratio and at different temperature has been analysed using the Jonscher's power law expression, $\sigma_{ac}(\omega) = A\omega^s$ with $0.65 \leq s \leq 0.94$. The decrease in frequency exponent s with increasing temperature suggests the correlated barrier hopping (CBH) mechanism of charge carrier transport. The overlapping of all the individual conductivity plots into a single master plot indicates the temperature independence of charge carrier relaxation dynamics in PPy nanotubes. Furthermore, the correlation between activation energies for dc and ac conduction shows that the transport in the PPy nanotubes is through the hopping mechanism.

HRTEM studies of SHI irradiated PPy nanotubes indicate denser structure at the low and moderate ion fluence (10^{10} - 5×10^{11} ions/cm^2), while PPy nanotubes irradiated at the highest ion fluence of 10^{12} ions/cm^2 used show the degradation of PPy nanotubes. Upon SHI irradiation, crystallinity of PPy nanotubes increases with increasing the irradiation fluence, while at the highest ion fluence (10^{12} ions/cm^2) crystallinity decreases as compared to that of the pristine PPy nanotubes. The increase in the vibrational band intensity with increasing irradiation fluence corresponds to the formation of functional groups, while the reduction in band intensity at the highest ion fluence corresponds to the degradation of the functional groups. Upon SHI irradiation, band position of π-π* transition remains unaffected; however the polaron absorption band edge makes a red shift with increasing irradiation fluence from 10^{10} to 5×10^{11}

ions/cm^2 and at the highest ion fluence of 10^{12} ions/cm^2, the polaron band edge makes a blue shift. With increasing the ion fluence, the optical band gap energy reduces and it increases at the investigated highest irradiated fluence. The indirect optical band gap energy is found to be lower than their corresponding direct band gap energy for both the pristine and irradiated PPy nanotubes. The reduction in optical band gap energy upon SHI irradiation is attributed to the formation of defects and clusters in the irradiated PPy nanotubes. Upon SHI irradiation, thermal stability of PPy nanotubes increases with increasing the irradiation fluence upto 5×10^{11} ions/cm^2, while thermal stability of PPy nanotubes decreases than that of the pristine sample at the highest ion fluence of 10^{12} ions/cm^2. Upon SHI irradiation, dielectric loss (ε'') at a given frequency increases with increasing irradiation fluence, which can be attributed to the increased dc conduction in the irradiated PPy nanotubes as a result of generation of increased concentration of free charge carriers. Upon SHI irradiation, in the low and moderate irradiation fluence (10^{10} - 5×10^{11} ions/cm^2), M'' relaxation peak shifts towards higher frequency with increasing the irradiation fluence, which reveals the enhancement of long range motion of charge carriers. However, at the highest irradiation fluence of 10^{12} ions/cm^2, M'' relaxation peak shifts towards lower frequency as compared to the pristine PPy nanotubes which results in enhanced relaxation time of charge carriers' motion at the highest irradiation fluence. The asymmetric nature of M'' relaxation peak indicates the non-Debye relaxation of charge carriers in the irradiated PPy nanotubes. The scaling of M'' spectra of the irradiated PPy nanotubes at different ion fluences indicates the irradiation fluence independent relaxation dynamics of charge carriers. Upon SHI irradiation, total conductivity of the irradiated PPy nanotubes increases with increasing the irradiation fluence, which can be attributed to the formation of crystalline structure besides formation of the conjugated double bonds. The decrease in total conductivity of the irradiated PPy nanotubes at the highest irradiation fluence of 10^{12} ions/cm^2 is due to the lowering of crystallinity as compared to that of the pristine PPy nanotubes. The decrease in the value of frequency exponent '*s*' with increasing temperature suggests that the charge carriers in the irradiated PPy nanotubes follow the correlated barrier hopping (CBH) transport mechanism. The room temperature scaling of conductivity spectra of the irradiated PPy nanotubes reveals the irradiation fluence independent conductivity relaxation mechanism.

CHAPTER-VII
Conclusions and Future Prospects

This chapter presents in detail the conclusions drawn from the present work. The limitations and future prospects in the emerging area of research in conducting polymer nanostructures and their swift heavy ion irradiation effects have also been briefly discussed at the end of this chapter.

7.1. Conclusions

The present work deals with the synthesis of polypyrrole (PPy) nanostructures viz. PPy nanoparticles, PPy nanofibers and PPy nanotubes using the micro-emulsion polymerization, interfacial polymerization and self-assembly polymerization techniques with a view to study their dielectric relaxation and electrical transports and swift heavy ion irradiation (SHI) effects. From each of the synthesized PPy nanostructures, the samples which have shown the best properties have been irradiated with 160 MeV Ni^{12+} ions and modifications in their different physico-chemical properties have been thoroughly investigated using different sophisticated characterization techniques and measurements. The major conclusions drawn from the present work are enumerated below:

System I: Polypyrrole nanoparticles: Dielectric relaxation and electrical transport studies and swift heavy ion irradiation effects

1. Transmission electron microscopy studies of PPy nanoparticles synthesized by the micro-emulsion polymerization method reveal that the average diameter of PPy nanoparticles decreases from 22 nm to 11 nm when sodium dodecylsulfate (SDS) surfactant concentration is increased from 0.01 M to 0.2 M. The size of PPy nanoparticles is directly correlated with the micelle's size since polymerization of pyrrole (Py) monomer is restricted in a localized environment due to encapsulation by the surfactant molecules. The increase in SDS surfactant concentration gives rise to smaller micelle dimension with greater stability due to lower value of Gibbs free energy. Smaller extent of Py monomer can encapsulate in such micelles resulting in decrease in average diameter of the PPy nanoparticles. However, HRTEM

micrographs of SHI irradiated PPy nanoparticles depict that upon SHI irradiation, there is no change in the spherical shape of PPy nanoparticles, but average diameter of nanoparticles increases with increasing the irradiation fluence. The pristine PPy nanoparticle's size of 11 nm increases to 18 nm when irradiated with the highest irradiation fluence of 10^{12} ions/cm^2.

2. X-ray diffraction studies depict that crystallinity of PPy nanoparticles increases with increasing SDS dopant cum surfactant concentration. The crystallinity of PPy nanoparticles chain increases from 20.18 % to 24.60 % with increasing SDS dopant concentration from 0.01 M to 0.2 M. XRD studies also reveal that upon SHI irradiation, crystallinity of PPy nanoparticles increases with increasing irradiation fluence. The crystallinity (25.12 %) of pristine PPy nanoparticles increases to 28.78 % upon SHI irradiation at the highest ion fluence of 10^{12} ions/cm^2. Moreover, extent of order of polymer chains increases to 10.37 Å from 9 Å, while the hopping distance decreases to 5.56 Å from 5.68 Å upon irradiation of PPy nanoparticles at the highest ion fluence of 10^{12} ions/cm^2. The increase in crystallinity of irradiated PPy nanoparticles can be ascribed to the systematic alignment of polymer chains by cross-linking or by formation of single or multiple helices along the ion trajectories due to large electronic energy deposition.

3. Fourier transmission infrared (FTIR) spectroscopy studies of PPy nanoparticles reveal that "effective conjugation length" increases with increasing SDS concentration. The increase in "effective conjugation length" can result in increase in electrical conductivity into PPy nanoparticles at higher SDS concentration. FTIR spectra of irradiated PPy nanopartilces show that the IR active vibrational bands have different cross sections for SHI irradiation and the N-H vibrational band at 3695 cm^{-1} is most sensitive to SHI irradiation with formation cross section of 5.77×10^{-13} cm^2 and effective radius of 7.58 nm.

4. UV-vis studies reveal that optical band gap energy (E_g) of PPy nanoparticles decreases with increasing the SDS dopant cum surfactant concentration. However, optical band gap energy of PPy nanoparticles also decreases with increasing the irradiation fluence, which can be attributed to the formation of conjugated structure (i.e. free radicals, double bonds etc.) upon SHI irradiation.

5. Thermo-gravimetric analysis (TGA) of PPy nanoparticles indicates that the thermal stability of PPy nanoparticles increases with increasing SDS dopant cum surfactant concentration. Also, upon SHI irradiation the degradation temperature at a particular weight loss increases with increasing irradiation fluence from 10^{10} to 10^{12} ions/cm^2. The enhanced thermal stability is attributed to the enhanced ordering of PPy nanoparticles chains which produces more crystalline structures in SHI irradiated PPy nanoparticles.

6. Dielectric permittivity spectra of PPy nanoparticles reveal that high value of dielectric permittivity (ε') at lower frequencies is due to the electrode polarization effect. With increasing SDS concentration, dielectric permittivity at a particular frequency increases which represents higher value of electrode polarization in PPy nanoparticles. The linear increase in the value of dielectric loss (ε'') with decreasing frequency suggests that dc loss is dominant at lower frequencies and it increases with increasing SDS molar concentration. Upon SHI irradiation in PPy nanoparticles, both electrode polarization and dc loss increase with increasing the irradiation fluence.

7. Studies of real part of modulus (M') of PPy nanoparticles exhibit that at lower frequencies**,** value of M' increases with increasing frequency which suggests that conduction process is due to the long range motion of charge carriers, whereas at higher frequencies, M' attains a maximum value and approaches to $M_\infty(\omega \to \infty)$ for all the samples of PPy nanoparticles, which indicates that the conduction is due to the short range motion of charge carriers. Studies of imaginary part of modulus M'' spectra reveal that charge carriers in PPy nanoparticles obey the non-Debye relaxation mechanism and relaxation time (τ) decreases with increasing SDS dopant concentration. Upon SHI irradiation, relaxation peak shifts towards higher frequency with increasing irradiation fluence, which indicates that long range motion of charge carriers increases in irradiated PPy nanoparticles.

8. Total conductivity of PPy nanoparticles increases with increasing SDS dopant concentration. At higher SDS concentration, incorporation of large number of SDS anions into the PPy nanoparticles chains reduces charge trapping centres which leads to participation a large number of charge carriers in the conducting process giving rise to increased conductivity. Low values of polaron binding energy (0.56 -

0.71 eV) calculated using the experimental values of frequency exponent *'s'* confirms the existence of single polarons as the dominant charge carriers in PPy nanoparticles. The decrease in frequency exponent '*s'* with increasing temperature suggests that correlated barrier hopping (CBH) is the dominant charge transport mechanism. Upon SHI irradiation, conductivity of PPy nanoparticles increases with increasing irradiation fluences. The increase in ac conductivity can be attributed to the increased degree of crystallinity with increasing fluence which is consistent with the XRD results. The decrease in value of *'s'* with increasing temperature reveals that charge carriers in irradiated PPy nanoparticles also follow the correlated barrier hopping (CBH) model.

System II: Polypyrrole nanofibers: Dielectric relaxation and electrical transport studies and swift heavy ion irradiation effects

1. HRTEM studies show that PPy nanofibers with average diameter ranging from 13 nm to 25 nm and length in micrometer range are formed. Smaller diameter PPy nanofibers are formed for short alkyl chain ABSA doped PPy nanofibers. The increasing diameter for different ABSA doped PPy nanofibers is as follows: PPy-(*p*-TSA)< PPy-(CSA)< PPy-(OBSA)< PPy-(DBSA). Also, the formation of twisted structure of PPy nanofibers suggests that alkylbenzenesulfonic acid doped PPy nanofibers are highly flexible. Upon SHI irradiation, average diameter and length of PPy nanofibers are unchanged, while a denser structure forms upon SHI, which can be attributed to the cross-linking of PPy nanofibers chains due to generation of free radicals and formation of bonds between the adjacent chains.
2. XRD studies of ABSA doped PPy nanofibers reveal that PPy nanofibers doped with shorter alkyl chain doped ABSA dopant exhibit higher crystallinity or ordering of the polymer chains. The increase in crystallinity of PPy nanofibers doped with different ABSA dopants is as follows: PPy-(DBSA)< PPy-(OBSA)< PPy-(CSA)< PPy-(*p*-TSA), while the ordering of *d*-spacing and hopping distance (*R*) is opposite to that of crystallinity order. The decrease in *d*-spacing as well as hopping distance (*R*) increases the probability of increasing interchain hopping of charge carriers, which consequently results in increase in electrical

conductivity in short alkyl chain doped PPy nanofibers. Moreover, XRD patterns of irradiated PPy nanofibers reveal that upon SHI irradiation, crystallinity of PPy nanofibers increases as compared to the pristine sample and increases with increasing irradiation fluence. Also, the appearance of new diffraction peak at $2\theta = 17^{o}$ at higher ion fluences (5×10^{11} - 10^{12} ions/cm^2) reveals the formation of new crystalline regions in SHI irradiated PPy nanofibers. Upon SHI irradiation, density of PPy nanofibers increases, which may be attributed to the formation of closely packed regions by chain folding, cross-linking of the polymer chains due to the high deposition of electronic energy along ions trajectories. On the other hand, hopping distance (*R*) of the SHI irradiated PPy nanofibers decreases as compared to the pristine sample. The decrease in hopping distance (*R*) can facilitate easy hopping of charge carriers which in turn results in increase in electrical conductivity in SHI irradiated PPy nanofibers.

3. FTIR studies of different ABSA doped PPy nanofibers sugget that the effective conjugation length is higher in the short alkyl chain (*p*-TSA) doped PPy nanofibers and its value increases in the following order: PPy-(DBSA)< PPy-(OBSA)< PPy-(CSA)< PPy-(*p*-TSA). The higher value of effective conjugation length in short alkyl chain ABSA doped PPy nanofibers can result in increase in electrical conductivity. The increase in vibrational band intensity upon SHI irradiation indicates formation of characteristic functional groups viz. C=C, C-H and C-H in the irradiated PPy nanofibers.

4. UV-visible studies of PPy nanofibers doped with different ABSA dopants reveal that short alkyl chain ABSA doped PPy nanofibers exhibit smaller optical band gap energy. The decrease in optical band gap energy can result in increase in electrical conductivity in short alkyl chain ABSA doped PPy nanofibers. However, both the direct and indirect optical band gap energy of SHI irradiated PPy nanofibers decrease as compared to that of the pristine sample. SHI irradiation induces the cleavage of C-C bonds and dehydrogenation of polymer chains by evolution of hydrogen atoms, which produces conjugated -C=C- bonds. The formation of conjugated bonds results in increase in number of carbon clusters in irradiated PPy nanofibers. During SHI irradiation, polymeric material gradually loses hydrogen atoms and enrichment of carbon atoms leads

to the formation of dehydrogenated amorphous carbon with optical band gap depending on the C/H ratio.

5. TGA studies of different ABSA doped PPy nanofibers suggest that short alkyl chain doped PPy nanofibers are thermally more stable than that of other ABSA doped PPy nanofibers. The increase in thermal stability of different ABSA doped PPy nanofibers is in the order of PPy-(DBSA)< PPy-(OBSA)< PPy-(CSA)< PPy-(*p*-TSA). The higher thermal stability in *p*-TSA doped PPy nanofibers originates because of the ordered arrangement of PPy nanofibers chains. Upon SHI irradiation, degradation temperature at a given weight loss increases with increasing ion fluence from 10^{10} ions/cm^2 to 10^{12} ions/cm^2, which is a direct evidence of enhancement of thermal stability in SHI irradiated PPy nanofibers over the pristine sample.

6. Both dielectric permittivity (ε') and dielectric loss (ε'') values are higher in short alkyl chain doped PPy nanofibers as compared to other ABSA doped PPy nanofibers. Moreover, upon SHI irradiation the values of dielectric permittivity and dielectric loss increase with increasing the irradiation fluence.

7. The imaginary modulus (M'') spectra of PPy nanofibers doped with different ABSA dopant indicate that PPy nanofibers doped with short alkyl chain ABSA dopant exhibit smaller relaxation time for charge carriers motion. Also, the asymmetric behavior of the relaxation peak suggests that relaxation mechanism in ABSA doped PPy nanofibers is non-Debye. The perfect overlap of all the individual M'' spectra onto a single master curve indicates that conductivity relaxation process in PPy nanofibers is independent of dopants. However, relaxation peak shifts towards higher frequencies with increasing irradiation fluence which indicates reduction in relaxation time in irradiated PPy nanofibers. Scaling of M'' spectra at different ion fluence suggests that the relaxation dynamics of charge carriers in SHI irradiated PPy nanofibers is independent of irradiation fluence.

8. Studies of ac conductivity reveal that PPy nanofibers doped with short alkyl chain *p*-TSA dopant have higher conductivity as compared to other ABSA doped PPy nanofibers. The decrease in frequency exponent *'s'* with increasing temperature suggests the correlated barrier hopping (CBH) mechanism for

transport of charge carriers in different ABSA doped PPy nanofibers. The scaling of ac conductivity spectra provides a common conductivity relaxation mechanism of charge carriers for different dopants in PPy nanofibers at different temperatures. Upon SHI irradiation, ac conductivity of PPy nanofibers increases and decrease in the value of frequency exponent *'s'* with increasing temperature suggest that correlated barrier hopping (CBH) is the dominant charge transport mechanism in SHI irradiated PPy nanofibers also. The effective barrier height calculations (0.288-0.362 eV) show that polarons are the majority charge carriers in pristine as well as irradiated PPy nanofibers. The scaling of ac conductivity at different ion fluence suggests that conductivity relaxation in irradiated PPy nanofibers is independent of the irradiation fluence.

System III: Polypyrrole nanotubes: Dielectric relaxation and electrical transport studies and swift heavy ion irradiation effects

1. HRTEM studies confirm that average diameter of PPy nanotubes increases from 102 nm to 128 nm with increasing the CSA/Py (dopant/monomer) molar ratio from 0.1:1 to 2:1. The size of tubular micelle increases with increasing CSA concentration which results in PPy nanotubes with larger diameters. Upon SHI irradiation, PPy nanotubes irradiated at the ion fluence of 5×10^{11} ions/cm^2 become more aligned and dense as compared to the pristine PPy nanotubes. However, at the highest irradiation fluence of 10^{12} ions/cm^2, degradation of PPy nanotubes results in random alignments of the PPy nanotubes.

2. XRD studies of PPy nanotubes reveal that crystallinity or ordering of PPy nanotubes chains increases from 25.28 % to 25.96 % and the average domain length increases from 5.78 Å to 6.65 Å with increasing CSA/Py molar ratio from 0.01:1 to 2:1. Moreover upon SHI irradiation, crystallinity of irradiated PPy nanotubes increases from 25.72 % to 31.94 % at the irradiation fluence of 5×10^{11} ions/cm^2, but the crystallinity decreases to 23.40 % at the highest irradiation fluence of 10^{12} ions/cm^2. The decrease in crystallinity at the highest ion fluence can be thought of disintegration of PPy nanotubes chains due to large deposition of electronic energy. Also, upon SHI irradiation the density of PPy nanotubes chains increases up to the ion fluence of 5×10^{11} ions/cm^2 due to

formation of closely packed regions by chain folding, cross-linking of the polymer chains or due to formation of single or multiple helices upon SHI irradiation.

3. FTIR studies depict that "effective conjugation length" increases with increasing CSA/Py ratio which suggests increase in electrical conductivity in PPy nanotubes at higher dopant/monomer ratio. The presence of the same main vibrational bands in SHI irradiated PPy nanotubes for all fluences indicate that the structure of PPy nanotubes is not destroyed upon SHI irradiation. Upon SHI irradiation, intensity of the vibrational bands increases as compared to the pristine PPy nanotubes up to the fluence of 5×10^{11} ions/cm^2, while at the highest ion fluence of 10^{12} ions/cm^2 used in the present work, the intensity of the vibration bands again decreases. The increase in vibration band intensity of irradiated PPy nanotubes indicates SHI irradiation induced cross-linking which increases their crystallinity. However, decrease in vibration band intensity at the highest ion fluence indicates the degradation of PPy nanotubes upon SHI irradiation, which corroborates the XRD results.

4. UV-visible studies of PPy nanotubes indicate that there is a decrease in optical band gap energy from 2.70 eV to 2.55 eV with increase in CSA/Py molar ratio from 0.01:1 to 2:1. The decrease in optical band gap energy is a direct consequence of enhancement of conjugation length in PPy nanotubes leading to an increase in electrical conductivity with increasing dopant/monomer molar ratio. Upon SHI irradiation, both the direct and indirect band gap energies of irradiated PPy nanotubes decrease with increasing ion fluence from 10^{10} ions/cm^2 to 5×10^{10} ions/cm^2, however at the highest ion fluence of 10^{12} ions/cm^2, both direct and indirect band gap energies decrease to a value smaller than that of pristine PPy nanotubes. Also, the value of indirect band gap energy is found to be lower than its corresponding direct band gap energy. The decrease in band gap energy can be attributed to the formation of defects upon SHI irradiation and enriched carbon clusters due to partial evolution of hydrogen. Moreover, upon SHI irradiation, number of carbon atoms per conjugation length (N) and carbon atoms per cluster (M) increase with increasing ion fluence from 10^{10} to 5×10^{11} ions/cm^2, while at the highest ion fluence of 10^{12} ions/cm^2, both the values of N and M decrease as compared to the pristine sample.

5. TGA studies show that with increasing dopant/monomer (CSA/Py) ratio, thermal stability of PPy nanotubes increases. At higher dopant/monomer ratio, due to availability of more dopant anions into the PPy nanotubes chains the interaction between the dopant and polymer chains increases which aligns the polymer chains in an ordered fashion, leading to increased crystallinity resulting in enhanced thermal stability of PPy nanotubes at higher CSA/Py molar ratio. The TGA analysis of irradiated PPy nanotubes indicates that upon SHI irradiation, thermal stability of PPy nanotubes increases with increasing the ion fluence from 10^{10} to 5×10^{11} ions/cm^2, while at the highest ion fluence of 10^{12} ions/cm^2, weight loss decreases to a value smaller than that of the pristine PPy nanotubes. It can be inferred from TGA results that PPy nanotubes irradiated with low and moderate ion fluence (10^{10} - 5×10^{11} ions/cm^2) are thermally and structurally more stable as compared to the PPy nanotubes irradiated with higher ion fluence of 10^{12} ions/cm^2.

6. At lower frequencies, both dielectric permittivity (ε') and dielectric loss (ε'') increase with increasing dopant/monomer (CSA/Py) ratio. Moreover, upon SHI irradiation, dielectric permittivity and dielectric loss of irradiated PPy nanotubes increase with increasing irradiation fluence up to 5×10^{11} ions/cm^2, while at the highest ion fluence of 10^{12} ions/cm^2, the dielectric permittivity and dielectric loss decrease to a value lower than that of pristine PPy nanotubes.

7. Studies of imaginary modulus M'' spectra of PPy nanotubes at different CSA/Py molar ratio show that relaxation time for charge carriers' motion decreases with increasing CSA/Py ratio. The overlap of M'' spectra at different CSA/Py ratio and at different temperature on a single master curve indicates that the relaxation dynamics of charge carriers in PPy nanotubes is independent of dopant/monomer molar ratio as well as of temperature. Upon SHI irradiation, also the relaxation peak in M'' spectra shifts towards the higher frequencies indicating increase in long range motion of charge carriers in irradiated PPy nanotubes which results in decrease in relaxation time of charge carriers' motion. However, at the highest ion fluence used of 10^{12} ions/cm^2, the relaxation time increases to a value higher than that of the pristine PPy nanotubes

indicating decrease in electrical conductivity of irradiated PPy nanotubes at the highest ion fluence.

8. Total conductivity of PPy nanotubes increases with increasing dopant/monomer (CSA/Py) ratio. The decrease in value of frequency exponent '*s*' with increasing dopant/monomer molar ratio indicates that the dispersion of ac conductivity with frequency reduces. The incorporation of dopant CSA anions into the PPy nanotubes chains reduces the charge trapping centres, leading to a large number of charge carrier participation in the conduction process. At higher CSA/Py ratio, number of charge carriers increases which can hop into the neighbouring sites resulting in an increase in electrical conduction. The temperature dependence studies of frequency exponent *'s'* display that charge carriers in PPy nanotubes follow the correlated barrier model. The scaling of ac conductivity at different temperatures indicates that the relaxation dynamics of charge carriers are temperature independent. Upon SHI irradiation, total conductivity of PPy nanotubes is increased as compared to that of the pristine PPy nanotubes, which can be attributed to the increased crystallinity besides formation of the conjugated double bonds. The charge carriers in irradiated PPy nanotubes also follow the CBH model. The scaling of conductivity spectra of irradiated PPy nanotubes at different ion fluence suggests that the conductivity relaxation is independent of the irradiation fluence.

7.2. Limitations and future prospects

The study carried out in the present thesis elucidate the synthesis of different nanostructures viz. nanoparticels, nanofibers and nanotubes of polypyrrole (PPy) using different synthesis methods, characterization of the synthesized nanostructures using different sophisticated techniques, understanding of the dielectric relaxation and electrical transport and swift heavy irradiation induced modifications in them. In spite of the rapid growth in the field of conducting polymer research, there are gap areas which have to be addressed in depth. The conduction mechanism in conducting polymers is still poorly understood. The metallic conductivity has already been achieved in conducting polymers, but the origin of the metallic nature in such materials is still not properly understood.

Among conducting polymers which have emerged as a new class of materials for research interest worldwide, polypyrrole (PPy) occupies a prominent place due to its potential application as compared to other conducting polymers. PPy is an attractive conducting polymer because of its high electrical conductivity, ease of synthesis, environmental stability, biocompatibility, thermal stability, easy processibility etc. The future prospects of the studies carried out in the present thesis are mentioned below:

1. The unique knowledge, gained from the overall studies in the present thesis can be extended to perform similar research by utilizing other nanostructures viz. nanorods, nanoneedles, nanocapsules of PPy and on different conducting polymers like polyaniline (PAni), poly(3,4-ethylenedioxythiophene) (PEDOT), polythiophene (PTh) etc.

2. Being a complex system, in depth studies should be carried out to deepen the understanding of the dielectric relaxation and electrical charge transport mechanisms in different conducting polymer nanostructures with the objective of fundamental interest and various potential applications in devices.

3. Further studies can be focused to find novel, reliable, cost effective synthesis methods for synthesizing different nanostructures of conducting polymers with a view to achieve better performance in device applications.

4. There has not been much focus on studies of swift heavy ion (SHI) irradiation induced modification effects on different physico-chemical properties of conducting polymer based different nanostructures.